

TOWARD THE RAPID GROWTH OF HIGH-QUALITY, POLYCRYSTALLINE RIMLESS,
AND LARGE AREA SINGLE CRYSTAL DIAMOND SUBSTRATES

By

Amanda Charris-Hernandez

A DISSERTATION

Submitted to
Michigan State University
In partial fulfillment of the requirements
for the degree of

Electrical Engineering - Doctor of Philosophy

2017

ABSTRACT

TOWARD THE RAPID GROWTH OF HIGH-QUALITY, POLYCRYSTALLINE RIMLESS, AND LARGE AREA SINGLE CRYSTAL DIAMOND SUBSTRATES

By

Amanda Charris-Hernandez

Silicon has been the common choice as semiconductor material since the 1960s, and it still constitutes more than 90 percent of the electronic device types available in the market. The most pressing and visible problem with silicon is its thermal conductivity. The use of cooling systems is inefficient and serve as a major source of waste. Electronic applications require an alternative to silicon that enables devices to be smaller, cooler, faster, powerful, and cleaner. Diamond is the ideal alternative material; it can perform at higher temperatures than silicon without degrading, it can be efficiently cooled, and it tolerates high voltages before breaking down. Therefore, the growth of high-quality single crystal diamond is imperative for further advancing optical and electronic applications of diamond. Industrial applications require large and defect-free SCDs grown at high growth rates and at low cost. The primary objective of this investigation is to address the big challenges facing the diamond growth: (1) the rapid growth, (2) the growth of high quality, and (3) the large volume growth of single crystal diamond (SCD). In this thesis research activity, the growth of SCD is performed in a MSU-design microwave plasma cavity reactor at a constant pressure of 240 Torr and high discharge power densities that are $> 500\text{W}/\text{cm}^3$. SCD substrates were successfully grown using specially selected and optimized pocket holder designs. These pocket holder designs create an appropriate thermal environment to shield the diamond substrate from the intense microwave

discharge. A growth recipe using these pocket holders was developed. This growth recipe controls the substrate temperature (T_s) and the incident microwave power (P_{inc}) in a prescribed function of growth time. This growth recipe allows for a polycrystalline diamond (PCD) rimless, uniform single SCD growth process. In one continuous process run PCD rimless and increased diamond surfaces areas of over 2 times were achieved. Specifically, an extensive exploration of the pocket holder diamond growth process was experimentally performed using 3.5 mm x 3.5 mm diamond seeds. During these experiments, the substrate temperature T_s was held constant at $1020^{\circ}\text{C} \pm 5^{\circ}\text{C}$ while the growth time, input power, and pocket depth were varied. Thick (up to 1.9 mm) and enlarged surfaces (up to 2 times) were grown in one continuous process run. After laser cutting and polishing high quality diamond plates with low-stress and low defect densities were obtained. By varying the pocket aperture, enlarged PCD rimless surfaces (up to 2.3 times) were grown in one process run. It was found that, there is a range of optimal pocket depths and apertures that can grow SCD both vertically and horizontally. One more diamond growth step was added to the smooth and large diamond top surfaces of the first growth step. In these extra growth experiments, the resulting grown SCD substrates had a top surface area that was enlarged up to 2.7 times. Finally, the lateral SCD growth versus time was photographically evaluated while the growing diamond substrate still was completely in the pocket. Results show the lateral growth of SCD as a function of time and also show the PCD growth on the substrate holder as a function of the time. This photographic technique is very useful in investigating in-situ CVD diamond growth as a function of time and can be employed in many other CVD diamond growth experiments.

Copyright by
AMANDA CHARRIS-HERNANDEZ
2016

Diamonds are forever, just as:
Sonia, Jonathan, Daimer, Ainara, and Sugi

TABLE OF CONTENTS

LIST OF TABLES	x
LIST OF FIGURES	xi
CHAPTER 1	1
INTRODUCTION.....	1
1.1 Motivation	1
1.2 Research Objectives.....	6
1.3 Thesis outline	11
CHAPTER 2	14
LITERATURE REVIEW: DIAMOND MATERIAL AND SINGLE CRYSTAL DIAMOND GROWTH VIA MICROWAVE PLASMA ASSISTED CHEMICAL VAPOR DEPOSITION	14
2.1 Introduction.....	14
2.2 Structure and Material Properties of Diamond.....	14
2.3 Historical Overview of the CVD Diamond Process	18
2.4 Processes of Diamond Growth	19
2.4.1 Phase Diagram of Carbon	19
2.4.2 HPHT Diamond Growth	20
2.4.3 CVD Diamond Growth	22
2.5 Physical and Chemical Aspects of CVD Diamond.....	22
2.5.1 General Overview of the Surface Reactions.....	22
2.5.2 The Specific Diamond Growth Reactions	27
2.5.3 Growth of Defects.....	31
2.5.4 Numerical Modeling of the Harris-Goodwin Model	33
2.6 MPACVD Growth of Diamond	35
2.6.1 Pyramidal Hillocks and Non-Epitaxial Crystallites	38
2.6.2 Step bunching	40
2.6.3 Effect of Growth Parameters.....	42
2.7 Review of Single Crystal Diamond Growth via MPACVD	53
2.7.1 Carnegie Institute of Washington, USA	54
2.7.2 Diamond Research Center, AIST, and Osaka University, Japan.....	56
2.7.3 LIMHP/CNRS, Paris, France – Recent Results	70
2.7.4 Gemological Institute, China University of Geosciences, China	85
2.7.5 Michigan State University, USA.....	89
CHAPTER 3	101
DESCRIPTION OF THE EXPERIMENTAL EQUIPMENT AND EXPERIMENTAL PROCEDURE	101
3.1 Introduction.....	101
3.2 Experimental Setup	101

3.2.1 Microwave Power Supply subsystem	103
3.2.2 Process Gas Delivery Subsystem	104
3.2.3 Vacuum Pumping Control Subsystem	104
3.2.4 Air and Water Cooling Control Subsystem	106
3.2.5 Exhaust Line Subsystem	108
3.2.6 Optical and Photographic Diagnostic Subsystem	109
3.2.7 The Main Operations Windows.....	113
3.2.8 Method of System Operation	116
3.3 Experimental Apparatus – MSU Reactor C	117
3.3.1 Overview.....	117
3.3.2 Electromagnetic Focus	118
3.3.3 Description of the Classic Reactor.....	120
3.4 Diamond Seeds for the Growth Process.....	124
3.4.1 The Diamond Seed Cleaning Procedure – Wet Chemistry.....	125
3.5 The Pocket Holder.....	127
3.5.1 Pocket Holder Preparation.....	128
3.5.2 Pocket Substrate Holder Configuration	128
3.6 System Startup	135
3.6.1 Introduction.....	135
3.6.2 The Diamond Seed Loading into the Microwave Cavity Reactor	136
3.6.3 Discharge ignition	137
3.6.4 Microwave Plasma Assisted CVD Processing	138
3.6.5 System Shutdown.....	140
3.6.6 Unloading the diamond substrate	141
3.7 Grown Diamond Substrates Measurements	141
3.7.1 Measurement of Substrate Temperature	142
3.7.2 Linear and Lateral growth rate (V_{100} and V_{111})	142
3.8 Main Analytical Instruments.....	144
3.8.1 SCD Surface Morphology and Surface Area	144
3.8.2 Scanning Electron Microscopy (SEM)	145
3.8.3 Secondary Ion Mass Spectrometry Analysis (SIMS)	146
3.8.4 Birefringence Imaging.....	147
3.8.5 Etch Pits Analysis	148
CHAPTER 4.....	151
MPACVD GROWTH OF SINGLE CRYSTALLINE DIAMOND SUBSTRATES WITH PCD RIMLESS AND EXPANDING SURFACES	151
4.1 Introduction.....	151
4.2 Background	152
4.3 Experimental details	154
4.4 The growth process recipe	155
4.5 Experimental results	157
4.6 The growth strategy	161
4.7 A comparison to earlier results	163
4.8 Summary remarks	164

CHAPTER 5	166
SINGLE CRYSTAL DIAMOND GROWTH AT CONSTANT SUBSTRATE TEMPERATURE (Ts)	166
5.1 Exploring Constant Substrate Temperature and Constant High Pressure SCD Growth Using Variable Pocket Holder Depths	166
5.1.1 Research Highlights	166
5.1.2. Introduction	167
5.1.3 Background	168
5.1.4 Experimental Details	171
5.2. The Single Crystal Diamond Growth Process	176
5.2.1 The SCD growth recipe: constant temperature deposition	176
5.2.2 Stopping the SCD growth process	179
5.2.4 Varying the input power and adjusting the reactor for the different pocket holder depth recipes.	183
5.3. Experimental Results	183
5.3.1 SCD Growth versus time	183
5.3.2 SCD growth versus pocket holder depth	188
5.4 SCD Plate Characterizations	196
5.4.1 Overview	196
5.4.2 Birefringence imaging	197
5.4.3 Etch pits analysis	200
5.4.4 Secondary ion mass spectroscopy (SIMS)	204
5.5 SCD growth versus methane concentration	205
5.5.1 Growth Conditions	205
5.5.2 Linear and Lateral Growth Rates	206
5.5.3 Surface morphology	208
5.6 Summary Remarks	210
 CHAPTER 6	 213
SINGLE CRYSTAL DIAMOND GROWTH: (1) USING VARIABLE POCKET HOLDER APERTURES AND (2) ADDING AN RE-GROWTH EXPERIMENTAL RUN	213
6.1 Introduction	213
6.2 Experimental Details: Variation of the Pocket Aperture	215
6.3 Experimental Results: Variation of the Pocket Aperture	216
6.3.1 SCD Growth versus time	216
6.3.2 SCD growth versus growth time, pocket width, and pocket depth: the evolution of the crystal versus time.	225
6.3.3 Summary Remarks: Variation of the Pocket Aperture	233
6.4 Experimental Details: SCD Re-growth and Expanding Surfaces	234
6.5 Experimental Results: SCD Re-growth and Expanding Surfaces	236
6.5.1 SCD Re-growth Criteria	236
6.5.2 SCD Re-growth – Expanded surfaces	239
6.5.3 Summary Remarks: SCD Re-growth and Expanding Surfaces	243

CHAPTER 7	244
PHOTOGRAPHIC EVALUATION OF THE SCD SURFACE GROWTH VERSUS TIME	244
7.1 Introduction	244
7.2 Photographic Images Processing and Video Creation	245
7.3 Data Acquisition	248
7.4 Preliminary Results	250
7.5 Summary Remarks.....	255
 CHAPTER 8	 256
SUMMARY AND FUTURE WORK.....	256
8.1 General Summary	256
8.2 Accomplishments	258
8.3 Publications Resulting from this Dissertation Research	260
8.4 Future Work	261
 REFERENCES.....	 262

LIST OF TABLES

Table 2. 1 Principles properties of diamond [21].	17
Table 2. 2 Growth rates ranges in MPACVD diamond growth [49]–[53].	38
Table 2. 3 Carnegie Institution of Washington diamond growth parameter reported.....	56
Table 2. 4 Growth parameters for SCD by Diamond Research Center, Japan	58
Table 2. 5 LIMHP/CNRS, Paris, France growth parameter reported.....	71
Table 3. 1 Theoretical TM_{013} and TM_{012} modes.....	120
Table 3. 2 Measured dimensions on HPHT seed	125
Table 5. 1 Growth parameters for SCD growth using the $d_2 = 2.3$ mm and $d_3 = 2.6$ mm pocket holder depths.....	184
Table 5. 2 Summary of different growth versus depth experiments for eleven samples at a substrate temperature of $1020 \pm 5^\circ\text{C}$	189
Table 6.1 Growth parameters for SCD growth using the $w_2 = 6.6$ mm and $w_3 = 7.0$ mm pocket holder apertures at a constant pocket depth of $d = 2.6$ mm	217
Table 6.2 Growth parameters for SCD growth using $w_3 = 7.0$ mm pocket holder aperture at pocket depth of $d = 2.9$ mm	222
Table 7.1 Measured and calculated values of the SCD areas and SCD lateral growth rate for ACH64, ACH55, and ACH78. An instrument manually collected the measured values, and the software collected the calculated.	251
Table 7. 2 Calculated values of the PCD inward growth on the pocket wall for experiments: ACH64, ACH55, and ACH78.	252

LIST OF FIGURES

Figure 2. 1 FCC structure of the diamond crystal [21].	15
Figure 2. 2 Pressure-temperature phase diagram for carbon [31].	20
Figure 2. 3 Schematic of the physical and chemical processes occurring during the CVD growth of diamond [34], [38].	24
Figure 2. 4 A schematic of the reaction process occurring at the diamond surface leading to the stepwise addition of CH ₃ species and diamond growth [33].	26
Figure 2.5 Process map in [CH ₃]-[H] space showing the operating ranges of the main CVD diamond growth processes (from [9]). The evolution of the operating point of the LIMHP reactor as a function of working pressure (from 50 to 300 mbar) and methane concentration.	34
Figure 2. 6 Map of surface morphologies as a function of misorientation angle from the (001) and methane/hydrogen ratio. Three types of morphologies appear. Atomically flat diamond is preferred, which only grows in the region (III) [43].	36
Figure 2.7 Optical microscope images of the epitaxial CVD diamond films grown at 1000°C (a) Sample overview (b) Magnification 20x [49]. (c) Optical micrograph of a 100 μm thick diamond film grown on an on-axis (001) oriented Ib substrate [57]. (d) and (e) CVD diamond film is grown at high temperature (1000°C and 920°C) exhibiting growth pyramids [56], [58].	39
Figure 2.8 Mechanism of two-dimensional nucleation on a wide terrace, beginning of hillock growth [59].	40
Figure 2. 9 Schematic view of step flow growth showing the diffusion of growth species to steps and subsequent flow of steps to the right [59].	41
Figure 2. 10 Optical micrographs of the grown surfaces of CVD diamond with (a), (b) no intentional N ₂ addition and (c) 2 ppm of N ₂ and (d) 6 ppm of N ₂ [58], [63].	42
Figure 2.11 Diamond growth rates as a function of substrate temperature at 4% methane concentration and a 3.8 kW microwave power [54]. Here C _{me} is the methane concentration.	43

Figure 2. 12 The influence of the methane concentration in the diamond growth rate [58]	45
Figure 2.13 Optical microscope images of the diamond films grown at 850°C with methane concentration of (a) 2% (b) 4% (c) 6% and (d) 8% [49].	47
Figure 2.14 Evolution of the growth rate of the CVD diamond films as a function of the injected MW power density in the discharge using 4% of CH ₄ (square dots) or 7% of CH ₄ (triangular dots) [75].	50
Figure 2.15 Optical microscope images of the surface morphology of epitaxially grown diamond films deposited on (001) oriented diamond substrates without (a, b) and with (c, d) nitrogen added to the gas phase [66].	52
Figure 2.16 Carnegie Institution's Geophysical Laboratory diamond is grown at high growth rates with and without nitrogen [14], [87]. (a) SCD plate, (b) 0.2 – 2.2 carat brilliantly cut and polished nitrogen doped light brown colored and near colorless SCD substrate, (c) examples of as-grown SCD substrates after annealing treatment and (d) in image (A) 2.4 carat single-crystal CVD diamond (B, C, D) 2.3 carat diamond after cut and polished [88].	55
Figure 2.17 A 4.65 carat, 10 mm thick SCD substrate grown with 24 deposition runs [10]	58
Figure 2.18 Large CVD diamonds grown by multi-steps high growth rate synthesis process. (a) 10 mm thick, 4.7 carat CVD diamond, (b) 9.6 mm thick, 3.5 carat CVD diamond, (c) 8.7 mm thick, 4.4 carat CVD diamond [11].	59
Figure 2.19 Schematics of newly designed substrate holder together with corresponding results of simulation of plasma, pictures of hydrogen plasma and observed diamond growth rates [102].	61
Figure 2.20 Schematic illustration of “enclosed type” and “open type” holders. The final depth of diamond after the growth “d” is indicated [10].	62
Figure 2.21 Optical microscope images of grown diamond after 1st growth (left) and repetition of growth (right) for open and enclosed type holder. Thicknesses of grown diamonds (t) are indicated in the pictures. A dashed circle indicates a crack formed by repetition of high rate growth [10].	63
Figure 2.22 Lift-off process with ion implantation [108].	64

Figure 2.23 Photograph of freestanding single-crystal CVD diamond plates produced by a lift-off process using ion implantation [94].	65
Figure 2.24 Schematic illustration of a crystal enlarging process by a combination of lift-off process and side-surface growth [94].	66
Figure 2. 25 (a) Photograph of a half-inch seed plate obtained by cutting and polishing the diamond in Fig. 5. (b) Photograph of a half-inch nitrogen-doped single-crystal CVD diamond plate produced under high growth rate (32 $\mu\text{m/h}$) from the seed plate by a lift-off process using ion implantation. (c) Polarized light microscope image of the half-inch single-crystal CVD diamond plate [94].	68
Figure 2. 26 Method steps to produce clones and tiled clones [109].	69
Figure 2. 27 An image of typical tiled clones [109].	70
Figure 2.28 Diamond growth rate as a function of nitrogen addition in the gas phase (MWPD = 95 W/cm^3). Optical and PL images obtained under UV light for an undoped free-standing CVD diamond crystal and a 2 ppm N_2 doped [56].	73
Figure 2.29 Optical images of the samples grown with (a) no intentional N_2 addition, (b) 2 ppm of N_2 (c) 6 ppm of N_2 and (d) 10 ppm of N_2 [63].	74
Figure 2. 30 Effect of growth temperature. Confocal laser microscopy images of 160 μm thick CVD films grown at (a) 920 $^\circ\text{C}$, 7 $\mu\text{m/h}$, (b) 870 $^\circ\text{C}$, 6 $\mu\text{m/h}$ doped [56].	75
Figure 2.31 Optical image of the free-standing CVD diamond samples obtained after laser cutting and polishing and grown with (1) no intentional N_2 addition, (2) 2 ppm of N_2 , (3) 4 ppm of N_2 in the gas phase [63].	76
Figure 2.32 Optical images of the diamond films grown at 95 W/cm^3 and 850 $^\circ\text{C}$ with (a) 2% CH_4 , (b) 4% CH_4 , (c) 6% CH_4 and (d) 7.2% CH_4 [58].	77
Figure 2. 33 From left to right, spatial distributions of microwave power density (MWPD), electron density (N_e), electron temperature (T_e), gas temperature (T_g) and atomic hydrogen density ($[\text{H}]$) for a pure hydrogen plasma ignited inside the LIMHP reactor [9].	78

Figure 2. 34 Schematics of the initial diamond substrate before polishing (a) and of substrates polished into a pyramidal-shape (b) type A, 20° {100}-misoriented, (c) type B, 20° {110}-misoriented [114].	79
Figure 2. 35. Optical images and 3D representation of the sample grown onto 20° {100}-misoriented pyramidal-shape substrates after several growth interruptions. The total thickness of the CVD layer is (a) 90 μm, (b) 270 μm, (c) 500 μm [114].	80
Figure 2.36 Schematic of the complete procedure of self-assembled metallic masks [121]	81
Figure 2. 37 Schematic representation of the experiments (a) Test sample, (b) Reference sample. After each etching step and the resulting final morphology is shown in a (c) test sample, (b) reference sample [121].	82
Figure 2. 38 A thick CVD diamond layer grown on an HPHT diamond substrate hollowed out by a large hole at the (b) beginning, (c) before, and (d) after merging of the growth fronts and disappearance of the hole [122].	83
Figure 2. 39 Laser microscope images of the CVD film grown on an HPHT substrate with a macro hole after plasma etching to reveal dislocations: (a) full-size image showing the underlying square substrate. (b), (c) zoomed into the regions above the substrate and above the hole, respectively, (d) PL UV image of the freestanding CVD diamond plate. (e) Birefringence image of the freestanding plate under cross-polarizers. The white dashed square indicate the position of the edges of the removed substrate [122].	84
Figure 2. 40 The schematic diagrams of the open type substrate holders and enclosed type substrate holders with different recess depths. (The yellow squares represent the seed crystals placed on the substrate holder or in the recess) [123].	86
Figure 2. 41 (a) HPHT seed grown by using an open type substrate holder (d=0mm); (b) HPHT seed grown by using an enclosed type substrate holder (d=2mm) [123].	87
Figure 2. 42 (a) The influence of the recess depth on the main surface growth rate. (b) The influence of the recess depth on the lateral surface and main surface growth rate ratio. Insets: the cross-section schematic diagrams of the samples grown with different recess depths [123].	88
Figure 2. 43 The influence of the recess depth on the FWHM of the diamond layers at the center part and the periphery [123].	89

Figure 2. 44 Comparison of reactor A, B and C (a) absorbed power density versus pressure and (b) growth rate versus pressure [18], [132].	91
Figure 2. 45 A cross-sectional view of SCD synthesis versus time in an open holder (a, b, c). d) The synthesized diamond after 35.5h of deposition time [20].	92
Figure 2. 46 Cross-sectional views of SCD growth process versus time in a pocket holder [20].	93
Figure 2. 47 Optical microscopy images of as-grown SCD substrates with (a) reduced PCD rim and (b) without a PCD rim [124].	94
Figure 2. 48 Birefringence images of a 221 μm thick CVD SCD plate with exposure times of (a) 500ms (b) 2000ms and (c) 5000ms [124].	95
Figure 2. 49 Photographs of the discharge above a 3.5 mm x 3.5 mm SCD substrate in a 1.5-inch molybdenum holder as the pressure is increased from 120 to 400 Torr. The absorbed power is kept constant at 2100 W [12].	96
Figure 2. 50 Discharge power density and volume as a function of the pressure for the discharges utilizing $P_{\text{abs}} = 2100 \text{ W}$ and 3% CH_4 as shown in Figure 2.49. The differentiation between the previously investigated moderate pressure regime and the high pressure regime is indicated by the green dashed line [12].	97
Figure 2. 51 Operational field map for Reactor B using a SCD substrate over the entire pressure regime	98
Figure 2.52 Linear growth rate and weight gain as a function of the process pressure and	99
Figure 2.53 Top surface of SCD films grown in the pressure range between 240 and 400Torr [12].	100
Figure 3. 1 Overall setup of MSU microwave plasma cavity Reactor C system [85]. ..	102
Figure 3. 2 Components of standard microwave power supply subsystem	103
Figure 3. 3 Cooling water supply	108
Figure 3. 4 Optical and Photographic subsystem on microwave cavity reactor C. (1) Pyrometer, (2) CANON camera.	110

Figure 3. 5 Camera Arduino control map for microwave cavity reactor C [134].	112
Figure 3. 6 (a) Diagram of the Arduino circuit and (b) photograph of the completed operational Arduino circuit [135].	113
Figure 3. 7 The standard view panel operation window	114
Figure 3. 8 The schematic view panel operation window	115
Figure 3. 9 Electromagnetic fields, TM _{01n} modes (n = 2 left, n = 3 right) [137].	118
Figure 3. 10 Three typical discharges (in green) that result from exciting the cylindrical cavity applicator with the TM ₀₁₃ mode [137]. The red lines are the magnetic field patterns and the blue lines are the electric field patterns.	119
Figure 3. 11 Cross-sectional view of the MCPR [139].	122
Figure 3. 12 Optical microscope image of the side view of the 3.5 mm x 3.5 mm x 1.4 mm HPHT seed.	125
Figure 3. 13 Isometric drawing view of a 64.7 mm substrate holder.	129
Figure 3. 14 (a) A schematic side view of the microwave cavity plasma Reactor C with a (b) zoom of the substrate holder setup.	130
Figure 3. 15 Side cross sectional view of conventional pocket holder (unit: mm) that was used in the experiments in Chapter 4.	132
Figure 3. 16 Drawings of the pocket holder for SCD growth at variable pocket depths (unit: inches) that was used in the experiments in Chapter 5.	133
Figure 3. 17 Side and top view of the pocket holder with a varied width (unit: mm)	134
Figure 3. 18 Side view of the pocket holder used for SCD re-growth process (unit: mm) that are described in Chapter 6.	135
Figure 3. 20 Plasma in an ideal contact with the substrate	138
Figure 3. 21 Operating field maps and matching, i.e., P_{ref}/P_{inc} , versus absorbed power for three constant pressure conditions: 120, 180, and 240 Torr [141].	140

Figure 3. 22 Optical microscope image of the side view of the as-grown diamond substrate. The red arrows show the lateral and linear growth direction. The dashed red lines identified the dimensions of l_1 and l_2 .	143
Figure 3. 23 Optical microscope image of the top view of the as-grown with a white circle drawn around the diamond shape.	145
Figure 3. 24 Schematic of SIMS analysis system [143]	147
Figure 3. 25 (a) optical image of ACH09 plate and (b) image enhanced	149
Figure 3. 26 General view of the images processing tool.	150
Figure 4. 1 Thick PCD rim growth on SCD substrate using a conventional open holder growth method.	153
Figure 4. 2 Growth process recipe displaying a process cycle variation of T_s and P_{inc} versus growth time for substrate ACH23 (shown in Figure 4.3).	156
Figure 4. 3 Optical microscope images of (a) ACH23. Close up views of the substrate in (b) – (d) show rimless growth with larger SCD area.	158
Figure 4. 4 Optical microscope images of (a) ACH24. Close up views of the substrate in (b) – (d) show rimless growth with larger SCD area.	159
Figure 4. 5 Side view images of (a) ACH23 and (b) ACH24 indicate outward growth of the CVD SCD substrates.	160
Figure 4. 6 SEM images of (a) ACH23 and (b) ACH24 indicate PCD rim free CVD SCD substrates.	160
Figure 4. 7 Outward growth of the CVD SCD substrates [20].	164
Figure 5. 1 Conventional pocket holder design geometry for SCD growth (top side). The pocket substrate holder placed on the reactor cooling stage (bottom side)	173
Figure 5. 2 Reactor operating field map	177
Figure 5. 3 Diamond growth recipe versus time for pocket depth of (a) $d_2 = 2.3$ mm and (b) $d_3 = 2.6$ mm	178

Figure 5. 4 (a) As-grown uncleaned SCD with the top surface is still entirely within the 2.6 mm deep pocket; (b) cross-sectional schematics when the grown diamond (in blue) is still within the pocket; (c) optical microscope images of side and top views of as-grown and cleaned diamond substrate (ACH02). Note that the bottom yellow region is the original HPHT diamond seed. The green square represents the the original seed boundary.....	180
Figure 5. 5 The ACH22-b SCD which has grown out the pocket; (b) the associated cross-sectional schematic of the grown SCD when it has grown out of pocket; (c) optical microscope images of side and top view of a grown diamond substrate (ACH22-b).....	182
Figure 5. 6 Optical microscope top surface images of substrates samples listed in Table 1. For $d_2 = 2.3$ mm (a) 10 hours, (b) 24 hours, and (c) 48 hours. For $d_3 = 2.6$ mm (d) 10 hours, (e) 24 hours, (f) 48 hours and (g) 60 hours.....	186
Figure 5. 7 Optical microscope images of the typical samples shown in Table 2 that were grown in pocket depths of (a) 2.0 mm, (b) 2.3 mm, (c) 2.6 mm and (d) 2.9 mm.....	190
Figure 5. 8 Morphology shapes and the growth rate versus pocket holder depth for experimental data for Table 5.1 and Table 5.2. The square surface is associated with pocket depths of 2.0 and 2.3 mm. The circular surface is associated with long runs of the pocket depth of 2.6 mm, and the octagon shape surface is associated with the shorter runs that used the pocket depths of 2.6 and 2.9 mm.	193
Figure 5. 9 The ratio between lateral growth rate, V_{110} , and vertically growth rate, V_{100} , versus pocket depth. Insets are SEM images of the corners of the SCD substrates.	194
Figure 5. 10 Plot summarizing the normalized lateral CVD area gain versus vertical thickness gain for different pocket depths for the experimental data listed in Tables 5.1 and 5.2.	195
Figure 5. 11 CVD plates after laser cutting and mechanical polishing. The measured thickness gain for each sample was: 274 μm for ACH22, 255 μm for ACH20 and 600 μm for ACH33.	197
Figure 5. 12 Examples of two as-grown SCD with their corresponding birefringence images. (a) ACH20 and (b) ACH33.	199
Figure 5. 13 (a) Etched surface of the polished CVD plate ACH33 and (b) Etched surface of a unpolished CVD plate ACH20.....	201

Figure 5. 14 SEM images of the pits in three different areas on CVD plate ACH09 (a) one side at the edge, (b) somewhere at the center (c) somewhere on the center of the top surface.	203
Figure 5. 15 Comparison of the etch pit density with recent results.	204
Figure 5. 16 Nitrogen concentration in (a) SCD CVD plate ACH33 and (b) SCD CVD plate ACH20. The red line indicates the detection limit of the instrument.	205
Figure 5.17 Growth rates of CVD diamond grown as a function of the methane concentration under growth conditions of 3.5 kW - 2.4 kW, 1020 °C and 240 Torr.	207
Figure 5.18 Optical microscope images of the top surface of grown SCD substrates for methane concentrations of (a) 4%, (b) 5%, (c) 6% and (d) 7%.	209
Figure 5. 19 Optical high magnification images of substrate grown at (a) 4 % methane and (b) 5 % methane.	210
Figure 6.1 Optical microscope top surface images of substrates listed in Table 6.1, for $w_2 = 6.6$ mm (a) 12 hours, (b) 16 hours, (c) 30 hours, (d) 30 hours, (e) 48 hours, (f) 50 hours, and (g) 55 hours. Note that ACH55 has smooth edges and a decreasing top surface.	218
Figure 6.2 Optical microscope top surface images of substrates listed in Table 6.1, for $w_3 = 7.0$ mm (a) ACH79 after 12 hours of growth, (b) ACH71 after 30 hours, and (c) ACH78 after 45 hours of growth.	221
Figure 6. 3 Optical microscope top surface and side view of images of substrates listed in Table 6.2, for $w_3 = 7.0$ mm a constant pocket depth of $d = 2.9$ mm (a) 45 hours, (b) 40 hours and (c) 50 hours. Note: that the substrate ACH72 have a dark spot on the left bottom side it is a crack on the top surface that was produced at the experimental run when the substrate was removed from the pocket.	223
Figure 6.4 The total average lateral growth rate versus pocket aperture at 12 and 45 hours of growth time	224
Figure 6.5 Normalized area gain versus growth time at different pocket configurations from experimental data provided in Table 6.1, Table 6.2, and selected results of Chapter 5 grown in pocket depth of 2.6 mm.	226

Figure 6.6 Plot summarizing the normalized lateral CVD area gain versus growth time for different pocket apertures and depths for the experimental data listed in Tables 6.1, Table 6.2, and selected data from Table 5.2.	227
Figure 6. 7 Photographic images in the frame time of 0, 12, 24, 40, 50 and 55 hours. The opaque yellow polygon layer represents the HPHT seed inside the pocket. The orange polygon layer identifies and outlines the grow SCD during the indicated time frames.....	229
Figure 6. 8 The ratio between lateral growth rate, V_{110} , and vertically growth rate, V_{100} , versus growth time for three different pocket holder apertures.	230
Figure 6.9 Plot summarizing the normalized lateral CVD area gain versus vertical thickness gain for different pocket holder geometries for the experimental selected data from Table 6.1 and Table 6.2 and the results of Chapter 5. Short run data and long run data from this section are indicated by the grown and res data points respectively.	232
Figure 6.10 Schematic of the re-growth process. After the 1 st growth step process, the grown substrate is placed in an optimized substrate holder.....	236
Figure 6.11 Optical microscope images of (a) top view of ACH26 after the 1 st growth step, (b) top view of ACH26-2 after the 2 nd growth step, and (c) side view of the ACH26-2.	238
Figure 6. 12 Optical microscope side view images of ACH36 after the (a) 1st growth step and (b) 2nd growth step.	239
Figure 6. 13 Optical microscope side view of (a) and (b) substrate ACH23 after the 1 st and 2 nd growth step, (a) and (b) substrate ACH27 after the 1 st and 2 nd growth step, and (e) top view and (f) side view of substrate ACH34 after the 1 st and 2 nd growth step.....	241
Figure 6. 14 Normalized lateral area gain versus vertical thickness gain	242
Figure 7.1 Experimental setup for photographs and video recording for SCD lateral growth analysis	247
Figure 7.2 Schematic of the data acquisition process. The photographed experiment showed in the flow diagram is ACH78. A total of 1277 pictures were captured.....	249

Figure 7.3 The outward SCD growth and the inward PCD growth versus growth time for substrate ACH64. 253

Figure 7.4 The outward SCD growth and the inward PCD growth versus growth time for (a) substrate ACH64 and (b) substrate ACH78..... 254

CHAPTER 1

INTRODUCTION

1.1 Motivation

Over centuries, diamond has been used as a precious gemstone and as an ultra-hard industrial material. Diamond unites a rich collection of distinctive physical and chemical properties, which makes it a valuable and strategic material for many engineering applications. The exceptional compact structure of diamond arises from two basic concepts: (i) the carbon atoms are small and light, with short range bonds in the diamond structure [1], and (ii) the carbon atoms form very strong covalent bonds [2]. It has long been acknowledged that diamond is an excellent material with other outstanding properties, such as optical, mechanical, thermal, electrochemical, chemical, and electronic properties [1], [3], [4], [5] that also outclass competing materials. When these properties are combined, they offer an engineering material with a tremendous potential for use in a wide range of applications in optics, semiconductors, microelectronics, biomedical and manufacturing engineering. However, despite its extraordinary potential for a wide variety of scientific and industrial applications, the high cost and the low volume of diamond substrate manufacturing limits the diamond material market to just a few high-end applications. Currently, the researchers are attempting to overcome the low volume

and small physical size of the CVD diamond by developing technologies that grow high-quality diamond at low manufacturing cost and larger sizes.

In order to overcome the availability and crystal quality issues, scientists have developed different technologies for diamond growth in the laboratory. Currently, the two major approaches that can growth diamonds are the high-pressure high-temperature (HPHT) process and the microwave plasma assisted chemical vapor deposition (MPACVD) process.

The HPHT technique to grow diamond from graphite to a single crystal seed that is suitable for jewelry was first to develop during the last several decades [6], [7]. The diamond crystals produced with the HPHT technique can have high purities but in the past, have been limited in size and cost. However, now HPHT crystals are grown up to 3 carats and are available commercially. The high cost is due to the large size of the manufacturing equipment, namely the large hydraulic presses that are required to grow these diamonds. To increase the sizes of the HPHT diamonds, the size of the hydraulic presses become quite large, resulting in an expensive cost. After being polished and being faceted, HPHT diamonds are rarely larger than 1.5 carats. In the past diamond crystal grown by HPHT, seed technique has not been suitable for electronic and optical applications. However, in the future, the availability of large and low-cost single crystal HPHT diamonds would not only impact the gem fine jewelry market but also would open up many more research and industry applications.

Recently, the MPACVD process has been identified as a very promising method for commercially growing high quality diamond [8]. In this process, the microwave power is coupled into the reactor via a coupling waveguide located at the top of a plasma cavity

reactor. A vacuum pump system is attached to the inside of the cavity applicator and maintains a constant working pressure while the input gases are flow into the bell jar located inside the cavity applicator. Compared with other diamond growth methods, the MPACVD process provides controlled and repeatable growth conditions versus time and the results can be reproduced at a reasonable cost. During the current decade, many scientists and engineers have developed standard MPACVD single crystal diamond (SCD) growing processes which overcome some of the constraints of the HPHT process. The CVD technology can provide diamond substrates with much larger sizes, higher quality and with high growth rates, i.e. 50 μm – 100 μm [9]–[11] [12] at high process pressures. This indicates that the MPACVD diamond growing method has the potential for becoming low-cost and high-quality diamond growth process.

The diamond growth by MPACVD has been investigated over a wide window of growth parameters, such as pressures, nitrogen content, methane concentration and reactor configurations. Most notably C.S. Yan et al. [13] in 2002, reported that MPACVD SCD crystals can be produced at growth rates up to 150 $\mu\text{m}/\text{h}$ at pressures of 200 Torr by adding a small amount of nitrogen into the gas fed (1 – 5 % N_2/CH_4). A few years later the followed up their previous results by demonstrating a ten carats of CVD grown SCD 1 cm in thickness at growth rates of up to 100 $\mu\text{m}/\text{h}$ at pressures up to 300 Torr with the addition of nitrogen concentrations (10 % N_2/CH_4) [14].

Most recently, In 2017 E.V.Bushuev. et al. [15] reported the growth of CVD diamond films at a constant pressure of 130 Torr and variable methane concentrations of 1%, 4%, 7%, 10%, and 13%. They found that growth rates strongly depended on the methane concentration and substrate temperature. The low growth rate (0.5 $\mu\text{m}/\text{h}$) was obtained

at 1% CH₄/H₂ at substrate temperature (T_s) = 800 °C. The higher growth rate (82 µm/h) was achieved at a high methane concentration of 13% at $T_s = 965 \text{ °C} \pm 15 \text{ °C}$. These results were consistent with the results measured earlier at Michigan State University by Lu et al. in 2013 [16].

Silva et al. [9] developed a numerical, theoretical plasma model that was used to calculate the species concentrations of a typical cylindrical microwave plasma reactor. This model calculated the species distribution of the different gas species in plasma discharge for diamond growth as a function the growth parameters, such as pressures, methane concentration, and substrate temperature. They concluded that at high temperatures, the desorption of CH₃ and C₂H₂ species becomes more rapid, and competes with the carbon incorporation reactions. At high pressures, there is a significant increase in atomic hydrogen density and the CH₃ radical density. As the operating pressure is increased both the hydrogen species densities, and the CH₃ radical densities increased, but the hydrogen density increased versus pressure 10 – 1000 times faster than the CH₃ concentration. Therefore, both the growth rate and the diamond quality increases [17].

This thesis investigation aims at encouraging the growth of high-quality single crystals: (1) at a very high growth rates and in an almost nitrogen-free growth process, (2) growth with an enlarged diamond top surface, and (3) SCD growth with a significantly reduced polycrystalline diamond (PCD) rim. The diamond growth for this thesis has been conducted with an MSU-design microwave plasma cavity reactor (MPCR) which is referred here to as Rector C. This reactor was initially designed and experimentally operated under the efficient and safe conditions as described by Y. Gu et al. [18].

This thesis investigated the growth of diamond versus various experimental variables under constant pressure condition of 240 Torr. The external input conditions versus time included (1) variable substrate temperatures, (2) variable input powers, (3) constant substrate temperatures, and (4) variable methane concentrations. Another variable that was investigated was the size and the shape of the substrate pocket holder. The pocket holder was introduced by Asmussen et al. [19] and later investigated by Nad et al. [20].

One goal of this thesis investigation was to explore the influence of the pocket holder geometry on the SCD growth process. The variable geometry of the pocket included: (1) several pocket holder depths, (2) several pocket holder apertures, (3) specially designed pocket holders that were used in large diamond seed growth experiments, and (4) specially designed pocket holders that were used in diamond re-growth substrates experiments.

Thus, this thesis investigates a broad range of growth parameters in order to achieve the rapid growth of single crystal diamond plates and cubes. The quality of the grown diamond materials was enhanced by eliminating the polycrystalline diamond that typically surrounds the diamond top surface. The top surfaces of the grown diamond were larger when compared to the grown diamond in previous MSU experimental thesis results. This research also includes some characterization techniques that allows the determination of quality of the grown substrates, such as, birefringence imaging, SIMS analysis, and SEM images. These characterization techniques are employed to evaluate the grown diamond material

1.2 Research Objectives

In this thesis research, the deposition of high quality, PCD rimless single crystal diamond SCD via MPACVD is investigated. The overall objective of this investigation is to develop experimental methods that enable the rapid growth of high quality, large volume, SCD using the pocket substrate holder configuration.

Ultimately it is desired to achieve this diamond growth in one controlled long process step. For this investigation, a series of experiments were performed that explore the growth of SCD over a wide range of input experimental variables. The specific experiments are described below and are divided into six tasks. Each task is described below as a separate set of experiments.

i) Task one

This set of experiments used a pocket holder that was held fixed and then the substrate temperature and microwave input power were varied as a function of the time. i.e. the experiments varied the process recipe, P_{inc} and T_s versus time. This task demonstrated that the application of a specific process recipe, i.e. the real-time control of the input microwave power and hence T_s versus time, over the process cycle, enabled the growth of thicker and larger area SCD while it also eliminates the PCD rim.

Specific objective:

SCD growth is investigated with the following variables:

- a) Constant pocket holder depth (d) and width (w) of $d = 2.3$ mm and $w = 6.0$ mm, respectively.

- b) Microwave input power was varied during the process cycle between of 2.9 kW – 1.9 kW
- c) Constant pressure of 240 Torr
- d) Constant methane concentration 5%
- e) The substrate temperature was varied as a function of the time over the range of 985°C – 1040°C

The detailed results of these experiments are covered in Chapter 4 of this thesis.

i) Task two

This task explored the SCD growth in a pocket holder by varying pocket depths, methane concentrations, and the process cycle. It was desired to grow thick, high-quality SCD without a PCD rim. Therefore, this experimental activity identified the experimental conditions that produced SCD growth without a PCD rim. The experiments were divided up into two sets: (1) when only the pocket holder depth was varied and (2) when only the methane concentration was varied. The experimental results identify pocket holder geometries that yielded PCD rimless growth and associated expanded top SCD surfaces.

Specific objective

This set of the experiments were made under a constant substrate temperature and a constant pressure condition. The microwave input power was varied versus time in order to hold the substrate temperature (T_s) constant. In particular, these experiments explored pocket holder growth under the following experimental conditions:

- a) Constant substrate temperature (T_s) of 1020°C \pm 5°C
- b) Constant pressure of 240 Torr

- c) Constant pocket holder aperture of 6.0 mm for four different pocket holder depths, i.e. 2.0 mm, 2.3 mm, 2.6 mm and 2.9 mm
- d) Variable process times between 12 hours and 60 hours
- e) Variable microwave input power between 2.0 kW and 3.5 kW.
- f) Variable methane concentration between 4% - 7%

The results of these experiments are covered in Chapter 5 of this thesis.

ii) Task three

These set of experiments explored the variation of the geometry of the pocket holder to promote the outward growth of the diamond surfaces. Based on the results of task one and two, two pocket holder depths were used: 2.6 mm and 2.9 mm and four different pocket aperture values were varied: from 6.0 mm, 6.6 mm, 7.0 mm, and 7.6 mm

Specific objective:

The objective was to improve the diamond outward growth of the diamond substrates by enlarging the top surface area. Diamond growth was investigated under the following experimental conditions:

- a) Constant pressure of 240 Torr
- b) Constant substrate temperature (T_s) of $1020^\circ\text{C} \pm 5^\circ\text{C}$
- c) Constant methane concentration (5%)
- d) Variable process time. i.e. 15 hours – 55 hours
- e) Two different pocket depths, i.e. 2.6 mm and 2.9 mm with the following pocket aperture widths of 6.0 mm, 6.6 mm, 7.0 mm, and 7.6 mm
- f) Variable microwave input power between 2.0 kW and 3.0 kW

The results of these experiments are described in Chapter 6 of this thesis.

iii) Task four

Continue the growth process by adding one additional growth step in order to grow thicker and larger area SCD plates.

Specific objective:

Based on the enlarged areas obtained from task one, two, and three the primary objective of this task is to add one growth step and continue expanding the thickness and the top surface area SCD. Re-growth was performed with the following variables:

- a) Specially design pocket holder configuration, i.e. $d = 3.6 \text{ mm}$, $w = 6.2 \text{ mm}$
- b) Microwave input power of $3.0 \text{ kW} - 2.0 \text{ kW}$
- c) Constant pressure of 240 Torr
- d) Constant methane concentration of 5%
- e) Variable process time of 45 hours
- f) Constant substrate temperature of $1020^\circ\text{C} \pm 5^\circ\text{C}$

The results of these experiments are covered in Chapter 7 of this thesis.

iv) Task five

This set of experiments explored the SCD growth when the diamond seed area is increased. The diamond growth process was carried out on large HPHT diamond seeds of $5.0 \text{ mm} \times 5.0 \text{ mm}$ and $7.0 \text{ mm} \times 7.0 \text{ mm}$. Also, a few experiments using $7.0 \text{ mm} \times 7.0 \text{ mm}$ microwave plasma CVD plates were performed.

Specific objective:

To reproduce the results obtained in previous tasks by using large HPHT seed and expand the final grown diamond area. The SCD growth was performed with the following variables:

- a) Specially design pocket holder configuration, i.e. $d = 2.6 \text{ mm}$, $w = 7.7 \text{ mm}$
- b) Constant pressure of 240 Torr
- c) Variable process time between 12 and 45 hours.
- d) Microwave input power of 3.0 kW – 2.0 kW
- e) Constant substrate temperature of $1000^{\circ}\text{C} \pm 5^{\circ}\text{C}$

The results of these experiments are covered in Chapter 8 of this thesis.

v) Task six

This tasks photographically monitors the SCD growth as a function of the time. This set of experiments reveals the evolution of the top SCD surfaces versus time. Photographs were taken during every minute throughout the process cycle in order to analyze the diamond surface evolution during the growth. The results of these experiments are covered in Chapter 9.

1.3 Thesis outline

This thesis is composed of 10 chapters. The thesis content is summarized in the paragraphs below.

Chapter 1 presents a short introduction and overview of the research project. It includes research motivations and research objectives. The major thesis objective is divided into six tasks where each task is described as a separate group of experiments.

Chapter 2 presents a literature review, including the structure and properties of the diamond material and a historical overview of the CVD diamond growth process. The diamond growth processes, i.e. HPHT diamond and CVD diamond growth are discussed. The physical and the chemical aspects of the CVD diamond were also mentioned here. Although the mechanism for diamond growth by CVD is a complex process, this chapter also describes in detail important factors that have to be considered in order to grow diamond by the CVD process. The growth of possible defects may also occur during the CVD growth process. Thus, this chapter presents a brief review of defects in the growing diamond is presented. The effect of the experimental growth variables, such as methane concentration, substrate temperature and the growth versus time aspects are also described. Lastly, a review of SCD growth via MPACVD using a pocket holder is described.

Chapter 3 presents some of the diamond growth experimental procedure and provides detailed description of the MSU Reactor C configuration that was used in this thesis investigation. Here an extensive description of the experimental apparatus is shown. The appearance, properties, and cleaning procedures of the diamond seeds are presented. Also, a description of the pocket holder configuration that was used in this thesis is

presented. The techniques used to characterize the grown diamond samples are also presented.

Chapter 4 investigates the SCD pocket growth process. This Chapter defined conventional, benchmark pocket holder configuration, i.e. the depth, d , and the width, w , of the pocket were held constant at 2.3 mm and 6.0 mm respectively. The process is carried out with this constant pocket geometry and with both a variable substrate temperature and a variable microwave input power as a function of the time. Flat and smooth diamond surfaces were grown with enlarged diamond surface areas due to a high lateral growth rate. These growth results were compared with earlier results [Nad] and showed an improvement in the diamond lateral growth area.

Chapter 5 presents the results of an investigation that explored the SCD growth which was held at a constant substrate temperature of $1020\text{ }^{\circ}\text{C} \pm 5^{\circ}\text{C}$ and a constant pressure of 240 Torr, and were conducted with a constant pocket aperture and with variable pocket depths. The pocket depths were: 2.0 mm, 2.3 mm, 2.6 mm and 2.9 mm. Results revealed that the deeper pockets do not grow larger area SCD crystals but have a reduced lateral growth rate and a reduced area gains and often lead to final SCD crystals with smaller ending surface areas than the initial seed surfaces areas. Shallow pockets have enhanced lateral growth rates and larger area gains. Also, in this chapter, the importance of stopping the diamond growth process before it grows out of the pocket is described in detail. The results from the experimental variation of the methane concentration for a fixed pocket holder are also presented. The results of the characterization techniques, such as SIMS analysis and birefringence images on selected CVD plates are presented.

In order to promote the outward diamond growth, Chapter 6 presents a set of experiments in which the pocket holder depth was held constant while the pocket aperture varied, i.e. the pocket widths were 6.0 mm, 6.6 mm and 7.0 mm. The results showed for a single experimental run the lateral diamond surface could be up to 2.3 times size than the initial original HPHT diamond seed area. The results of the SCD re-growth experiments are shown. One more diamond growth step is added to the smooth and large diamond top surfaces of the first growth step. In these extra growth experiments, the diamond top surface was further enlarged. A new pocket holder was designed to allow the expansion of the top surface area. A new holder configuration is described. The resulting grown SCD substrates had a top surface area that was 2.5 times original HPHT diamond seed area.

In Chapter 7 photographs were taken during several typical diamond growth processes in order to analyze the plasma variation and the lateral SCD growth as a function of the growth time. The results show top surfaces area growths as a function of time and also show the PCD growth on the holder as a function of the time. This result indicated that the PCD growth on the holder should be minimized.

Finally, Chapter 8 presents the conclusions and summary of this thesis research. Also, different future activities are suggested to continue to expand the diamond lateral growth.

CHAPTER 2

LITERATURE REVIEW: DIAMOND MATERIAL AND SINGLE CRYSTAL DIAMOND GROWTH VIA MICROWAVE PLASMA ASSISTED CHEMICAL VAPOR DEPOSITION

2.1 Introduction

Diamond is one of the most unique materials which have ever been discovered. It has a group of excellent physical and chemical properties. Whether it comes from nature or it is human-made, it has superior material properties when compared with all other materials. However, currently, the lab-grown diamond materials usually have few defects that are commonly seen in the natural diamonds. Among the diamond growth methods, chemical vapor deposition (CVD) of diamond has recently received a great deal of attention in the material sciences because it has been used in many new applications of diamond that had previously been either too expensive to implement or too difficult to make.

2.2 Structure and Material Properties of Diamond

Diamond is the sp^3 -bonded allotrope of carbon. Figure 2.1 shows a unit cell of a diamond crystal, which is composed of eight corner atoms, six face-centered atoms and

four internal atoms along the cube diagonals. A diamond unit cell contains eight C atoms. The crystal structure can be viewed as two interpenetrating FCC lattices, offset from one another along a body diagonal by one-quarter of its length. Each carbon atom bonds with four other carbon atoms to form a tetrahedral configuration.

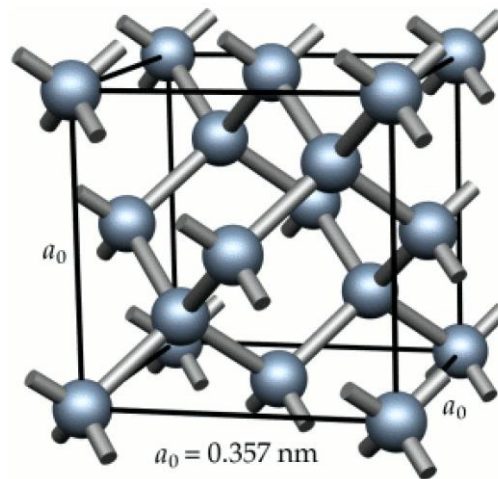


Figure 2. 1 FCC structure of the diamond crystal [21].

At room temperature, the lattice constant a_0 for diamond is equal to 3.567 \AA (0.3567 nm), from which a few other quantities can be derived. The C-C bond length d is equal to a quarter of the cube diagonals, that is: $d = \sqrt{3}a/4 \cong 1.54 \text{ \AA}$

The corresponding C atomic radius, R , is given by:

$$R = \frac{d}{2} = 0.077 \text{ nm} \quad (1)$$

And its Atomic Packing Factor (APF) can be calculated as:

$$APF = \frac{\text{volume.of.atoms.in.a.unit.cell}}{\text{total.unit.cell.volume}} = \frac{V_s}{V_c} \quad (2)$$

The volume of a sphere is $\frac{4}{3}\pi R^3$, since there are eight atoms in diamond unit cell, therefore,

$$V_s = (8) \frac{4}{3} \pi R^3 = \frac{32}{3} \pi R^3 \quad (3)$$

And the total unit cell volume for diamond is $V_c = a_0^3$. From equation (1), we have

$$R = d/2 = \frac{\sqrt{3}}{4} a_0 / 2 = \frac{\sqrt{3}}{8} a_0 \quad (4)$$

Therefore,

$$APF = \frac{V_s}{V_c} = \frac{\frac{32}{3} \pi \left(\frac{\sqrt{3}}{8} a_0 \right)^3}{a_0^3} = 0.34 \quad (5)$$

The density can be calculated by

$$\rho = \frac{nA}{V_c N_A} \quad (6)$$

Where:

n is the atomic number in each diamond unit cell;

A is the atomic weight, for carbon, it is 12.011 g/mol;

N_A is the Avogadro number; it is 6.023×10^{23} atoms/mol

Hence,

$$\rho = \frac{(8 \text{ atoms/unit.cell}) \cdot (12.011 \text{ g/mol})}{(0.357 \text{ nm})^3 \cdot (6.023 \times 10^{23} \text{ atoms/mol})} = 3.515 \text{ g/cm}^3 \quad (7)$$

This value is much higher than that of graphite (approximately 2.3 g/cm³)

The structure of diamond accounts for its outstanding properties. Some of the outstanding properties of diamond are listed below in Table 2.1.

Table 2. 1 Principles properties of diamond [21].

Property	Value	Units
Hardness	1.0×10^4	kg/mm ²
Strength, tensile	>1.2	GPa
Friction Coefficient	0.03	Dimensionless
Sound velocity	1.8×10^4	m/s
Density	3.52	g/cm ³
Young's modulus	1.22	GPa
Thermal expansion coefficient	1.1×10^{-6}	K ⁻¹
Thermal conductivity	900 – 2320	W/mK
Debye temperature	2000	K
Optical transmissivity (from nm to far IR)	225	Dimensionless
Dielectric constant	5.7	Dimensionless
Electron mobility	1800 – 2200	cm ² /V-sec
Hole mobility	1200 – 1600	cm ² /V-sec
Electron saturation velocity	2.7×10^7	cm/s
Work function on (111) surface	Negative	eV
Bandgap	5.45 – 5.50	eV
Resistivity	$10^{13} - 10^{16}$	Ω -cm

These properties demonstrate the suitability of diamond as a potential candidate to be an engineered research material for many applications. It is well-known that diamond is the hardest substance found in nature, and it is well-known that diamond is four times harder than the next hardest natural mineral, corundum (sapphire and ruby) [22]. Regarding diamond's physical properties, diamond is the ultimate material in several ways including: (1) its extreme hardness, (2) it has a value of 10 on the Mohs scale of mineral hardness, and (3) it is at the top of the hardness scale. Diamond has excellent properties including a wide-range of optical properties; excellent thermal conductivity; low coefficient of thermal expansion; the highest melting point; and remarkable semiconductor properties [23].

2.3 Historical Overview of the CVD Diamond Process

The synthesis of diamond has been pursued ever since the French chemist Antoine Laurent Lavoisier discovered that diamond was a form of crystalline carbon [24]. The first report describing successful diamond synthesis using HPHT methods was published in 1955 [25], in which diamond was crystallized from solvated metal carbon at high pressures of pressures of 7 – 10 GPa and temperatures of $\sim 1800^{\circ}\text{C}$. Experiments with low-pressure synthesis had been ongoing in both the United States and the Soviet Union during the same period. In 1962 the first patent emerged by William Eversole at the Union Carbide Corporation [26] who reported diamond synthesis under low pressure by a CVD method. The diamond was grown on diamond substrates with the use of carbon-containing gasses at a pressure of 10 bar and a temperature of around $800 - 1000^{\circ}\text{C}$. In the mid-1970's Spitzyn a Soviet group [27] showed that diamond crystallization by CVD should preferably be carried out at reduced pressure. Also, he reported diamond crystals up to several tens of microns in thickness were also grown on non-diamond substrates. This is a significant achievement as growth had only previously been possible on diamond substrates. In 1974 research on CVD diamond growth was initiated in Japan. During 1981 S. Matsumoto et al. [28] reported using a Hot Filament CVD technique in which atomic hydrogen was incorporated into the growth process to give good quality films on some substrates with significantly better deposition rates, making lab-grown diamond for the first time potentially commercially attractive. They also were the first to report on rapidly growing diamond by microwave plasma assisted CVD. Diamond was grown at pressures of 10 - 100 Torr and temperatures were around $800 - 1000^{\circ}\text{C}$. Widespread interest developed from there, and at present many other plasmas assisted, and thermally

assisted CVD deposition methods have been established. The deposition method that currently has the best potential for obtaining high-quality diamond substrates is the microwave plasma assisted CVD (MPACVD) [29].

2.4 Processes of Diamond Growth

2.4.1 Phase Diagram of Carbon

Figure 2.2 shows the phase diagram of carbon, describing the equilibrium phase structure of carbon at different temperatures and pressures [30]. It can be seen from the Figure 2.2, under relatively low pressures (the bottom region of the Figure), graphite, the most common form of carbon, and is stable from room temperature up to its melting temperature at approximately 4000°C. Whereas diamond is meta-stable at low-pressure, low-temperature conditions and stable only at very high pressures. Diamond exists in nature. However, natural diamond is scarce and costly. This has motivated scientists around the world for more than one century to explore the laboratory growth of diamond using various techniques with different C sources. At present high-temperature high pressure (HPHT) and chemical vapor deposition (CVD) are the most two commonly used techniques for diamond [29].

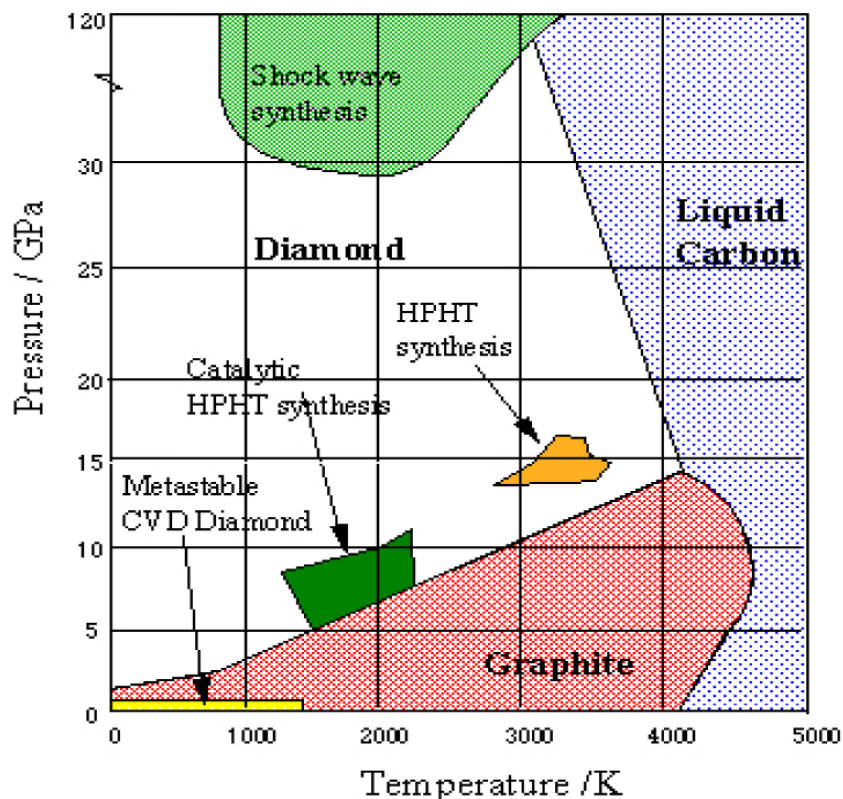


Figure 2. 2 Pressure-temperature phase diagram for carbon [31].

2.4.2 HPHT Diamond Growth

Since both diamond and graphite are pure carbon allotropes, and graphite is richly available in the earth, the synthesis of diamond using graphite is reasonable. Although the difference in standard enthalpies for diamond and graphite is only 2.9 kJ.mol⁻¹ [30], a large activation barrier separates these two carbon phases and prevents the mutual conversion between them at room temperature under atmospheric pressure conditions.

The phase diagram of carbon, shown in Figure 2.2, indicates the appropriate directions towards the conversion of graphite to diamond. Although graphite is stable at room temperature and low pressures, diamond, whose density is much higher than graphite (3.52 g/cm³ for diamond and 2.25 g/cm³ for graphite), becomes more stable with

high pressure. However, the thermal energy at room temperature is not enough to break the C-C bonds in graphite, and the diffusion of carbon is very difficult. Thus, the high temperature is also a requirement to convert graphite into diamond. The fact that natural diamond is produced at high pressure and high temperature in volcanic shafts also suggests the possibility of diamond growth through heating graphite under extremely high pressures. The HPHT diamond growth process essentially duplicates the natural diamond formation process, and the synthesized diamond exhibits similar properties [4] to naturally formed diamond.

The first two reports describing successful diamond growth using HPHT methods were first published by Everlose in 1955 [25], and by the General Electric in the 1960s [31]. Growth pressures as high as 12.5 GPa and associated temperatures as high as 3000 °C were reported. Since then, the HPHT technique has been the main method to produce “industrial diamond” for several decades. During the HPHT process, the transformed diamond must be cooled under high pressure in order to avoid its transformation back into graphite. However, these conditions are very harsh and costly to achieve. Fortunately, it is possible to overcome these limitations via solvent-catalyst reaction [4].

The solvent-catalyst process was invented and developed by General Electric [4], [32]. It established a reaction route with activation energy lower than that of the direct transformation, and thus a faster transformation under more benign conditions is feasible. As a result, the solvent-catalyst HPHT diamond growth is readily performed and has been widely used in industry to produce a diamond. The solvent-catalysts used during the HPHT process are transition metals and their alloys, including Fe, Co, Cr, Ni, Pt and their alloys. These metal-solvents can break the bonds between carbon atoms, dissolve

carbon and improve the diffusion of carbon to the growing diamond surface. The most common catalysts currently applied include Fe-Ni and Co-Fe alloys [4].

The main advantages of the HPHT grown diamond over the natural one are the ability to control the uniformity, size, crystal habit, crystal friability, the higher general quality and consistency [33]. Research in HPHT diamond growing is continuing in the direction to lower the production costs and to increase the crystal size.

2.4.3 CVD Diamond Growth

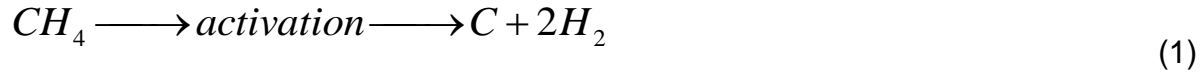
Besides the high processing cost, the diamond synthesized by HPHT is usually in the form of powders/particles or small bulk materials with the size ranging from nanometers to a few millimeters. These disadvantages limit its more widely technological applications [33]. The discovery that it is possible to grow PCD diamond films in the 1980s has further increased the world's attention improving diamond technologies. These experiments by Matsumoto et. al. [34], [35] demonstrated that it is possible to produce polycrystalline diamond thin films by CVD techniques. Their experiments typically used hydrogen (H_2) and methane (CH_4) gas mixtures at low pressures (vacuum < 75 Torr). Their CVD grown diamond displayed mechanical, tribological, and even electronic properties comparable to those of natural diamond, as shown in Table 2.1 [15-19].

2.5 Physical and Chemical Aspects of CVD Diamond

2.5.1 General Overview of the Surface Reactions

The homoepitaxial growth, by which diamonds grow from diamond crystal seed, has been intensively studied since the 1960's. At first sight, the reaction in CVD of diamond

seems to be very simple and only involves the decomposition of the carbon-containing species, e.g. CH₄ as follows [4]



As a matter of fact, the mechanism of growing diamond by CVD is a complex integration of many factors and has not been fully understood. Nevertheless, it has been found that there are two essential conditions which are crucial for the process [36]: (a) the activation of the carbon containing species and (b) the presence of the atomic H.

The growth of diamond from the chemical vapor phase takes place through a group of chemical reactions with a competition between the formation of diamond structures and non-diamond (including graphitic) structures. In the diamond growth using hydrogen (H₂) and methane (CH₄) gas mixtures as the reactants, Figure 2.3 demonstrates the possible physical and chemical processes that are involved in CVD diamond growth [33], [37].

Firstly, reactive gasses of CH₄ and H₂ are mixed and then the gas mixture is introduced into the reactor. Then they pass through a high temperature or energetic region where the molecules in the gas phases are broken and activated to form reactive radicals and atoms by, for example a microwave plasma. It is believed that CH₄ decomposes into two primary stable species: the methyl radical (CH₃) and acetylene (C₂H₂) [38]. Beyond the activation region, these reactive species continue to be transported and mixed by forced flow, diffusion as well as convection throughout the reactor and undergo a complex set of chemical reactions until they strike the substrate surface.

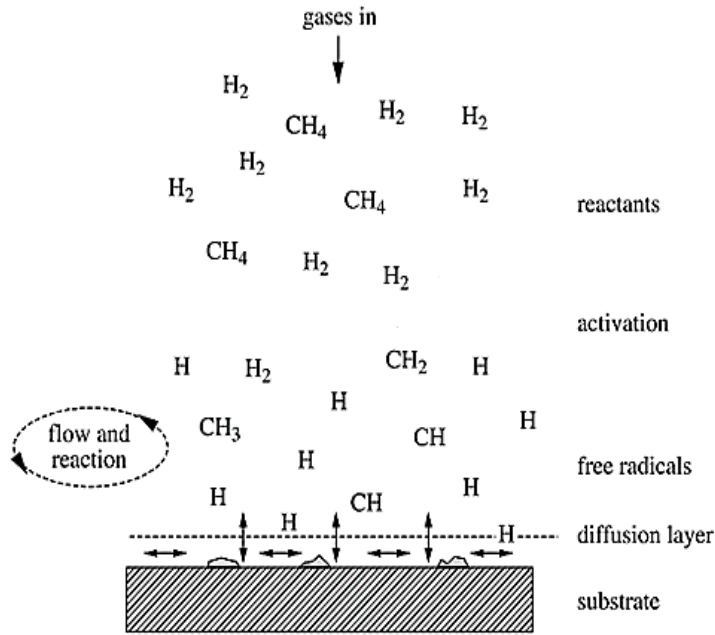


Figure 2. 3 Schematic of the physical and chemical processes occurring during the CVD growth of diamond [34], [38].

On the substrate surface, various processes may occur. The species can either be absorbed by the surface or be desorbed again back into the gas phase. They can diffuse along and into the substrate surface or react with the substrate to form various structures depending on the processing conditions and exposed substrate surface states.

Hydrogen, plays an essential role in the deposition of diamond thin films by CVD it is created by dissociation of H_2 due to the impact of electrons or due to other thermal dissociation processes. Atomic hydrogen, which promotes reactions, is among key ingredients in the chemical vapor deposition process [39]. The main functions of atomic H in the diamond deposition include:

- 1) Keeping diamond lattice stable by terminating the dangling bonds (presence of high-energy sites) on the surface of diamond films.
- 2) Creation of dangling bonds for carbon-containing radicals, e.g. CH_3 , to be attached to the growing diamond surface by reacting with the H on the diamond surface to form H_2 .
- 3) Creation of CH_3 radicals by reacting with CH_4 . Even though CH_3 radicals are predominantly created through the decomposition of CH_4 by thermal dissociation or impact dissociation, the reaction between H atoms and CH_4 will also create CH_3 radicals, which can then be attached to suitable surface sites to grow diamond.

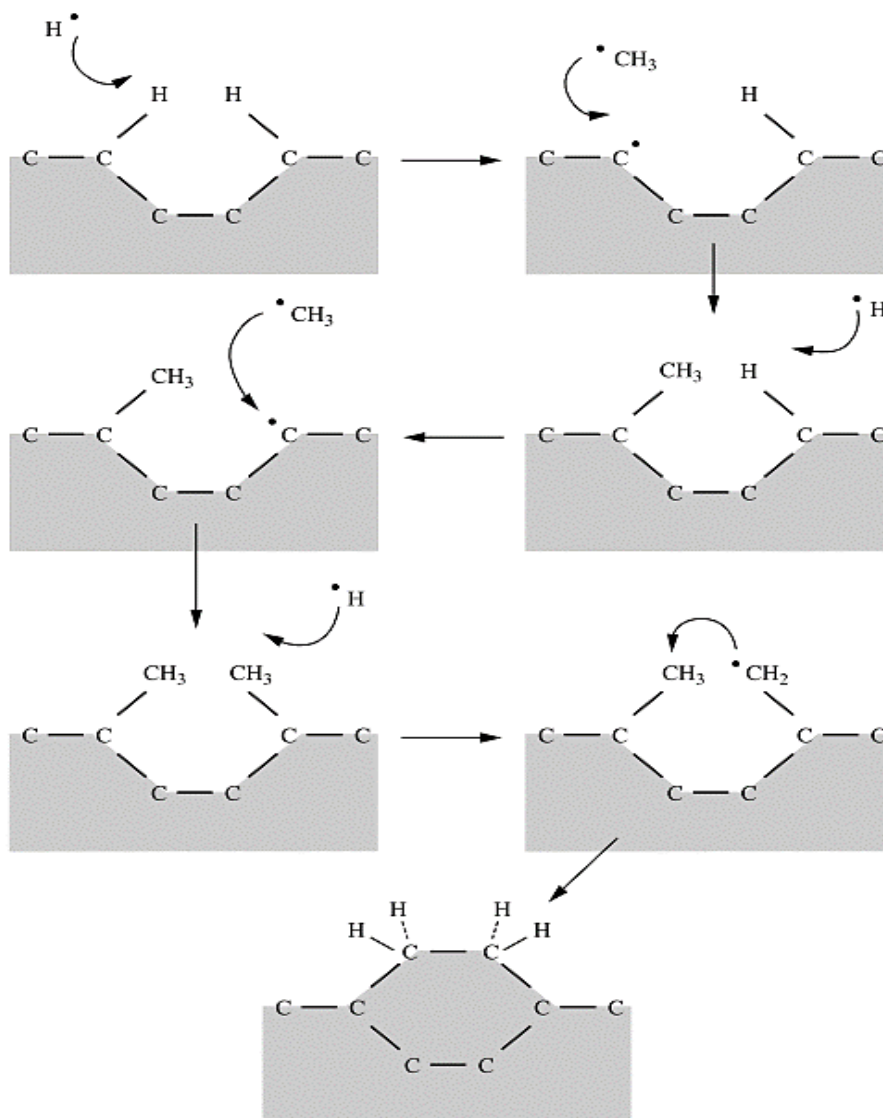


Figure 2. 4 A schematic of the reaction process occurring at the diamond surface leading to the stepwise addition of CH_3 species and diamond growth [33].

A schematic diagram of growth of diamond involving atomic hydrogen on the (100) plane is shown in Figure 2.4 [40]. Diamond growth can be considered as a stepwise addition of carbon atoms to the existing diamond lattice, catalyzed by the presence of excessive atomic H. At first, the reaction between the atomic H in the gas phase and the

H atom bonded to the sp^3 carbon dangling bond induces the formation of H_2 gas, leaving behind a reactive surface site. CH_3 radicals (gas phase) then collide and react with the reactive surface site, adding a carbon atom to the lattice. The same process of H atom abstraction and CH_3 addition may happen on the adjacent site. The further H abstraction on one of the chemisorbed groups creates a radical, which attracts another nearby carbon group to form the ring structure, locking the two carbon atoms in the diamond lattice.

2.5.2 The Specific Diamond Growth Reactions

Numerous synthesis and decomposition reactions are involved in the diamond growth process. Goodwin's [17] scaling model summarizes the essential growth sub-processes and highlights the essentials of diamond CVD growth. As mentioned earlier, once the active species form, there are several sub processes taking place on the surface of the diamond growth: activation of surface sites, adsorption/desorption of active radicals, and incorporation of adsorbates into the diamond crystal lattice. The following are the four basic sub processes included in this model:

(1) Surface Activation

A steady-state surface radical site coverage is established in this process. In the growth atmosphere, there are many active species besides the precursor gases themselves. The atomic hydrogen and active carbon radicals are part of the active species. Carbon atom on the surface of the diamond layer has one dangling bond, which is usually terminated by hydrogen. The surface activation process is to remove this termination hydrogen and leave the free active carbon atom with an open dangling bond

(see Figure 2.4). The following reaction describes this abstraction of surface-terminating hydrogen by gas-phase atomic hydrogen:



Here C_dH represents a generic hydrogenated surface site, and C_d^* represents the site with an open dangling bond after the hydrogen is removed (a radical carbon site). k_1 is the reaction rate constant for the flux of atomic hydrogen $[H]$ on the surface. k_2 is the reaction rate constant for the adsorption of an atomic hydrogen on the surface. This radical carbon site, C_d^* reacts with atomic hydrogen on the surface and this reaction is expressed as:



With these two reactions, the rate of creating C_d^* is expressed as:

$$r_1 = k_1[C_dH][H] + k_{-2}[C_dH], \quad (4)$$

And the rate of recombining C_d^* back to C_dH is:

$$r_1 = k_{-1}[C_d^*][H_2] + k_2[C_d^*][H] \quad (5)$$

(2) Adsorption

In the adsorption process, active hydrocarbon species in the atmosphere attach to the diamond surface at the radical sites (the ones with open dangling bonds) and combine with the diamond carbon atoms. This process is described as:



Where C_dA represents the adsorbates formed by the active carbon radical species (C_nH_m) and surface diamond carbon atoms (C_d^*) and k_3 is the reaction rate constant for the adsorption of a carbon containing radical on the surface.

(3) Desorption

Desorption is the reverse process of adsorption. In this process, the surface adsorbates return to the gas phase either thermally or chemically. In the thermal desorption process, the carbon radical species are removed from the surface via the thermal energy, which is expressed as:



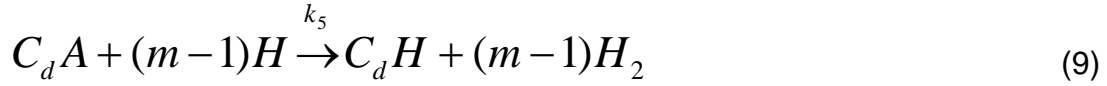
Where k_4 is the reaction rate constant for the thermal desorption of a radical from the surface. In the chemical desorption process, the carbon species are removed with the assistance of atomic hydrogen. The atomic hydrogen returns the attached carbon radical to the gas phase as the carbon precursor species. Chemical desorption is usually called “etching”. Desorption of atomic hydrogen is explained as:



Where k_5 is the reaction rate constant for the abstraction of an atomic hydrogen from the adsorbed carbon containing radical. Desorption is a critical process for the crystalline diamond growth, where the incorporation of the growth species occurs primarily at surface steps, which then move across the crystal surface. The desorption sub-process serves to remove the undesired adsorbates on the substrate surface and facilitates diamond growth.

(4) Incorporation

This is the process by which diamond grows. In this process, the adsorbates C_dA are incorporated into the diamond lattice with the assistance of atomic hydrogen, as indicated by the reaction:



Where m represents heavier molecules. During this process, atomic hydrogen promotes the incorporation by assisting the removal of the byproducts of the gas phase. The incorporated portion of the active carbon radical species stays at the substrate and forms a new layer of diamond.

The conditions that determine the rate of the four mechanisms listed above are surface temperature, gas phase atomic hydrogen concentration at the surface, and gas phase radical carbon concentration at the surface. In the steady-state conditions, this set of reactions can be combined to give a growth rate G of:

$$G = k_3 \frac{n_s}{n_d} \left(\frac{k_1}{k_1 + k_2} \right) \frac{[CH_3][H]}{\frac{k_4}{k_5} + [H]} \quad (10)$$

Where n_s is the surface site density (2.61×10^{-9} mol/cm²), and n_d is the molar density of diamond (0.2939 mol/cm³). With the simplification of the growth process, Harris and Goodwin [17] predicted the steady state radical fraction and simplified the growth rate equation (10) further:

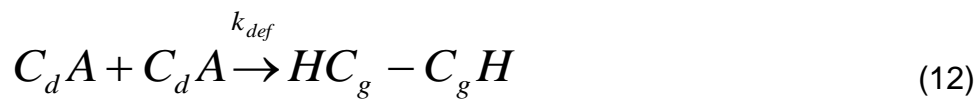
$$G = 1.8 \times 10^{11} \frac{[CH_3][H]}{5 \times 10^{-9} + [H]} \quad (11)$$

The chemical growth reactions have been investigated from early 1990's, and many of these complicated growth processes have been simplified into several chemical reactions as discussed in the references [17], [41], [42].

2.5.3 Growth of Defects

The challenge in the diamond growth process with higher rates is to do so while maintaining high-quality diamond growth, i.e. low defect density. There are many types of point and extended defects in diamond CVD growth process, such as sp^2 carbon, substitutional impurities, vacancies, interstitials, dislocations, twins, etc. [17]. Their generation depends on the local chemical environment. Out of different possible defects, Goodwin's scaling model predicts the incorporation of sp^2 carbon.

The underlying assumption of the defect generation model is that defects are generated when an adsorbate reacts with a nearby adsorbate before it is fully incorporated into the lattice. Once two of them react to form a sp^2 group, they are usually overgrown as a sp^2 defect. The reaction is written as:



Therefore, the defect fraction, X_{def} in the grown surface will be:

$$X_{def} = \frac{k_{def} [C_d A]^2}{k_i [C_d A][H]} \quad (13)$$

Where $k_{def}[C_d A]^2$ is defined as the rate of defect generation and $k_i[C_d A][H]$ is the rate of diamond formation. According to equation (10):

$$[C_d A] = \frac{n_d}{k_i} \frac{G}{[H]^2} \quad (14)$$

And from equation (12) and (13):

$$X_{def} = \frac{k_{def} n_d G}{k_i^2 [H]^2} \quad (15)$$

Where k_i is a constant at a given temperature. Therefore, the defect fraction in the grown diamond is proportional to the growth rate and inversely proportional to the square of the amount of atomic hydrogen on the surface at a constant substrate temperature. In general, if the defect generation reaction depends on $[H]$ and the diamond formation reaction has more than 1st order dependence on $[H]$, the defect fraction in the grown film will be:

$$X_{def} = \frac{k_{def} n_d G}{k_i^2 [H]^n} \quad (16)$$

This relationship predicts that the film quality and growth rate are inversely related, and the increase of atomic hydrogen at the surface improves film quality.

2.5.4 Numerical Modeling of the Harris-Goodwin Model

F. Silva et al. [9] developed numerical plasma models to compute the [H] and [CH₃] concentrations in the gas phase as a function of the deposition parameters, i.e. pressure, microwave power, and methane concentration. They noticed that in their reactor the electron temperature drops from 15000 to 10000 K, and the gas temperature varies from 2000 to 3600 K as the pressure increases from 37.5 Torr to 225 Torr. This is due to the increase in electron-heavy species collision frequency which results in an enhanced energy transfer from the electron gas to the heavy molecule species. They pointed out that, at low pressure (< few tens of Torr), H is mainly produced by the direct electron-impact dissociation reaction:



However, at higher pressure, H is mainly produced by the thermal dissociation of hydrogen molecules:



This result shows that as pressure increases and the gas temperature increases to more than 1400 K, then there is an associated significant increase in atomic hydrogen density [H]. The modeling results also show that at low pressures, the CH₃ radical production in the plasma bulk is governed by H-atom concentration through the reaction:



Here M is the third body. At high pressure, CH₃ production is still due to CH₄ dissociation through collisions with H atoms through the following reaction:



This reaction mainly takes place very close to the substrate surface. In fact, the production rate of CH_3 also depends on the gas temperature. An optimal CH_3 production is obtained for gas temperatures of 1200 – 2200 K. Also, they calculated for their MPACVD reactor the operating points regarding H-atom and CH_3 -radical concentrations for different pressures and input power discharge conditions and then plotted them on the process map from Goodwin [17] in $[\text{CH}_3]$ - $[\text{H}]$ space showing the operating ranges of the primary CVD diamond growth processes. The process map is shown in Figure 2.5.

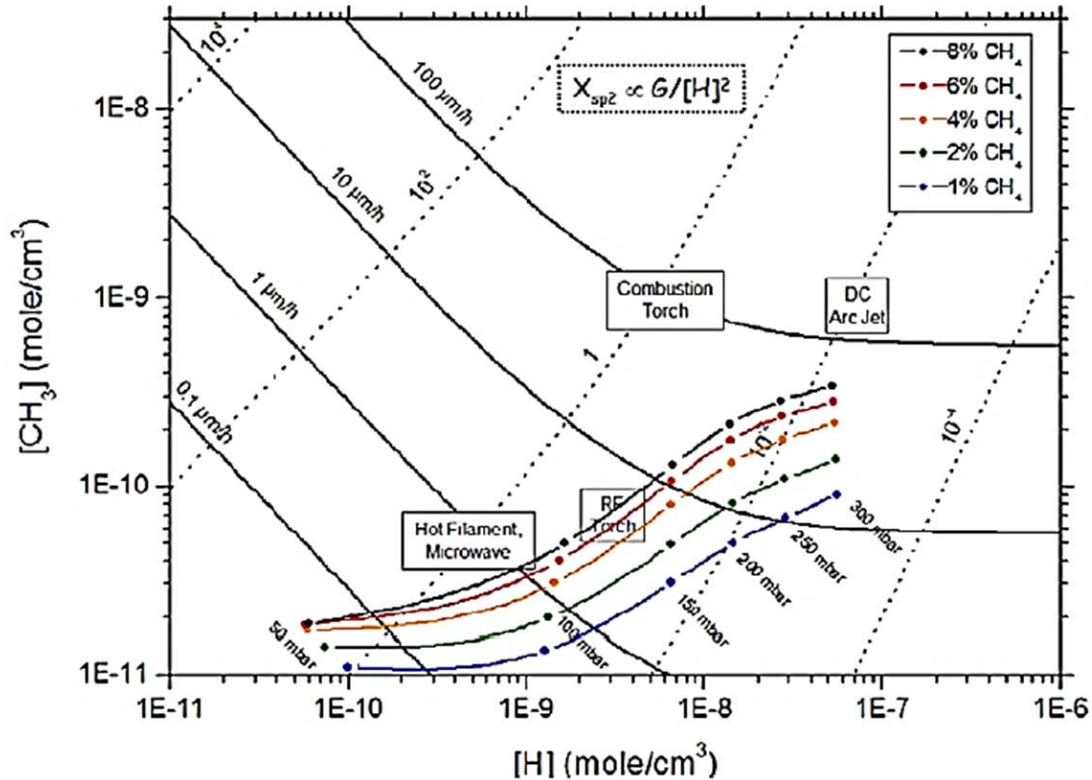


Figure 2.5 Process map in $[\text{CH}_3]$ - $[\text{H}]$ space showing the operating ranges of the main CVD diamond growth processes (from [9]). The evolution of the operating point of the LIMHP reactor as a function of working pressure (from 50 to 300 mbar) and methane concentration.

In Figure 2.5 the flux of the methyl radicals is plotted against that of the atomic hydrogen. This plot shows a dotted black line, which indicates the constant graphitic defect fraction contours (equation 16). The solid black lines indicate the constant growth rates on the (100) oriented diamond surface (equation 11). For a given methane concentration, the increase in the pressure from 37.5 to 225 Torr leads to three orders of magnitude increase of the H-atom concentration and one order of magnitude increase of CH₃ radical concentration. The results show an increase of growth rate to several tens of $\mu\text{m/h}$. As one would expect, at a constant pressure, the relative defect density with an 8% methane concentration is higher than that with a 1% methane concentration. However, for a constant methane concentration, the diamond quality can be improved by increasing the operating pressure. Consequently, it shows that increasing methane concentration at high pressure leads to a significant increase in the growth rate without compromising the film quality. That implies that at higher pressures the growth rate increases and high-quality diamond can be grown with higher methane concentrations than at lower pressure. The high diamond quality, high growth rate synthesis window increases with the high-pressure operation

2.6 MPACVD Growth of Diamond

This section reviews the basic principles of nucleation and experimental growth results on a single crystal diamond surface deposited by CVD process. Before reviewing previous research on diamond growth first the important aspects of homoepitaxy growth are discussed.

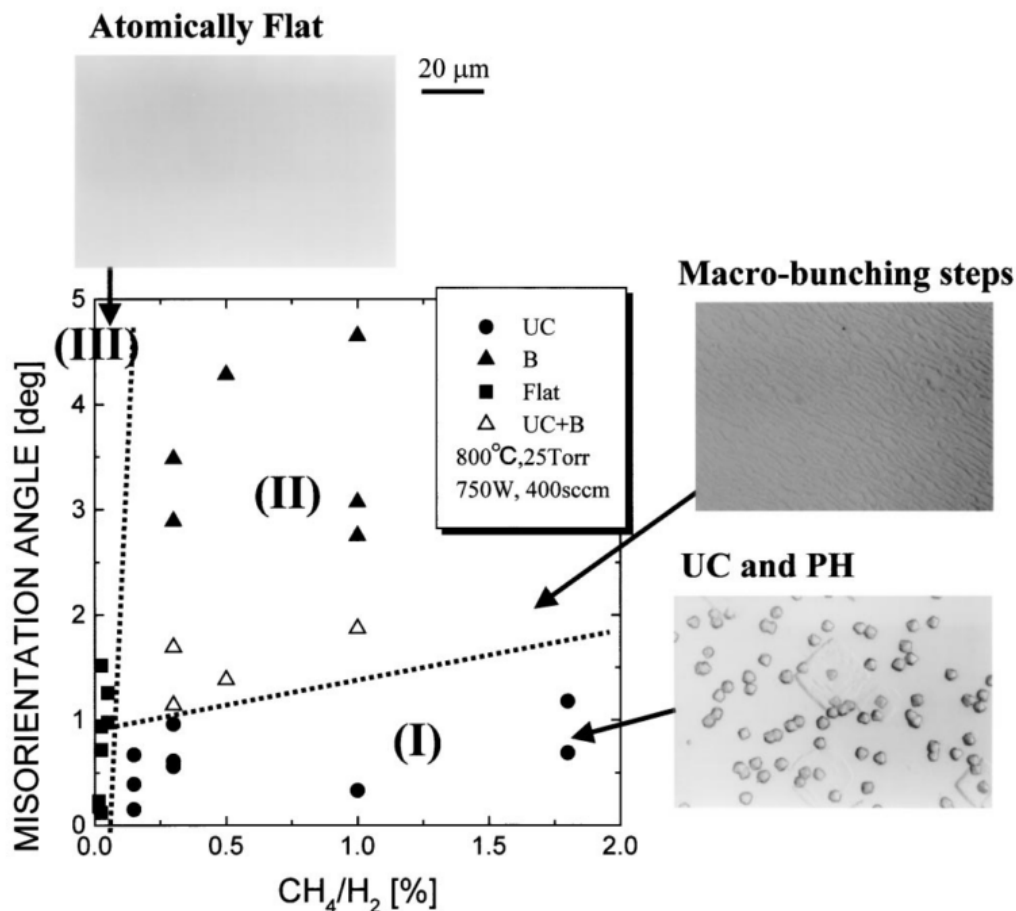


Figure 2. 6 Map of surface morphologies as a function of misorientation angle from the (001) and methane/hydrogen ratio. Three types of morphologies appear. Atomically flat diamond is preferred, which only grows in the region (III) [43].

Diamond growth by the microwave plasma assisted CVD (MPACVD) method was grown first by Kamo et al. in 1988 by growing on a polycrystalline diamond substrate [44]. After this demonstration, the investigations moved forward to the homoepitaxial diamond growth on natural or HPHT Type Ib substrates. At the early stage of the investigations, the reported growth rates were typically lower than $1\mu\text{m/h}$ [45]–[47]. Also, methane concentrations, usually defined as the ratio of methane to hydrogen flow rates, had to be

maintained at 0.025% to suppress the growth of defects. Results revealed visible defects in the homoepitaxial diamond growth: no-epitaxial crystallites (UC), pyramidal hillocks (PH), and macro-step bunching [43], [47]. Takeuchi et al. [43] grew homoepitaxial diamond films on substrates with different misorientation angles from the (001). They produced a map of diamond surface morphologies as a function of misorientation angle and methane concentration as shown in Figure 2.6.

However, additional works demonstrated that a different region of parameter space could be effective in growing diamond at much higher rates. Yan et al. grew diamond at rates approaching 40 $\mu\text{m/h}$ in the presence of nitrogen [48] with a growth temperature of 1500°C, pressure between 150 – 200 Torr and methane concentrations from 1% to 6%. Growth rates were increased to 150 $\mu\text{m/h}$ by introducing 1% – 5% N_2 relative to methane flow, and methane flow up to 12% of the hydrogen flow [13].

At a later stage, by lowering the growth temperatures to 700 – 800°C and increasing the microwave power density, fairly high growth rates were achieved in the absence of nitrogen [49]–[53]. Also, whereas gas pressures previously used ranged from 20 - 50 Torr [54], for high growth rates the experimental pressures were increased to 100 – 200 Torr. The microwave power densities were around 5 W/cm^3 but for high growth rates increased to 30 – 100 W/cm^3 [54]. Table 2.3 summarizes the growth pressures, the growth rates, and the power density ranges of these experiments.

Table 2. 2 Growth rates ranges in MPACVD diamond growth [49]–[53].

Parameter	Growth rate < 1 $\mu\text{m/h}$	Growth rate
		100 $\mu\text{m/h}$ with N_2 20 $\mu\text{m/h}$ without N_2
Power density (W/cm^3)	5	30 – 100
Substrate Temperature ($^{\circ}\text{C}$)	600 – 900	700 – 1200
Pressure (Torr)	20 – 50	100 – 200

2.6.1 Pyramidal Hillocks and Non-Epitaxial Crystallites

On the (100) diamond surface, the most frequent defect is the pyramidal hillock, either with a flat top surface or with a sharp truncated top containing a non-epitaxial crystallite [55]. The sides of this hillock are aligned with $[110]$. Under certain growth conditions, such as substrate temperature and methane concentration, the hillock grows very rapidly compared to its surroundings [49]. Figure 2.7 shows a homoepitaxial diamond surface with pyramidal hillocks; the pyramids are usually truncated with non-epitaxial crystallites on the top. Tallaire et al. [56] reported above 900°C a roughening of the crystal surface due to the formation of pyramidal hillocks defects, while at reasonably lower temperature the surface remains smooth.

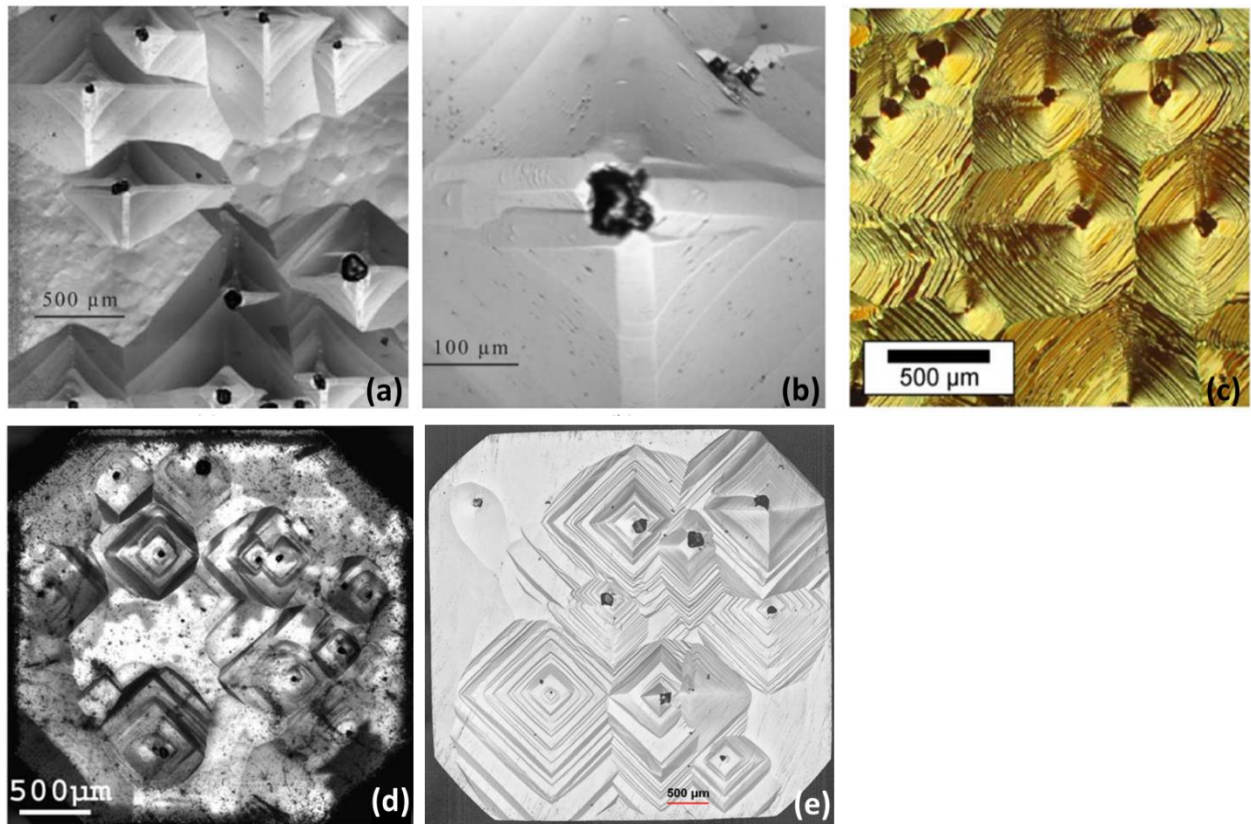


Figure 2.7 Optical microscope images of the epitaxial CVD diamond films grown at 1000°C (a) Sample overview (b) Magnification 20x [49]. (c) Optical micrograph of a 100 μm thick diamond film grown on an on-axis (001) oriented Ib substrate [57]. (d) and (e) CVD diamond film is grown at high temperature (1000°C and 920°C) exhibiting growth pyramids [56], [58].

Lee et al. [59]–[61] reported the type of growth strongly depends on the diffusion of the growth species on the surface, the rate at which growth species are deposited on the surface from the vapor phase, and the width of the terraces on the growth surface. If the terrace width is long compared to the diffusion length, then the growth species tend to deposit on the middle of the terraces, instead of diffusing to the steps. The results in two-

dimensional nucleation, as shown in Figure 2.8. Then, the two-dimensional nuclei provide shorter steps for further growth along the sides of the hillock. Non-epitaxial crystallites grow on surface defects by enhanced secondary nucleation [59]. At higher temperature, these non-epitaxial crystallites grow very fast and provide step edges for further growth.

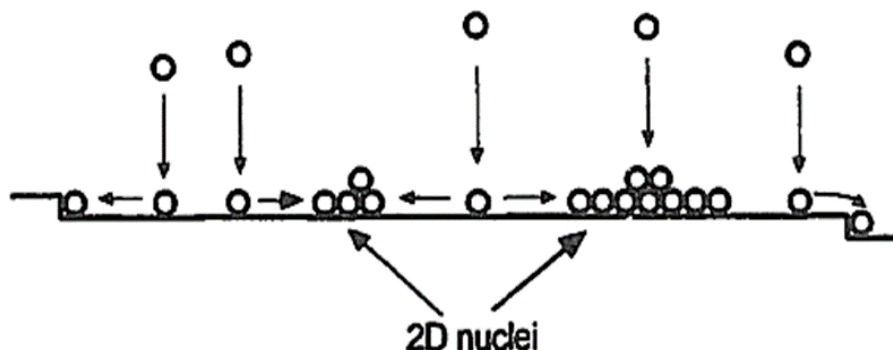


Figure 2.8 Mechanism of two-dimensional nucleation on a wide terrace, beginning of hillock growth [59].

2.6.2 Step bunching

If the diffusion length of the growth species is larger than the terrace width, the growth species diffuse toward the steps [59] because of the lower potential there. In this growth model, the steps appear to flow across the growth surface. A schematic view of the step flow growth mechanism is shown in Figure 2.9. At high temperatures and low methane concentrations a step flow increases on the diamond surfaces. Several reports have appeared on single crystal diamond growth in step flow mode on the substrate surfaces [43], [45], [58], [62]–[65].

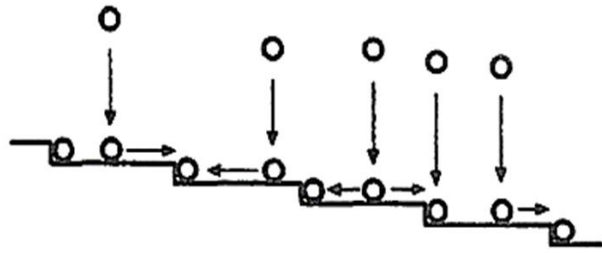


Figure 2. 9 Schematic view of step flow growth showing the diffusion of growth species to steps and subsequent flow of steps to the right [59].

During growth, impurities or defects may obstruct the transport of diamond growth species to a particular step [66], so that flow ceases, but other steps will flow to that position and become pinned. If this process continues, many steps will become bunched at that position leading to a macroscopically high step. That is referred to as macro-step bunching. Figure 2.10 shows macro-steps bunching in homoepitaxial diamond growth.

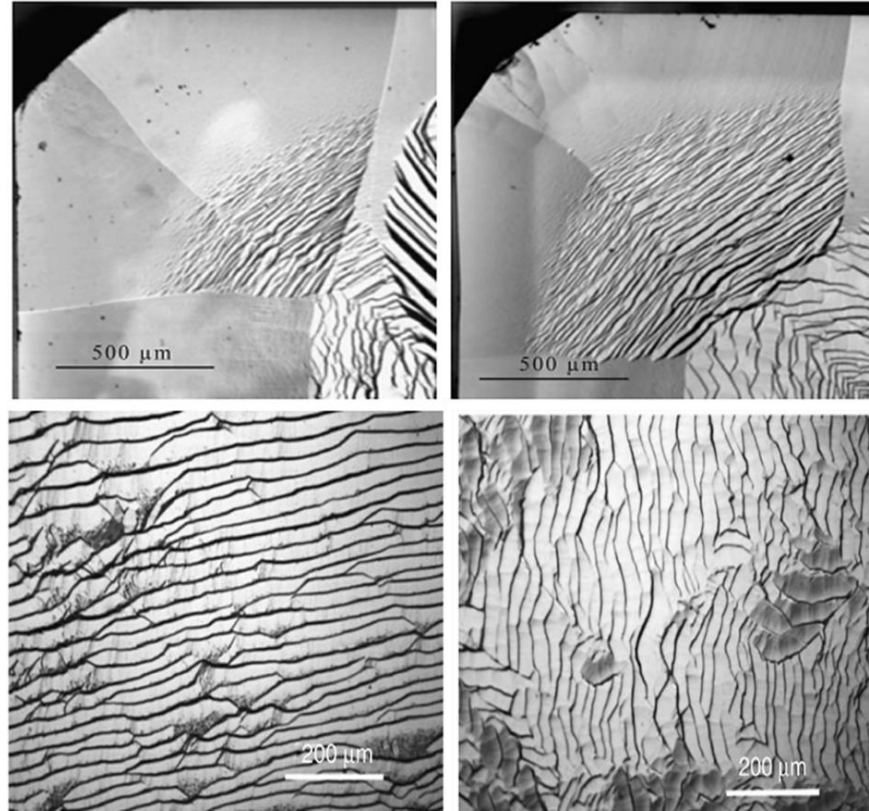


Figure 2. 10 Optical micrographs of the grown surfaces of CVD diamond with (a), (b) no intentional N₂ addition and (c) 2 ppm of N₂ and (d) 6 ppm of N₂ [58], [63].

2.6.3 Effect of Growth Parameters

2.6.3.1 Substrate Temperature

The substrate temperature is known to be a most important parameter in SCD growth. Diamond has been grown over a large range of temperatures of several hundred centigrades, focused around 700 – 1300 °C. Numerous investigations have shown significant effects on the growth rate and crystal morphology of the CVD diamonds at different substrate temperatures.

The diamond growth rate, R_g was modeled with an Arrhenius relationship using an associated activation energy, E_a and the growth temperature, T [67], [68]. The general expression is:

$$R_g = Ae^{(-E_a/K_B T)}$$

The relation showed a substrate temperature between 800 – 1000°C for a maximum growth rate. Diamond growth in this temperature region is controlled by chemical reaction kinetics rather than by surface diffusion.

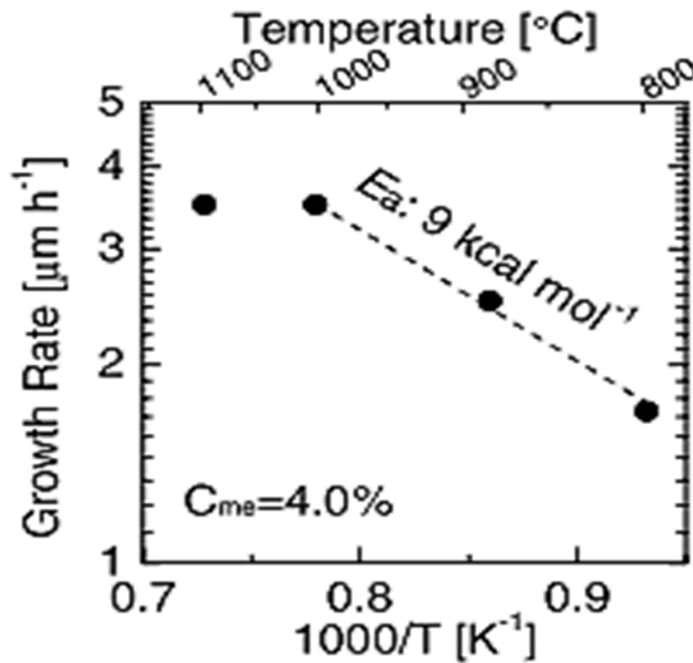


Figure 2.11 Diamond growth rates as a function of substrate temperature at 4% methane concentration and a 3.8 kW microwave power [54]. Here C_{me} is the methane concentration.

Above 1000 °C, the growth rate no longer obeys the above relation but saturates. The growth changes to a diffusion-controlled mode, with a weaker temperature dependence. Values of E_a for temperatures between 735 – 970°C were reported as 8 ± 3 , 18 ± 2 and 12 ± 4 kcal/mol, respectively, for (100) and (110) and (111) diamond surfaces [69]. A. Gicquel et al. [67] reported in the temperature range 700 - 850°C activation energy in the range 11 – 16 kcal/mol. Different growth conditions and reactor geometries will change E_a , so that the use of these parameters may be sensitive to local conditions. Figure 2.11 shows a plot of growth rate versus substrate temperature.

At temperatures above 1200°C, graphite starts to form [54]. At temperatures lower than 700°C, the diamond growth rate is very low, and the diamond surfaces are rough and defective with a non-optimal crystal morphologies [58]. Furthermore, the growth of smooth and flat diamond surfaces also has been reported at 700°C [50]. This apparent contradiction may not exist if growth also depends on other parameters such as methane and nitrogen concentrations, and reactor geometries. Usually, there is a small temperature window in which defect-free diamond can be grown.

2.6.3.2 Methane Concentration

In this thesis, investigation methane is used as the main source of carbon to grow diamond, and the amount of methane present it usually referred to the methane concentration. Methane concentration is defined as the flow rate ratio of methane gas to total gas, which is typically composed mainly of hydrogen. Because the methane gas flow rate is small under typical growth conditions, the methane concentration is often defined as the flow rate ratio of methane gas to hydrogen gas (CH_4/H_2).

Methane concentration in the gas phase significantly affects the diamond growth rate and the morphology of diamond. It has been shown the growth rate is found to be linearly proportional to methane concentration. Figure 2.12 shows a plot of growth rate versus methane concentration at 850°C without nitrogen from Achard et al. [58]. The results indicate a slightly linear relationship between methane concentration and growth rate. In contrast, Bogdan et al. [70] reported a sublinear result in which the surface topography and the growth rate does not change dramatically by increasing the methane content from 6% to 15% methane concentration. Teraji et al. [54] reported a linear relationship from 1% to 5% methane, then a linear dependence up to 32% methane at 890°C. Whereas; the growth rate always increases as methane concentration increases, the proportionality coefficient can be sensitive to other growth parameters.

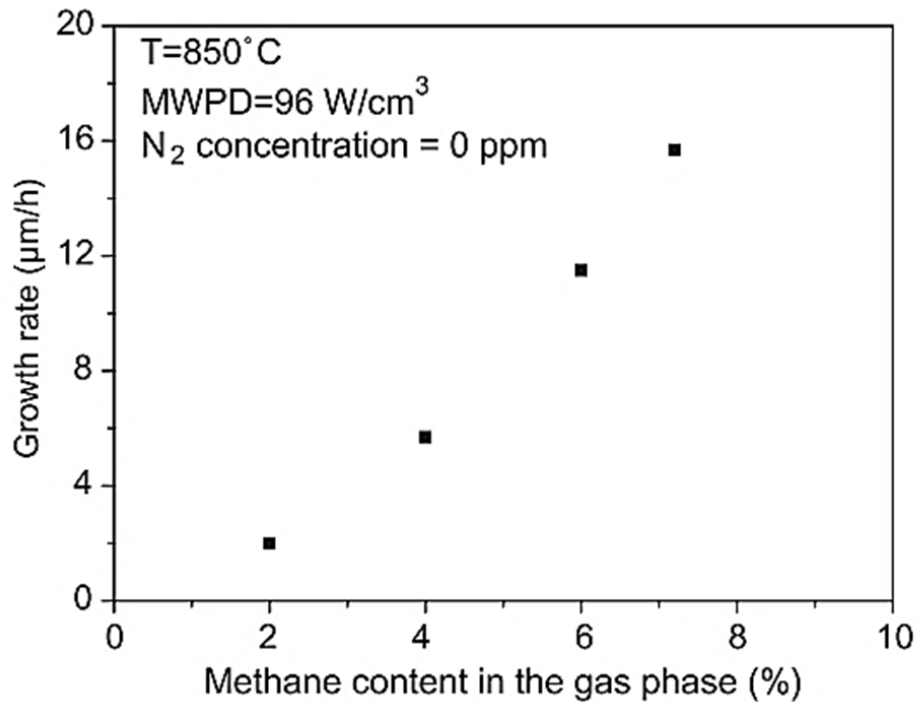


Figure 2. 12 The influence of the methane concentration in the diamond growth rate [58]

Furthermore, some authors reported that the variation of methane concentration improved the surface morphology on the diamond crystal. Bogdan et al. [70] reported a smooth diamond surface grown at 15% methane concentration at 700°C. Achard et al. [58] published diamond surfaces with macro-step bunching when they increased the methane concentration from 4 to 6%. At 2% methane concentration, they found the diamond surface to be highly pitted.

Some authors reported the methane concentration should be reduced below 1% to obtain high-quality diamond films with a flat surface and non-epitaxial crystalline [71], [72]. However, the growth rate under such conditions is very low ($<1 \mu\text{m/h}$) which is not desirable for the growth of thick diamond substrates. Tallaire et. al. [49] subsequently reported when the concentration of CH_4 was increased; the surface morphology was improved.

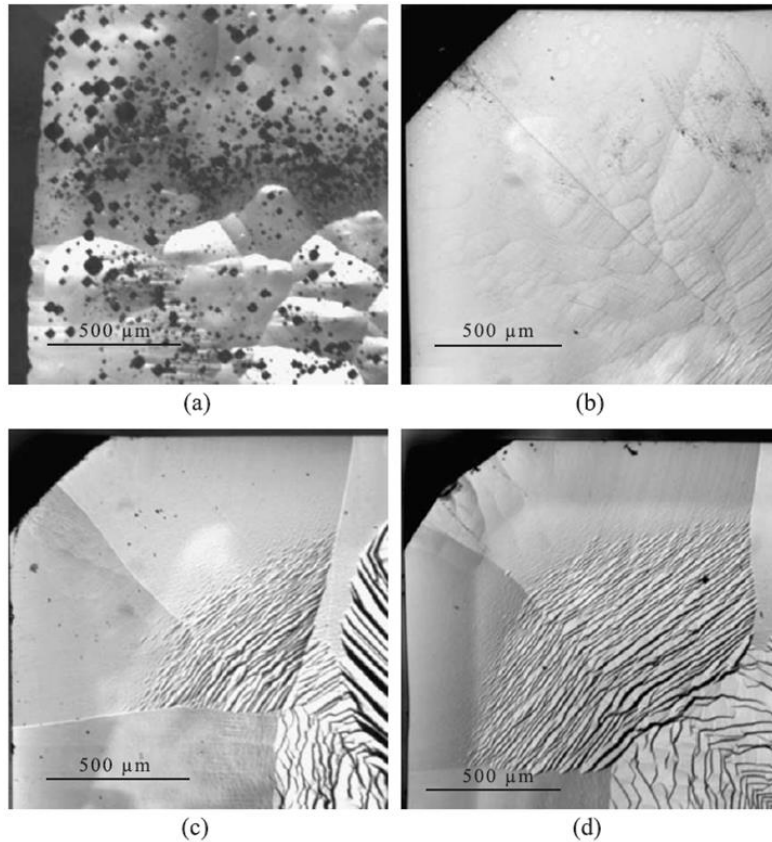


Figure 2.13 Optical microscope images of the diamond films grown at 850°C with methane concentration of (a) 2% (b) 4% (c) 6% and (d) 8% [49].

Figure 2.12 shows the optical microscope images of the CVD diamond films grown at 850°C with 2%, 4%, 6% and 7% of methane concentration (CH_4). With 2% of CH_4 , the growth rate was 2 $\mu\text{m/h}$, and the film surface was very rough, exhibiting a significant number of pits. It was suggested that this could be a consequence of a high etch rate by atomic hydrogen during growth enhanced at such high microwave power. This statement was also reported by Lee et al. [59] in which at 6% and 8% CH_4 the diamond morphology showed micro steps with the surface close to the single domain structure, at 1% and 2% CH_4 concentration. The surface shows hillocks, and random growth morphology occurred with the double domain structure.

2.6.3.3 Process Gas Pressure

The process gas pressure has an influence on the size and energetics of the microwave plasma. As pressure increases, the size of the plasma ball becomes smaller since the mean free path of the ions becomes shorter. This also has been experimentally demonstrated [16], [73]. This influences the substrate temperature, since the power density may become greater in the vicinity of the substrate. In a microwave plasma CVD system, the electrons in the plasma are accelerated by the high-frequency electric field, but the ions cannot follow the microwave field, due to their heavy mass, leading to a low ion temperature. The ion temperature can be increased by enhancing collisions with hot electrons, brought about by a higher gas density. When the total gas pressure is low, the ionization rate in the plasma is also low with only a relatively small number of electrons available for creating atomic hydrogen and carbon radical species. This results in low densities of growth radical species and results in a low growth rate that is attributable to low excitation density of these species.

At higher pressures and power densities, the ionization rate is higher, and the frequency of collisions between the ions and electrons become larger, which increases the ion gas temperature. That ultimately leads to an increase in the density of carbon growth species and atomic hydrogen. Mokuno et al. [11] found the growth rate increasing almost linearly with pressure in their microwave plasma CVD reactor in the presence of nitrogen. Li et al. [74] investigated the growth rate and quality of diamond film with pressure up to 125 Torr. They reported a linear dependence on the growth rate and the pressure when operating with a fixed methane concentration. Also demonstrated was that

the diamond quality increased with increasing pressure. Yan et al. [48] reported a five-fold increase in growth rate when the pressure was changed from 60 to 200 Torr.

2.6.3.4 Microwave Power Density

The microwave plasma density on the substrate surface is enhanced with increasing the gas pressure because the plasma density increases as pressure increases. The diamond growth rate is strongly affected by increasing the radical species densities on the substrate. Consequently, the growth rate increases as pressure increases.

CH₃ carbon radicals can be formed at the plasma boundary because CH₄ molecules that are decomposed in the plasma center are possibly cooled at the boundary because of that region's low gas temperature. When the microwave input power which creates the plasma is weak while the pressure is substantially high, recombination reactions among precursors become considerable. Consequently, the methane concentration dependence on the growth rate changes from linear to sublinear with the pressure increasing [54]. This fact implies that the microwave power density must be high to produce a sufficient quantity of radicals when the pressure increased.

Tallaire et al. [75] observed a three-fold increase, from 3 $\mu\text{m}/\text{h}$ to 8.5 $\mu\text{m}/\text{h}$ in growth rate, with a change of microwave power density from 65 to 125 W/cm^3 . They also used a pulsed microwave source to increase the peak power density and while maintaining a constant average power density. They observed an increased growth rate of 40%, with the conclusion that peak power density, not average power density, is responsible for the enhanced growth rate. The deposition rate also increased by increases in both the power density and the methane concentration. They found that the growth rate can be increased

six-fold by increasing both methane concentration up to 7% and microwave power density up to 125 W/cm^3 . The results are shown in Figure 2.14.

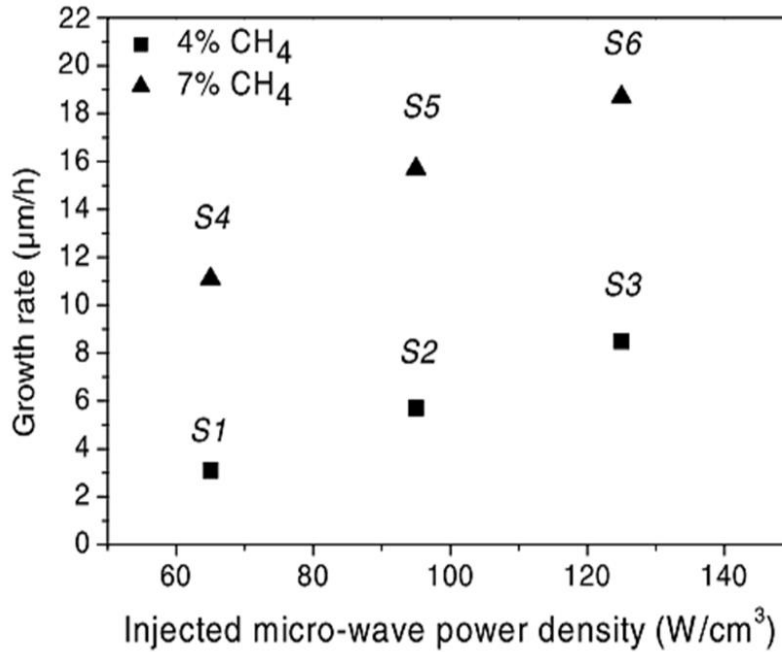


Figure 2.14 Evolution of the growth rate of the CVD diamond films as a function of the injected MW power density in the discharge using 4% of CH_4 (square dots) or 7% of CH_4 (triangular dots) [75].

2.6.3.5 Nitrogen

Nitrogen is an important impurity that plays an essential role in the growth of CVD diamonds. Nitrogen forms several defects centers in diamond and reduces the optical transparency in the region above 1.7 eV and show an absorption band in the infrared at wavelengths beyond $9 \mu\text{m}$ due to the enhancement of defect induced one-photon absorption [76]. Small amounts of nitrogen into the gas phase also has been shown to have a large influence on the morphological and growth rate of CVD diamond.

The nitrogen can change the diamond surface texture to a pattern of crystallites with rectangular coplanar (001) facets, thereby reducing the surface roughness and improving the crystalline quality [77]. Furthermore, it generally induces an increase in the deposition rate by factor of 2 to 10 [13], [52], [58], [66], [78], [79]. These authors suggested that a controlled amount of nitrogen in the gas phase enhances the abstraction of hydrogen on the diamond surface. This increases the diamond phase and influences the growth rate. However, has been found that significant amounts of nitrogen cause deterioration of the films or even inhibit diamond growth [80].

It has been shown from many experiments that the influence of nitrogen on the growth and morphology of diamond grown (100) and (111) faces is completely different. Theije et. al. [66] have shown that diamond films which grown on (001) surfaces in the presence of nitrogen have an entirely different morphology from diamond films grown without nitrogen. Whereas the latter is quite smooth with many squares, shallow growth hillocks and grown polycrystalline on the edges, the morphology of the diamond films with nitrogen is determined by the presence of step bunches, see Figure 2.14. The nitrogen in the films acts as an impurity impinging on a growing surface, thereby destabilizing uniform step trains by hampering the propagation of individual steps, leading to a step bunching instability [81]. So far, the mechanism by which nitrogen influences the (001) diamond growth is not well understood. The mechanism such as surface poisoning or the generation of additional growth steps has been considered [77]. According to a theory based on defect-induced stabilization of diamond growth [82], diamond growth is only thermodynamically possible by the creation of vacancies, since a diamond vacancy can be created with lower energy than a graphite vacancy. If nitrogen is doped into diamond,

the Fermi level at the growth surface is shifted towards the conduction band, which reduces the energy of vacancy formation in diamond, but not in graphite, so that diamond growth is favored over graphite.

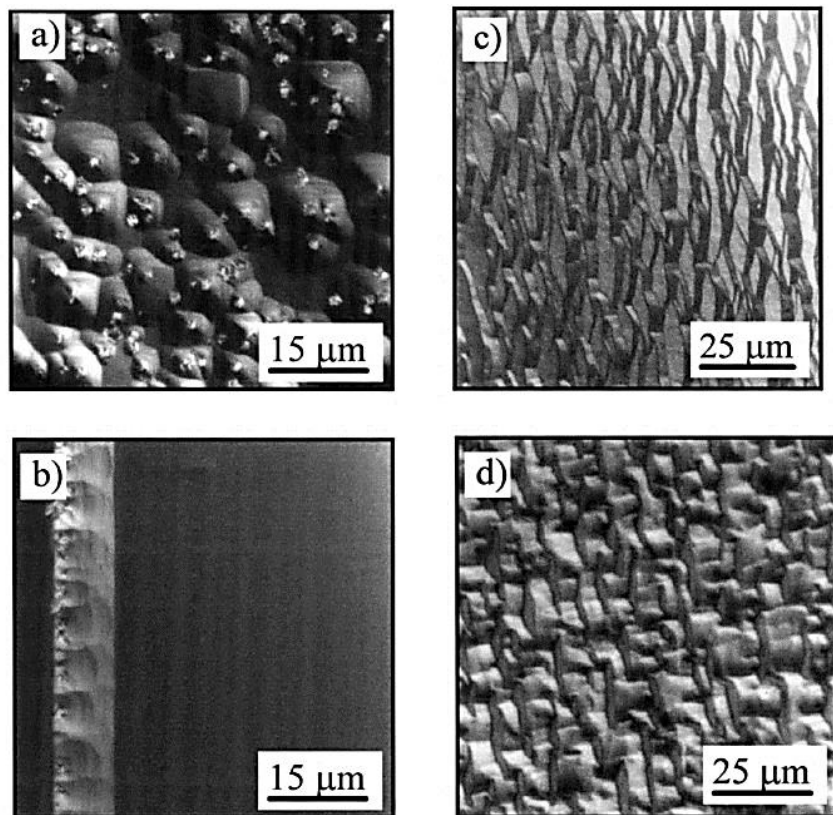


Figure 2.15 Optical microscope images of the surface morphology of epitaxially grown diamond films deposited on (001) oriented diamond substrates without (a, b) and with (c, d) nitrogen added to the gas phase [66].

The morphology of the diamond grown on (111) oriented shows a different morphology upon nitrogen addition. Without nitrogen addition, these surfaces are a

smooth with many shallow growth hillocks and a few micro twins. However, upon nitrogen addition, a significant increase in twin formation is observed [83].

A lot of nitrogen concentrations were found to deteriorate the diamond film and decrease the growth rate. That is attributed to the increased amount of carbon/nitrogen ratio, which would reduce the concentration of growth promoting CH_3 radicals in the gas phase. The carbon/nitrogen ratio may competitively adsorb onto vacant diamond growth sites and then induce increased twinning and stacking faults [84].

The role of nitrogen in the growth and the diamond surface continues to be of interest to the diamond researchers either to considerably improve the growth rate, the morphology or to improve the diamond applications. In this thesis investigation, no nitrogen is added to the diamond growth process.

2.7 Review of Single Crystal Diamond Growth via MPACVD

The overview of single crystal diamond growth via microwave plasma assisted chemical vapor deposition is focused on the role of growth parameters on the diamond growth process. A SCDs growth review is summarized below by groups of researchers worldwide. Each group has contributed enormously to develop strategies to grow diamonds. The following is a compilation of recent breakthroughs since 2014. Previous SCD growth investigations have been described in other MSU Ph.D. research dissertations, for example from J. Lu and S. Nad [85], [86].

2.7.1 Carnegie Institute of Washington, USA

Researchers at the Carnegie Institution's Geophysical Laboratory have demonstrated growth up to 10-carat SCD at rapid growth rates (150 micrometers per hour) depending on the growth conditions, using a microwave plasma assisted chemical vapor deposition (MPACVD) process. The diamond crystals were grown at high temperatures range of 1100 - 1300°C. The high growth rate was achieved by adding a small amount of nitrogen gas into the conventional hydrogen and methane gas mixture at high temperatures. However, the high growth rate is limited by the growth time due to the thick polycrystalline diamonds which are also deposited on the substrate holder [13]. To avoid the PCD growth, they performed the growth in multiple runs, in which the run was stopped and crystal was taken out to remove the polycrystalline diamond that was formed during a deposition run. After PCD removable the run was resumed and then the growth was continued again. This careful control of growth was also believed helpful to prevent cracks. The details of the process were not provided.

An example of a diamond produced by the above technique is shown in Figure 2.16 (a). The large crystal was cut from a 13.5 carat rough diamond block grown at around 50 $\mu\text{m/h}$ in the absence of impurities other than hydrogen. Optical microscopy revealed that the CVD diamond is clear and relatively free of inclusions and cracks. There are no visible layers (or growth interfaces) and striations from cross-sectional view within the thickness above 5 mm. The as-grown, 2.3-carat, brilliant cut diamond was color designated as near colorless. It also has high optical quality and clarity without visible layers.

The results showed the growth morphology and diamond color strongly depend on temperature. Additionally, the results showed smooth and dark brown diamond substrates

at 1000 – 1100°C brown at 1100 – 1200°C, and tinted yellow at 1200 – 1220°C. Step flow-type with pyramid-like octahedra tinted yellow formed at 1230 – 1400°C, spherical black diamond-like carbon was produced below 1000°C, and twinned or polycrystalline diamond resulted at temperatures over 1300°C.

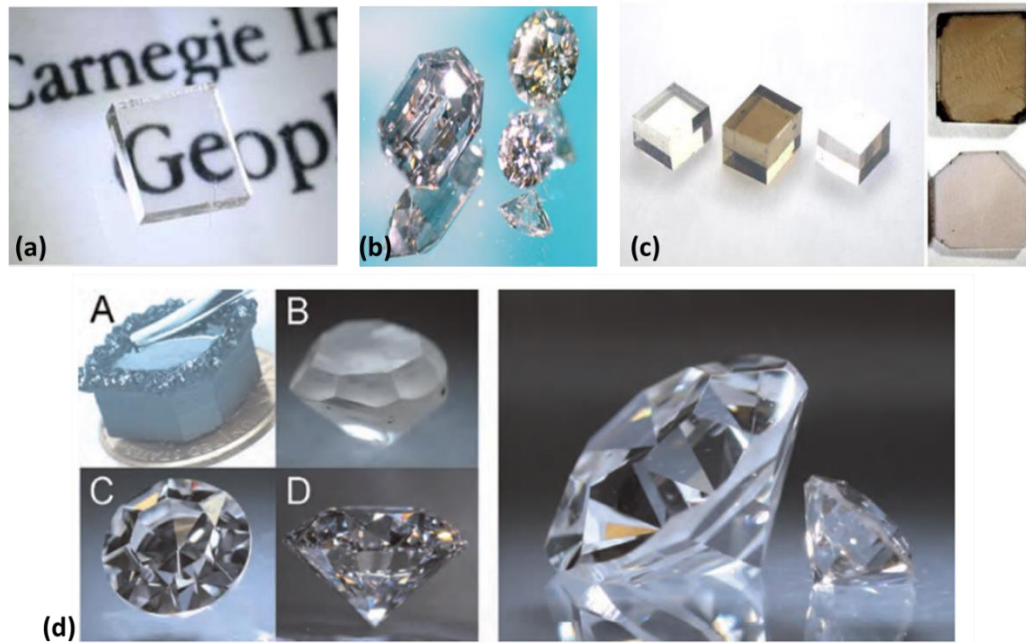


Figure 2.16 Carnegie Institution's Geophysical Laboratory diamond is grown at high growth rates with and without nitrogen [14], [87]. (a) SCD plate, (b) 0.2 – 2.2 carat brilliantly cut and polished nitrogen doped light brown colored and near colorless SCD substrate, (c) examples of as-grown SCD substrates after annealing treatment and (d) in image (A) 2.4 carat single-crystal CVD diamond (B, C, D) 2.3 carat diamond after cut and polished [88].

The temperature range for smooth, yellow-tint growth is a very narrow 1200 – 1220°C. Figure 2.16 (a) and Figure 2.16 (c) shows a photograph of an as-grown CVD polished

diamond. It was grown with at a growth rate of 58 $\mu\text{m/h}$ at 1200°C. The improved growth techniques for producing colorless SCD have been summarized in Table 2.3.

Table 2. 3 Carnegie Institution of Washington diamond growth parameter reported

Carnegie Institution of Washington, U.S.A.		
Growth parameter	Description	Reference
Reactor type	ASTeX/Seki reactor	[14]
Substrate seeds	HPHT type Ib (9 mm x 9 mm) and synthesized SCD with (100) surfaces	[13], [14]
Substrate pre-treatment	cleaned ultrasonically with acetone.	[14]
Gas chemistry	5-20% CH_4/H_2 , 0.2-10% O_2/CH_4 . High purity methane (99.9995%) and 0.2 – 5% N_2/CH_4	[14]
Pressure	150 – 300 Torr	[14], [88], [89]
Input power	3-5 kW	[14], [88], [89]
Discharge power density	50 – 100 W/cm^3	[88]
Substrate temperature	1000 °C to 1500 °C	[14], [88], [89] [90]
Growth rate	40 – 100 $\mu\text{m/h}$.	[79][90]

2.7.2 Diamond Research Center, AIST, and Osaka University, Japan

The Diamond Research Center of Japan National Institute of Advanced Industrial Science and Technology (AIST) from Osaka University in Japan has been working on the homoepitaxial growth of diamond during the past 14 years [10], [11], [91]–[95] [96]–[100]. They have achieved significant progress in the SCD growth process, which is summarized here in two groups, (1) high rate repetitive SCD growth, and (2) effect of the Molybdenum holder on the diamond growth process.

In order to grow large area CVD SCD substrates with the help of the high growth rate, the AIST research group implemented a method called, (1) high rate repetitive SCD growth. In this approach consists of adding a multi-step growth process on the same substrate to grow very thick SCD substrates. They reported high growth rates which ranged from 30 to 150 $\mu\text{m/h}$ at pressures up to 220 Torr with nitrogen additions of over 0.1% [10], [11], [91]. In this approach it was necessary to interrupt the growth within a limited time and then clean the substrate holder to avoid the build-up of the polycrystalline diamond on the substrate holder. Figure 2.17 and Figure 2.18 shows large diamond crystals with thicknesses of 8.7 – 10 mm and weight of 3.4 – 4.5 carat were successfully grown on a 3.5 mm x 3.5 mm x 0.5 mm diamond seed after 24 separate deposition steps at 68 $\mu\text{m/h}$ for a total of 150 hours. The growth temperature was 1130 °C, and the pressure was 24 kPa (180 Torr). The flow rate of nitrogen was 0.6 sccm (0.12% N_2/H_2) [10]. The high rate SCD growth was performed using a standard [11], [91] 2.45 GHz, AX-5250 5 kW-MPCVD system produced by Seki Technotron Corp. The specific experimental conditions are summarized in the following table:

Table 2. 4 Growth parameters for SCD by Diamond Research Center, Japan

Diamond Research Center, AIST, and Osaka University, Japan		
Growth parameter	Description	Reference
Reactor type	Seki Technotron Corp	[14]
Substrate seeds	HPHT type Ib (3 mm x 3 mm x 0.5 mm)	[10], [11]
Substrate pre-treatment	Hydrogen etching for 30 minutes	[10], [11]
Gas chemistry	500 sccm H ₂ (6N) / 60 sccm CH ₄ (6N) / 0.6-1.8 sccm N ₂ (4N) (12% CH ₄ / H ₂ , 0.12-0.36% N ₂ / H ₂).	[10], [11], [91]
Pressure	130 - 220 Torr.	[10], [11],[14], [91]
Input power	1 – 3.7 kW.	[10], [11],[14], [91] [94]
Discharge power density	50 – 150 W/cm ³	[10], [11],[14], [91] [94]
Substrate temperature	1000°C – 1300°C and 1130°C	[10], [11],[14], [91] [94]
Growth rate	30 – 100 µm/h. (was estimated from the net weight gain)	[11], [91]

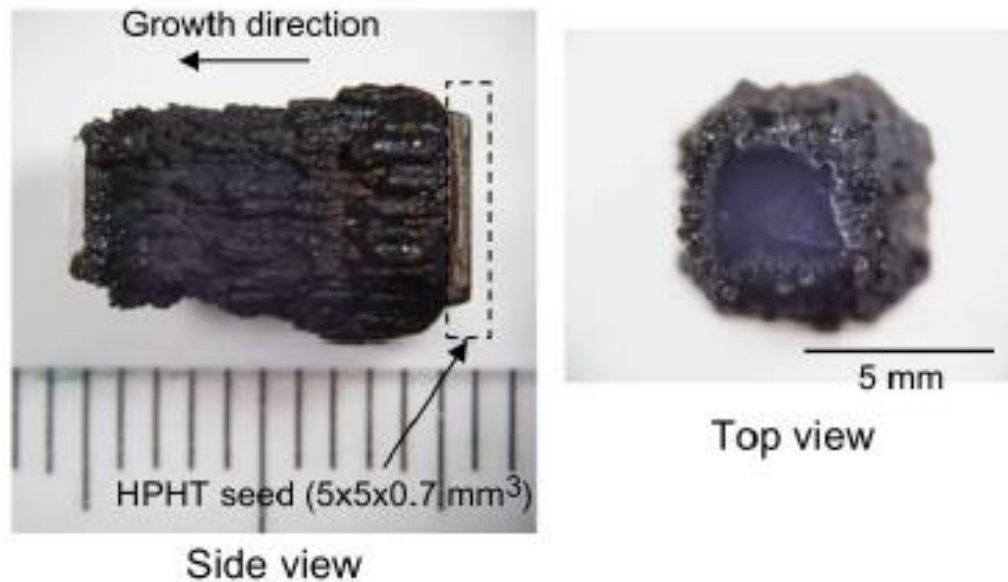


Figure 2.17 A 4.65 carat, 10 mm thick SCD substrate grown with 24 deposition runs [10]

The high growth rate was enhanced due to the nitrogen on the gas feed. Even though the side surface was covered with polycrystalline diamond, the top surface of the synthesized SCD maintained smooth and flat surface morphology. By investigating the Raman spectra over a cross section that was cut from one large synthesized SCD crystal, the thick diamond crystal was showed to be of high quality ($\text{FWHM} < 1.85 \text{ cm}^{-1}$) [92]. Note in Figures 2.17 and 2.18; that the grown SCD area is significantly smaller than the original HPHT seed due to the thick polycrystalline rim around the SCD grown surface. This indicates that the thicker the grown SCD crystal, the smaller is the area of the top surface.

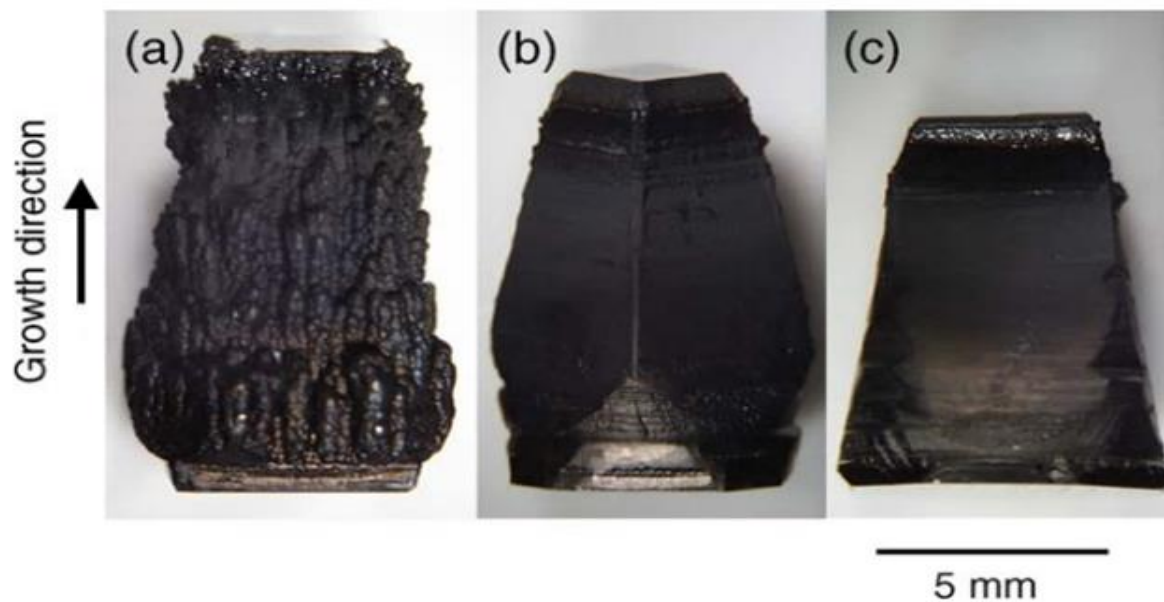


Figure 2.18 Large CVD diamonds grown by multi-steps high growth rate synthesis process. (a) 10 mm thick, 4.7 carat CVD diamond, (b) 9.6 mm thick, 3.5 carat CVD diamond, (c) 8.7 mm thick, 4.4 carat CVD diamond [11].

In the research topic (2) numerical and experimental studies of several experimental and numerical simulation data to show the distribution of gas and electric field intensity within the conventional reactor configuration [101].

For the research topic (2) effect of the Molybdenum holder on the diamond growth process, a new molybdenum substrate holder designs were fabricated to increase the growth rate over time [10], [102]. The designs also were simulated to demonstrate the effect of different reactor variables, such as substrate temperature, gas flow distribution, and electric field intensity, over time [103], [104]. The schematics of the newly designed substrate holders together with corresponding results of the numerical calculation of plasma, the pictures of hydrogen plasma and the observed diamond growth rates are shown in Figure 2.19. The numerical calculation showed that the magnitude of the electrical field around the substrate increases as the radius decreases.

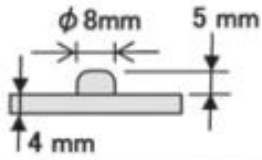


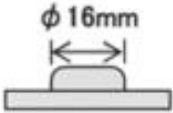
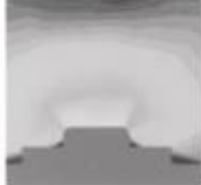
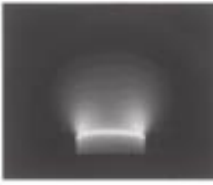
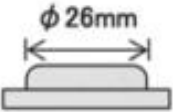

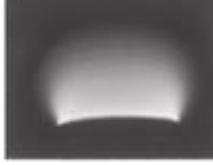
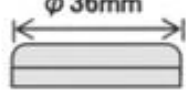
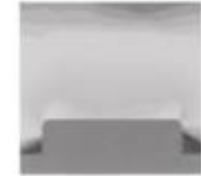
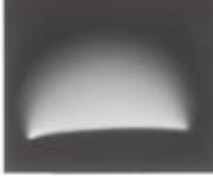
Holders	Numerical Results	Hydrogen Plasma (observed)	Diamond Growth Rates (observed)
			~30 $\mu\text{m/h}$
			~30 $\mu\text{m/h}$
			~10 $\mu\text{m/h}$
			~5 $\mu\text{m/h}$

Figure 2.19 Schematics of newly designed substrate holder together with corresponding results of simulation of plasma, pictures of hydrogen plasma and observed diamond growth rates [102].

As a result, the diamond growth rate of the 8-mm holder was 30 $\mu\text{m/h}$, and for the holder with 36 mm the growth rate was 5 $\mu\text{m/h}$. However, after optimizing the 8-mm holder's shape, they obtained a growth rate of 50 $\mu\text{m/h}$. The configurations of these substrate holders were previously called an open holder and an enclosed holder [10].

Figure 2.20 shows a schematic illustration of two types of the substrate holders. For enclosed type holder, "d" is defined as the final depth of diamond relative to the top surface of the holder after the growth. As since the thickness of diamond increases during the growth, "d" is defined as an average depth of diamond during the growth.

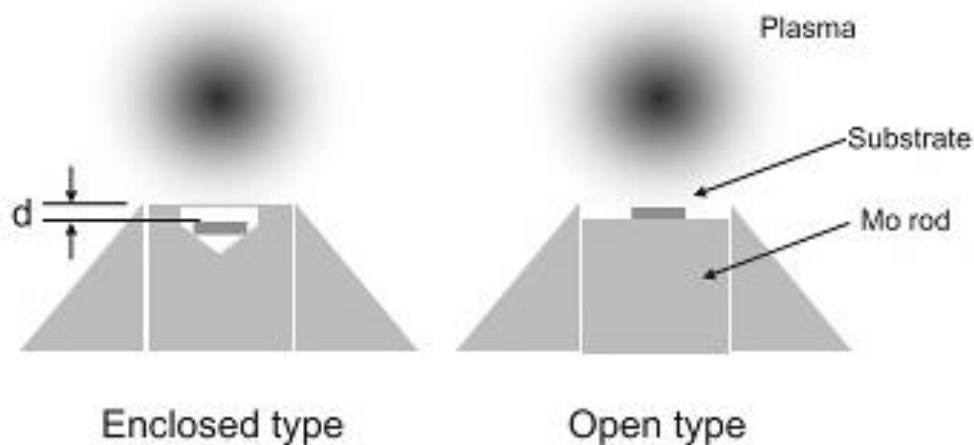


Figure 2.20 Schematic illustration of “enclosed type” and “open type” holders. The final depth of diamond after the growth “d” is indicated [10].

They observed that the substrate holder configuration plays a significant role in the quality and the growth rate. The substrates grown in an enclosed holder displayed a smooth surface as compared to those grown in the open holders as shown in Figure 2.21. After the first run, the grown diamond substrates by the open type holder indicate the promotion of edge growth. In contrast, the grown diamond substrates by the enclosed type holder show macroscopically flat surface morphology, and there is no promotion of growth at the rim part compared with those by open type holder.

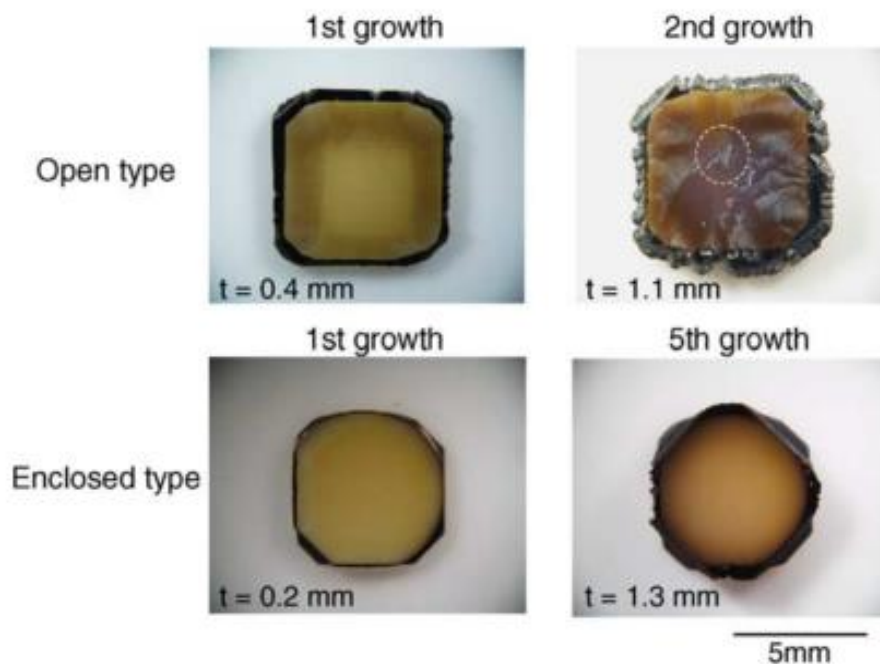


Figure 2.21 Optical microscope images of grown diamond after 1st growth (left) and repetition of growth (right) for open and enclosed type holder. Thicknesses of grown diamonds (t) are indicated in the pictures. A dashed circle indicates a crack formed by repetition of high rate growth [10].

After the 2nd growth for open type holder, though relatively high growth rate ($87 \mu\text{m/h}$) is obtained, a crack appeared in the center part, and no additional growth cannot be applied without polishing the surface. In contrast, by using enclosed type holder, the surface morphology is dramatically improved, and smooth and flat surface morphology without growth hillocks or no epitaxial crystallites was obtained even after the 5th growth. See Figure 2.21.

In order to increase the single crystal diamond surface area, one additional approach was reported from AIST group; it is the production of diamond plates by a lift-off process.

As a standard procedure, the fabrication of SCD plates involves a conventional laser cutting method, in which the grown substrate is separated from the HPHT seed. However, during the laser cutting method and polishing, several hundreds of microns of diamond are lost during the cutting process [12]. Thus a lift-off process using ion implantation was developed to produce large and thick SCD plates and reduce material losses [94], [105]–[110].

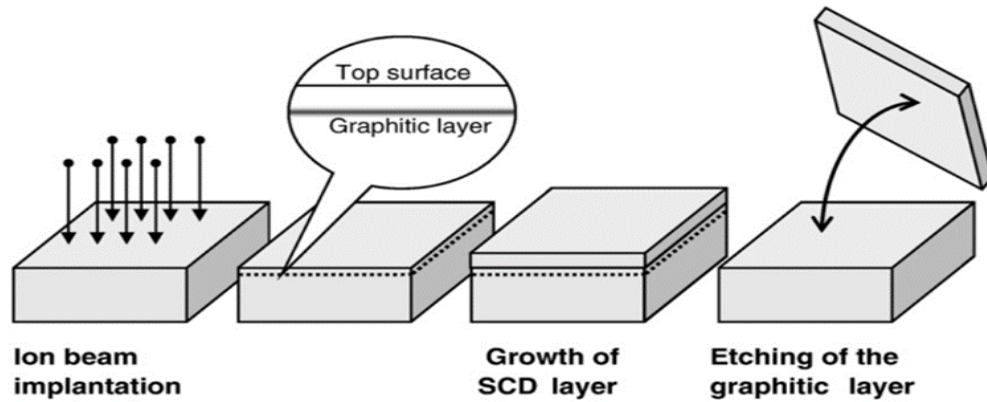


Figure 2.22 Lift-off process with ion implantation [108].

The steps of the lift-off process is shown in Figure 2.22. The lift-off process consists of a high energy ion (3 MeV) beam being injected into the top surface of the seed substrate, resulting in the formation of a graphitic layer beneath the top surface (first two steps are shown on Figure 2.22). The ions are implanted with a shot of 2×10^{16} ions/cm². After this, an SCD layer was grown on the top surface of the substrate by using the high growth rate diamond method described in the section above (third image from left in Figure 2.22). The next step is etching away the graphitic layer using a non-contact electrochemical etching method [111]. The grown SCD plate was obtained as a

freestanding wafer (right-hand image in Figure 2.22). Due to the thickness of the graphitic layer and depth of this layer from the top surface are substantially small, a few micrometers, the loss of material from the seed crystal is always negligible.

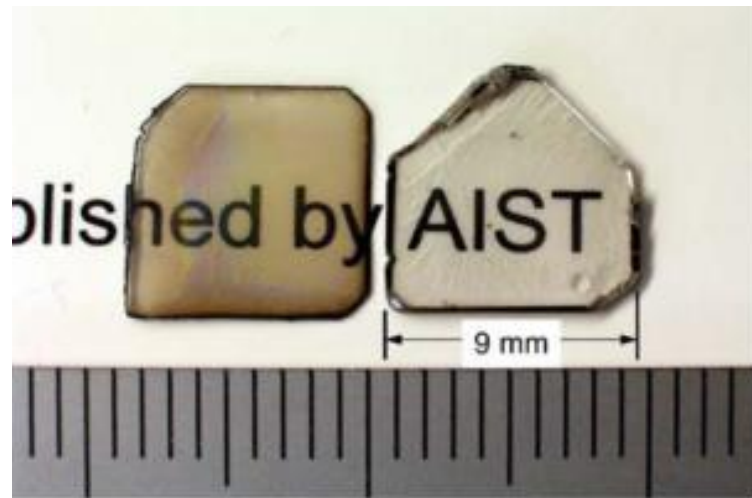


Figure 2.23 Photograph of freestanding single-crystal CVD diamond plates produced by a lift-off process using ion implantation [94].

Figure 2.23 shows a photograph of two plates, which were produced by the lift-off process using ion implantation. The first plate is a nitrogen-doped diamond (left hand on the Figure 2.23) and the second plate is an undoped single crystal diamond plate. The nitrogen-doped CVD diamond grown four-times at approximately at a growth rate of $34 \mu\text{m/h}$ and was successfully separated from the seed to produce a plate to a thickness of $470 \mu\text{m}$. The undoped CVD plate also growth four times at an average growth rate of $7.8 \mu\text{m/h}$. Compared with the nitrogen-doped diamond which is brown, the undoped diamond is colorless. The plates were successfully separated from the HPHT seed by the lift-off process. However, there is still a size limitation for the CVD diamond plates produced.

The size was limited by the size of the original seed. Then they tested a new process to fabricate larger CVD diamond plates by combining the lift-off process and side surface growth [94]. The process steps are shown in Figure 2.24.

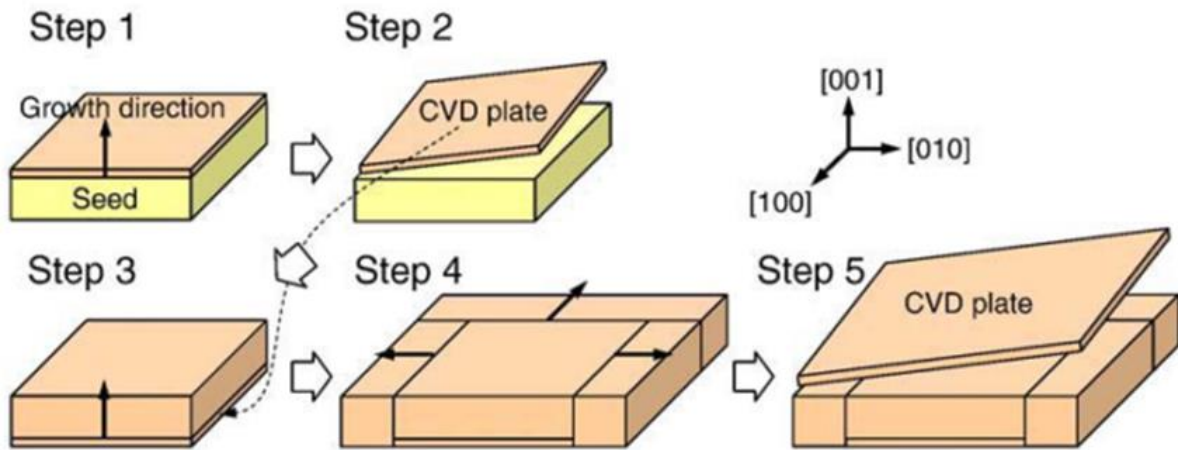


Figure 2.24 Schematic illustration of a crystal enlarging process by a combination of lift-off process and side-surface growth [94].

An HPHT diamond seed with the size of 10 mm x 10 mm was used to assemble a single crystal CVD diamond plate with the same cross section and a thickness of 0.4 mm by the lift-off process (steps 1 and 2, Figure 2.24). The assembled plate was then grown to a thickness of 3.7 mm with the multi-step high growth rate diamond process with 0.12% nitrogen addition (step 3, Figure 2.24). The resultant SCD was laser cut and polished to create side (100) faces. A diamond layer of a thickness of 3 - 4 mm was grown on three of the faces (step 4, Figure 2.24). This produced a half-inch (12.6 mm x 13.3 mm x 3.7 mm) SCD. This diamond was laser cut to form two pieces of a (001) seed plate.

One of the plates was polished and used as a seed substrate for the lift-off process (step 5, Figure 2.24). Thick diamond of 0.2 mm was grown on the seed by the high-rate growth of 32 $\mu\text{m}/\text{h}$ with nitrogen addition, and the film was successfully separated from the seed. Figures 2.25 (a) and (b) shows photographs of the polished seed plate and a separated half-inch single-crystal diamond plate. The results indicated the combination of both processes is effective for enlarging the area of single-crystal CVD diamond plates. Also, the enlarged seed plate can be used to produce large undoped single-crystal CVD diamond plates.

Further, the AIST group introduced the so-called “mosaic wafers” process. This method was developed to fabricate 1-inch size diamond wafer [108]–[110]. They introduced an efficient way to build a mosaic wafer with smooth and almost invisible boundaries. The key point of the technique is the use of same single seed substrates which are “cloned” from the same “mother” substrate using lift-off process. The final diamond wafer made of those clones is referred as “tiled clones” [109].

The method to produce clones and tiled clones is shown in Figure 2.26. By using the lift-off process with the ion implantation method described above, “clones,” i.e. thin SCD plates, were obtained. Each “clone” SCD plate had similar crystallographic characteristics over the large cross section area of the seed substrate. For example, in steps (1 – 4) of Figure 2.26, four clone substrate plates are grown from one seed substrate with a size of about 10 mm x 10 mm.

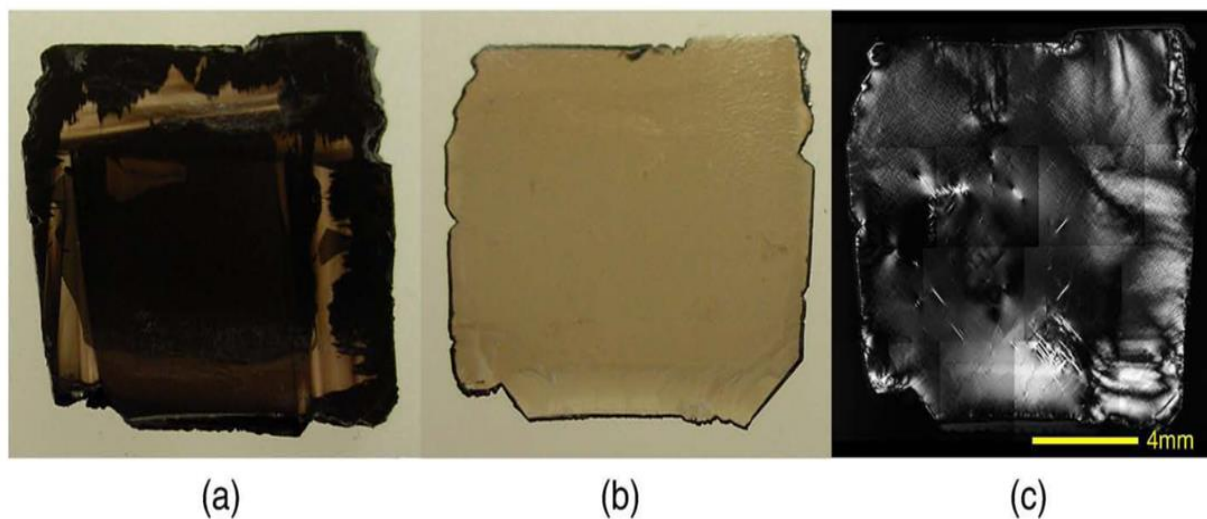


Figure 2. 25 (a) Photograph of a half-inch seed plate obtained by cutting and polishing the diamond in Fig. 5. (b) Photograph of a half-inch nitrogen-doped single-crystal CVD diamond plate produced under high growth rate ($32 \mu\text{m/h}$) from the seed plate by a lift-off process using ion implantation. (c) Polarized light microscope image of the half-inch single-crystal CVD diamond plate [94].

These clones were aligned manually with each other to within less than $500 \mu\text{m}$, to make a tiled clone (step 5 in Figure 2.26). The diamond layers were grown on both sides of the tiled clone wafer. A free-standing clone of the tiled clone can be produced by using lift-off process again (step 6 in Figure 2.26).

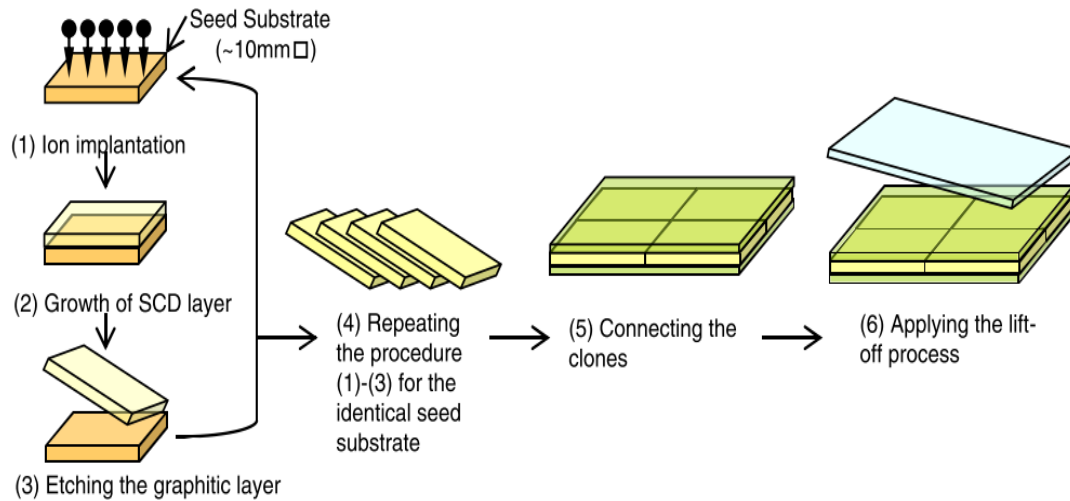


Figure 2. 26 Method steps to produce clones and tiled clones [109].

An image of a typical free-standing clone of a tiled clone is shown in Figure 2.27. The arrows in Figure 2.27 indicate the locations of the boundaries between the connected clones. Each connected clone was about 10mm x 10mm, which is the same as the seed substrate, and gave a free-standing wafer around 20mm x 20mm. The shape of the tiled clones was almost square. From the Figure 2.27, one can see the boundaries between the connected clones are almost invisible. In addition, the fabricated wafer has no obvious cracks. The results show that the use of cloned substrates is very efficient in enlarging diamond plate area. However, increasing the number of the constituent diamond plates can cause degradation in quality and cracks on the diamond surface. Thus, in order to further fabricate high-quality large area SCD plates, enlargement of the SCD substrate still appears to be very important.

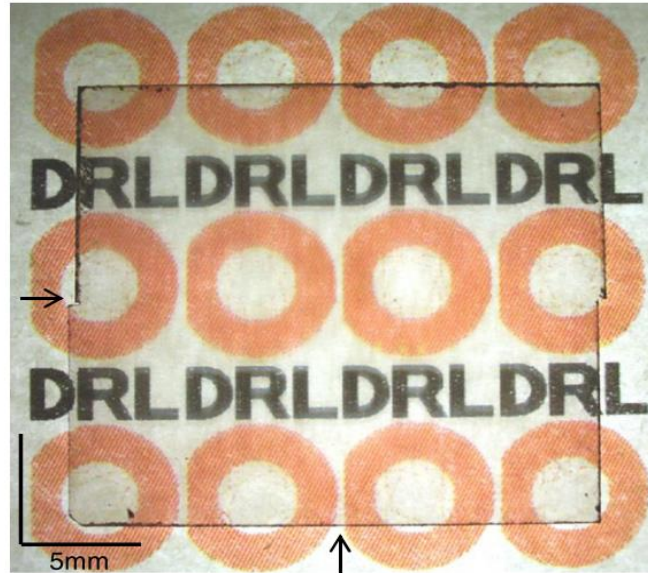


Figure 2. 27 An image of typical tiled clones [109].

2.7.3 LIMHP/CNRS, Paris, France – Recent Results

The diamond group of Laboratoire des Sciences des Procédés et des Matériaux, France has explored the SCD growth process both scientifically and technologically, regarding size, purity and crystalline quality of the diamond. Their contributions have been in diamond growth experiments and diamond growth simulation [9], [42], [49], [58], [63], [65], [112]–[114]. The main research focus of the France group can be classified into four research topics: (1) effect of growth parameters specifically for the homoepitaxial deposition of high-quality thick diamond films [49], [58], [63], [115]–[117]. (2) Microwave engineering plasma modeling; here, the influence of the deposition process parameters on the production rate of the growth species and CVD diamond growth kinetics, and different designs of plasma reactors [9], [118] [119]. For large surface area homoepitaxial CVD diamond growth, (3) the influence of the presence of multiple growth sectors on the substrate surface and geometric modeling of CVD diamond crystal growth was

investigated [112], [113], [120]. Most recently they investigated (4) the reduction of dislocations by using a self-assembled metallic mask and by the growth of diamond on an HPHT diamond substrate hollowed out by a large hole [121], [122].

In research topic (1) homoepitaxial thick diamond substrates were grown by a microwave plasma CVD at high microwave power densities at temperatures ranging from 800 °C to 950 °C and with nitrogen addition [49], [58], [115], [117]. It was shown that the growth rate could be increased by factors of up to 2.5 by adding small concentrations (2 to 10 ppm) of nitrogen to the gas phase. The specific experimental conditions are summarized in the following table:

Table 2. 5 LIMHP/CNRS, Paris, France growth parameter reported

LIMHP/CNRS, Paris, France		
Growth parameter	Description	Reference
Reactor type	LIMHP reactor	[9], [118] [119].
Substrate seeds	HPHT type Ib (3 mm x 3 mm x 1.5 mm)	[56]
Substrate pre-treatment	Wet-chemical cleaning and then a 2-hour H ₂ /O ₂ plasma etching of the HPHT substrates.	films [49], [58], [63], [115]–[117]
Gas chemistry	purified hydrogen (9N), 2-7% highly pure methane (6N) and nitrogen. Nitrogen concentration was varied between 0 and 200 ppm.	[49], [58], [63], [115]–[117]
Pressure	50 - 300 mbar	[9], [118] [119]
Input power	2 – 4 kW.	[9], [118] [119]
Discharge power density	60 – 130 W/cm ³	[9], [118] [119]
Substrate temperature	800°C – 1000°C	[49], [58], [63], [115]–[117]
Growth rate	5 – 55 µm/h	[49], [58], [63], [115]–[117]

They claim that the addition of nitrogen as low as a few ppm in the gas phase resulted in a strong increase in the growth rate. At a pressure of 220 mbar (165 Torr), 10 ppm of N₂ improves growth rates by more than a factor of 2. This is shown in Figure 2.28. This low amount of nitrogen enabled the growth of uncoloured “optical-grade” free-standing CVD diamond film. It was reported that a maximum deposition rate of 55 µm/h was achieved by introducing 200 ppm of nitrogen at 875°C. Before polishing grown diamond substrates, surface morphology is shown in Figure 2.29. The images reveal that the nitrogen incorporation on the growth process drastically deteriorates the morphology of the diamond films. When the diamond was grown without intentional nitrogen addition (Figure 2.29 (a)) the surface was very smooth and rough morphologies without non-epitaxial crystallites, were obtained when the amount of added nitrogen was not greater than 2 ppm (Figure 2.29 (b), (c) and (d)). Thus, the addition of N₂ usually prevents the formation of twins on (100) surfaces allowing extending the maximum deposition temperature to a higher value but at the expense of crystal purity. The acceptable temperature range is relatively narrow and there is only little room for growth rate improvement using this parameter [56].

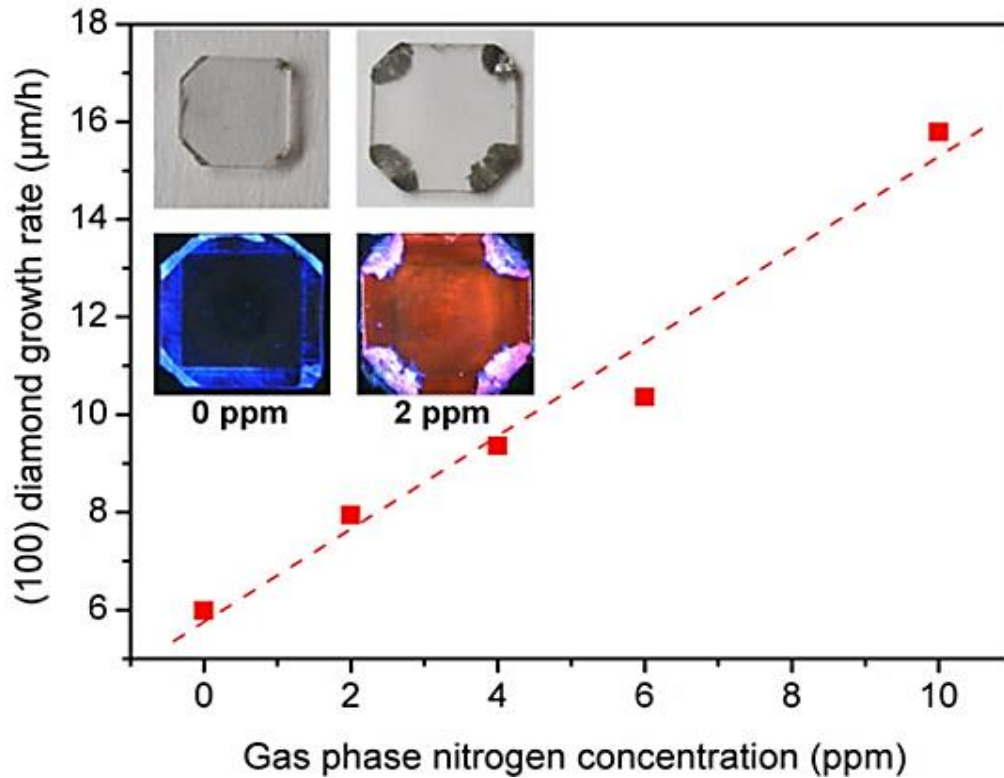


Figure 2.28 Diamond growth rate as a function of nitrogen addition in the gas phase (MWPD = 95 W/cm³). Optical and PL images obtained under UV light for an undoped free-standing CVD diamond crystal and a 2 ppm N₂ doped [56].

It was also reported that going to high a temperature under high purity conditions plagues the surface morphologies for single crystal diamond. Above 900°C, we observe a roughening of the crystal surface due to the formation of typical pyramidal defects (Figure 2.30 (a), 920 C, 7 μm/h) while at reasonably lower temperature the surface remains smooth (Figure 2.30 (b), 870°C, 6 μm/h). At high-temperature twinning is promoted on existing defects such as screw dislocations emerging at the surface. Moreover, a favorable ratio of growth rates in (100) and (111) directions (defining the α parameter) ensures that once formed twins will survive and overgrow [56].

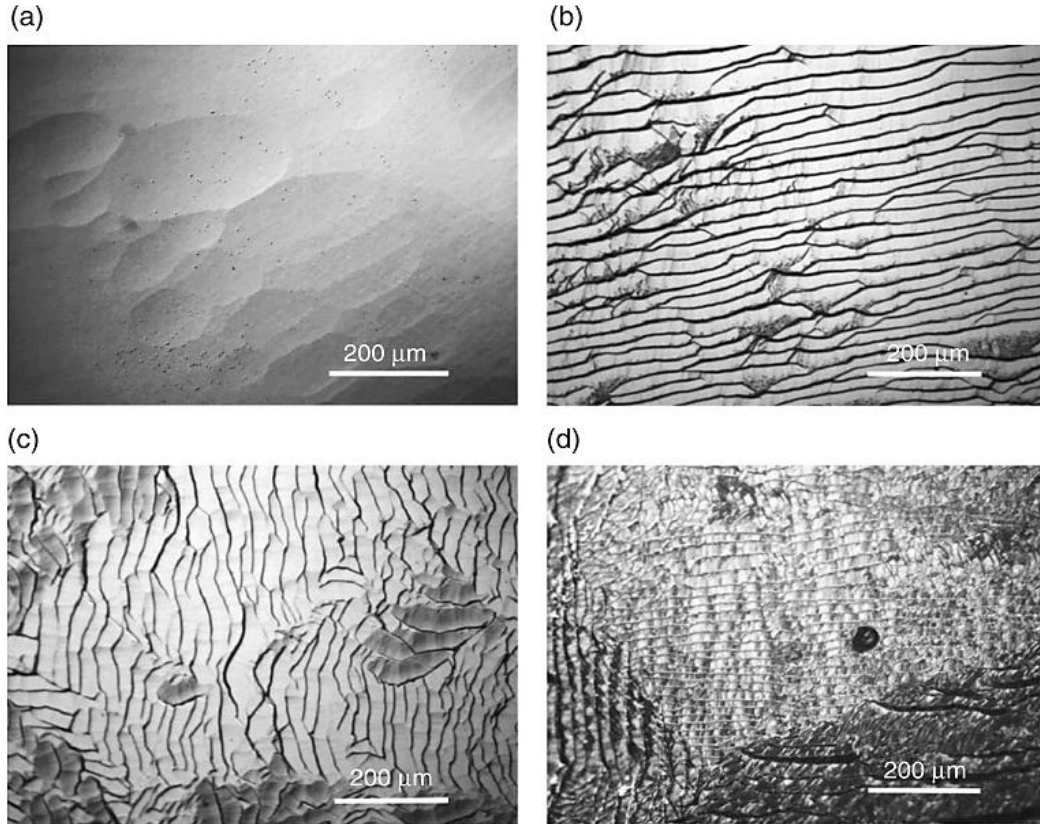


Figure 2.29 Optical images of the samples grown with (a) no intentional N_2 addition, (b) 2 ppm of N_2 (c) 6 ppm of N_2 and (d) 10 ppm of N_2 [63].

The high-quality free-standing CVD diamond plates are shown in Figure 2.31. From a macroscopic point of view, all the crystals have very good optical quality. They are all very clear and relatively free of inclusions. The black corners of the samples (2) in Figure 2.31 indicate that the (111) triangular corners were more defective by nitrogen than the (100)-faces. Thus the (100) top surfaces are virtually free of defects regardless of the amount of incorporated nitrogen.

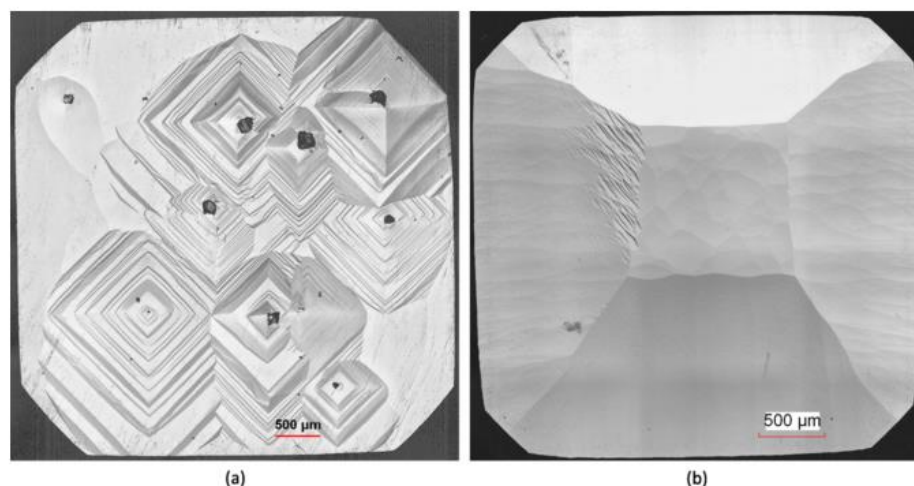


Figure 2. 30 Effect of growth temperature. Confocal laser microscopy images of 160 μm thick CVD films grown at (a) 920 $^{\circ}\text{C}$, 7 $\mu\text{m}/\text{h}$, (b) 870 $^{\circ}\text{C}$, 6 $\mu\text{m}/\text{h}$ doped [56].

Additionally, the methane concentration was varied while the power density of the substrate temperature was held constant, i.e. 95 W/cm^3 and 850 $^{\circ}\text{C}$ respectively. The result showed a growth rate that increases from 2 to 16 $\mu\text{m}/\text{h}$ as the concentration of methane increases from 2% to 7.2%. This behavior is attributed to the variation of the concentration of CH_3 and atomic hydrogen at the diamond surface [49], [58]. The morphology of the grown diamonds is shown in Figure 2.32. With 2% of CH_4 , the film surface is very rough exhibiting a large number of etch pits. This could be a consequence of a high etch rate by atomic hydrogen during growth at such high microwave power density and a low percentage of CH_4 . The etch-pits progressively disappeared and the surface improved up to 4% of methane. The films were grown at 6% and 7.2% of methane shown good quality with no no-epitaxial crystallites, but step bunching could be observed in some parts of the samples (Figure 2.32 (c) and (d)) [58].

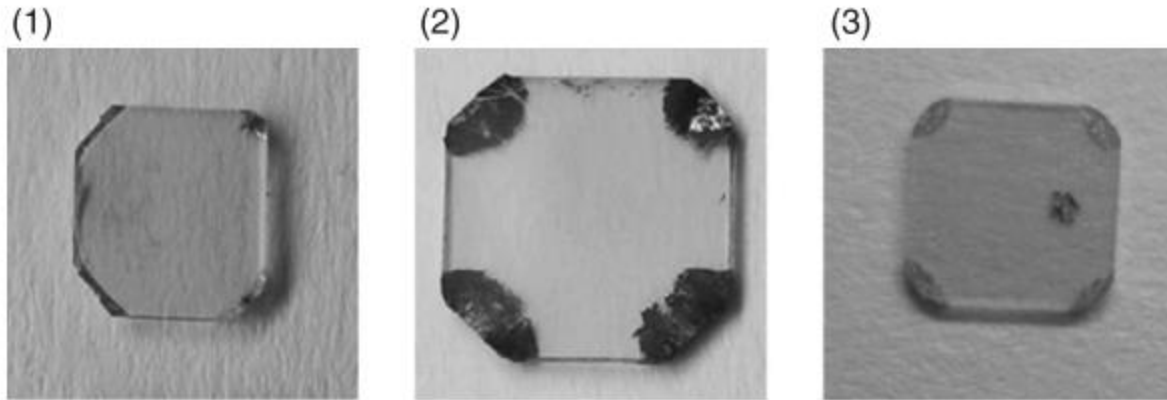


Figure 2.31 Optical image of the free-standing CVD diamond samples obtained after laser cutting and polishing and grown with (1) no intentional N_2 addition, (2) 2 ppm of N_2 , (3) 4 ppm of N_2 in the gas phase [63].

In research topic (2) microwave engineering plasma modeling; the influence of the deposition process parameters on the production rate of the growth species and CVD diamond growth kinetics, and different designs of plasma reactors have been studied. Using their reactor geometry, they have developed plasma models to compute the $[H]$ and $[CH_3]$ in the gas phase as a function of the deposition parameters, i.e. pressure, microwave power and methane concentration [9], [118], [119]. Their investigations show that the use of high microwave power density (MWPD) plasmas are necessary to promote atomic hydrogen concentrations that are high enough to ensure the deposition of high purity diamond films at large growth rates. MWPD, electron density (N_e), electron temperature (T_e), gas temperature (T_g) and the atomic hydrogen $[H]$ density has been modeled extensively for a pure hydrogen discharge. Figure 2.33 shows the evolution of the distribution of these quantities for a working pressure that ranges from 50 to 300 mbar.

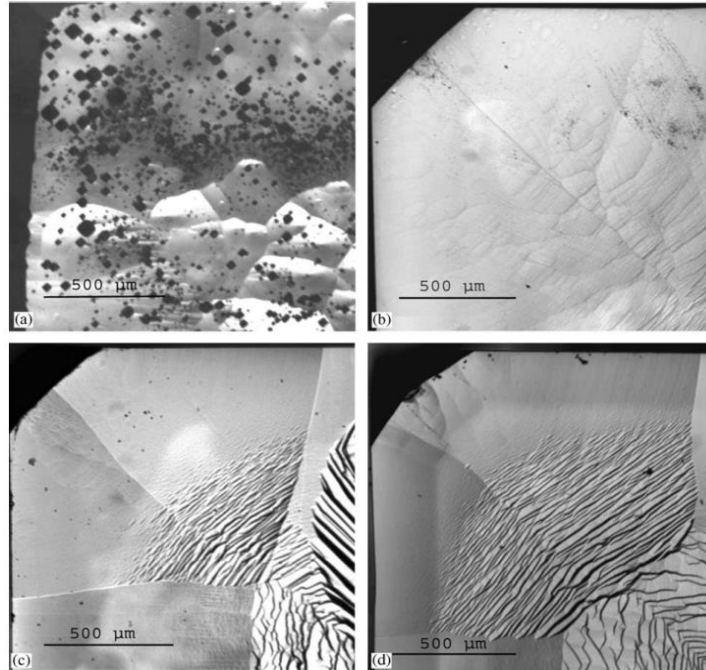


Figure 2.32 Optical images of the diamond films grown at 95 W/cm^3 and $850 \text{ }^\circ\text{C}$ with (a) 2% CH_4 , (b) 4% CH_4 , (c) 6% CH_4 and (d) 7.2% CH_4 [58].

The microwave power was adjusted at each pressure so as to maintain a constant plasma volume [9]. The result revealed the importance of working at high pressure in order to obtain simultaneously high growth rates and high film quality. Also, the importance of the substrate holder to provide precise control of the surface temperature, which is a challenging at high pressure.

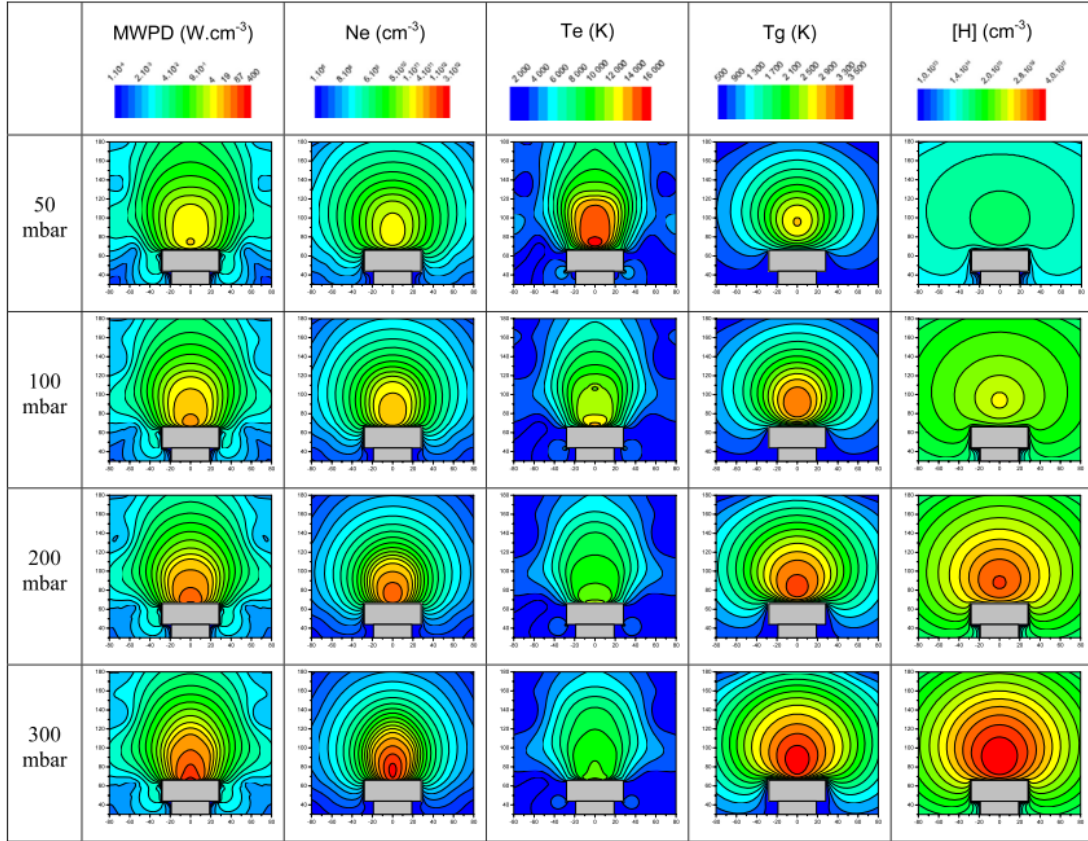


Figure 2. 33 From left to right, spatial distributions of microwave power density (MWPD), electron density (N_e), electron temperature (T_e), gas temperature (T_g) and atomic hydrogen density ($[H]$) for a pure hydrogen plasma ignited inside the LIMHP reactor [9].

In research topic (3) they investigated the influence of the presence of multiple growth sectors on the substrate surface and geometric modeling of CVD diamond crystals [112], [113], [120]. In 2008 a geometric model of the growth of any cubic lattice material was introduced by F. Silva et al [120]. The model showed a complete mapping of the final morphology state of growing diamond, as a function of the growth rates of the crystalline planes: (100), (111), (110), and (113). This geometric model was subsequently extended with experimental results [56]. The results reported indicated the dependence of the

growth parameters on the diamond crystal faces. The finding showed that (113) faces usually have the lowest growth rate and rough surfaces. The (111) face have high growth dislocations whereas (100) and (110) faces have a higher average growth rate and low densities dislocations.

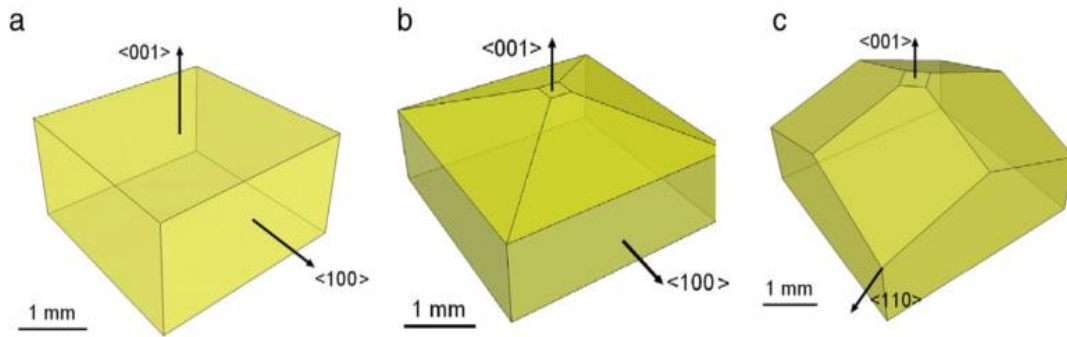


Figure 2. 34 Schematics of the initial diamond substrate before polishing (a) and of substrates polished into a pyramidal-shape (b) type A, 20° {100}-misoriented, (c) type B, 20° {110}-misoriented [114].

In an attempt to solve those issues, the growth on pyramidal-shape substrates having different angles and orientations was carried out. The schematic of the initial diamond substrate and the substrate into a pyramidal-shape are shown in Figure 2.34. The growth process was performed at substrate temperature of 850°C with 5% methane concentration at a power density of 100 W/cm^3 . The HPHT substrate has both their lateral and top faces oriented along the (100) directions. They were then polished into a pyramidal-shape for which the lateral sides of the pyramid were inclined by an off-angle of 20° , 30° or 40° along either the (100) directions.

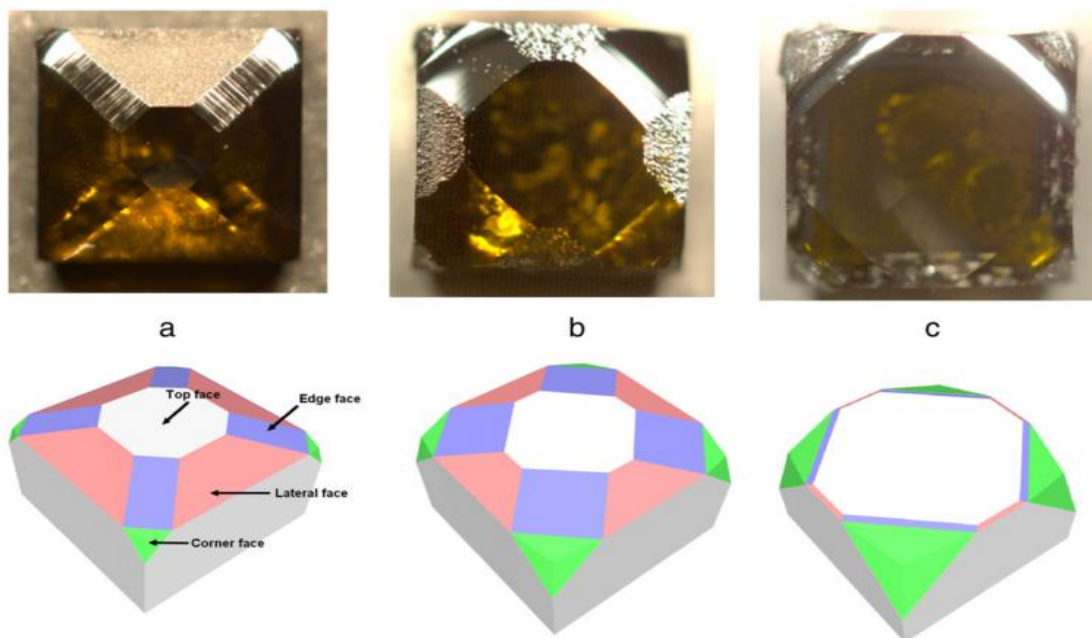


Figure 2. 35. Optical images and 3D representation of the sample grown onto $20^\circ \{100\}$ -misoriented pyramidal-shape substrates after several growth interruptions. The total thickness of the CVD layer is (a) 90 μm , (b) 270 μm , (c) 500 μm [114].

The grown substrates show the different diamond faces morphologies as well the lateral growth in (110), (111), and (113) after the first growth run (90 μm) as seen in Figure 2.35 (a). It was also demonstrated the high growth rate of the lateral growth was led by the (110) face. After 500 μm thickness, a partial overgrowth was observed in the samples. The minimum thickness required for complete disappearance of these faces reaching up to 2.2 mm. As was expected in the central part the results showed high etch-pit density. The other part of the crystal around the central square shows a reduced etch-pit density [114].

Following up these results, research topic (4) was the reduction of dislocations by using the self-assembled metallic mask and by the growth of diamond on an HPHT

diamond substrate hollowed out by a large hole. First, a new growth strategy was introduced aiming at preventing threading dislocations from propagating into CVD diamond layers. It was based on the selective masking of existing defects revealed at the surface of the substrates by Pt nanoparticles. The procedure was used to selectively mask substrate defects with metallic nanoparticles in an attempt to decrease dislocation densities. See Figure 2.36. Step 1 aims at revealing extended defects at the crystal surface by an adapted etching treatment. Step 2 is the coating of the surface by a thin CVD platinum film. Step 3 is a thermal treatment so that nanoparticles self-assemble to the etch-pits on the surface. Step 4 is the PACVD diamond overgrowth to embed Pt particles. Step 5 is a final etching treatment to reveal and count extended defects. The full process can be repeated several times to improve its efficiency as illustrated by the red arrow in Figure 2.36.

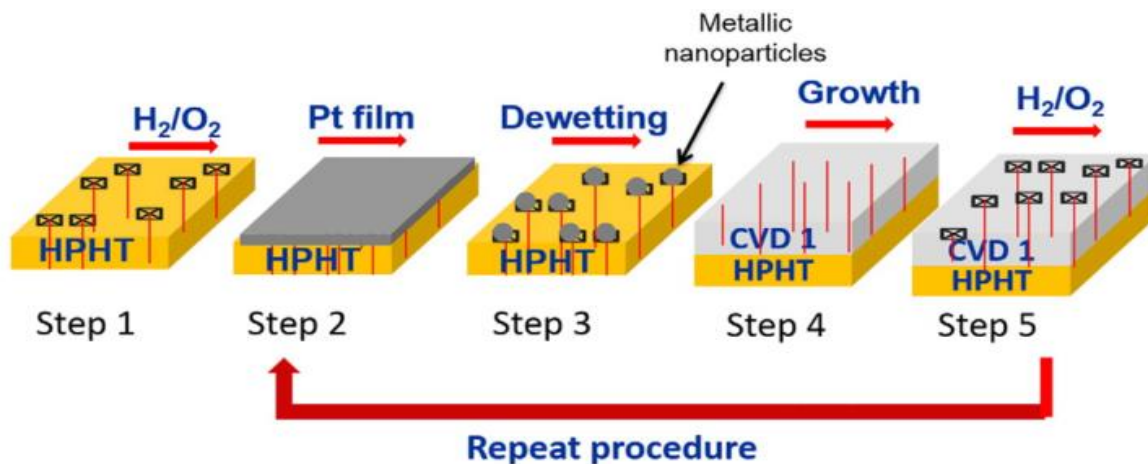


Figure 2.36 Schematic of the complete procedure of self-assembled metallic masks [121]

The experiments carried out consist of three successive growth runs with a thickness of about $80\mu m$. A Test sample was etched and masked with metallic nanoparticles at

each step following the procedure described in Figure 3.36. Another reference sample was etched but not masked coated with Pt. Finally, a short etching run aiming at revealing dislocations was performed leading to the appearance of etch-pits at the surface. The schematic representation of the experiments is shown in Figure 2.37 (a) and (b) and the results in Figure 2.37 (c) and (d). Results revealed that in the reference sample the defect density increased with every growth layers up to $\sim 1 \times 10^7 \text{ cm}^{-2}$. On the other hand, after the third growth run the test sample revealed a decrease in the defect density to $\sim 10^6 \text{ cm}^{-2}$. The values showed satisfactory results on the reduction of the defects. Although the defect density is still high, it remains low as compared to HPHT substrates.

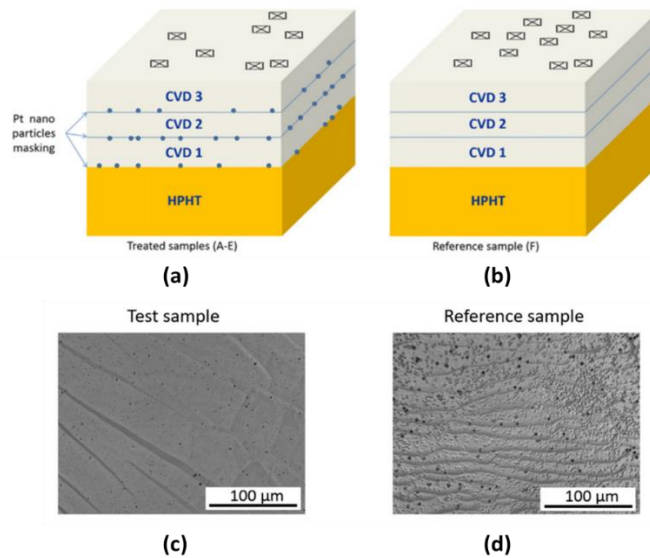


Figure 2. 37 Schematic representation of the experiments (a) Test sample, (b) Reference sample. After each etching step and the resulting final morphology is shown in a (c) test sample, (b) reference sample [121].

Lastly, in the research topic (4) Tallaire et al. [122] investigated the reduction of dislocations by lateral growth over a macroscopic hole. Standard cubic-shape HPHT Ib substrates were hollowed out to create a square-shaped through hole (Figure 2.38 (a)) with $2 \times 2 \text{ mm}^2$ dimensions.

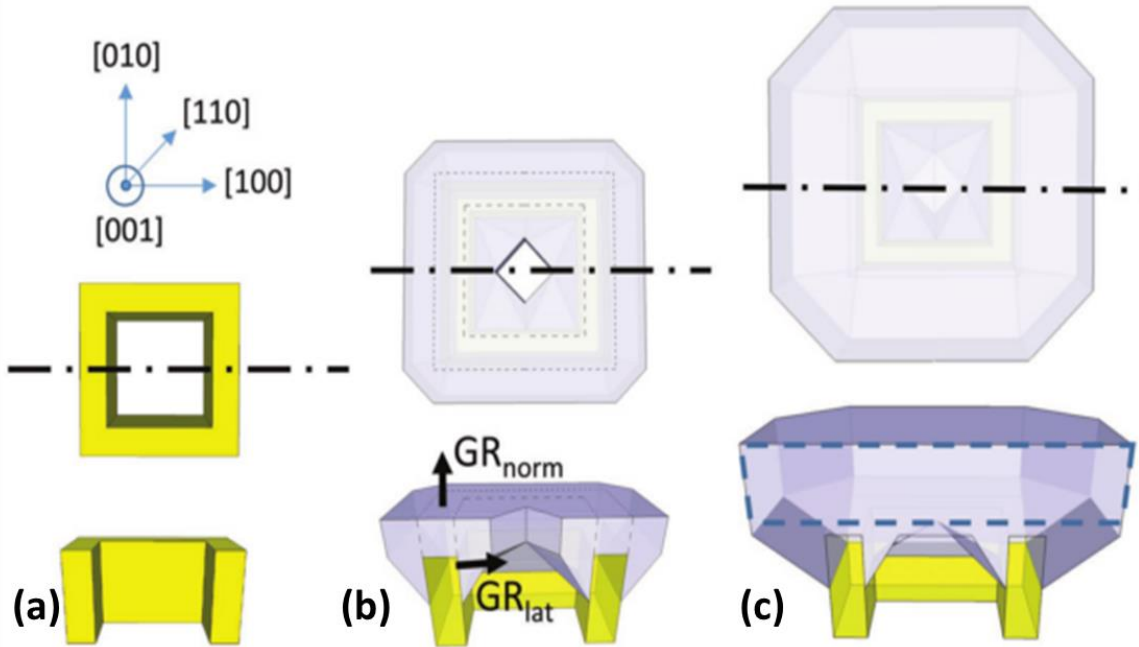


Figure 2. 38 A thick CVD diamond layer grown on an HPHT diamond substrate hollowed out by a large hole at the (b) beginning, (c) before, and (d) after merging of the growth fronts and disappearance of the hole [122].

The growth lasted for 112 h, resulting in a final thickness of $980 \text{ }\mu\text{m}$ (i.e., a normal growth rate of $8.75 \text{ }\mu\text{m/h}$). After that time, it is noticeable that the central hole completely disappeared, leaving a top surface free of any un-epitaxial defects. The central part is smooth with macro steps bunched preferentially along (110) directions at the edges as seen in Figure 2.39 (a).

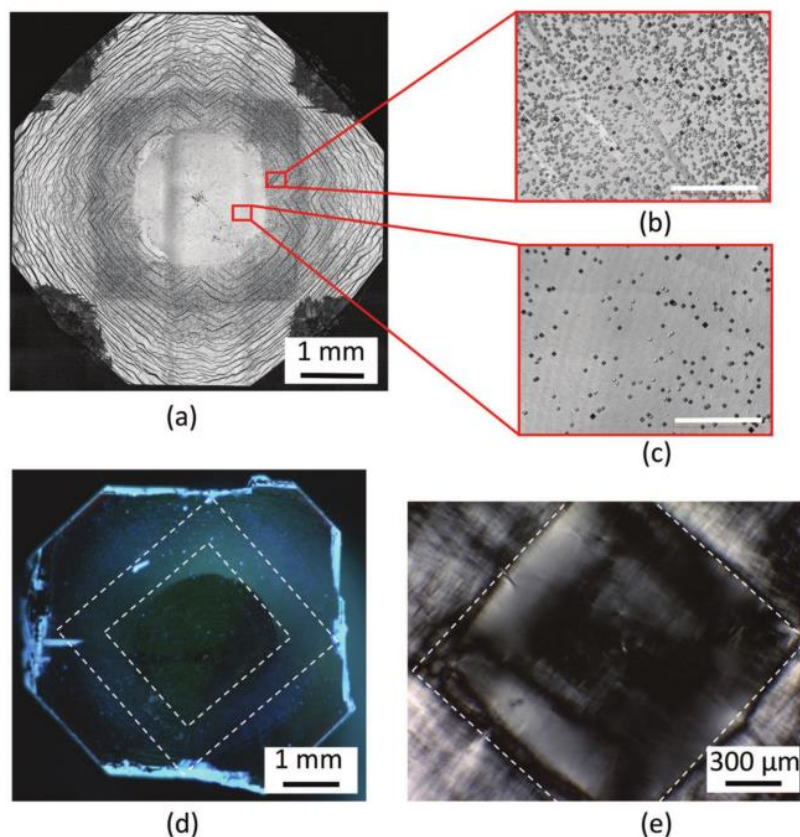


Figure 2. 39 Laser microscope images of the CVD film grown on an HPHT substrate with a macro hole after plasma etching to reveal dislocations: full-size image showing the underlying square substrate. (b), (c) zoomed into the regions above the substrate and above the hole, respectively, (d) PL UV image of the freestanding CVD diamond plate. (e) Birefringence image of the freestanding plate under cross-polarizers. The white dashed square indicate the position of the edges of the removed substrate [122].

The defect density in the center was found to be around $2 \times 10^3 \text{ cm}^{-2}$, while it was at least an order of magnitude higher in the region above the substrate (Figure 2.39 (b) and (c)). The PL UV image where the position of the substrate is indicated by dashed white

lines shows only light blue luminescence in Figure 2.39 (d). The birefringence image shows only limited birefringence with a low number of cross-shape dislocations. On the other hand, the region outside the dotted square exhibits much stronger birefringence, see Figure 2.39 (e).

In summary, the results indicate a tremendous improvement in the defect density on the CVD diamond substrates. The hollowed diamond seed seems to be an excellent approach to grow high-quality CVD diamond at low cost.

2.7.4 Gemological Institute, China University of Geosciences, China

G. Wu et al. [123] recently used a specially designed substrate holder with a circular recess, in which the seed crystal was placed. By designing substrate holders with different recess depths and a seed crystal with the different side surface, crystallographic orientations determine the influence of the recess depths and the crystallographic orientation of seed sides on the growth quality. They utilized a conventional open holder, in which the seed is placed in a flat holder and an enclosed holder. They also used an enclosed holder. This substrate holder was varied for four different recess depths, i.e. 0.5 mm, 1.0 mm, 1.5 mm and 2.0 mm. The schematic of the substrate holder is shown in Figure 2.40. The experiments were performed on (100)-oriented 3.5 x 3.5mm x ~ 1.4 mm HPHT type Ib seeds under the following experimental conditions: the pressure of 80 – 100 Torr, 3 – 5% methane concentration, 0.1 – 0.5 sccm of N₂ and an input power in the range of 1.8 – 2.2 kW. All samples were pre-treated in H₂ plasma for 1 hours.

Figure 2.41 (a) shows an optical image of the 150- μ m-thick diamond layer grown using the open type substrate holder with the growth conditions of 850 – 900 °C, 82 Torr, and

a CH₄/H₂ ratio of 3% and 0.5 sccm of N₂. The sample that was grown used the open type substrate holder (d = 0 mm) showed a concave surface morphology with overgrowth at the periphery compared to the flat surface of the center part. In contrast, they also grew on a HPHT seed placed in enclosed holder. Figure 2.41(b) shows the 110 μm thick diamond layer grown in the enclosed type substrate holder (d = 2 mm) under the same conditions as for the experiments of Figure 2.41(a). The result shows an overall smooth surface and less polycrystalline material at the periphery.

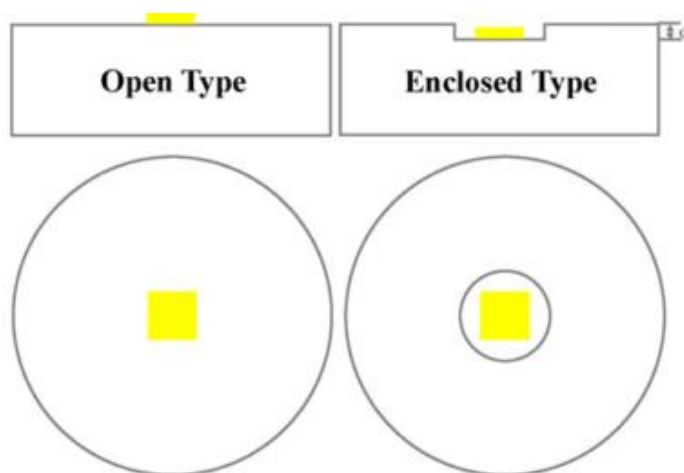


Figure 2. 40 The schematic diagrams of the open type substrate holders and enclosed type substrate holders with different recess depths. (The yellow squares represent the seed crystals placed on the substrate holder or in the recess) [123].

The partial results demonstrated that as the recess depth increases, the formation of polycrystalline diamonds on the periphery is controlled effectively. The growth rate versus recess depth was evaluated on the grown substrates; the results showed when

the recess depth increases, the growth rate of the samples decreases significantly, especially without the addition of nitrogen, as seen in Figure 2.42 (a).

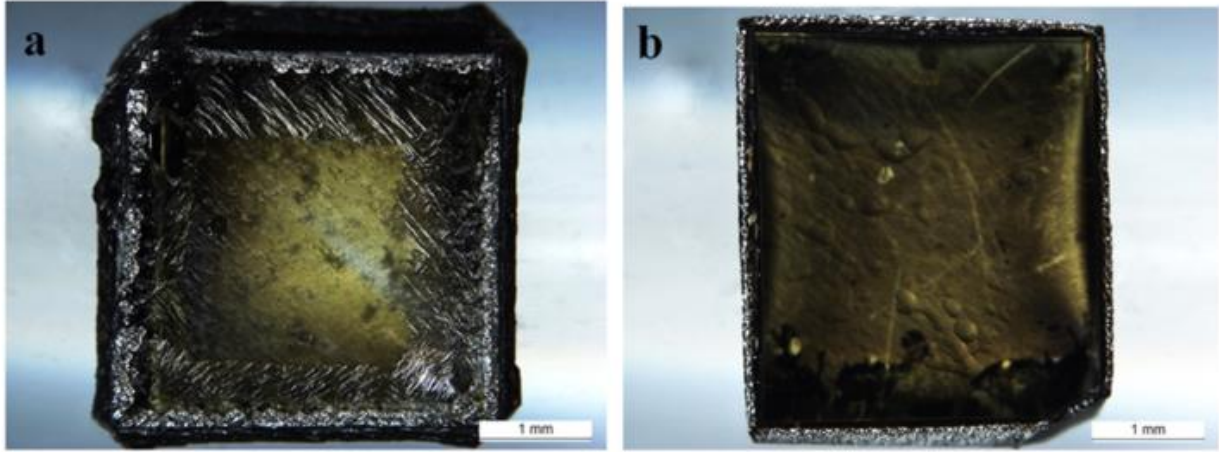


Figure 2. 41 (a) HPHT seed grown by using an open type substrate holder ($d=0\text{mm}$); (b) HPHT seed grown by using an enclosed type substrate holder ($d=2\text{mm}$) [123].

The lateral surface and the top surface growth rate ratio were plotted versus recess depth in Figure 2.42(b). The results showed that the lateral growth of the sample decreased significantly as the recess increased.

Raman spectroscopy was performed at the periphery and center of the grown samples as a function of the recess depth to evaluate the quality of the crystals. See Figure 2.43. The crystalline quality of the center part varies little when $d \leq 1\text{mm}$, and then degrades significantly when $d=2\text{mm}$. The substrate holder obtains the best crystalline quality at the center part with the Raman shift FWHM of 3.4 cm^{-1} with a recess depth of $d=0.5$ or 1mm , in which the top surface of the seed crystal is above or at the same level as the surface of the substrate holder.

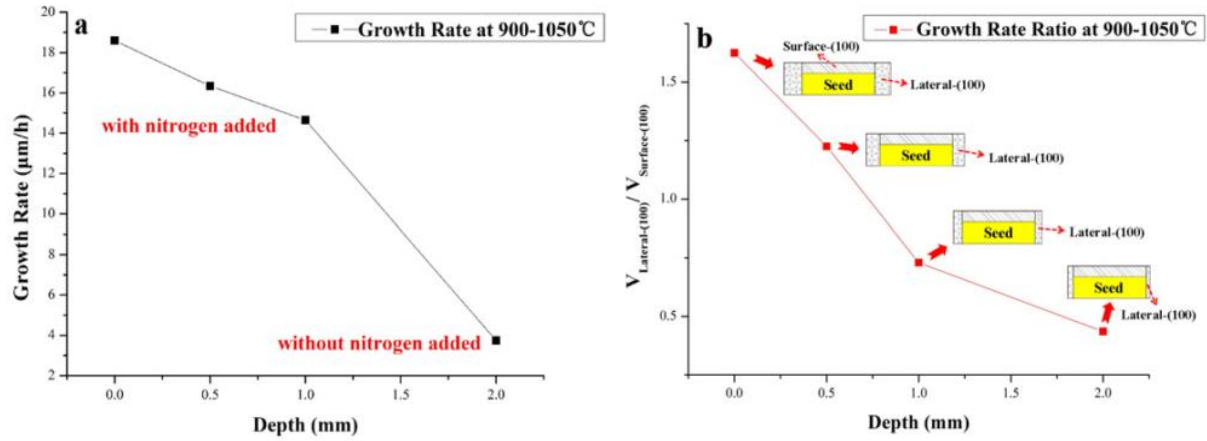


Figure 2. 42 (a) The influence of the recess depth on the main surface growth rate. (b) The influence of the recess depth on the lateral surface and main surface growth rate ratio. Insets: the cross-section schematic diagrams of the samples grown with different recess depths [123].

When $d = 2\text{ mm}$, the FWHM of the sample at the center part is 4.1 cm^{-1} , while the crystalline quality at the periphery is better than that at the center part. As the recess depth increases to when $d = 2\text{ mm}$, the crystalline quality when $d = 2\text{ mm}$, already surpasses that at the center part. At $d \leq 1\text{ mm}$, the top surface of the seed crystal can contact the plasma to some extent, and the plasma above the center part of the seed crystal is quite uniform. Hence, a variation of the recess depth has little effect on the crystalline quality of the center part of the diamond layer.

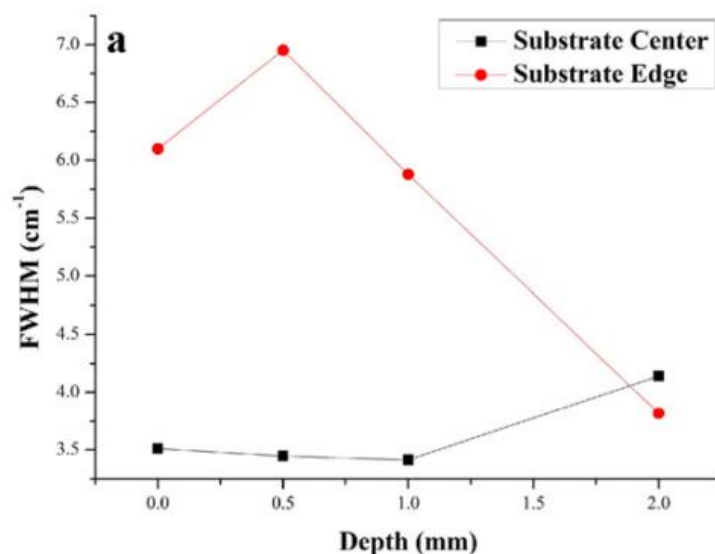


Figure 2. 43 The influence of the recess depth on the FWHM of the diamond layers at the center part and the periphery [123].

In summary, this investigation showed that as the recess depth increases the polycrystalline diamond growth was controlled and was reduced adequately. Samples with a good crystalline quality were grown at low growth rates (3 $\mu\text{m}/\text{h}$). The best-grown substrates considering the crystalline quality and growth rate were grown in substrate holder with a recess depth of $d = 1 \text{ mm}$.

2.7.5 Michigan State University, USA

The diamond growth research at Michigan State University has provided an extensive understanding of CVD diamond growth since the late 1990s. The relevant research topics in the MSU laboratories includes: (1) the development of microwave plasma reactor to enhance the growth rate [16], [18], [73], (2) substrate holder configurations to improve

SCD quality [20], [86], [124], [125], and most recently (3) the devilment of SCD growth process at high-pressure [12].

In research topic (1) three generations of microwave plasma cavity reactor (MPC) were developed and called reactor A, B, and C. The first generation of the MPC, was designed to be operated at pressures in the range of 60 – 100 Torr for polycrystalline diamond growth [126], [127], [128], [129],[130] . The next generation design modified the reactor to allow diamond growth at higher pressures, higher power densities and higher growth rates. A cooling stage was added and PCD films were grown at 145 Torr [126], [131]. As a relevant output, the polycrystalline films were grown at 7 $\mu\text{m/h}$ with a power density up to 43 W/cm^3 [73]. This new design identified as here Reactor A improved the growth rate, and increased the operating pressure to 180 Torr. An additional important modification was the further improvement of the cooling stage and the substrate holder, i.e. a reduction in the diameter, to enhance the operating pressure and to allow operation at higher microwave power densities. The new modification MPCR was called reactor B and was initially redesigned to operate at pressures up to 240 Torr. Initially, polycrystalline diamond films were grown at 240 Torr with at 475 W/cm^3 power densities at an approximate growth rate of 21 $\mu\text{m/h}$ [73]. Further experiments performed by Lu et al. [16] demonstrated an increased growth rate in SCD substrates up to 45 $\mu\text{m/h}$ at 240 Torr due to additions of nitrogen into the gas fed and a higher methane concentration of 7%. The crystal quality was determined by Raman spectroscopy and indicated low stress with better quality than HPHT type Ib seeds.

Y. Gu et al. [18], [132] designed the last generation of MSU microwave plasma cavity, called reactor C for the purpose of operating at higher: pressure, power densities and

growth rates. Experimental results showed safe and efficient operational conditions at pressures from 240 to 300 Torr. A comparison of the SCD growth regime is shown in Figure 2.44 for all three reactor designs. Reactor C presents significant advantages over the reactor A and B. Figure 2.44 (a) displays evidence that the power density reaches to 1000 W/cm^3 at 300 Torr. It is about twenty times as high as that for reactor A and two times as high for reactor B. The growth rate also was enhanced. See Figure 2.44 (b). At 7% methane concentration in which reactor B reached to 45 um/h , the growth rate for reactor C was 60 um/h . This fact confirmed the advantage of reactor C over the previous designs in terms of high pressure operating conditions. All diamond substrates discussed in this thesis investigation have been grown with reactor C. The design detail of reactor C have been presented in detail in Chapter 3.

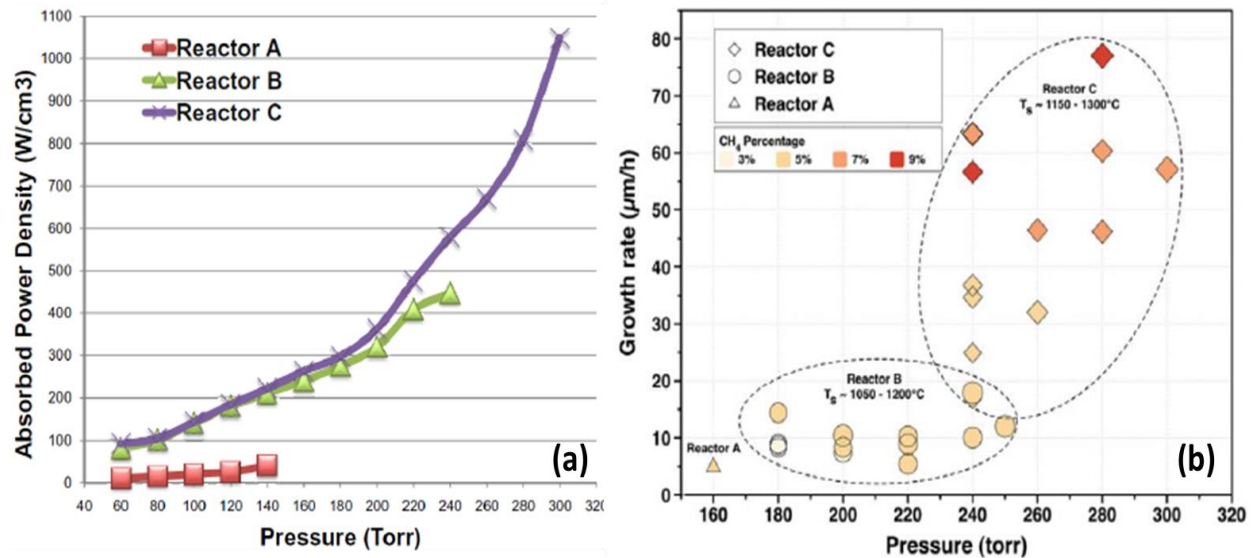


Figure 2. 44 Comparison of reactor A, B and C (a) absorbed power density versus pressure and (b) growth rate versus pressure [18], [132].

In addition to the development of microwave plasma reactors Asmussen et al. [133] also introduced a different molybdenum substrate holder designs for growing the SCD. Initially, the shallow recess holder was used exclusively to constraint the diamond seed and ensure a constant holding position during the growth process. Nad et al. [20] studied the variation of the substrate holder geometry on the SCD growth and how the growth of the PCD rim could be overcome. The first geometry explored was called open holder. In an open holder, SCD growth experiments were used as a group of controlled benchmark experiments. In this first geometry, the HPHT diamond seed is placed directly on a flat molybdenum substrate holder as is shown in Figure 2.45 (a). During the growth process, the top, edges and the side surfaces of the seed are directly exposed to the active discharge and to the impressed microwave electric fields that exist in the substrate discharge boundary interface.

The open holder experiments observations showed that during the growth process, SCD is grown on the top surface of the seed substrate, Figure 2.45 (a).

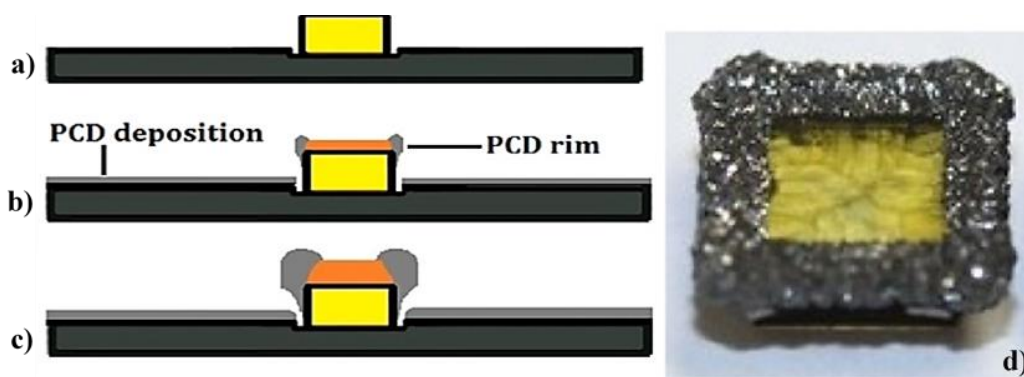


Figure 2. 45 A cross-sectional view of SCD synthesis versus time in an open holder (a, b, c). d) The synthesized diamond after 35.5h of deposition time [20].

Simultaneously PCD is also grown on the top edges and the sides of the seed. As shown in Figure 2.45 (b), an additional PCD layer is also grown on the top of the molybdenum holder. As the synthesis process proceeds versus time (Figure 2.45 (c)), the PCD layers increase and a PCD rim completely encloses the SCD top surface edges. Eventually, a PCD rim grows vertically upward, horizontally outward and radially inward into the SCD top surface. As a result, decreased useful SCD surfaces were obtained. A thick PCD rim as shown in Figure 2.45 (d) was formed completely around the top surface.

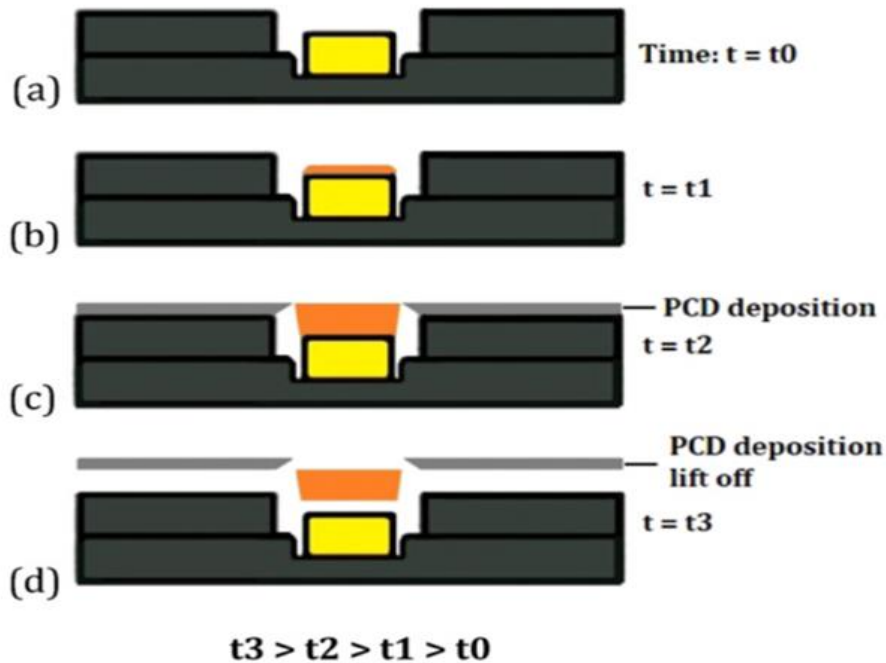


Figure 2. 46 Cross-sectional views of SCD growth process versus time in a pocket holder [20].

In order to improve the localized control of the SCD synthesis process, a new holder design geometry called pocket holder was proposed. In the pocket holder, the diamond seed is placed within a recess, or a “well” that adjusted into the water-cooled molybdenum

substrate holder, as is shown in Figure 2.46 (a). The pocket was designed for the purpose to protect the SCD seed from the intense microwave plasma and from any microwave fields that may be concentrated on the hot edges of the substrate in the open holder configuration. Successful SCD growth was demonstrated, under the pocket growth conditions the diamond grew with a greatly reduced PCD rim or with a completely eliminated PCD. Examples are displayed in Figure 2.47 (a) and (b) respectively.

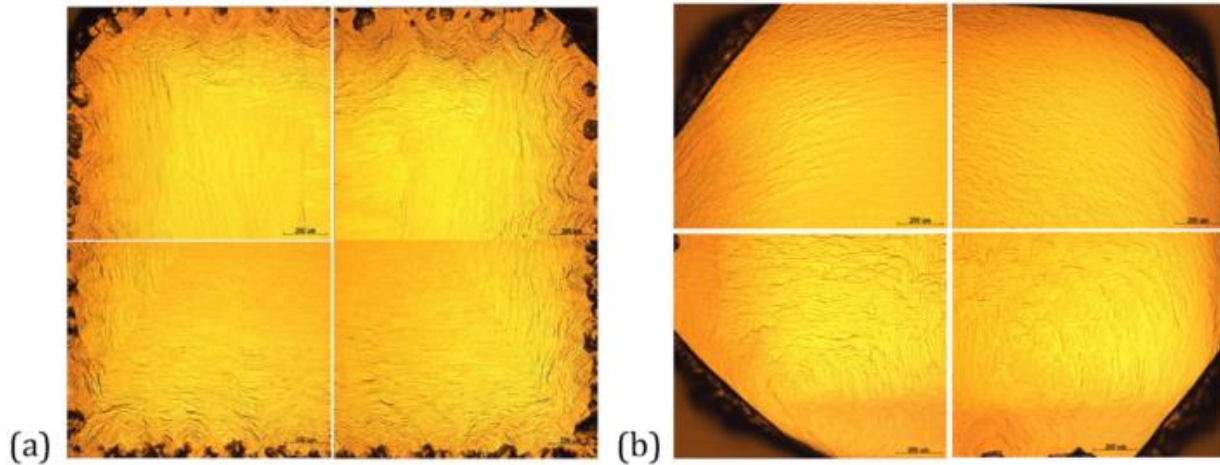


Figure 2. 47 Optical microscopy images of as-grown SCD substrates with (a) reduced PCD rim and (b) without a PCD rim [124].

The pocket holder effect was proven by the following experiment. One HPHT seed was cut at an angle to the (100) growth direction. The angled seed allowed that one side of the growing diamond to grow out of the pocket while the other edges remain into the pocket. The left edge of the substrate shows a PCD rim in contrast to the right edge. This difference is due to the fact that the left edge emerges out of the recess of the pocket

holder with increasing growth time before the other edges. Thus, that side is subjected to the plasma and the intense microwave fields and a PCD forms. The effect of the rim on the synthesized SCD plate is clearly visible in Figure 2.48 which shows a birefringence images with an exposure time of 500 ms, 2000 ms, and 5000ms. The right edge of the CVD SCD plate exhibits very low stress as compared to that in the left edge.



Figure 2. 48 Birefringence images of a 221 μm thick CVD SCD plate with exposure times of (a) 500ms (b) 2000ms and (c) 5000ms [124].

In summary, by utilizing the pocket holder design the successful synthesis of CVD SCD substrates without the formation of any PCD rim on the CVD grown SCD was demonstrated. The reduction of the PCD rim in the synthesized SCD substrates leads to stress-free high-quality CVD SCD plates.

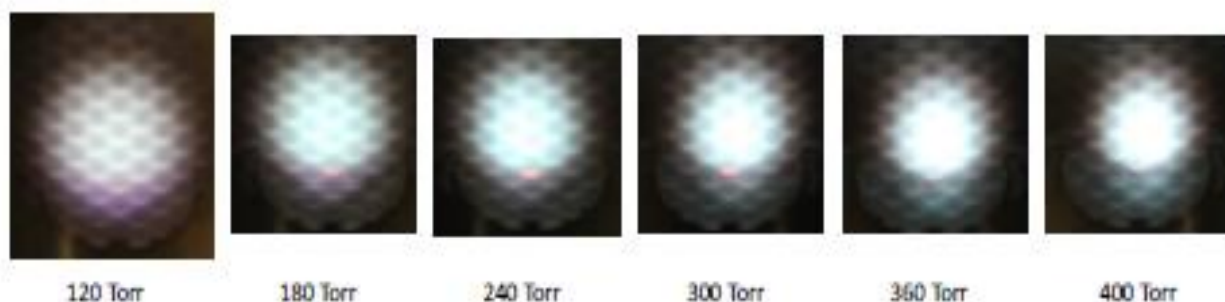


Figure 2. 49 Photographs of the discharge above a 3.5 mm x 3.5 mm SCD substrate in a 1.5-inch molybdenum holder as the pressure is increased from 120 to 400 Torr. The absorbed power is kept constant at 2100 W [12].

The recent results at MSU include exploring the growth of SCD at high operating pressure up to 400 Torr. The first high-pressure exploration was developed by Muehle [12] utilizing the highly filtered continuous microwave power supply in a reactor B design to determine the power density up to 400 Torr. A set of experiments were performed at constant microwave input power of 2100 W while the pressure increased. Figure 2.49 shows the photographs of the discharges between 120 and 400Torr. The estimated plasma volumes and the calculated absorbed discharge power densities are plotted versus pressure in Figure 2.50. The graph shows that the plasma volume is decreasing for increasing process pressure while the absorbed input power level is held constant. This results in an increase of the absorbed discharge power density with increasing pressure. The discharge showed a volume of 7.6 cm^3 at 120 Torr and 3.1 cm^3 to 400 Torr for a constant absorbed power of 2100 W shown in Figure 2.50.

It was observed that the absorbed discharge power density had linear increase from 275.4 to 526.4 W/cm³ for moderate pressures from 120 to 300 Torr. While at higher pressures up to 400 Torr the absorbed power density increases super linear to 671.3 W/cm³. These results show a significant increase in the absorbed power density at high-pressures.

The second exploration, a reactor operational field map at the pressure from 120 Torr to 400 Torr. The analyzing of the substrate temperature and the pressure as a function of the absorbed power was presented. The changes in absorbed power densities when increasing the overall absorbed input power for certain pressures were observed, specifically for the pressures of 320, 360 and 400 Torr.

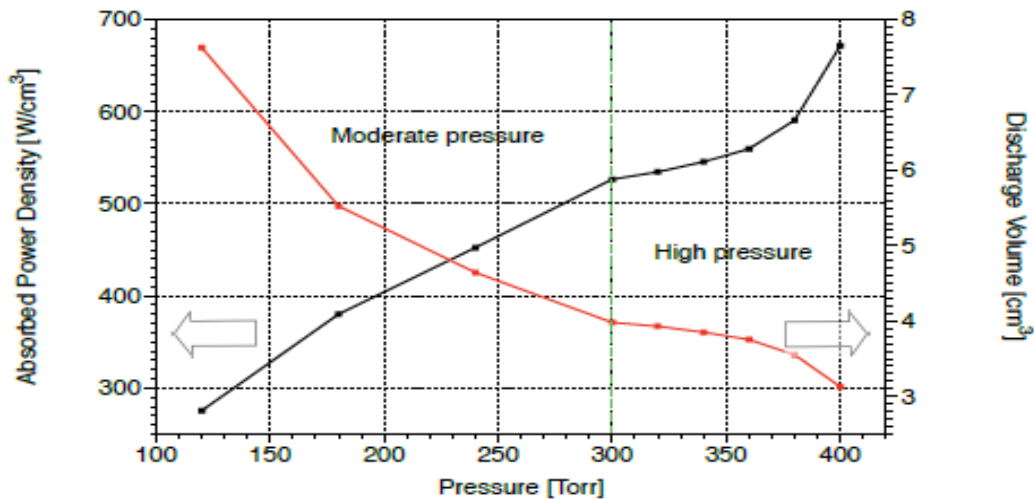


Figure 2. 50 Discharge power density and volume as a function of the pressure for the discharges utilizing $P_{abs} = 2100$ W and 3% CH₄ as shown in Figure 2.49. The differentiation between the previously investigated moderate pressure regime and the high pressure regime is indicated by the green dashed line [12].

The substrate temperature and pressure as a function of the absorbed power were also studied. The results for the entire 120 to 400 Torr pressure regions are plotted in Figure 2.51. It can be seen that all curves can be described with a linear approximation with the higher substrate temperature at pressures > 300 Torr with absorbed power > 2500 W.

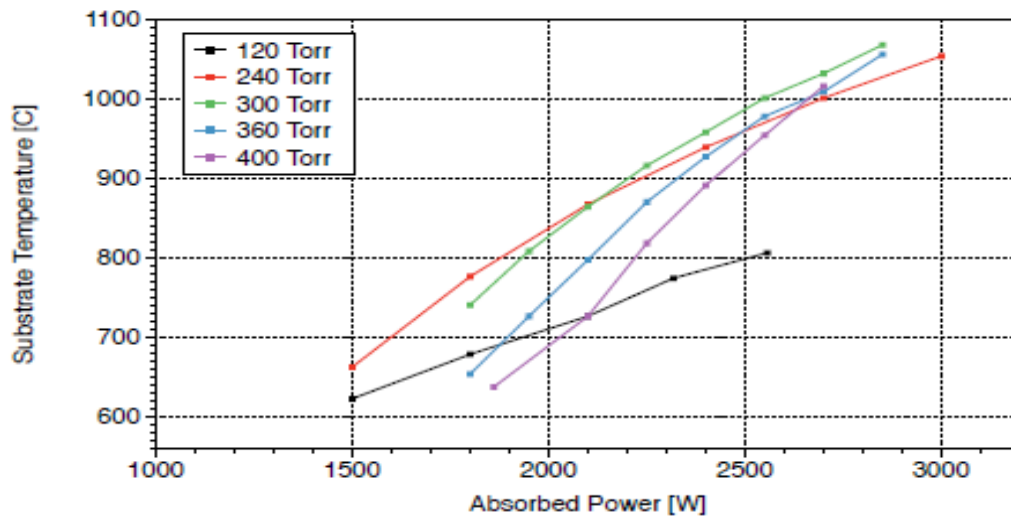


Figure 2. 51 Operational field map for Reactor B using a SCD substrate over the entire pressure regime

Additional to the plasma analysis, a set of four growth experiments were performed lasting 20 hours at 5% methane concentration at the pressure windows between 180 and 400 Torr. The experimental growth rate and weight gain as a function of the process pressure were measured and are plotted in Figure 2.52. The data showed an almost linear increase in the growth rate could be seen up to 380 Torr. The growth rate tripled from 9.3 to 28.1 $\mu\text{m/h}$ when the pressure increased from 180 to 380 Torr. When the

pressure is increased further from 380 Torr to 400 Torr, the growth rate flattens out. This was attributed as the pressure increases the distance between the discharge and the substrate also increases, that means that the region of high density $[\text{CH}_3]$ creation decreased directly above the substrate [12]. The increase of the weight gain as function of the pressure follows the growth rate behavior.

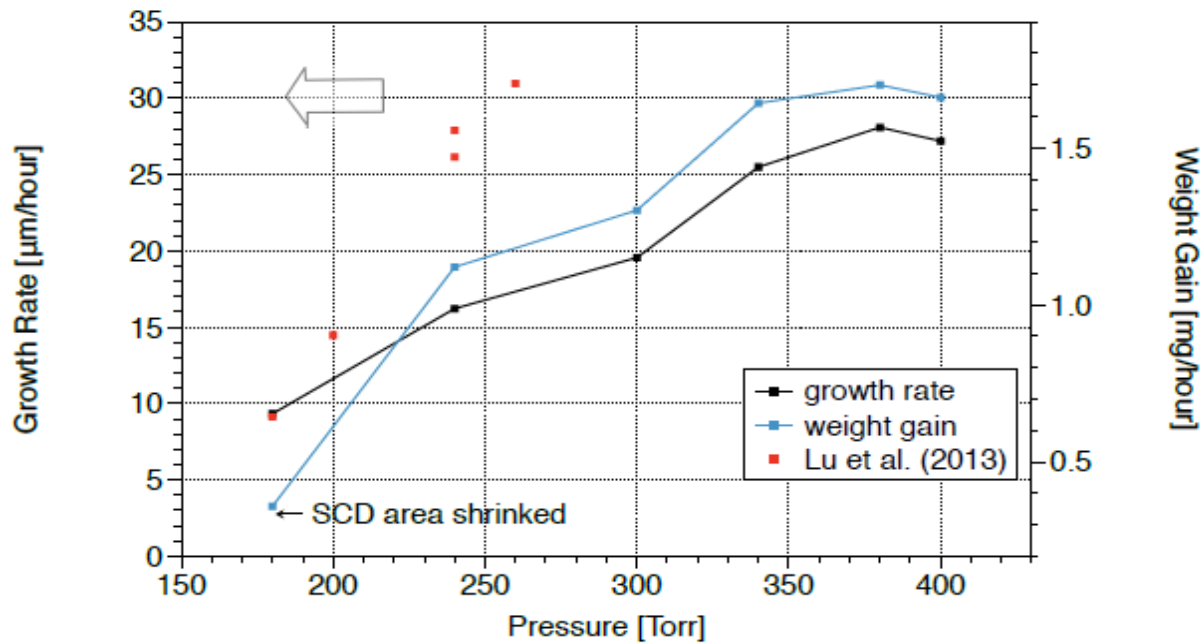


Figure 2.52 Linear growth rate and weight gain as a function of the process pressure and comparing the growth rates to previously reported results by Lu et al. [16], [12].

The morphology of the grown SCD films after deposition without additional processing can be seen in Figure 2.53. It was observed no PCD formation occurred throughout the entire pressure regime. The experiments used a pocket holder design similar to the design that already was optimized for rimless growth [20], [125]. The grown substrates

have an enlarged top SCD area of ~ 1.4 times that the original HPHT seed area. The top SCD surfaces seem to not have major defects.

Thus, successful safe and efficient operating high-pressure conditions up to 400 Torr for MSU reactor B have been found. The growth rate and substrate temperature showed a linear dependence with the pressure. SCDs with a smooth top surface and with reduced PCD rim were grown at 400 Torr by using a pocket holder. Overall, results indicated the advantage of increasing the pressure to enable a rapid growth of SCD substrates.

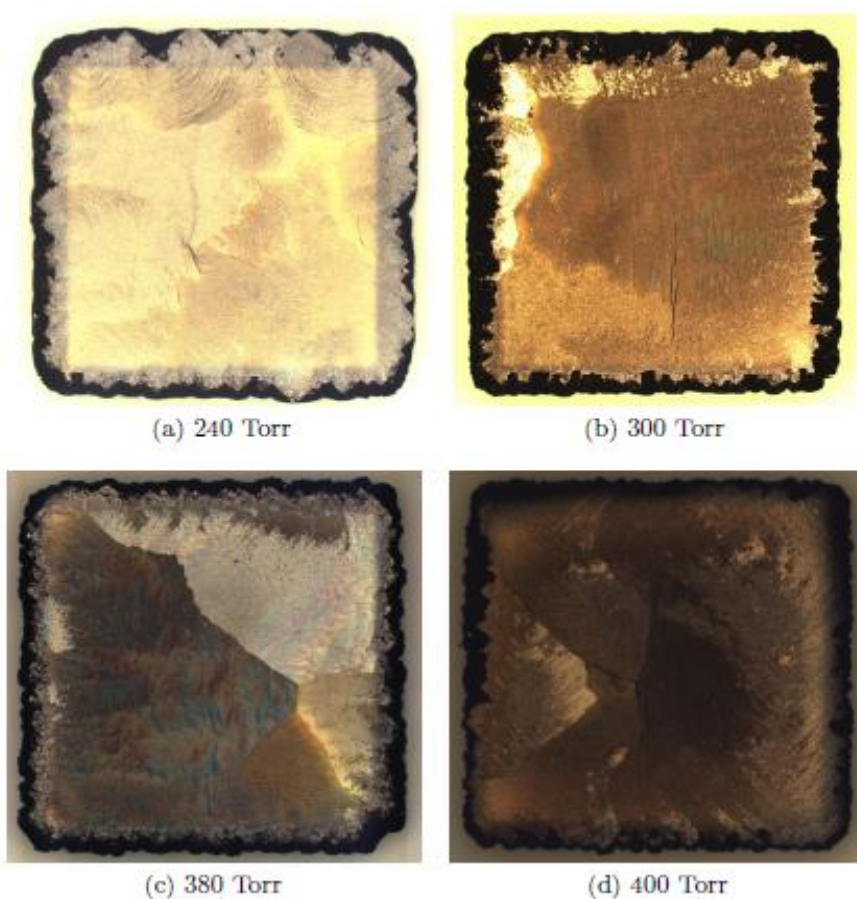


Figure 2.53 Top surface of SCD films grown in the pressure range between 240 and 400Torr [12].

CHAPTER 3

DESCRIPTION OF THE EXPERIMENTAL EQUIPMENT AND EXPERIMENTAL PROCEDURE

3.1 Introduction

This chapter presents a description of the microwave plasma assisted chemical vapor deposition (MPACVD) reactor system. This reactor system was used in all the experiments described in this thesis investigation. The first section begins with an overview of the typical experimental microwave plasma cavity Reactor C system. The second section, describes the associated sub-systems that comprise the classical microwave reactor system. The internal parts of the experimental system and standard operation are also discussed. The next section, describes in detail the pocket holder configuration. Finally, a brief discussion of the main analytical instruments is presented.

3.2 Experimental Setup

A typical schematic of the entire microwave cavity plasma reactor C system is shown in Figure 3.1, it illustrates the basic system design. The schematics below show the important components of the system and subsystems. The experimental sub-systems are described as follows: (1) microwave power delivery, (2) the process gas delivery, (3)

the vacuum pumping control, (4) the pressure control, (5) the air and water control, (6) the exhaust line, (7) the optical and photographic diagnostics, (8) the computer control, and (7) the microwave cavity reactor subsystems.

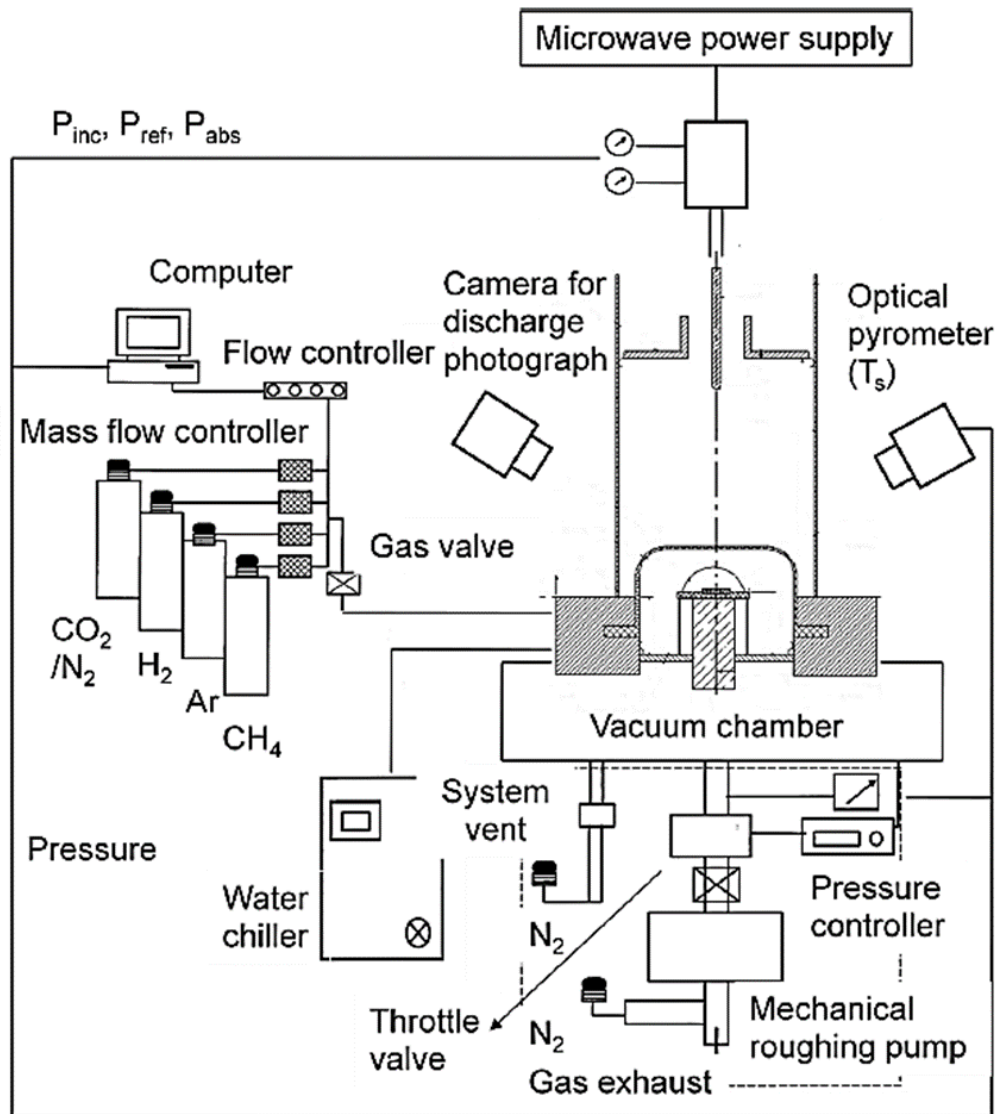


Figure 3. 1 Overall setup of MSU microwave plasma cavity Reactor C system [85].

3.2.1 Microwave Power Supply subsystem

Figure 3.2 (a) shows the key components of a microwave power supply processing subsystem. The microwave power is generated in the power supply, transferred via waveguides to a coupling probe and coupled into the material loaded applicator. In the case of microwave plasma processing the “material load” consists of the cooling stage, substrate holders, the substrate material, and the processing plasma. The continuously variable 10 kW adjustable from 10 -100% microwave power is displayed in Figure 3.2 (b) and is equipped with a microwave power supply of a frequency of 2450 MHz \pm 10 MHz and a 15 kW CW S-band magnetron with a typical 68% efficiency. The output of the magnetron power supply is connected to a circulator that isolates and protects the power supply from any power that may be reflected from microwave reactor. The reflected power is led to a water-cooled dummy load which is impedance matched.

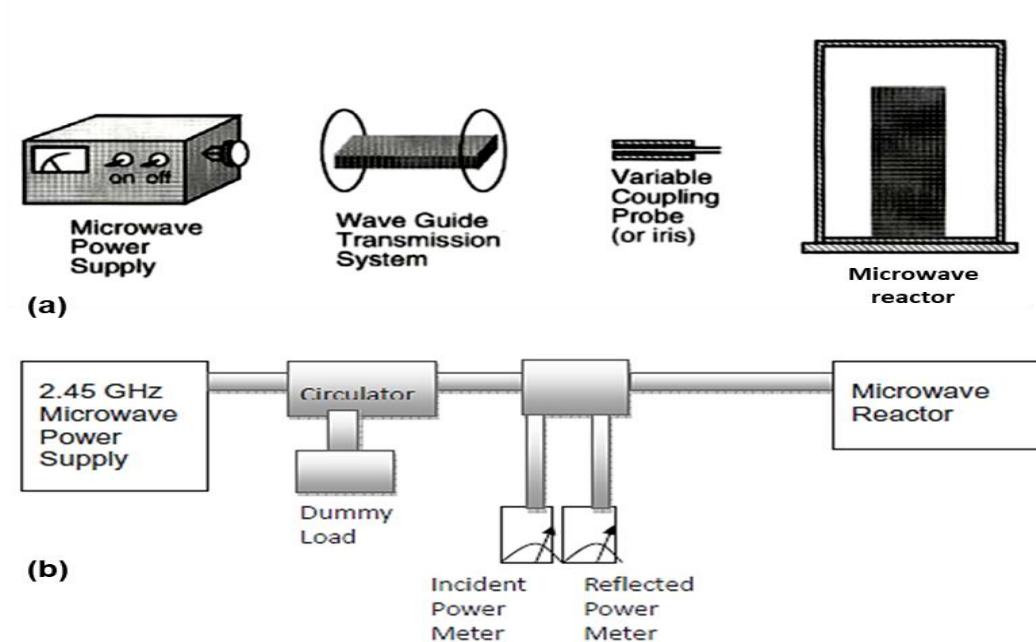


Figure 3. 2 Components of standard microwave power supply subsystem

The absorbed power P_{abs} is $P_{\text{inc}} - P_{\text{ref}}$, which is measured as the incident power, P_{inc} , minus the reflected power, P_{ref} , and is one of the major input variables. Microwave power measurements are made using dual-directional power couplers inserted in the waveguide between the circulator and microwave reactor.

3.2.2 Process Gas Delivery Subsystem

The gases used in this thesis for the diamond growth process are: nitrogen, hydrogen, and methane. The compressed feed gases had the following compositions: 99.9995% purity (Total impurities < 5 ppm, N_2 < 3 ppm) for Hydrogen, 99.999% purity (Total impurities < 10ppm, N_2 < 5 ppm) for Methane. Mass flow controllers (MFC) are devices used to measure and control the flow of gases. The MKS Type 1179A general purpose mass flow controller controls the processing gases at a particular range of flow rates. A signal is sent to the control panel. The total flow rate ranges from tens to hundreds of sccm (standard cubic centimeters per minute) in this diamond growth process. These controlled flow rate feed gases are mixed and delivered to the discharge chamber.

3.2.3 Vacuum Pumping Control Subsystem

The pressure control subsystem is used to maintain the desired pressure in the deposition chamber. During the process, the vacuum pumping system pumps the reacted gases out of the deposition chamber continuously. In this thesis diamond CVD processes operated in the pressure range of a 10 Torr to 240 Torr. The pressure was maintained by using a mechanical roughing pump. A TRIVAC D 16 BCS two-stage rotary vane vacuum pump was used. The pressure in the deposition chamber was maintained by an automatic

throttle valve located between the chamber and the pump. The pressure was measured by a pressure gauge MKS Type 141A which is a variable capacitance sensor consisting of rigidly attached capacitive electrodes located on the back or reference side of a metal diaphragm. The reference side is permanently evacuated and sealed and thus makes the pressure measurement independent of the gas type or composition. When pressure is applied to the diaphragm; its deflection produces a change in the distance between the electrodes and the diaphragm and a resultant capacitance change. The signal is sent to a pressure controller in the main control panel. The control system automatically adjusts the throttle valve to achieve the desired pressure in the deposition chamber.

3.2.4 Pressure Control Subsystem

The pressure control subsystem is used to maintain the desired pressure in the deposition chamber. During the process, the vacuum pumping system will pump the reacted gases out of the deposition chamber continuously. In this thesis investigation, most of the diamond growth processes operated at the pressure of 240 Torr. The pressure was maintained by using a mechanical roughing pump. In this research system, a TRIVAC D 16 BCS two-stage rotary vane vacuum pump is used. The pressure in the deposition chamber is maintained by an automatic throttle valve located between the deposition chamber and the pump. The pressure is measured by a pressure gauge MKS Type 141A. When pressure is applied to the diaphragm, its deflection produces a change in the distance between the electrodes and the diaphragm and a resultant capacitance change. The signal is sent to a pressure controller in the main control panel. The control

system automatically adjusts the throttle valve to achieve the desired pressure in the deposition chamber.

The system leak rate is an important variable in CVD diamond growth. The pressure changing rate (mTorr/hr) needs to be estimated based on the residual gas, N₂, from the leaking of the vacuum system. The system leak rate is performed before of the diamond growth process. After the system is pumped down the throttle valve is closed manually by pressing close. The pressure before the throttle valve is closed is noted and the pressure after approximately one hour is noted just before opening the throttle valve. These values are namely as P_{initial} and P_{final} respectively. After an “overnight pumping down” the base pressure is $\approx 4.0 \times 10^{-6}$ Torr. Since the leaking gas is air and air is mostly nitrogen, we can estimate the residual nitrogen from the leaking of the vacuum system as:

$$Leak_rate(mTorr/h) = \frac{P_{final} - P_{initial}}{time}$$

Here the time is the number of hours which the throttle valve is closed, i.e. ≈ 1 hour. For all experiments reported in this thesis, the N₂ leak was between 0.1 and 2 mTorr/h.

3.2.4 Air and Water Cooling Control Subsystem

The cooling system used is a closed circuit with a minimum water inlet temperature of 19°C. Water recirculation systems are preferred since, apart from saving water, they help to assure a high standard of coolant purity. The water used for cooling must not contain any suspended matter which may block the coolant system. It must also be free of corrosives which might attack the metal lines on the system. To prevent electrolysis, the

water must have high electrical resistance. The mineral content and the electrical conductivity of the cooling water must be periodically checked and improved, if necessary.

The cooling water must also be free from all traces of greasy substances, as even a thin film of grease may form a critical barrier on the cooler causing extreme anode temperature. Greasy, oily, or metal particles in the water may be removed by repeated flushing of the cooling ducts with a rinsing agent. The cleaning process should be terminated with a flushing with distilled water. The cause for such greasy deposits will usually be found somewhere in the cooling system, i.e. water pump, hose, etc. Also, the entire system must be periodically cleaned by flushing and rinsing. The cooling water supply in the microwave generator is described in Figure 3.3.

For air cooling, there are usually two air blowers used to cool the quartz bell jar through an inlet in the cavity wall. An air blower is also placed beside the magnetron to cool the power supply from outside when the growth process is running. An air fan is positioned around the cavity to cool the external cavity walls.

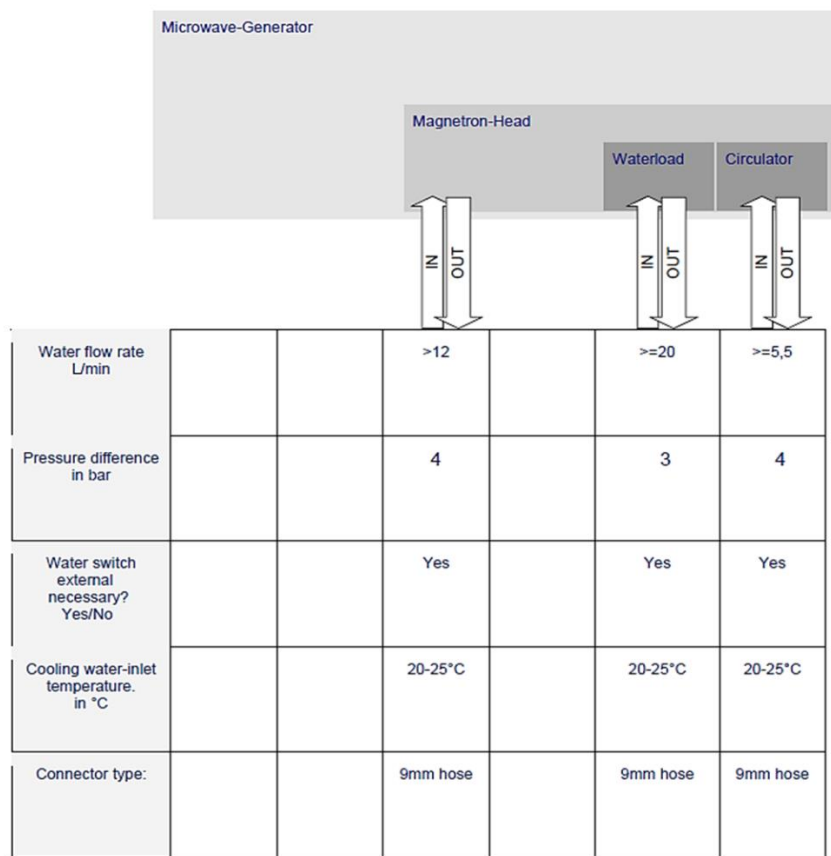


Figure 3. 3 Cooling water supply

3.2.5 Exhaust Line Subsystem

The exhaust subsystem is one of the safety precautions. A nitrogen purge is used as a dilution of the hydrogen-dominated exhaust gases at the exit of the mechanical roughing pump. Usually, the flow rate of a nitrogen purge is 10 times of the total flow rate of flammable output gases. The nitrogen dilution thus reduces the methane and hydrogen exhaust gas concentration to a nonflammable level at the exit of the mechanical roughing pump. The safety interlock system measures the pressure of the processing gases to prevent any over pressurizing when hydrogen is present in the system.

3.2.6 Optical and Photographic Diagnostic Subsystem

The optical and photographic subsystem is composed of a pyrometer to measure the substrate's temperature, and a digital camera to capture images of the discharge and the diamond seeds.

The portable optical emission pyrometer (IRCON Ultimax Infrared Thermometer UX CL1; Figure 3.4 (1)) is used to measure at a fixed wavelength ("two-color") of 0.96 μm . The reading temperature range is between 600 - 3000 $^{\circ}\text{C}$, while the emissivity during the diamond growth process was 0.1. As shown in Figure 3.4, the pyrometer was positioned at a high angle in front of the screened window with visibility through the cavity wall. The pyrometer was set on a tripod at all times to keep the measurement results consistent.



Figure 3. 4 Optical and Photographic subsystem on microwave cavity reactor C. (1) Pyrometer, (2) CANON camera.

The position and height of the tripod were not changed throughout all experiments. Since the substrate position was below the screened window, and the thermal emission was focused through the quartz bell-jar at an incident angle of approximately 65° to the center of the sample. The measurements were usually taken multiple times, and the most

repeatable reading was recorded. Once the microwave input power was changed, a stable substrate temperature reading was obtained after a 1 - 2 minutes lapse. The position of the pyrometer, the incident angle, and the measured position of the sample were held constant during the experiments. It was also understood that due to the intense emission from the discharge, the measurement of the absolute value of the substrate temperature by a pyrometer could not be accurate. Nevertheless, the measurements presented here are repeatable and thus serve from run to run as a relative experimental substrate temperature measurement that can be compared with previous works.

During the diamond growth process, a series of photographs were taken on (1) the discharge hovering over the substrate and (2) the growing diamond surface as the microwave input power varied. A CANON EOS 20D 8.2-megapixel semi-professional digital single-lens reflex camera with 60-mm lens was used to capture the images at a high angle through another screened window located adjacent to the pyrometer (Figure 3.4 (2)). The window was also just above the top of the bell jar. The camera was located at a fixed position on a tripod outside of the reactor at an incident angle of approximately 75° to maintain a comparable fixed reference position. For comparison between the images, all parameters were held constant for all experimental conditions - such as the focal length was kept at 60 mm, and the camera was perfectly focused on the substrate rather than the bell jar or cavity spyhole (screened window).

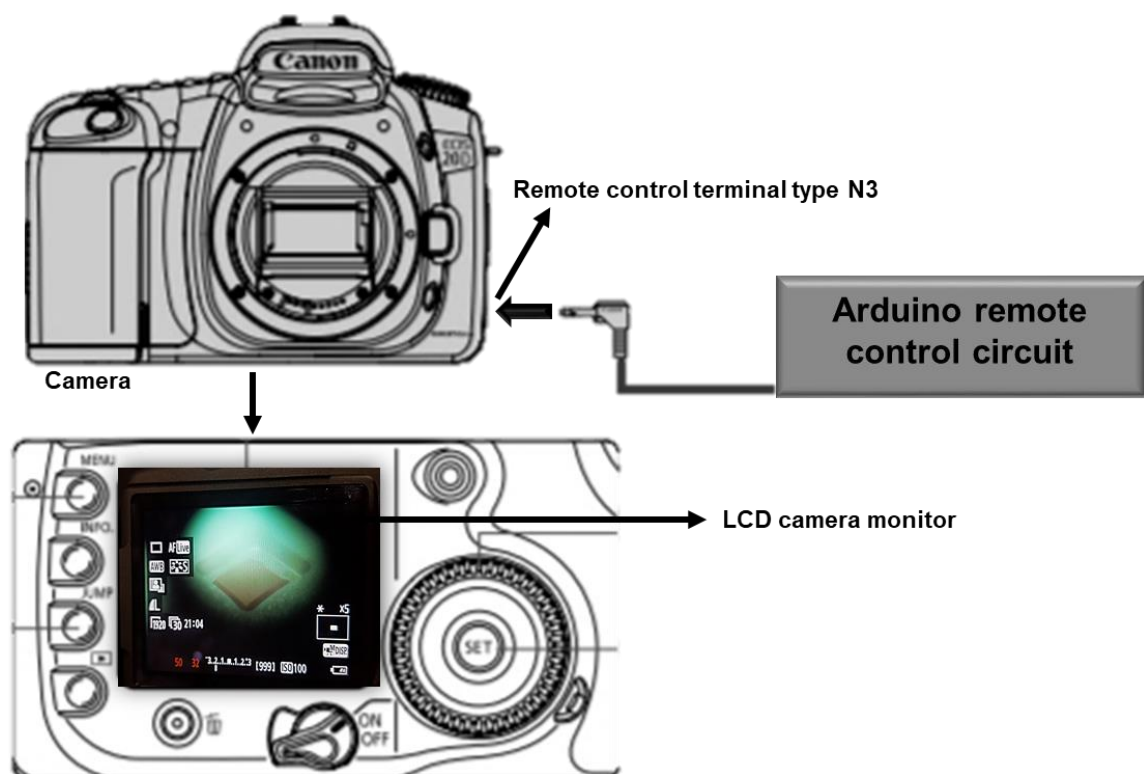


Figure 3. 5 Camera Arduino control map for microwave cavity reactor C [134].

To carefully control the plasma discharge and the diamond growth evolution, several photographs were automatically taken every two minutes by an Arduino remote control circuit; see Figure 3.5. The Canon EOS 20D camera has a port on the right side for a remote switch with a type N3 terminal in which an appropriate pinout was connected. The pinout used was a 2.5 mm (sub-mini) head with 3 cores ((1) ground, (2) focus, and (3) shutter). One side of the pin was connected to the remote camera port, and the other was connected to pin 8 on the Arduino circuit. The Arduino connects to 2 different channels on the relay board to control the focus and the shutter of the camera. The relays are used to isolate the camera circuit from that of the Arduino. A complete diagram of the circuit is shown in Figure 3.6. By connecting the camera to an Arduino, all three contact sections are shorted together, causing the camera shutter to be released. The core (1) is the

ground connector. Therefore, the core (1; ground) and (3; shutter) causes the camera to trigger. The first digital image was captured 5 seconds after the power switch is turned on, the next images are captured and stored every two minutes.

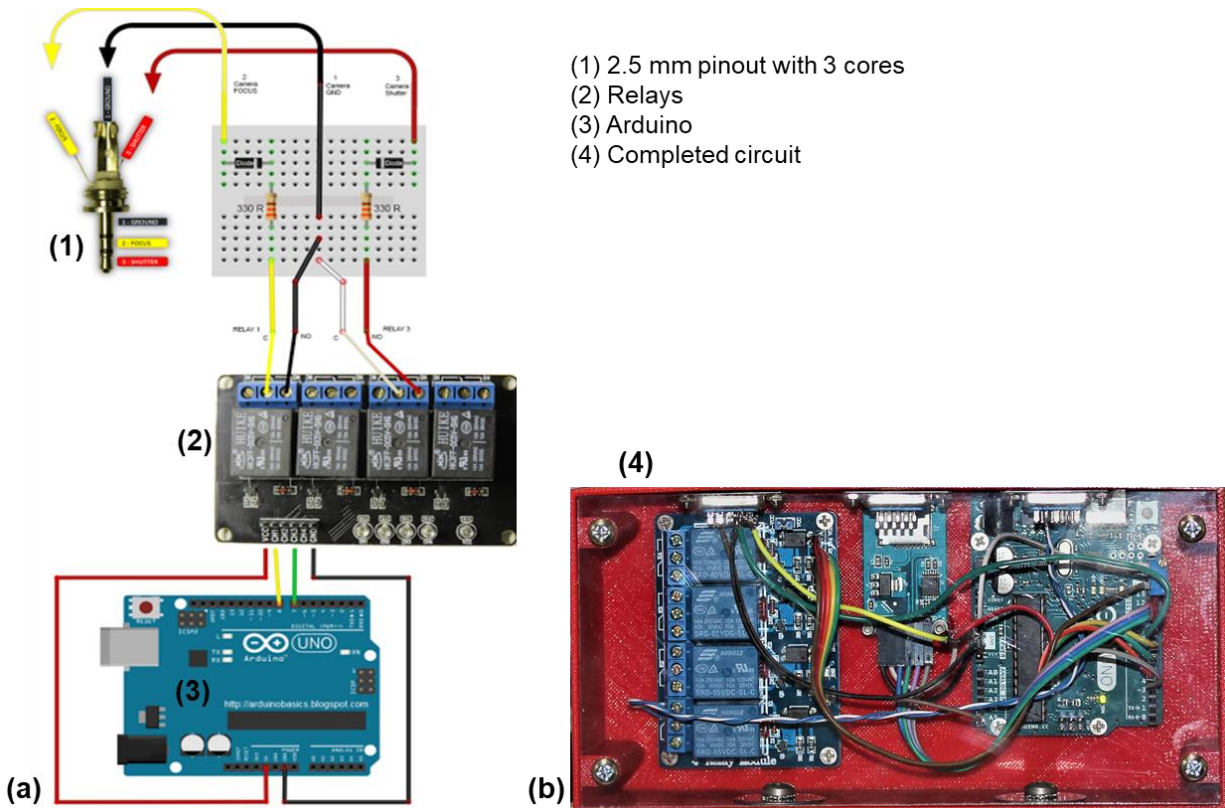


Figure 3. 6 (a) Diagram of the Arduino circuit and (b) photograph of the completed operational Arduino circuit [135].

3.2.7 The Main Operations Windows

Two windows provide a system wide collection of tools for operating the system. The Standard view panel is shown in Figure 3.7 and provides controls and indicators grouped by function. The schematic view window is shown in Figure 3.8 and provides controls and

indicators organized according to the schematic block diagram view. In both views, you can observe the current status of the machine and can access and adjust control set-points for subsystems or components, far as the adjustment is allowed by the current interlock or operation status of the reactor.

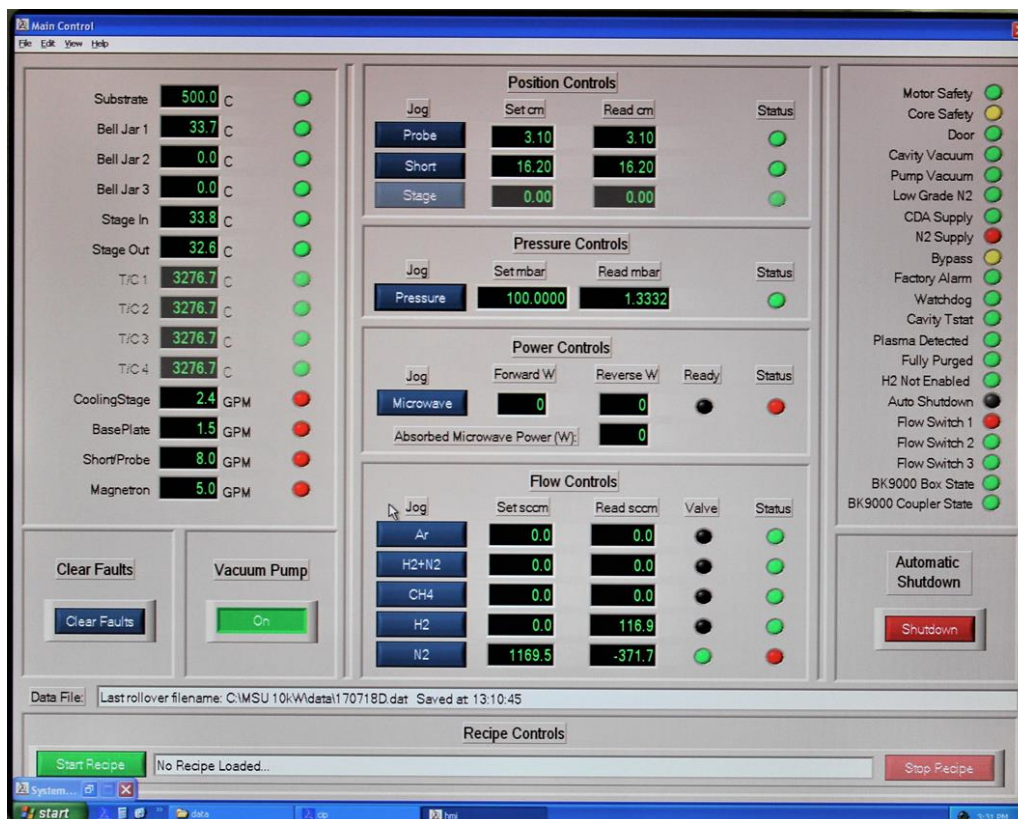


Figure 3. 7 The standard view panel operation window

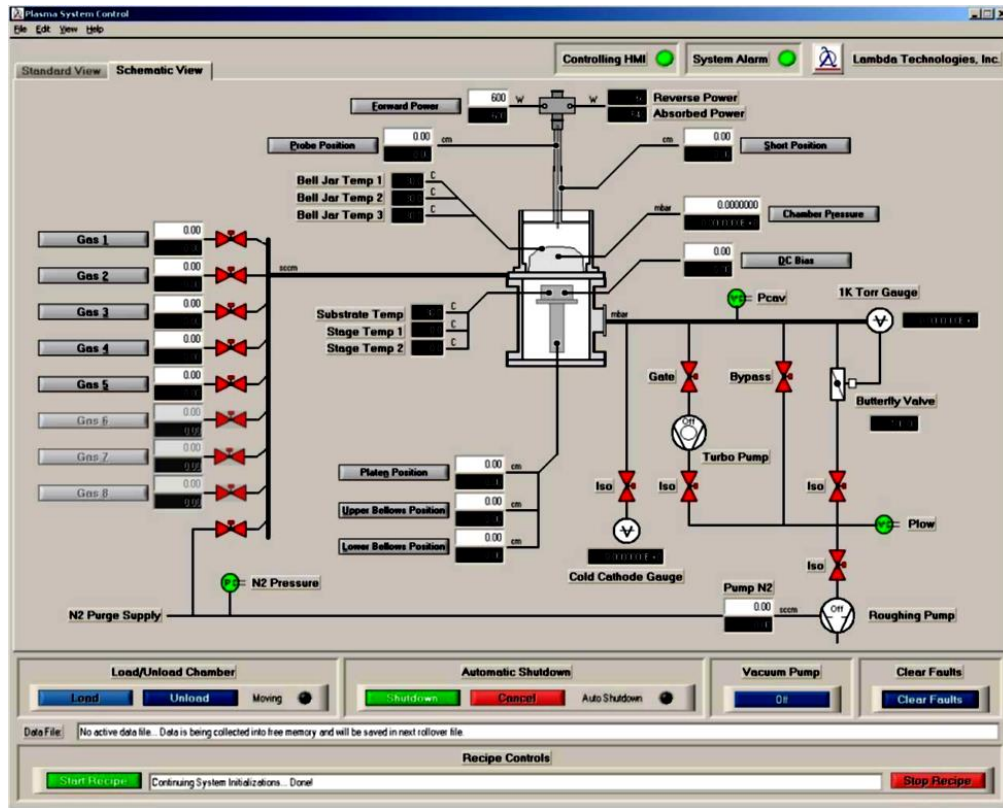


Figure 3. 8 The schematic view panel operation window

In general, this window is used to display the state of the tool. Some control functions (substrate load/unload and clear faults) are available directly from this window. Most other control functions (such as adjusting the setting of power, vacuum pressure or mass flow) are available by opening the “Job Panel” for a specific subsystem. As an introduction, the Operations Window is divided as follows:

1. Upper Left Pane: Interlock Status
2. Lower Left Pane: Sensor Readings
3. Middle Panes: Subsystem settings and status.
4. Right Panes: System Functions
5. Bottom Pane: Automatic Recipe Control & Status

The upper left pane in the standard panel window displays the current state of system interlocks and limits. Generally, the color-coding of these simulated LED indicators is as follows: (1) Green: status is okay, ready for operation, (2) Yellow: status is not in operation range, and (3) Red: fault status, out of range during operation.

3.2.8 Method of System Operation

This section provides information on the efficient and safe operation of the tunable microwave cavity plasma reactor C as well as to gain insight on how process parameters control the plasma discharge. The system is automated with computer control, and is substantially equipped with in-situ diagnostics and safety interlocks. Those features enable the user to control the current system state based on frequently observing the plasma as well as the overall system data such as pressure, reflected power, substrate, and system component temperatures during the process. The microwave power delivery system is designed to efficiently couple the microwave energy to the processing plasma for deposition and etching applications. The pressure and the microwave power can be adjusted any time during the process, which influences, for example, the dimension of the plasma discharge and the seed surface temperature. It is self-evident that there must be an optimum for a given process; the discharge should not be too large to avoid contact with the quartz dome.

3.3 Experimental Apparatus – MSU Reactor C

3.3.1 Overview

The reactor setup employs a microwave discharge and uses a vacuum chamber with a rotary pump that runs continuously during the process. The pressure inside the chamber is kept constant, by a throttle valve, while all gases are fed into the chamber with desired and steady flow rates. Unlike HPHT synthesis, which is typically carried out at pressures in excess of 5 GPa (~50,000 atmospheres), diamond CVD is usually carried out at a fraction of one atmosphere mainly for the sake of safety concerning the use of explosive gas mixtures and because of the limits for plasma generation. The conditions of low pressure (sub-atmospheric pressures) and low temperature for diamond CVD are actually in favor of growth of graphite instead of the diamond according to the phase diagram of carbon (Figure 2.2) [136], due to the fact that graphite is thermodynamically stable while diamond is kinetically stable or so-called metastable.

Molybdenum is used as the substrate holder for homoepitaxy growth of SCD. The microwave energy is introduced into the chamber to generate a discharge. The gas molecules are dissociated to generate carbon atoms for deposition onto the substrate surface. Microwave plasma assisted CVD (MPACVD), is currently the most widely used technique for diamond deposition. The diamond substrate is heated by, the bombardment by energetic plasma species, and the exothermic recombination of radicals, such as atomic hydrogen, on the diamond growing surface.

The plasma formed typically has a ball or hemispherical shape and sits right on top of the substrate, which increases the efficiency of mass transport of diamond growing radicals to the diamond surface for deposition.

3.3.2 Electromagnetic Focus

The cavity is a hollow metallic cylinder. Since the cylinder wall is electrically conductive, the amplitude of the electric field parallel along the cylinder wall must be very small. By applying these boundary conditions on the electromagnetic waves, many characteristic transverse electric field patterns can occur in the hollow cylinder. Each field pattern focuses the microwave power at defined locations inside the cavity.

Two transverse magnetic (TM, no magnetic field in the direction of radiation propagation) modes that are useful for the purpose of establishing a localized plasma discharge are shown in Figure 3.9.

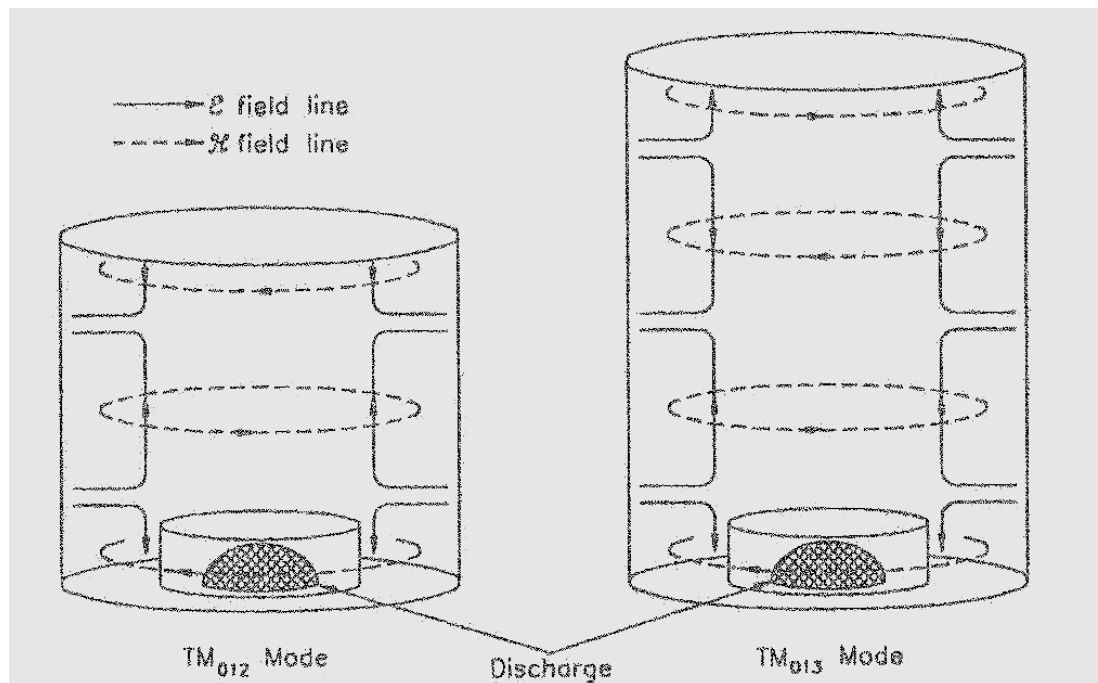


Figure 3. 9 Electromagnetic fields, TM_{01n} modes ($n = 2$ left, $n = 3$ right) [137].

The electromagnetic power distribution in the TM_{01} modes is constant in the annular direction around the vertical axis of the cavity and has a center maximum in the radial direction. The microwave radiation is coupled into the cylinder via an antenna (probe) reaching a quarter wavelength through the top plate of the cylinder and the region of concentrated power on the very bottom of the cavity is selected for the plasma formation. The TM_{013} mode offers a larger distance between the near-field of the probe and the discharge region. Figure 3.10 shows three discharges that can result from the TM_{013} mode excitation.

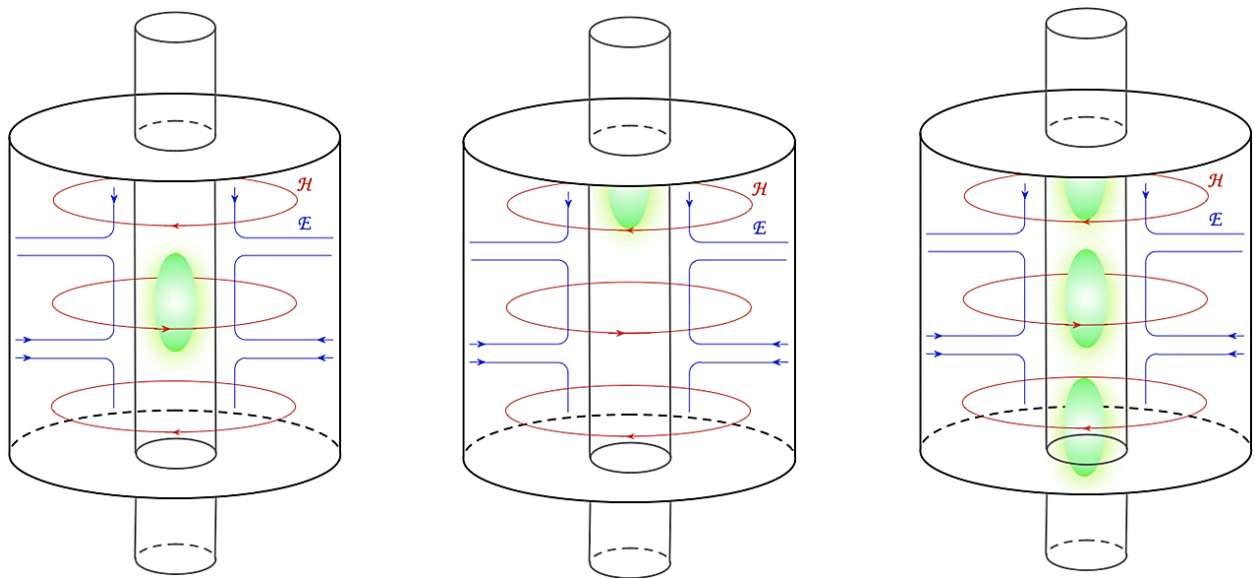


Figure 3. 10 Three typical discharges (in green) that result from exciting the cylindrical cavity applicator with the TM_{013} mode [137]. The red lines are the magnetic field patterns and the blue lines are the electric field patterns.

The actual dimensions of the intensity field depend on the dimensions of the cylinder (inner diameter and length) and the frequency of the microwave radiation. The cavity length (short position) L_s and the penetration depth of the probe L_p have been calculated for two cavity designs and are summarized in Yajun Gu's PhD thesis [132] and in papers [18], [138].

Note the theoretical dimensions given in Table 3.1 are used as starting points for the actual cavity to a diamond deposition process. These numbers could have varied by several mm to optimize the process either way during or before diamond deposition and are the same from one substrate holder geometry to another substrate holder geometry.

Table 3. 1 Theoretical TM_{013} and TM_{012} modes

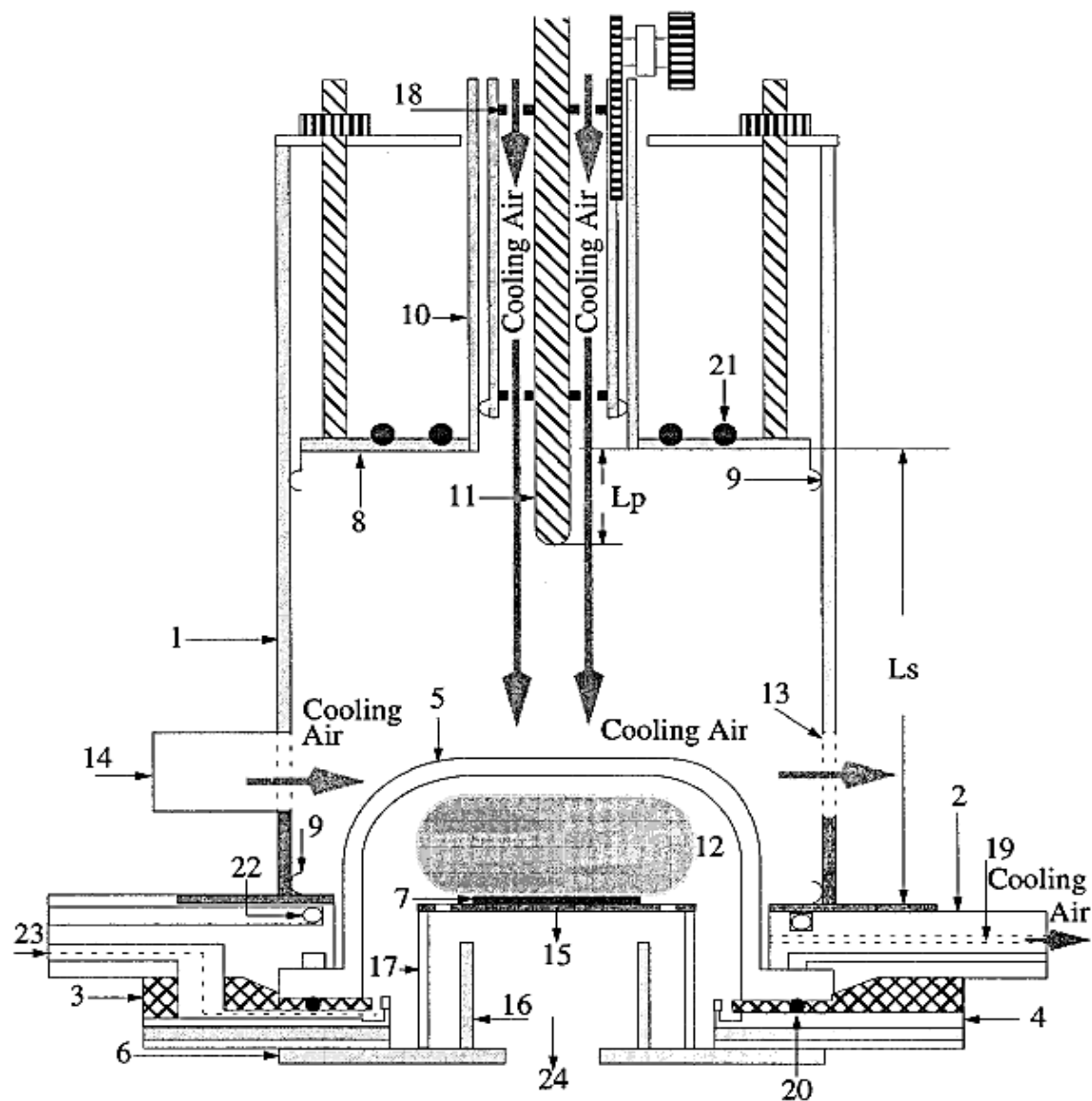
Frequency in MHz	2450		915	
Cavity radius in cm	8.90		21.75	
Mode	TM_{013}	TM_{012}	TM_{013}	TM_{012}
Calculated cavity height L_s in cm	21.6	14.4	60.2	40.1
Calculated cavity height L_p in cm	8.2	8.2	3.1	3.1

All the experiments carried out in this thesis research employed Reactor C that used a hybrid mode excitation as described in detail in reference [18], [132]. A hybrid TM_{01n} mode plus a TEM_{001} mode was excited. Then L_s was 16.20 cm

3.3.3 Description of the Classic Reactor

To use the cavity to drive a plasma discharge a microwave transparent quartz dome is placed at the bottom of the cavity. This allows containing the plasma in a low-pressure environment inside the quartz dome while the cavity is at atmospheric pressure. The reactor design described below creates a hemisphere-shaped plasma in close contact with the substrate and thus allows the coating of large substrate surfaces. For a 2.45 GHz

excitation, diamond films can uniformly be deposited over three to four inches diameter (80 cm²) substrates, and when excited with 915 MHz the substrate deposition width can be scaled to over eight inches and deposition areas can exceed 320 cm². Additionally, this reactor concept is also operationally versatile. That is, it can be adjusted to deposit diamond over a wide range of experimental conditions; i.e. it can deposit diamond on a variety of substrates, at pressures of 0.5-300 Torr, with variable power levels of (1) 500 W – 6 kW at 2.45 GHz [18] and (2) 3 kW – 15 kW at 915 MHz [138] .



Legend

- | | | |
|-----------------------------|----------------------------|--------------------------|
| (1) Cavity Side Wall | (2) Baseplate | (3) Annular Plate |
| (4) Distribution Plate | (5) Quartz Dome | (6) Holder-baseplate |
| (7) Substrate | (8) Sliding Short | (9) Finger Stock |
| (10) Coaxial Waveguide | (11) Excitation Probe | (12) Plasma discharge |
| (13) View Window (grid) | (13) Air Blower Outlet | (14) Air Blower Inlet |
| (15) Flow Pattern Regulator | (15) Substrate Holder | (16) Metal Tube |
| (17) Quartz Tube | (18) Teflon Pieces | (19) Optical Access Port |
| (20) Seal O-ring | (21) Cooling Sliding Short | (22) Cooling Baseplate |
| (23) Gas Inlet | (24) Gas Outlet | |

Figure 3. 11 Cross-sectional view of the MCPR [139].

Figure 3.11 shows a cross-sectional view of a typical microwave cavity plasma reactor configured for operation in the thermally floating substrate mode because it is placed in a quartz tube (17) located on the holder base plate. As shown, the cavity applicator sidewall (1) is made of a 17.8 cm inside diameter cylindrical brass tube. This brass tube forms the outer conducting shell of the cavity applicator and is electrically shorted to a water-cooled baseplate assembly (2-4) and a water-cooled (21) sliding short (8) via finger stock (9). Thus, the cylindrical volume bounded by the sliding short, the cavity applicator sidewall and the base plate forms the cavity applicator electromagnetic excitation region. The TM_{013} electromagnetic mode is excited inside the 17.8 cm diameter cavity applicator by applying 2.45 GHz microwave power and length tuning the applicator to about 21.3 cm. Once the microwave energy is coupled into the cavity and the reactor pressure is reduced to approximately 4 Torr a discharge can be ignited inside the quartz dome with 500 – 1000 W of microwave energy.

It has been observed experimentally that the discharge loaded TM_{013} mode will produce an ellipsoid-like discharge (12) which is in good contact with the substrate (7). Continuous wave (CW) microwave power, typically at 2.45 GHz, is coupled into the cylindrical cavity applicator through a mechanically tunable coaxial excitation probe (11). This probe is the center conductor of the coaxial waveguide (10), which is attached to the center of the sliding short (8). The movement of the sliding short sliding changes the applicator length, L_s , while the variation of the coaxial probe (10) position adjusts the depth of penetration of the coaxial excitation probe, L_p , inside the cavity.

Positions for discharge ignition are $L_s = 21.3$ cm and $L_p = 3.0$ cm for the classic reactor. Ignition positions for Reactor C, are $L_s = 16.2$ cm and $L_p = 3.0$ cm. Then as the reactor

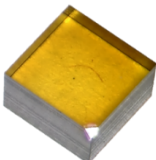
system and discharge are brought up to the desired steady-state diamond deposition process conditions the applicator length, L_s , is iteratively adjusted to reduce the reflected power and to achieve the desired process results such as deposition uniformity. The probe depth, L_p , is kept constant for all experiments.

3.4 Diamond Seeds for the Growth Process

Commercially available high-pressure high temperature (HPHT) diamond single crystal plates, type Ib (100), with typical sizes of 3.5 mm x 3.5 mm x 1.4 mm from Sumitomo Electric Industries were used as seed substrates for homoepitaxial growth of CVD diamond single crystals. For most SCD growth experiments presented in this dissertation, the dimensions of the HPHT diamond seeds that were used were 3.5 mm x 3.5 mm and have a thickness size of ≈ 1.4 mm.

Note that the two biggest surface areas of the HPHT seeds were mechanically polished, and the other four faces were not. Moreover, the most commonly used HPHT seeds in this thesis were the 3.5 mm x 3.5 mm seeds listed in Table 3.2. These seeds have a slight difference between the top and bottom areas dimensions. See Figure 3.12. Although both surfaces were mechanically polished, the top surface was always used as deposition surface in the experiments, and the seed was always placed with 3.5 mm x 3.5 mm face up in the pocket holder. HPHT seeds have a golden-yellow color because the diamond contains 10 – 1.0 ppm nitrogen in the crystal. They are classified as type Ib diamond. These diamond seeds typically have defect densities of $10^4 - 10^5 \text{ cm}^{-2}$, which is considered high [140].

Table 3. 2 Measured dimensions on HPHT seed

Shape	Commercial supplier	Thickness (mm)	Length (mm)	Width (mm)	Area (mm ²)
	Sumitomo Electric	1.4 ± 0.1	3.7 at the top 3.5 at the bottom	3.7 at the top 3.5 at the bottom	13.7

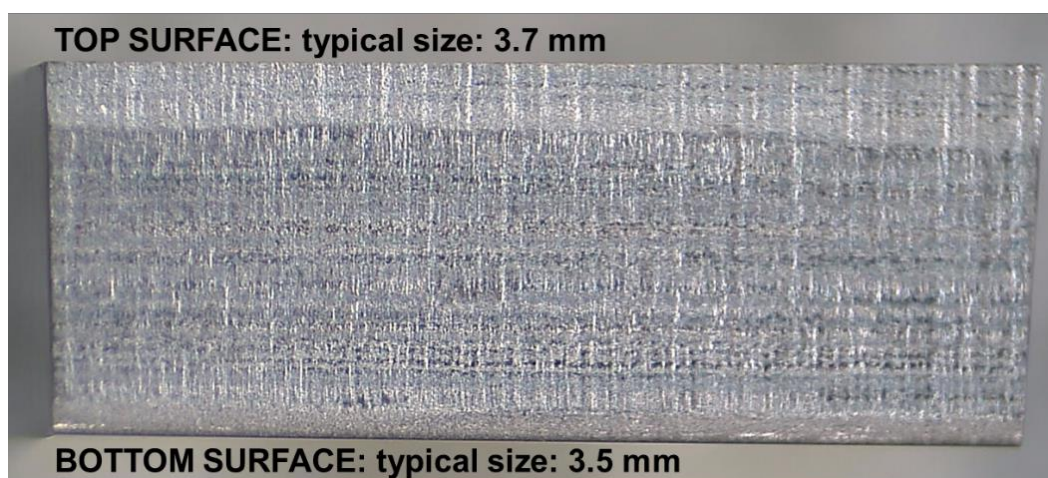


Figure 3. 12 Optical microscope image of the side view of the 3.5 mm x 3.5 mm x 1.4 mm HPHT seed.

3.4.1 The Diamond Seed Cleaning Procedure – Wet Chemistry

Prior to each deposition experiment the HPHT single crystal diamond seed was first cleaned by a wet chemical cleaning procedure in order to remove any metallic, graphite and organic material contamination. The cleaning procedure is described in the following steps:

1. Nitric acid (40 mL) + Sulfuric acid (40 mL) mixed in a pyrex beaker, placed on the

heater (set to 300 °C) for 30 minutes. Then, rinse the sample in DI water.

2. Hydrochloric acid (40 mL) in a pyrex beaker, placed on the heater (set to 300°C) for 20 minutes. Then, rinse the sample in DI water.
3. Ultrasonic cleaning: Ultrasonic bath cleaning with Acetone (30 mL) in a pyrex beaker for 15 minutes.
4. Ultrasonic cleaning: Ultrasonic bath cleaning with Methanol (30 mL) in a pyrex beaker for 15 minutes.
5. Final rinsing and drying: Rinse seed with DI water and blow with nitrogen to remove water.

Once the cleaning procedure was completed, the substrate seed is placed in the substrate holder and loaded into the reactor chamber.

After the diamond growth was finished and the grown diamond was taken out of the reactor, it was cleaned following the same wet-chemical cleaning procedure which was described in above in the following order:

1. Nitric acid (40 mL) + Sulfuric acid (40 mL) mixed in a pyrex beaker, placed on the heater at 300 °C
2. The process above was repeated until the grown substrate was clean. This cleaning varied from 1 – 3 hours depending on the final conditions of the substrate.
3. Ultrasonic cleaning: Ultrasonic bath cleaning with Methanol (30 mL) in a pyrex beaker for 20 minutes.
4. Blow with nitrogen, and then place the cleaned diamond in a pantry box.

The cleaning process was intended to remove oils, any metallic, graphite and organic material contamination. The substrate cleaning process should be done in an appropriate

laboratory facility. The acidic cleaning steps must be carried out in a fume hood following relevant operational instructions. Before and after each experiment the quartz bell jar is cleaned with ethanol to remove any graphite residues on the dome walls. Often the grown SCD plate was removed from the seed by laser cutting. Then the deposition surface and the bottom surface of the CVD diamond plate were mechanically polished, and then a single crystal CVD diamond plate was fabricated for characterization.

3.5 The Pocket Holder

The holder dimensions play an important role in the deposition of large SCD substrates. Many experiments have used the conventional open holder for CVD diamond growth. The “open holder geometry” is defined here as a holder geometry where the diamond seed is placed on a large flat open holder surface. This has been reported in [20]. These experiments indicated that if one used a flat open holder design, thereby exposing the diamond directly to the discharge and directly to the microwave electromagnetic fields, a PCD rim is deposited and forms around the grown SCD material. Reference [123] recently also has demonstrated a decrease in the diamond crystal quality when an open holder configuration is used.

In this thesis investigation, different pocket holder designs have been used for the diamond growth experiments. All pocket holders used in this thesis have been manufactured from molybdenum obtained from Ed Fagan Inc. and made by the machine shop in the Department of Physics at MSU.

The variable geometry of the pocket included: (1) different pockets holder depths, (2) different pocket holder apertures, (3) specially designed pocket holders that were used in

the large diamond seed growth experiments, and (4) specially designed pocket holders that were used in the diamond substrate re-growth experiments

3.5.1 Pocket Holder Preparation

In order to reuse the holder and start the growth process under the same conditions, the holders had to be cleaned before each experimental run. Before every growth process the molybdenum, substrate holders are cleaned according to the following suitable cleaning procedure:

1. The molybdenum substrate holders were sand blasted in order to ensure and promote desirable growth process conditions.
2. Ultrasonic cleaning of all molybdenum pieces with methanol
3. Rinsing and nitrogen blowing; and
4. Drying the Moly pieces in an oven at ~ 100 °C for approximately 20 minutes.

Thus, the sand blasting and the other cleaning steps removed all PCD that remained from any earlier diamond growth run. Hence every new experimental run began under the same starting conditions with the same clean substrate holder.

3.5.2 Pocket Substrate Holder Configuration

The pocket holder configuration and dimensions are an important component of the diamond growth system and have a significant role in the diamond growth process. The substrate holder consists of two separated parts. One is named the substrate holder and the second is called the pocket holder. Both are shown in Figure 3.14 (b) (2) and (3) respectively. The substrate holder (2) is a 64.7 mm diameter holder with holes drilled

around the circumference. See Figure 3.13. These holes allow the exhaust gases to flow out of the system via the underlying quartz tube. This quartz tube directs the exhaust gases to flow out of the system through 4 holes drilled into the cavity bottom conducting short plate (4). A circular groove, concentric to the cooling stage holds a quartz tube (1) shown in Figure 3.14 (b). The inner concentric part of the substrate holder has placed directly above and in contact with the top of the cooling stage, see Figure 3.13 (2). The substrate holder sits slightly separated at the top of the tube to allow for the vertical expansion of the quartz tube. For all the diamond growth process reported here, the substrate holder was held constant with the dimensions as indicated in Figure 3.13.

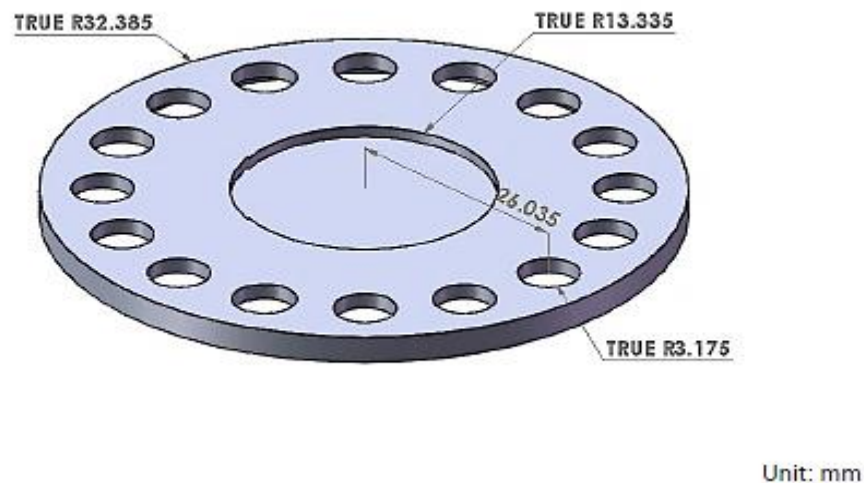


Figure 3. 13 Isometric drawing view of a 64.7 mm substrate holder.

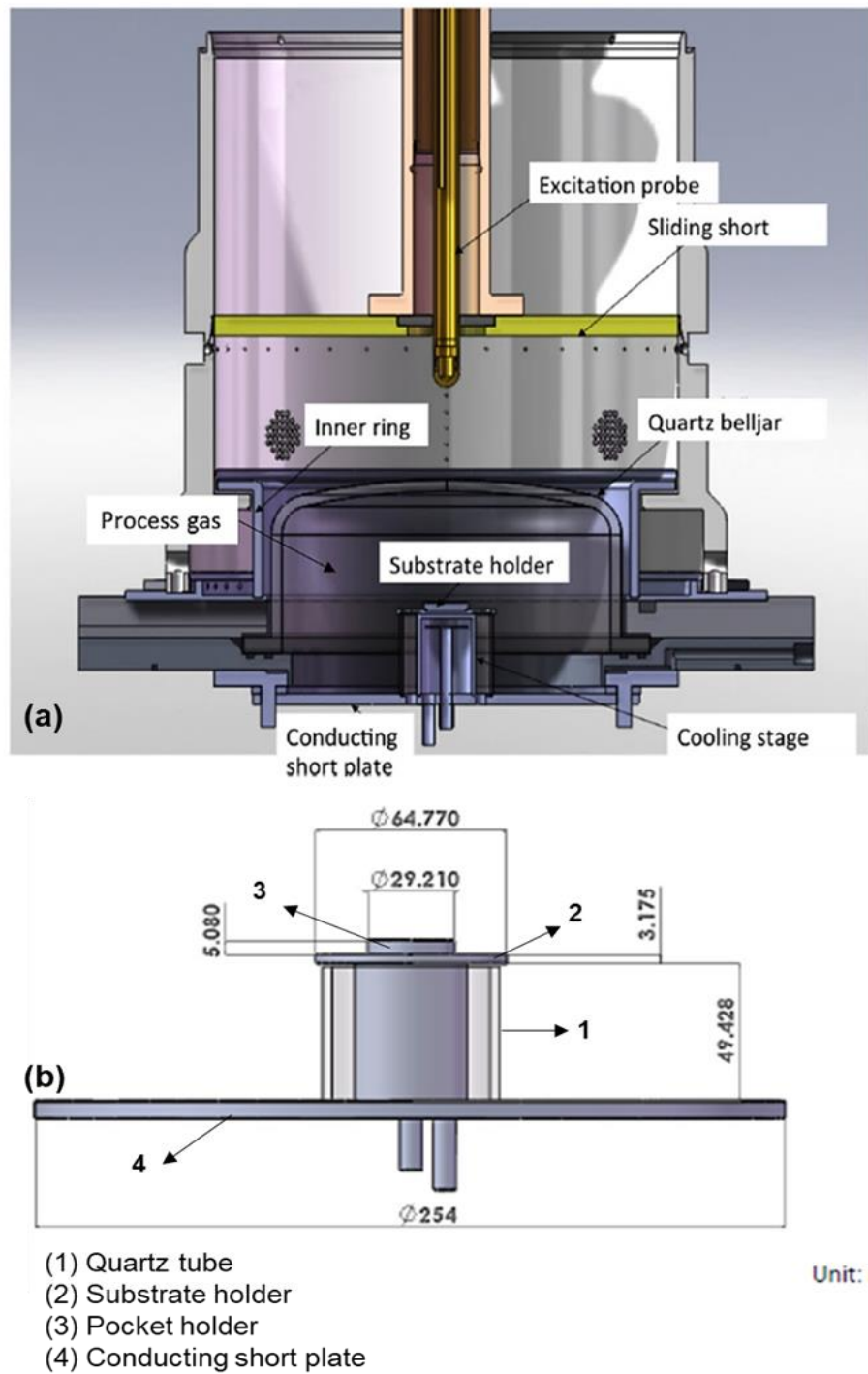


Figure 3. 14 (a) A schematic side view of the microwave cavity plasma Reactor C with a (b) zoom of the substrate holder setup.

The conventional pocket holder geometry has a 29.2 mm diameter top molybdenum piece (3). This diameter fits in the inner diameter of the concentric part of the substrate holder of 64.7 mm (2). Both pieces fit on and directly above the cooling stage (Figure 3.14 (b)). The pocket holder has a centered “pocket” which contains a step bottom. The holder is shown in Figure 3.15 with the important dimensions indicated. The width of the pocket is 6.0 mm, while the HPHT seed used in this investigation has a width of 3.5 mm on the bottom side. The bottom step is needed to keep the seed centered inside the pocket. The dimensions of the bottom step are 4.2 mm x 4.2 mm in the area and have a height of 1.0 mm. The height of the upper step is 1.3 mm, and the depth of the pocket is therefore 2.3 mm. The results of the grown diamonds using this conventional pocket are presented in Chapter 4.

In addition to the conventional pocket holder shown in Figure 3.15, in this thesis investigation, four different pocket holder geometries were used. The first pocket geometry strategically varied the pocket depth while the pocket aperture was held constant. The pocket depths were 2.0 mm, 2.6 mm and 2.9 mm. Here, the only modified dimension is the height of the upper step, as is shown in Figure 3.16. The thickness of the pocket holder with a depth of 2.9 mm might be slightly readjusted to allow the diamond growth to take place within the appropriate substrate temperature window. The results of the grown diamonds using this conventional pocket are presented in Chapter 5.

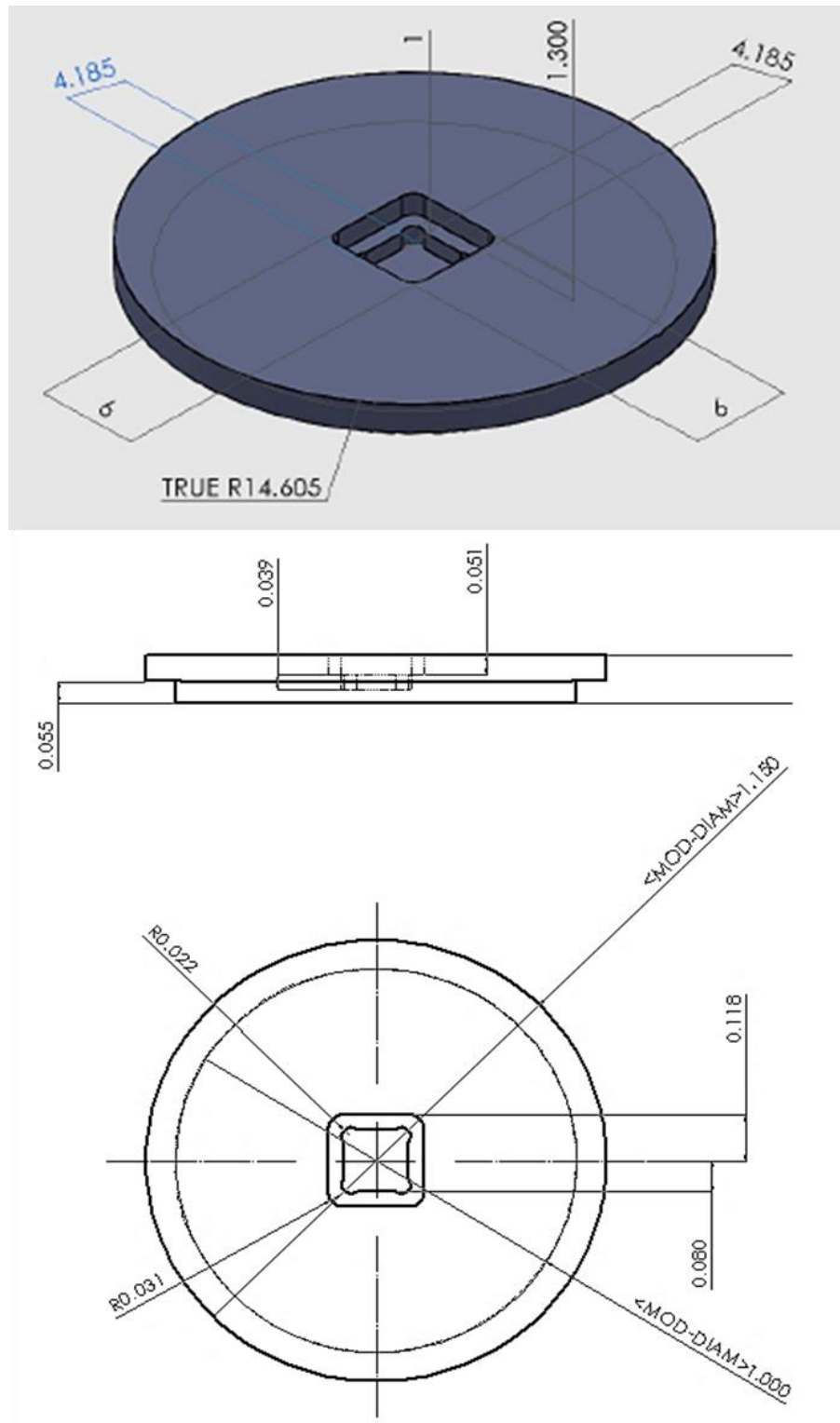


Figure 3. 15 Side cross sectional view of conventional pocket holder (unit: mm) that was used in the experiments in Chapter 4.

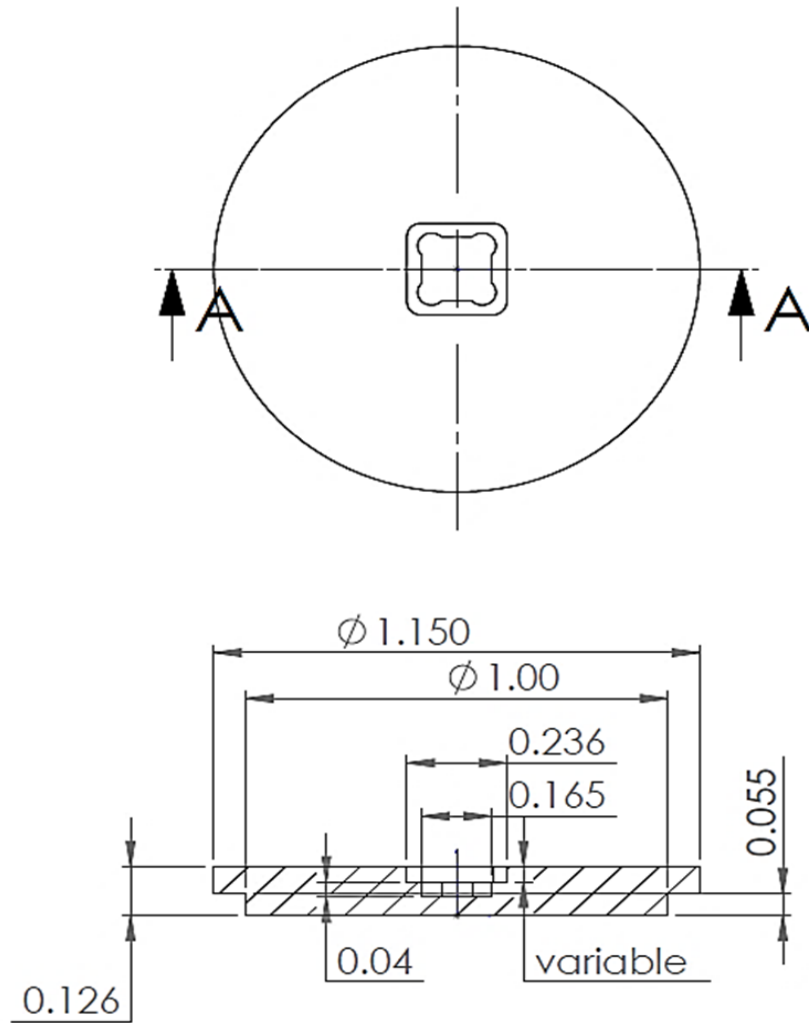


Figure 3. 16 Drawings of the pocket holder for SCD growth at variable pocket depths (unit: inches) that was used in the experiments in Chapter 5.

The second holder geometry varied the pocket holder aperture or width strategically. In this new design, the pocket depth was held constant at 2.6 mm while the aperture length, w , varied from 6.6 mm, to 7.0 mm and 7.6 mm. A drawing of this pocket holder is shown in Figure 3.17. Also, the thickness of the holder is held constant at 3.2 mm. Note,

the bottom pocket was varied from 4.2 mm to 3.8 mm to avoid slight variations on the seed position. These holders were used in the experiments that are described in Chapter 6.

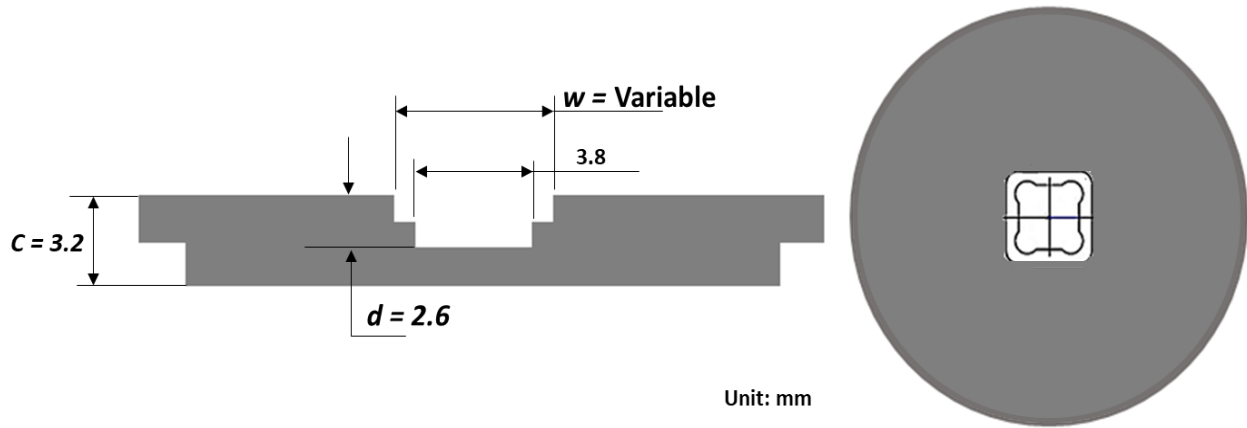


Figure 3. 17 Side and top view of the pocket holder with a varied width (unit: mm)

The third pocket holder geometry was designed for the SCD re-growth experiments. Here, a second growth step was added on top of the grown SCD substrates which usually have a thickness of 1.5 mm and lateral growth area of 26 mm². Therefore, the new pocket holder design has a strategical depth of 3.6 mm and a pocket width of 8.2 mm as is shown in Figure 3.18. The results of the grown diamonds using this conventional pocket are presented in Chapter 6.

The fourth pocket holder was designed for the SCD growth process on large area HPHT seeds. Here the depth of the bottom pocket and the width changed based on the area of the seeds. An example of this pocket is shown in Figure 3.19. This holder is designed for HPHT seed of 5.0 mm x 5.0 mm x 1.2 mm. In the event of larger seeds, just

the bottom pocket is modified and the pocket depth is held constant at 2.6 mm. The results of the grown diamonds using this conventional pocket are presented in Chapter 7.

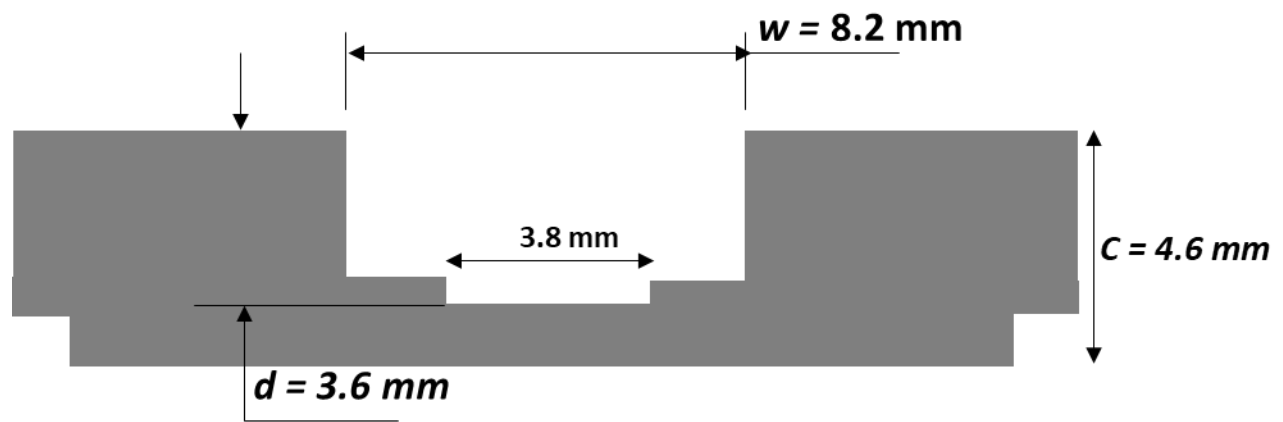


Figure 3. 18 Side view of the pocket holder used for SCD re-growth process (unit: mm) that are described in Chapter 6.

3.6 System Startup

3.6.1 Introduction

Before starting a new experiment, the mechanical and electrical components of the system are turned on before the process is started. At the start of each experimental run, the system is pumped down over night, i.e. ~ 12 hours in order to ensure that all the air inside the chamber is evacuated and there is no leak and residual gas left inside the chamber. Accordingly, it is suitable to employ the following procedure described below in Sections 3.6.2 - 3.6.6

3.6.2 The Diamond Seed Loading into the Microwave Cavity Reactor

Once the seed was cleaned, the system was prepared for loading the seed into the cavity reactor and then to initiate the experimental run. Typically, the setup of cavity Reactor C for loading the diamond seeds is shown in Figure 3.14 (b). The system is comprised of a stainless-steel cooling stage, a quartz tube (1), three plastic O-rings, and the molybdenum holders (2) and (3). The loading process is as follows:

1. The quartz bell jar is shown in Figure 3.10 (a) and the quartz tube shown in Figure 3.10 (b) (1) are cleaned with ethanol.
2. The substrate holder (3) with the diamond seed is carefully placed above, and a good contact with the cooling stage and then the quartz bell jar is set into place and during pump down the O-rings seal the vacuum.
3. The door of the vacuum chamber (not shown) is tightened, and then the vacuum pump is turned on.
4. Click the “Rough Down” button on the computer software (open the throttle valve) to allow the pumping down of the system.
5. The outer shell of the cavity is mechanically moved down slowly until is aligned with eight screws on the upper side of the cooling base plate. Nuts are tightened.
6. Usually, the system is pumped down overnight (~ 12 hours) before the discharge ignition.

3.6.3 Discharge ignition

After an ~12 hours of pumping down to about 5.0×10^{-6} Torr, the discharge ignition is as follows:

1. Turn on all the gas inlet valves, i.e. nitrogen, hydrogen, and methane.
2. Turn on the cooling water and the microwave power supply
3. Adjusted the cavity applicator sliding short to an adequate length position. This length is about 16.25 ± 5 cm.
4. The discharge is ignited by adjusting the pressure to 10 Torr and then by increasing the instant microwave power and coupling this power into the applicators.
5. After discharge ignition, the cavity applicator may have to be further adjusted by a slight tuning of the sliding short until the incident microwave power is matched into the cavity (reduce the reflected power to close to zero). For plasma processing a good to excellent power, match means that almost all of the microwave incident power is coupled into the applicator. When comparing incident and reflected power levels, the reflected power should be less than 15% of the incident power. Note that it is not necessary to achieve “zero reflected power.”
6. Once the microwave discharge is created the operating pressure is increased to the desired process conditions (flows, pressure, power). While increasing the pressure from the ignition pressure of a few Torr to higher processing pressure the sliding short and input microwave power are readjusted to place and keep the discharge over and in good contact with the substrate. After the desired pressure and the desired gas flow are reached, the microwave power is further adjusted to achieve an excellent temperature uniformity over the substrate.

3.6.4 Microwave Plasma Assisted CVD Processing

As outlined above the objective of tuning the microwave power delivery (i.e. short, reflected power) and the process parameters (i.e. pressure, flows, power) is to achieve a uniform distribution of the desired temperature across the substrate surface. A uniform temperature distribution is needed to achieve a uniform diamond growth in terms of thickness distribution and material quality.

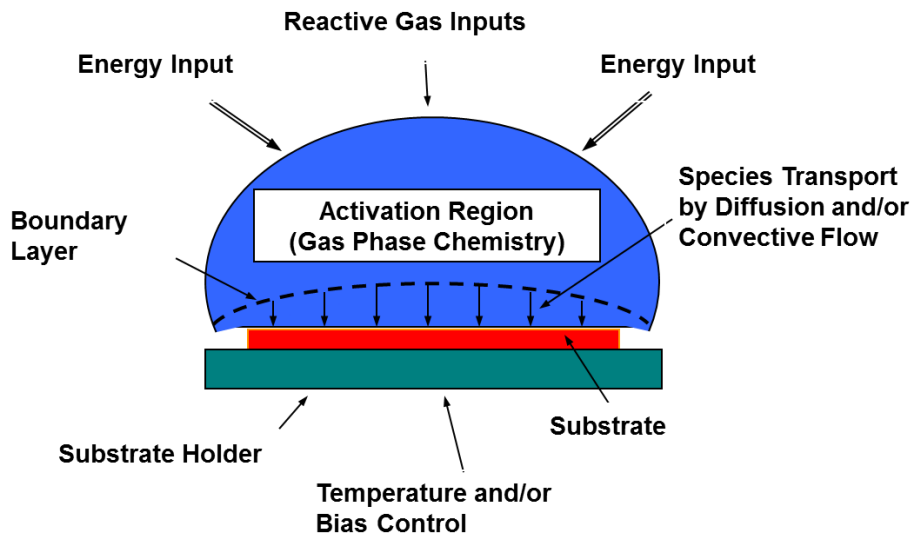


Figure 3. 19 Plasma in an ideal contact with the substrate

Figure 3.20 is a sketch of the plasma discharge region in ideal contact with the substrate surface. The plasma covers the entire substrate surface area but does not extend far beyond and thus remains contained and does not touch the quartz dome. If the discharge were too small, non-uniform deposition would occur.

The plasma discharge volume depends on pressure and absorbed power. At a given pressure increase in power will increase the size of the discharge. At a given power an increase of the pressure will reduce the size of the discharge. Subsequently, there exists an optimal region in the pressure-power parameter space in which the plasma discharge volume will just cover the substrate surface. See (see Figure 3.21).

The absolute temperature is critical for the particular diamond deposition process and may range from 600 - 1100°C. Higher temperatures yield higher growth rates. The temperature depends strongly on the pressure and weakly on the absorbed power (see Figure 3.21). As a consequence, the pressure of the system and the reactor cooling systems are adjusted to achieve the desired growth temperature window. Then, the input power is adjusted to vary the plasma discharge volume over the processing surface area. The details are shown in Figure 3.21 and also see reference [141], [142] for further details.

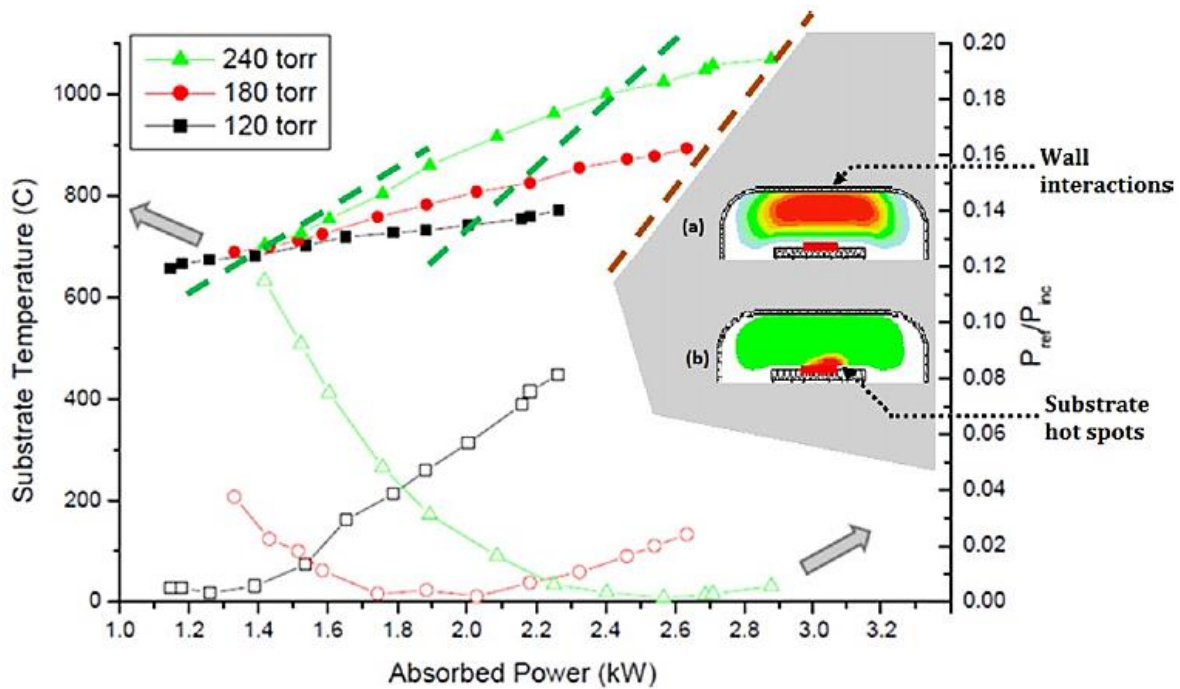


Figure 3. 20 Operating field maps and matching, i.e., P_{ref}/P_{inc} , versus absorbed power for three constant pressure conditions: 120, 180, and 240 Torr [141].

3.6.5 System Shutdown

Once the experimental run has been completed: the software is turned off in the following order:

1. The microwave input power is decreased to 2000 W
2. The methane is turned off
3. The pressure is turned down twenty Torr by twenty Torr until 100 Torr
4. Then the microwave input power is turned off
5. Hydrogen gas flow is set at zero (0)
6. Throttle valve is opened

The system is turned off in the following order:

1. Hydrogen and methane gas lines
2. Microwave power supply
3. Water chiller

3.6.6 Unloading the diamond substrate

Once the system is cooled down, the diamond substrate is unloaded from the reactor.

1. Release the eight nuts in the outer cavity shell and lift off the cavity shell via the mechanical system.
2. Open the nitrogen gas line (nitrogen flows into the vacuum chamber during the venting process)
3. Close the throttle valve and waited until the pressure is ≈ 750 Torr, then the vacuum chamber door can be pulled open
4. Remove the bell jar, take out the substrate holder with the grown diamond still inside the pocket holder.
5. Place back the bell jar, open the throttle valve then to pump down the reactor chamber in order to leave the system under vacuum.

Leave the system under vacuum until loading for the next experiment.

3.7 Grown Diamond Substrates Measurements

Before, during and after the growth process or the hydrogen etching experiments, several different measurements were taken on the substrate. There were four important

diamond growth outputs: (1) the substrate temperature measurement, (2) linear growth rate, (3) the weight diamond gain, and (4) lateral growth rate.

3.7.1 Measurement of Substrate Temperature

Throughout the growth process, the substrate temperature was measured with a 0.96 μm wavelength monochromatic optical pyrometer with an emissivity of 0.1. Two-color pyrometer temperature measurements were also made under the same experimental conditions and were approximately 100 K higher than the one-color measurements over the 800 K–1200 K temperature range of the experiments presented here. As shown in Figure 3.4 the pyrometer was placed on a tripod which was kept fixed at a constant position for all temperature measurements to ensure that all measures are under the same experimental conditions.

3.7.2 Linear and Lateral growth rate (V_{100} and V_{111})

This thesis research measures two diamond growth rates, i.e. linear growth rate, V_{100} and lateral growth rate, V_{111} . These individual notations owe its name to the preferential directions growth directions on the diamond seed.

The linear growth rate is calculated by the measurement of the thickness of the substrate before and after the growth process by a linear encoder Model: Solatron DR600. Five measurements points on the top surface on the diamond seed were taken to calculate the thickness. One point was in the center, and the other four points are near each corner. Once the measurements were completed the values were averaged. These measured values were named the initial linear encoder, L_{initial} . The same method was

used for the grown diamond surfaces; these are named after linear encoder, L_{after} . After these measured were made the following equation calculates the linear growth rate:

$$V_{(100)} (\mu m / h) = \frac{(L_{after}) - (L_{initial})}{time}$$

Time refers to the total diamond growth process in hours. The lateral growth rate is calculated with the dimensions of the outward growth lengths l_1 and l_2 as is shown in Figure 3.22. Where L is the total length of the grown substrate, (i.e. $L = l_1 + l_2 + 3.6 \text{ mm}$). The measurements of these dimensions are recorded using digital microscope KEYENCE VHX-5000; usually at 30X magnification.

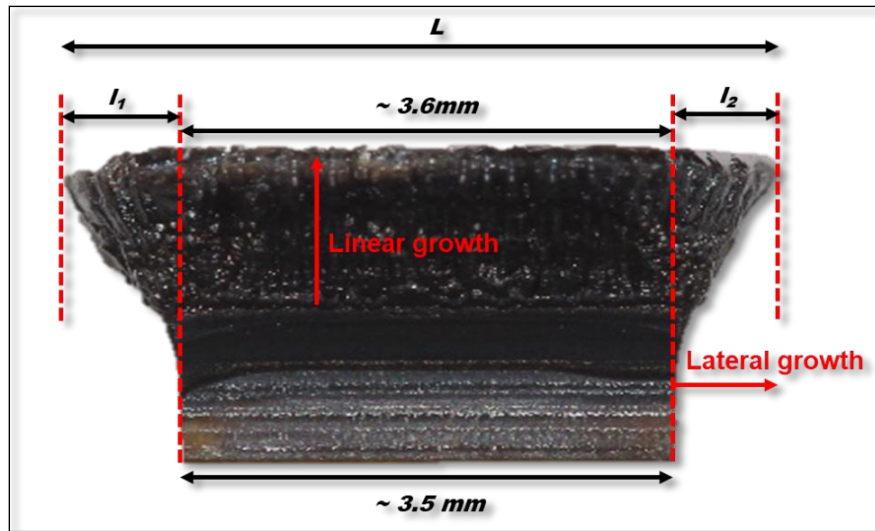


Figure 3. 21 Optical microscope image of the side view of the as-grown diamond substrate. The red arrows show the lateral and linear growth direction. The dashed red lines identified the dimensions of l_1 and l_2 .

Once the measurements are completed, the following equation calculates the lateral growth rate:

$$V_{(110)} (\mu m / h) = \frac{(L - 3.6)/2}{time}$$

In the event that outward growth is not uniform on both sides, the lateral growth rate would be considered as an average of both dimensions, i.e. l_1 and l_2 . Only the linear and lateral growth rates data are reported in this dissertation since they yielded a more accurate linear growth rate than weight gain data.

3.8 Main Analytical Instruments

3.8.1 SCD Surface Morphology and Surface Area

A digital microscope KEYENCE VHX-5000 was used to capture the optical images of the top surfaces. Optical images of the top surface were taken of each experimental run to analyze the surface morphology and the crystal shapes of the SCD grown substrates. The top surface area was then calculated from these images by drawing the outline of the irregular top surface and using the software VHX-500 to determine the area based on the shape and size of the top surface. The irregular shapes and the jagged edges of the top surfaces were taken into account by the VAX-500 software integration techniques as is shown in Figure 3.23. With this instrument, the defects, surface smoothness, and transparency on the diamond top surface were also observed and analyzed.

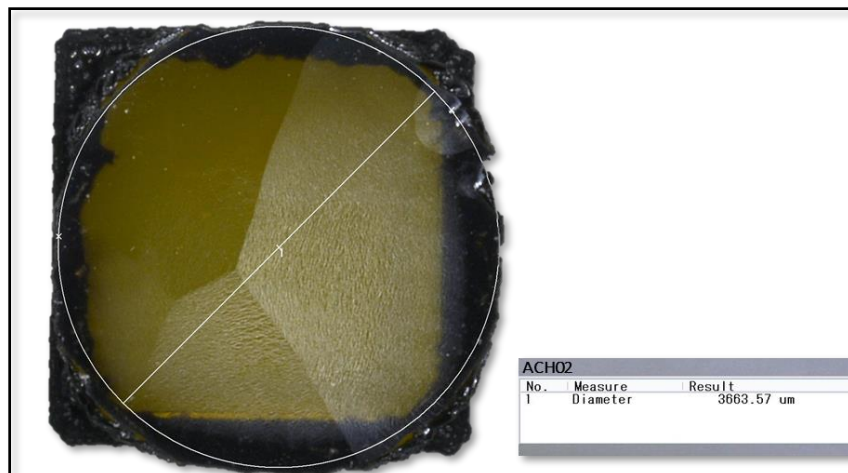


Figure 3. 22 Optical microscope image of the top view of the as-grown with a white circle drawn around the diamond shape.

3.8.2 Scanning Electron Microscopy (SEM)

SEM is one of the most widely used surface characterization techniques. It images the sample surface by scanning it with a high-energy electron beam. Electrons are thermionically emitted from an electron gun fitted with a filament cathode. Tungsten is normally used as the filament in thermionic electron guns, due to its high melting point and low vapor pressure allowing it to be heated for the easy electron emission. When the emitted electrons pass through a condensing lens, made by a coil of current-carrying wire, they are collimated into a small beam by forces from a focusing magnetic field. After the condensing lens, there is another coil which scans the beam of electrons over the sample. The electron beam is finally focused to a small spot on the sample surface by a final objective lens. All the SEM components are contained inside a vacuum chamber to minimize electron-gas interactions. The SEM images reported in this thesis were taken in

the MSU Engineering Composite Center by using a Carl Zeiss Variable Pressure SEM EVO LS25.

3.8.3 Secondary Ion Mass Spectrometry Analysis (SIMS)

Secondary ion mass spectrometry (SIMS) is an analytical technique that detects very low concentrations of dopants and impurities. It can provide elemental depth profiles over a depth range from a few angstroms to tens of micrometers. SIMS is a good analytical method with excellent detection sensitivity for impurities, with ppm or lower detection sensitivity. Compared to Raman spectra, it can directly detect the impurities concentrations in the diamond crystal and determine the quality of the diamond. However, due to the high cost of the measurement, in this thesis investigation, only a limited number of SCD samples were analyzed by SIMS.

Figure 3.24 shows a schematic diagram of a SIMS analysis system. As shown in the figure, a focused primary ion beam (usually O^+ or Cs^+) was generated by an ion gun [143]. The sample was sputtered or etched with the ion beam. Secondary ions formed during the sputtering process were extracted and analyzed by using a mass spectrometer (usually a quadrupole or magnetic sector). The secondary ions can range in concentration from matrix levels down to sub-ppm trace levels.

The SIMS analysis results reported in this thesis investigation was done by Evans Analytical Group [143]. The SCD surfaces were etched by the ion beam and profiled over a depth of 12 μm . The detection limits were 2×10^{15} atoms/cm³. The particular element that was chosen to detect was nitrogen; it is an important impurity that is presented in this CVD growth experiments that occur in plasma Reactor C.

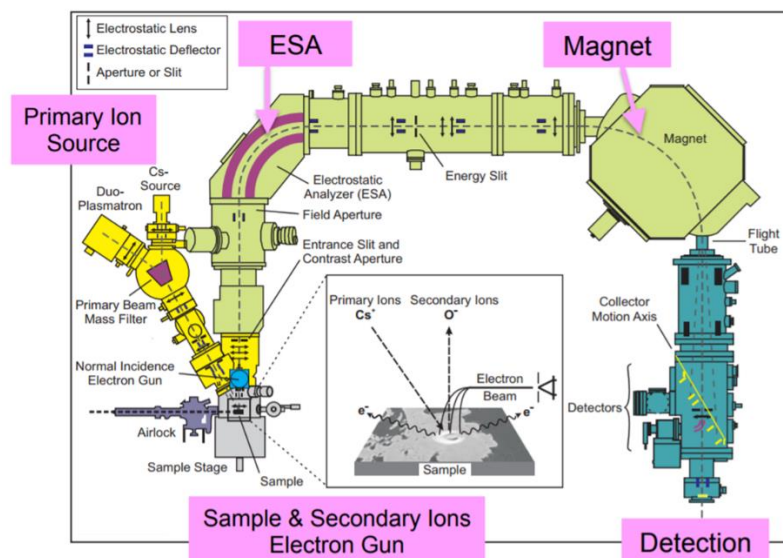


Figure 3. 23 Schematic of SIMS analysis system [143].

3.8.4 Birefringence Imaging

Birefringence is the optical property of a material having a refractive index that depends on the polarization and propagation direction of light. The birefringence is often quantified as the maximum difference between refractive indices exhibited by a crystal material [144].

Birefringence imaging is an effective method for checking the stress level in the crystal. By examining the birefringence patterns of grown single crystal diamonds, the spatial distribution of internal crystal stresses could be obtained. Like optical transmission measurements, the birefringence imaging also required diamond plates with smooth and flat surfaces which should be parallel with each other.

Here, an optical microscope (Nikon Eclipse ME600) was used to take the birefringence images. Two quarter-wavelength retardation filters were positioned at 90°

offset rotation. The diamond plates were placed between the filters. The microscope was used in transmission mode. In this setup, an unstressed cubic diamond crystal that was optically isotropic would appear black in the image. However, stress and strains in the crystal could make the optical properties anisotropic and cause birefringence, which lead to an observable light intensity distribution through the crystal.

3.8.5 Etch Pits Analysis

Hydrogen plasma etching of the diamond surface is a simple method to reveal defects and dislocations. The hydrogen etching process attacks the weak chemical bonding around defects and dislocations in the diamond surface, leading to the formation of etch pits. Two main sources of extended defects in CVD crystals can be identified: (i) dislocations induced by the substrate's surface state and its polishing, (ii) dislocations that directly originate from defects in the bulk of the substrate such as stacking faults. The generated dislocations tend to thread through the CVD film parallel to the growth direction [145], [146] .

Etch pits were formed on the free-standing CVD plates and HPHT seed oriented (100) using a hydrogen plasma. Photographs of the plates and seeds were taken at different magnification, such as 30 x, 100 x and 700 x to observe the etch pits patterns.

In order to calculate the etch pit density, the images were processed by using MATLAB Image Segmentation. This image processing method involves a new MATLAB code to improve the contrast of the pictures and thus made an easy way to detect the defects on the surface. The MATLAB images processing tool creates uncluttered images which satisfy the conditions to the programming to detect the defects on the surface. The

procedure to process the images is broken into three steps: (1) the digital image processing, (2) code generation (3) identify and correct possible errors in the defects recognition.

Step (1): A selected image is imported into the software. Then, the image is enhanced by contrast adjustment, morphological filtering, deblurring, and other image enhancement tools. An example is shown in Figure 3.25. The images enhanced may also include removing noise, removing motion blur, reconstruction, and other morphological operations.

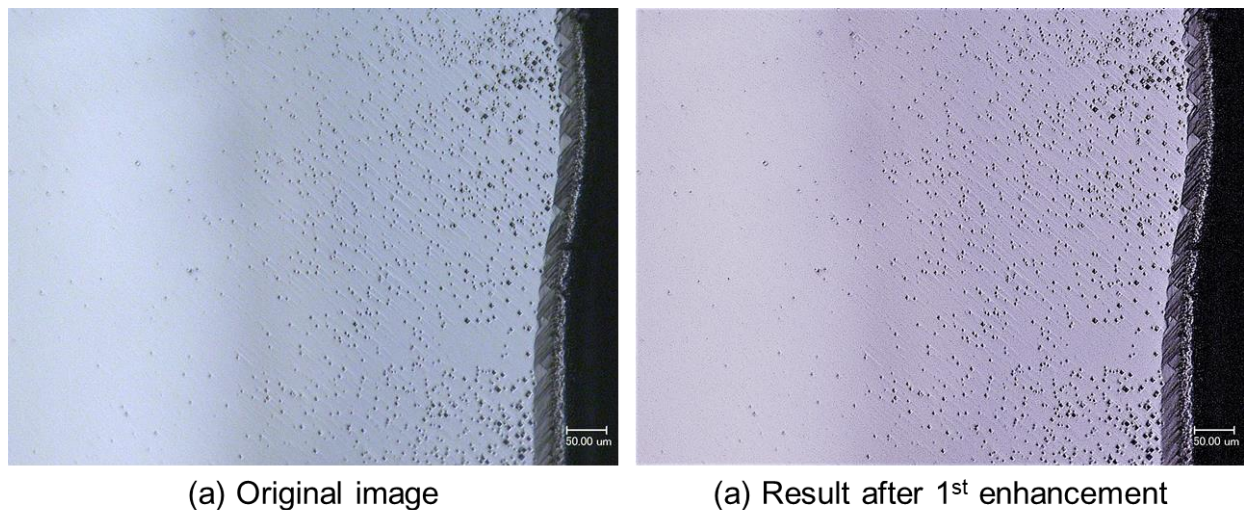


Figure 3. 24 (a) optical image of ACH09 plate and (b) image enhanced

Once the image is enhanced, it is analyzed. Image analysis is the process of extracting meaningful information from images such as finding shapes, counting objects, identifying colors, or measuring object properties. The toolbox provides comprehensive functions for image analysis tasks such as statistical analysis and property measurement.

These tools are selected based on the characteristic of the image. An example of the image processing in a CVD plate, ACH22, is shown in Figure 3.26.

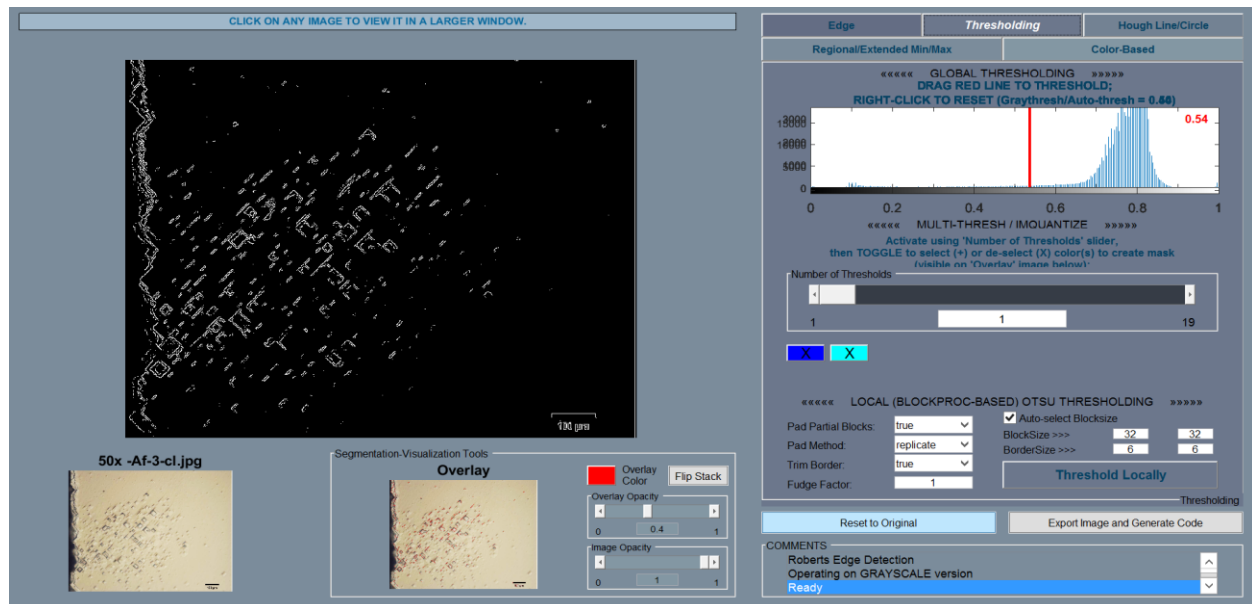


Figure 3. 25 General view of the images processing tool.

Once the image is completed, the step (2) is to generate the MATLAB code. Each image processed generates a code that should be exported to MATLAB platform. These codes are added to the complete analysis code that was previously created in MATLAB. Finally, the program used a set of reference-standard algorithms and visualization functions for analysis and proper measurement of the etch pits on the surface.

This new etch pits method allows one to have accurate etch pits density measurements in short periods of time. Each image can be processed in 15 - 20 minutes, in comparison with the conventional method in which the process had usually taken in 2 - 5 hours.

CHAPTER 4

MPACVD GROWTH OF SINGLE CRYSTALLINE DIAMOND SUBSTRATES WITH PCD RIMLESS AND EXPANDING SURFACES

4.1 Introduction

Single crystal diamond (SCD) growth was performed in optimized pocket substrate holders at a high pressure of 240 Torr and a high-power density of $500\text{W}/\text{cm}^3$. In an effort to overcome the challenges of growing large area SCD substrates without a corresponding polycrystalline diamond (PCD) rim, a growth recipe using these pocket holders was developed. This growth recipe controls the substrate temperature (T_s) and the incident microwave power (P_{inc}) in a prescribed function of growth time. Through this process, the feasibility to enlarge the SCD substrate in situ, i.e., during the growth itself is shown. By allowing the temperature to increase from 980°C to 1040°C , then reducing the temperature, and then allowing it to drift up again, the deposition process alternates between the fast growth of the different crystal directions (i.e., $\{110\}$, $\{111\}$, and $\{100\}$) and a slow growth to smoothen the top surface. This leads to an increased lateral SCD

growth. The slow growth of the crystal faces in turn leads to a smooth and enlarged top surface. Certain strategies such as the termination of the growth process at the appropriate time are critical in obtaining flat and smooth SCD surfaces without the formation of any PCD rim. The SCD substrates grown via this method have been analyzed by optical and scanning electron microscopies. The lateral SCD surface area increased between 1.7 and 2 times greater than the initial seed surface area during one continuous run. The deposited SCDs have high growth rates of $\approx 30 \mu\text{m/h}$ resulting in smooth, flat and rimless substrates, hence indicating the improvement in the quality and morphology of the deposited substrates.

4.2 Background

As the world is becoming more technologically advanced, engineering applications require novel materials. The unique and excellent properties of diamond make it one such special material that can be utilized in high-end optical and electronic applications. In the past, it has been very difficult to grow and manufacture both large area and high-quality diamond that is needed for many commercial applications. Recently, it was pointed out that microwave plasma assisted chemical vapor deposition (MPACVD) offers the most convenient method of growing high-quality SCD substrates [29]. Different MPACVD techniques like the mosaic wafer and side growth method, have been utilized by several groups to grow large area SCDs ([94], [109], [147], [148]). However, the deposition of large area SCD substrates via MPACVD still presents challenges; i.e. during the growth process, the usable SCD area shrinks due to the unwanted growth of a PCD rim around the SCD substrate. Figure 4.1 shows the results of such a conventional MPACVD SCD

growth. The SCD was grown with $\text{CH}_4/\text{H}_2 = 5\%$, and $T_s \approx 1020^\circ\text{C}$ for 19.5 h. In order to prevent process runaway during the growth cycle, the pressure and power were reduced from the initial values of 240 Torr and 1.9–1.6 kW, to their ending values of 130 Torr, and 2.3–1.9 kW. Mokuno et. al [10] observed that when using an enclosed substrate holder the SCD surface initially slightly increases during the 0.5 mm to 1 mm of growth and then as the growth process proceeds, it decreases and becomes surrounded by a polycrystalline rim. In order to address the challenge of rim growth and also to simultaneously enlarge the grown SCD size, it is imperative to develop growth processes that minimize the PCD rim formation while increasing the lateral SCD surface area during growth.

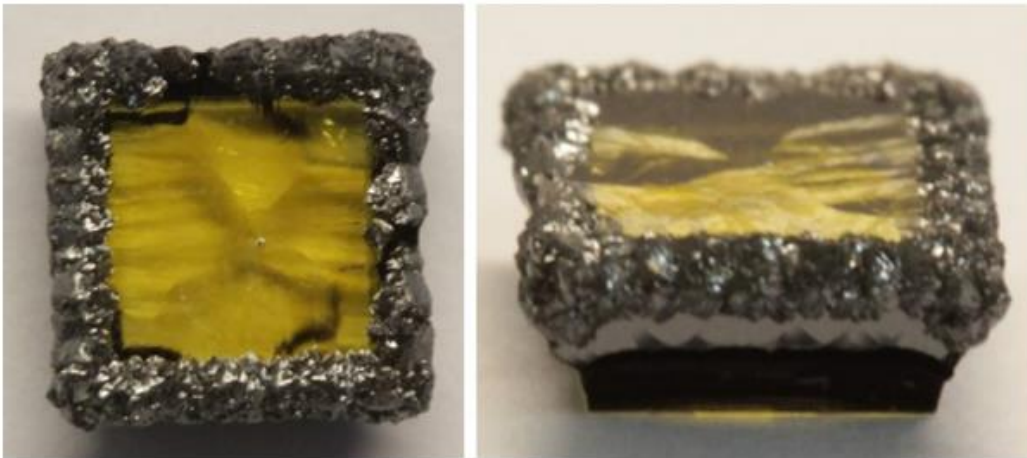


Figure 4. 1 Thick PCD rim growth on SCD substrate using a conventional open holder growth method.

A substrate holder, identified here as a pocket holder, was designed and built in an effort to overcome these problems. In a series of exploratory experiments, this holder

demonstrated the growth of thick (0.4 – 1.6 mm) and low-stress SCD with almost no rim, and created a SCD top surface with a larger lateral area (1.23 – 2.5 times) than the original seed area [20]. These substrates grown in a pocket holder were of type IIa diamond quality. Recently, G. Wu et.al., investigated the growth dependence versus the enclosed holder depth at modest pressures (80 – 100 Torr) [123]. Presented here are experimental details of an SCD process recipe that utilizes a pocket holder and enables both the growth of the larger area and rimless SCD substrates. The pocket holder process was optimized under high pressure (240 Torr) and high microwave power density conditions for large area SCD growth by varying versus time two important growth process variables: substrate temperature (T_s) and incident power (P_{inc}). By real-time controlling the input microwave power and hence T_s , this optimized process recipe enabled the growth of thicker and larger area SCD without creating a PCD rim.

4.3 Experimental details

The experiments were carried out in the microwave cavity plasma reactor (MCPR) C configuration. The design and operation of this reactor has been discussed in a previous publication [18] and also is detailed in Chapter 3 of this thesis. The residual nitrogen concentration caused by any vacuum system leaks or input gas impurities was ~10 ppm. The reactor was operated in a safe and efficient region as described in ([16], [141]). Such a reactor design allows the growth of SCDs at high pressures (> 240 Torr) and high-power densities (> 500 W/cm³) over long growth durations (10 – 72 hours). This pocket holder design was presented in Chapter 3 as a conventional substrate pocket holder depth, i.e. $d = 2.3$ mm and $w = 6$ mm. For the specific experiments mentioned here, the constant

variables include the growth on HPHT type Ib (100) oriented seeds at a pressure of 240 Torr (i.e. 320 mbar), a hydrogen flow rate of 400 sccm, and a methane flow rate of 20 sccm (i.e. 5% CH₄/H₂). In all experiments, the reactor was always well matched. Thus, the input power was approximately equal to P_{inc} . The varying parameters are (a) P_{inc} : from 3 kW to 1.96 kW and (b) growth times between 40 – 46 hours.

4.4 The growth process recipe

The process recipe independently varies P_{inc} versus time (see Figure 4.2) to intelligently control T_s over the process cycle. An example of the variation of P_{inc} and T_s versus time for such a process recipe is shown in Figure 4.2. This recipe was used to grow the SCD, ACH23, shown in Figure 4.2 and Figure 4.3 displays the independently controlled variation of P_{inc} versus growth time (red curve) and the corresponding T_s variations (blue curve).

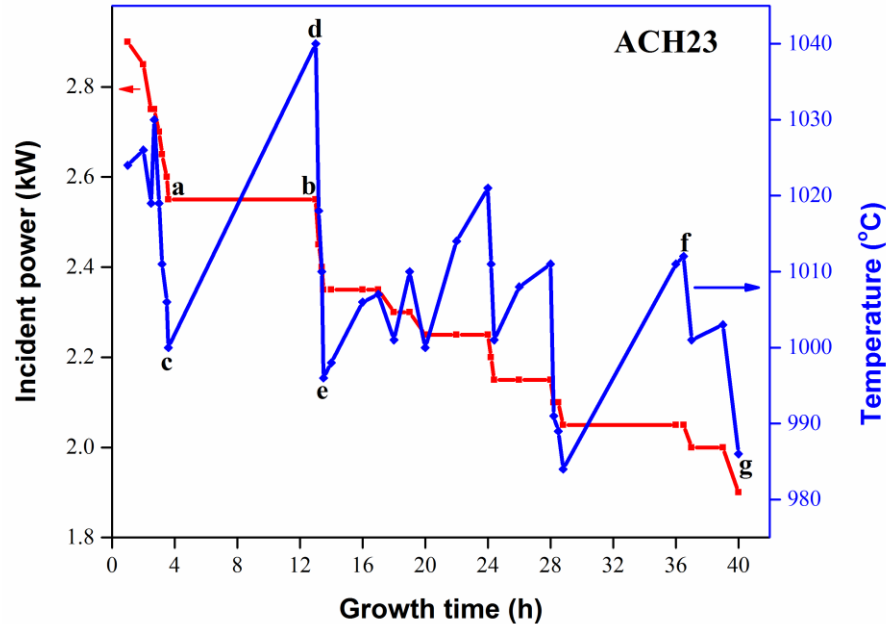


Figure 4. 2 Growth process recipe displaying a process cycle variation of T_s and P_{inc} versus growth time for substrate ACH23 (shown in Figure 4.3).

When operating at these high pressures and high-power densities, as the SCD grows, real temperature control is necessary to keep T_s within the 1040°C – 980°C SCD growth window. Normally during a process cycle, T_s drifts upward, i.e. it increases, versus time as the SCD grow [20]. As a result, the input power must be decreased versus time in order to keep T_s within the SCD growth window. In Figure 4.2 this decrease is shown over the entire process cycle as the continuously decreasing P_{inc} versus time curve. Superimposed on this required steady power decrease are several short temperature upward drifts that the input process recipe allows to occur over a fraction of the process cycle. These are necessary in order to provide desirable deposition conditions on the substrate during specific portions of the process cycle. The strategy behind these short time temperature variations is discussed below.

4.5 Experimental results

Using the variation in T_s and P_{inc} versus growth time (shown in Figure 4.2) SCD substrates were grown in a 2.3 mm deep pocket holder. Figures 6.3 and 6.4 show examples of rimless and larger area SCD growth. Note the improvement of the top surface over the conventionally grown substrate shown in Figure 4.1. ACH23 (Figure 4.3) was grown in one step for 40 hours, with a thickness of 1.2 mm, and a growth rate of 30 $\mu\text{m/hr}$. Similarly, ACH24 was grown in one step for 46 hours, with a thickness of 1.34 mm and a growth rate of $\sim 29.2 \mu\text{m/hr}$. High magnification optical microscope images of these two substrates, in Figures 4.3 and 4.4, show growth without a rim. The top surface of the CVD SCD substrate is smooth and flat with no major defects on the surface. The dimensions of the growth surface for these two substrates were 23.28 mm^2 and 27.30 mm^2 respectively. Thus, the lateral surface area of the CVD SCD substrate increased by ~ 1.7 times for ACH23 and ~ 2 times for ACH24 over the initial SCD seed surface area (i.e. 13.69 mm^2). The outward growth of the SCD substrates is clearly seen in Figure 4.5 (a) and (b).

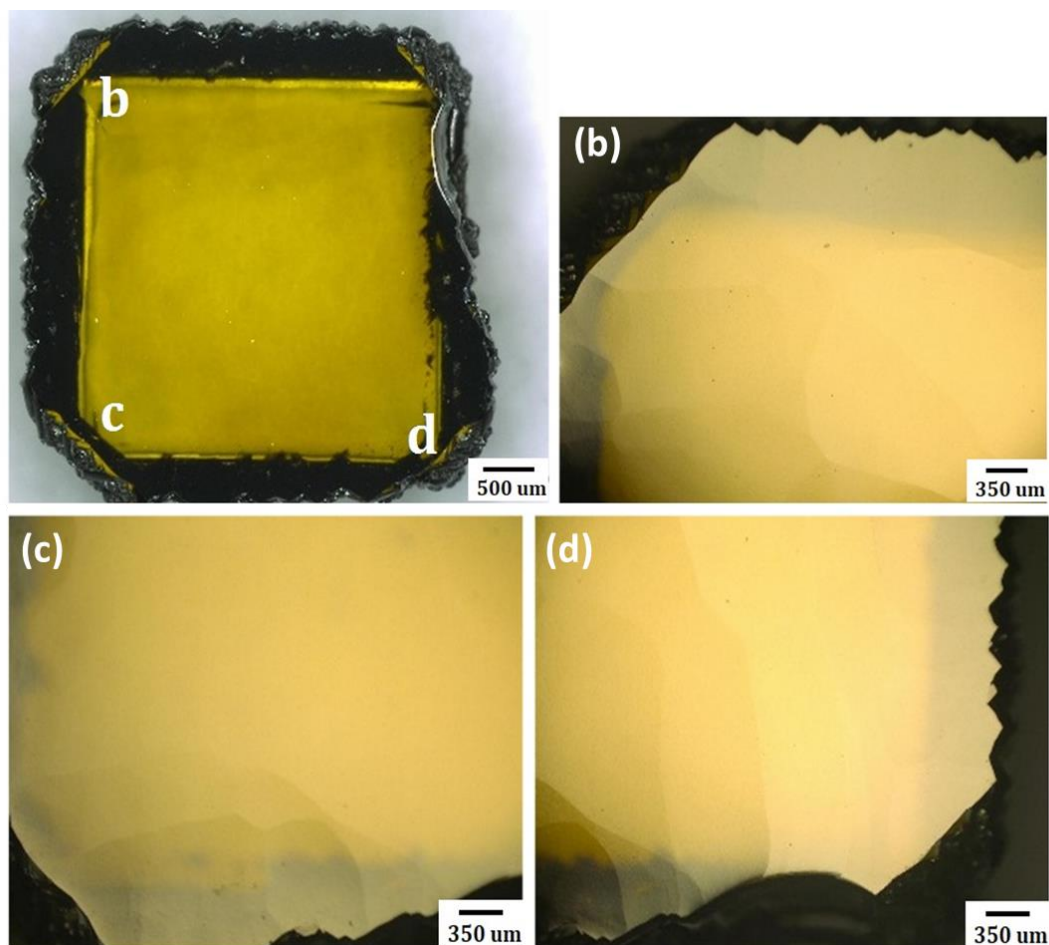


Figure 4. 3 Optical microscope images of (a) ACH23. Close up views of the substrate in (b) – (d) show rimless growth with larger SCD area.

The substrates were also evaluated under scanning electron microscope (SEM) and the images are shown in Figures 4.6 (a) and (b). No rim was found around the edges of the surfaces and the top surface was observed to be flat with no non-epitaxial growth at the edges and corners. It was also observed that the (110), (111) and the (100) crystal faces grew simultaneously during this process leading to the enlargement of the CVD SCD substrate.

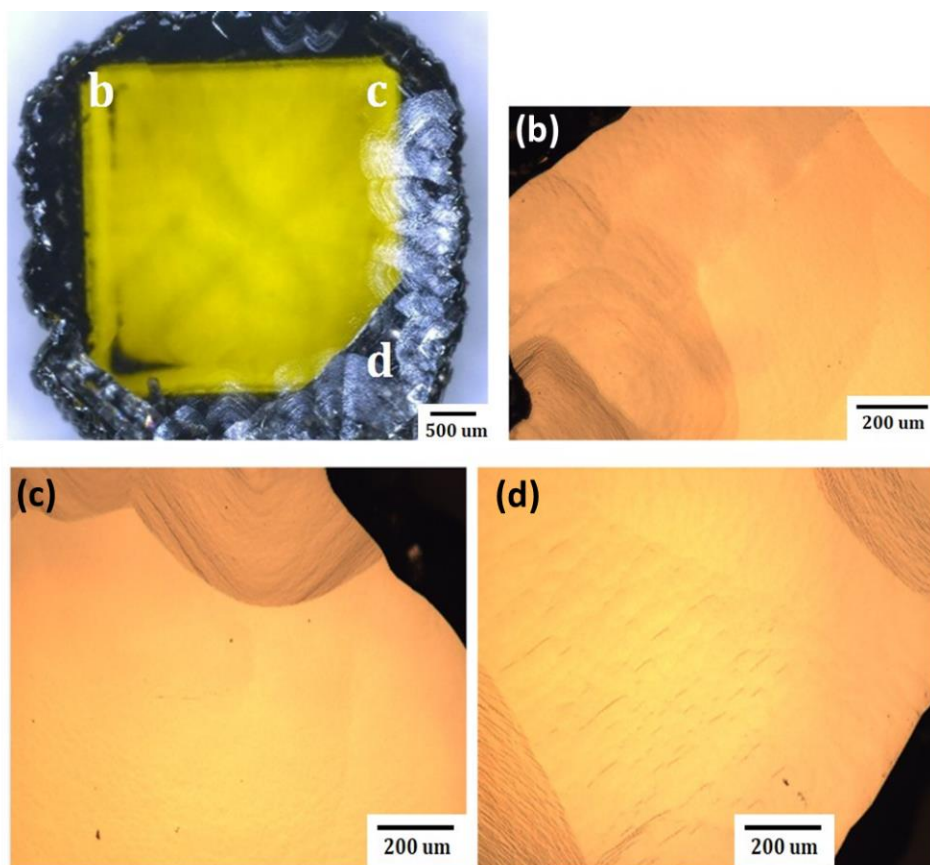


Figure 4. 4 Optical microscope images of (a) ACH24. Close up views of the substrate in (b) – (d) show rimless growth with larger SCD area.

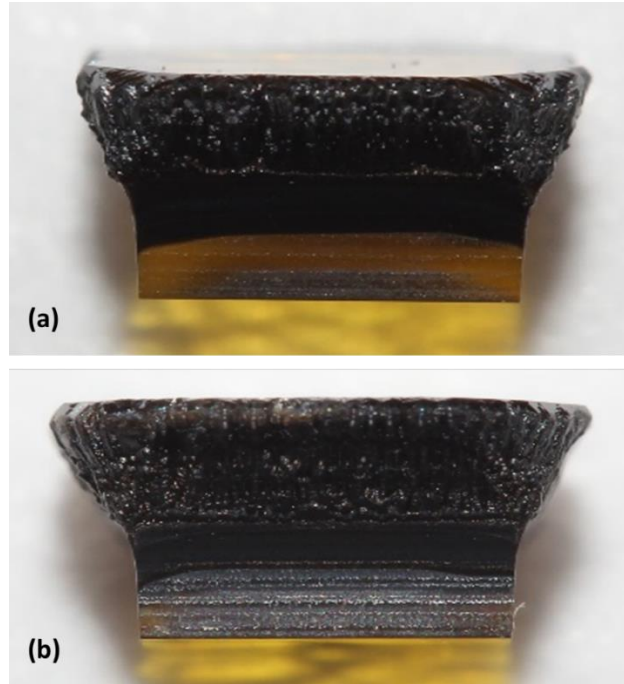


Figure 4. 5 Side view images of (a) ACH23 and (b) ACH24 indicate outward growth of the CVD SCD substrates.

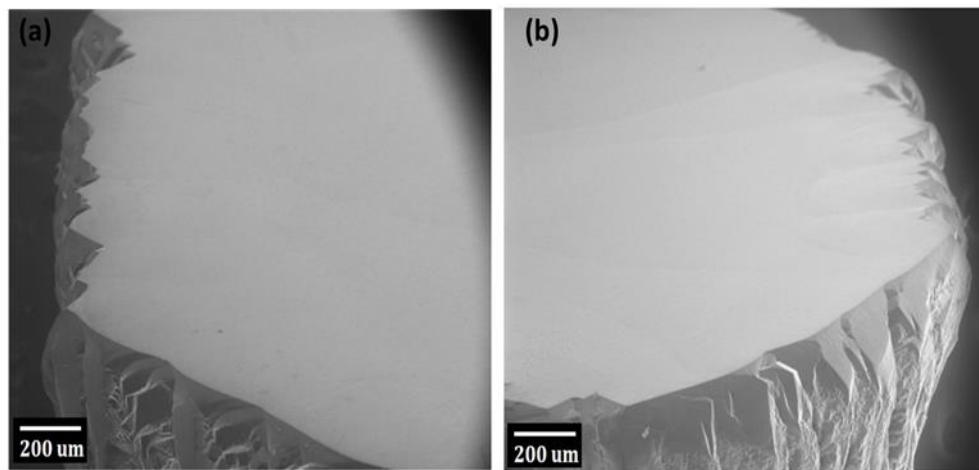


Figure 4. 6 SEM images of (a) ACH23 and (b) ACH24 indicate PCD rim free CVD SCD substrates.

4.6 The growth strategy

As has been discussed in [113], [149], the growth rates of (100), (110) and (111) crystal faces and hence α , and β growth parameters [56], are dependent on T_s . Thus far, previous publications on diamond growth discuss the growth of SCDs with a constant temperature over a certain growth time [148], [150]. The objective of this work is to control the concentration of radical species density over the seed substrate and T_s versus time in order to obtain a high, uniform growth rate without the formation of a PCD rim. To achieve this objective, P_{inc} and hence T_s were varied versus growth time.

It has been observed that the growth rates of (111) and (113) faces increase at higher T_s [149]. Therefore, in this process for the first few hours, T_s is kept high at $\sim 1020^\circ\text{C}$. At this high T_s , the entire seed surface is at a uniform temperature which allows the hot and dissociated gas radicals to deposit uniformly over the entire substrate surface. As a result, the corners, edges and the center of the substrate start growing uniformly without a rim. Once the growth has been initiated for the entire surface in the first 10 – 12 hours, it has been observed in our experiments that the diamond grows uniformly over the entire substrate. T_s was then lowered versus time to $\sim 980 - 990^\circ\text{C}$ in small steps of $\sim 5^\circ\text{C}$ by decreasing P_{inc} . As growth proceeds, the substrate thickness increases, and T_s also increases since the substrate surface approaches closer to the intense plasma. During this process, the temperature is controlled and allowed to drift upward to $\sim 1020^\circ\text{C}$ following which T_s has reduced again to $\sim 990^\circ\text{C}$ by reducing P_{inc} . Such a temperature variation is followed throughout the process cycle. This real-time temperature variation both promotes the outward growth and produces a smooth, improved morphology of the SCD crystal.

An example of the variation of T_s and P_{inc} as a function of growth time is shown in Figure 4.2 for substrate ACH23 (Figure 4.3). Initially when T_s is high ($\sim 1030^\circ\text{C}$), the growth rates of the different crystal faces are also high allowing the outward SCD growth. For the next several hours, the temperature was first lowered to $\sim 1000^\circ\text{C}$ (to point “c” in Figure 6.2) by lowering P_{inc} (to point “a” in Figure 4.2). A hypothesis is that this lower temperature growth aids in obtaining a smooth top SCD surface. Although the growth rates decrease slightly, the entire surface grows more uniformly and improves the surface morphology. During the ensuing growth period, P_{inc} is kept constant from point “a” to “b” in Figure 4.2. However, during that period, as seen in Figure 4.2, T_s drifts upward from point “c” ($\sim 1000^\circ\text{C}$) to “d” ($\sim 1040^\circ\text{C}$), since the top of the growing crystal surface approaches the intense plasma as a function of time. This again allows the fast growth of the crystal faces, especially in the $\langle 110 \rangle$ and $\langle 111 \rangle$ directions. After this the temperature is lowered to 996°C (point “e” in Figure 4.2) by reducing P_{inc} . The temperature variations between the high (like point “f” in Figure 4.2) and lower (like point “e” in Figure 4.2) temperature states promote the different growth rates of the different crystal orientations versus time. These temperature fluctuations are carried out throughout the growth cycle (Figure 4.2). An important fact to note is that near the end of the run, T_s is reduced from point “f” to “g” ($\sim 985^\circ\text{C}$). This temperature decreases at the end of the run and then stopping of the process at the right time is critical in preventing the SCD from penetrating into the discharge. When T_s and P_{inc} are not controlled and the substrate grows into the discharge, a thick PCD rim has been observed the rim is similar to that shown in Figure 4.1. The strategies mentioned here ensure the growth of a flat and even surface with

sharp edges and without any rim (see Figure 4.6). Growth processes with similar temperature variation were followed for the other substrates discussed here.

4.7 A comparison to earlier results

In order to quantify the outward growth of the CVD SCD substrates, the lateral area gain (i.e. final CVD SCD top area/original seed top area) of the final growth surfaces was plotted as a function of the vertical thickness gain as shown in Figure 6.7. Except for the colored data points, this plot is reproduced from Figure 15 in [20]. The black data points from the original figure are used as comparative reference data. The data points for substrates ACH23 and ACH24 are represented by the yellow and red data points in Figure 4.7, respectively. The data points from these substrates, located within the dashed oval in Figure 4.7, correspond to the trend observed in the substrates grown earlier with a pocket holder using the MCPRs ([18], [73]) operating at different temperature and power conditions. The blue data point was also grown at the same recipe conditions and the black data within the dashed oval was grown by Y. Gu [132] using a similar recipe growth method. However, with the variation of T_s as described in Figure 4.2, it is now possible to obtain a larger lateral growth of the final CVD SCD substrate surface along with a high vertical thickness gain.

This growth process allows the deposition of high quality and large, i.e. ~2 times the initial seed area SCD substrates. By varying T_s and P_{inc} as a function of the growth time, a high growth of (110) and (111) crystal faces is enabled such that a high lateral growth rate may now be achieved. PCD rim growth was also eliminated. Hence, without the PCD rim, the grown SCDs may now be analyzed more effectively. These rimless substrates

also reduce post processing time as it is not necessary to trim the PCD off. With the lack of rim growth, the stress and hence cracking in the crystals will also be reduced considerable, thereby improving the quality of the grown substrates. It is feasible to build on this process and develop additional similar growth recipes for the further enlargement and growth of larger and thicker SCDs with single to multi – step growth runs.

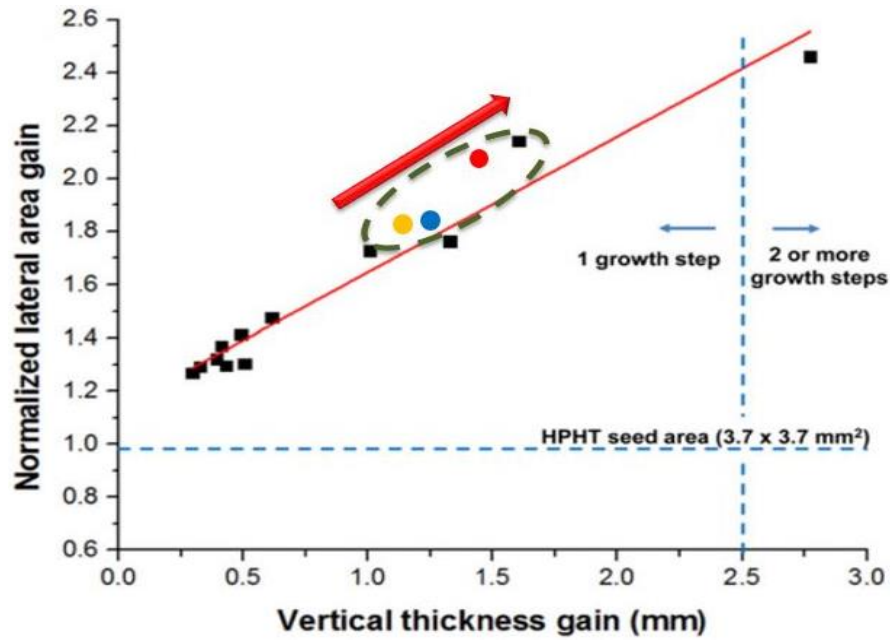


Figure 4. 7 Outward growth of the CVD SCD substrates [20].

4.8 Summary remarks

The growth recipe described in this research is a special case of the MPACVD growth of SCDs in a pocket holder. This particular case of MPACVD growth process depends on the pocket holder dimensions, the behavior of P_{inc} versus time and also on the corresponding behavior of T_s versus time. However, it was developed empirically. There

may be other possible special recipes to grow different PCD rimless SCD shapes. Some of these are currently under investigation.

CHAPTER 5

SINGLE CRYSTAL DIAMOND GROWTH AT CONSTANT SUBSTRATE TEMPERATURE (T_s)

5.1 Exploring Constant Substrate Temperature and Constant High Pressure SCD Growth Using Variable Pocket Holder Depths

5.1.1 Research Highlights

- Polycrystalline diamond (PCD) rimless, single crystal diamond (SCD) growth is demonstrated in an optimized pocket holder.
- A constant substrate temperature process control recipe over the entire process cycle is demonstrated.
- The influence of the pocket holder depth on the morphology and area of the grown SCD is revealed.

5.1.2. Introduction

SCD substrates were successfully synthesized using an optimized pocket holder design. The pocket holder design creates an appropriate thermal environment to shield the diamond substrate from the intense microwave discharge. This substrate configuration allows for a polycrystalline diamond (PCD) rimless, uniform single crystal diamond (SCD) growth process. Square shaped pocket holders with a constant width but with varying depths were used. The SCD growth procedures were carried out via microwave plasma assisted chemical vapor deposition (MPACVD) in a 2.45 GHz microwave cavity plasma reactor C [18] at a constant pressure of 240 Torr and high power density of $\sim 500 \text{ W/cm}^3$. By continuously adjusting incident microwave power (P_{inc}), the substrate temperature (T_s) was held at $1020^\circ\text{C} \pm 5^\circ\text{C}$ throughout the entire process cycle. Under these growth conditions, the crystal morphologies exhibited a smooth and flat surface. The average growth rate of the SCDs varied between 30 – 24 $\mu\text{m/h}$ as the pocket depth increased from 2.0 to 2.9 mm. The PCD rim was eliminated for all pocket depths and the shape of the final, as grown, top SCD surface varied from a square to a circular shape as the pocket holder depth increased. When using the 2.0 mm and 2.3 mm pockets, the final top SCD surface area increased to almost twice the original HPHT diamond seed area and the lateral growth rate was slightly larger than the vertical growth rate. Birefringence imaging of the grown CVD diamond indicated low stress and SIMS analysis indicated nitrogen concentration levels in the freestanding, CVD diamond plates were in the range of 50 ppb to 140 ppb.

5.1.3 Background

A current challenge facing the SCD growing research community is the development of plasma assisted CVD process methods that enable the growth of large area and high-quality SCD crystals while operating under high growth rate, high pressure diamond deposition conditions [8]. A major problem with the growth of large area SCD substrates is that as the diamond grows thicker, the top surface area of the crystal becomes smaller. As a result, the top SCD growth surface is smaller than the original HPHT diamond seed surface, and the shrinking top surface is surrounded by a thick PCD rim [11], [20].

Currently, several research groups are trying to overcome these problems by developing alternative large area growth methods. Several of these methods are (1) the mosaic growth approach [148], (2) the flipped crystal growth approach [110] and (3) the flipped side growth approach [108]. While progress has been made in growing SCD substrates by these methods, each has problems such as limited growth size, growth process starts and stop interruptions, crystal stress and cracking, and excessively long growth times that are required to grow the large diamond substrates. The requirement of rapidly and efficiently growing high quality SCD imposes the additional condition of growing diamond under high growth rate and high-pressure diamond deposition conditions.

There are still considerable technical obstacles that must be overcome before robust and efficient SCD growth processes are available. These processes must enable the rapid growth of large and high quality SCD substrates. Therefore, fundamental microwave plasma assisted chemical vapor deposition (MPACVD) SCD growth approaches are investigated in this chapter. These growth approaches have shown promise to rapidly grow

high-quality SCD, without the formation of PCD rim and also with an expanding SCD growth surface area.

One such fundamental experimental SCD growth approach is to investigate MPACVD SCD growth using a “pocket holder” [3] [125]. Recent experiments have demonstrated that by employing a ‘pocket holder” MPACVD process it is possible to grow thick (> 1.4 mm) and high quality SCDs while simultaneously reducing the PCD rim that surrounds the top growing surface [20], [124]. The specific process consists of the following experimental procedure: (1) placing a HPHT diamond seed in an optimized pocket holder geometry, (2) controlling the substrate temperature, T_s , versus time over the entire process cycle, and then (3) ending the process run when the SCD grows out of the holder configuration. By employing such growth strategies thick ($200\text{ }\mu\text{m} - 1.4\text{ mm}$), free-standing SCD plates were produced in one uninterrupted process step. When the process was extended to a few separate growth steps, thick SCD diamond plates and cubes ($\sim 5\text{ mm} \times 5\text{ mm} \times 4.5\text{ mm}$) were produced [20]. Thus, pocket holder diamond growth can not only reduce the growth of PCD rims that are usually observed during MPACVD growth, but the process can expand the top SCD surface laterally as the SCD thickness increases [20], [124]. Recently we have shown that the application of a specific process recipe, i.e. the real – time control of the input microwave power and hence T_s versus time, over the process cycle, enabled the growth of thick and larger area SCD while eliminating the PCD rim [125]. The experimental details of this process are presented in the next chapter, chapter 6 of this thesis.

Another recent investigation summarized results from experiments that also employed pocket holder MPACVD SCD diamond growth versus the holder depth [123]. The

experiments were carried out at 80-100 Torr and with 3-5% methane growth environment. The holder depth was varied from a flat holder to a depth of 2.0 mm to grow several hundred-micron thick SCD plates. When operating at these low and moderate pressures, the use of the pocket holder reduced the diamond growth rate but improved the crystalline quality and the internal stress of the grown SCD. It is important to note that the experiments that are presented here were executed under considerably different conditions than those in reference. The diamond growth is performed at the high pressure of 240 Torr, with high power density discharges of approximately 500 W/cm^3 , and over a large range of pockets depths. Hence the diamond growth rate, diamond size, and diamond crystal quality were expected to be different over previously reported results [123].

In previous publications [20], [124], [125] have described some specifically optimized higher pressure and MPACVD growth results. Only a few data points were presented in [20]. In [125] using a fixed pocket geometry depth of 2.3 mm experiments were described where the input power and substrate temperature were varied versus time over the process cycle. In summary, the results presented in [20], [125] explore pocket holder growth over a limited experimental window.

In this chapter, the objective is to explore diamond growth over a larger and different experimental input window. The process cycle time is determined by the time it takes to grow the SCD out of the pocket. Four different pocket holder depths, i.e. four different substrate holder geometries, are investigated. An input power versus time recipe was established for each pocket depth in order to achieve the desired constant substrate temperature over an entire process cycle run. Therefore, a different process recipe was

developed for each pocket holder depth. During each entire process cycle run, the substrate temperature is held approximately constant within $1020^{\circ}\text{C} \pm 5^{\circ}\text{C}$ by adjusting the input microwave power versus time. Our results show that rimless growth can be achieved over a range of pocket depths and input power versus time process cycles. However deeper pockets yield smaller final top surfaces and in fact can result in final surfaces that are smaller the original seed surface. These experiments provide a deeper understanding of the pocket holder growth versus the pocket depth/input power variable, as well as provide insight on how to further improve SCD growth in a particular pocket holder geometry.

5.1.4 Experimental Details

The growth procedure was carried out via MPACVD in a 2.45 GHz microwave cavity plasma, reactor C [18] at 240 Torr and by using a high power density discharge of approximately 500 W/cm^3 . The residual nitrogen concentration caused by any vacuum system leaks or input gas impurities was held below 10 ppm. In the experimental runs presented here the nitrogen concentration was less than 10 ppm. However, the nitrogen concentration could vary from 5 ppm to 9 ppm from run to run. SCDs were grown on HPHT type 1b, (100)-oriented (on all sides) single crystal diamond seeds for 10 – 74 hours with H_2 flow rates of 400 sccm and a methane concentration of 5%. A feed gas mixture of hydrogen and methane gases with purity levels of 99.9995% and 99.999% respectively was used for all experiments.

As is discussed in [20], the holder dimensions play an important role in the deposition of large SCD substrates. Many experiments have used the conventional open

holder for CVD diamond growth. The “open holder geometry” is defined here as a holder geometry where the diamond seed is placed on a large flat open holder surface. This has been reported in [10], [11], [20], [151]. These experiments indicated that if one used a flat open holder design, thereby exposing the diamond directly to the discharge and directly to the electromagnetic field, a PCD rim is deposited and forms around the grown SCD material. Reference [150] recently also has demonstrated a significant decrease in the total top surface area of the SCD when using the open holder configuration.

The SCD was placed in a pocket holder as discussed in [20] and a series of pocket holder experiments were performed. The generic pocket holder shown in Figure 5.1 (a), was used in all the experiments. Two important variables when growing a large, smooth and flat top diamond surface are the pocket holder depth (d_n) and the pocket width (w) as is shown in Figure 5.1 (a). The HPHT diamond seeds used in all experiments were placed in four different pocket holder depths. The pocket width, w was held constant at 6.0 mm for all pockets. The pocket holder was redesigned to accommodate the different pocket depths. The redesign slightly adjusted the holder thickness, c , to allow the diamond growth to take place within the appropriate substrate temperature window. During each process cycle, a pocket holder was placed in the reactor as shown in Figure 5.1 (b).

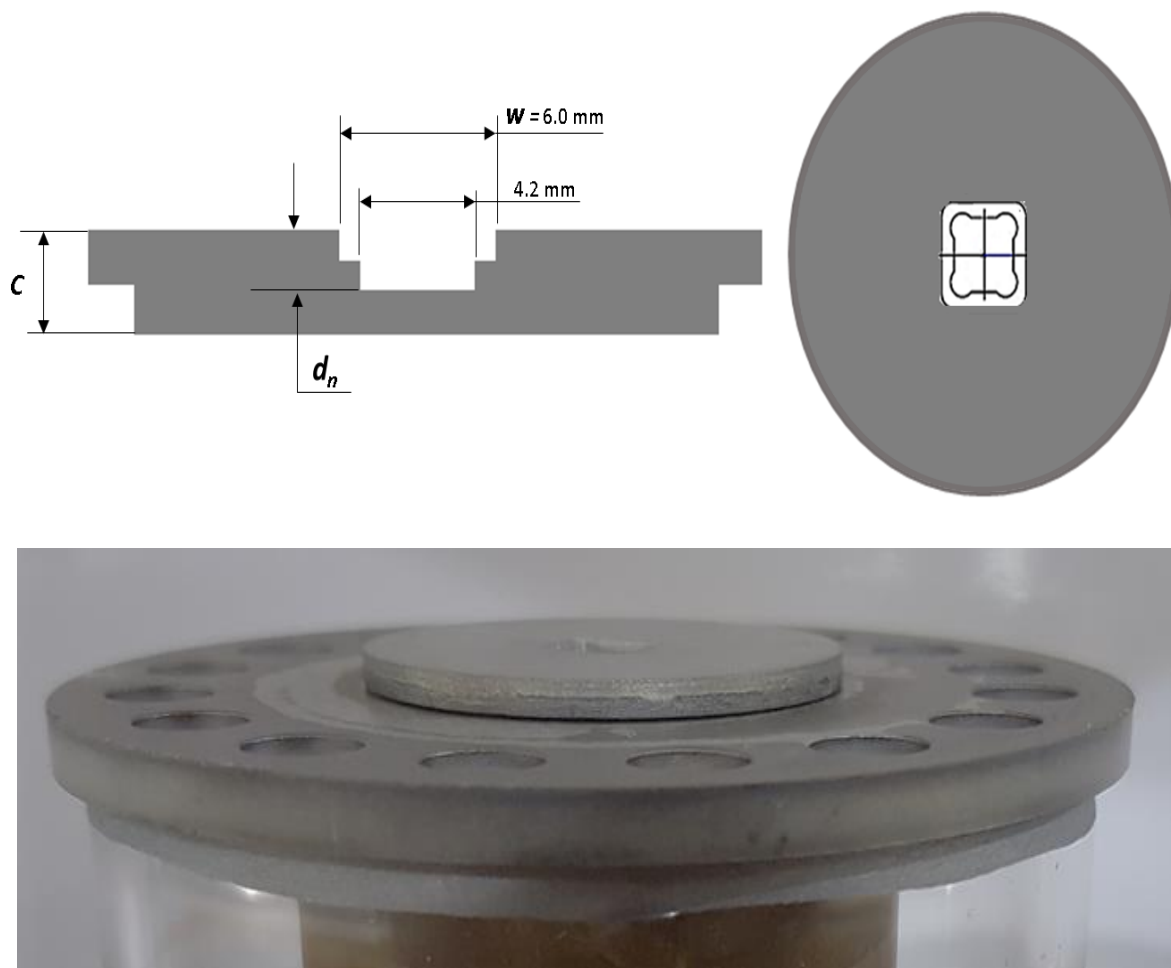


Figure 5. 1 Conventional pocket holder design geometry for SCD growth (top side). The pocket substrate holder placed on the reactor cooling stage (bottom side).

Before loading the diamond seeds into the reactor, they were carefully cleaned with two freshly prepared chemicals etch solutions. The first solution was made from a nitric and sulfuric acid mixture in a [1:1] ratio heated at 350°C. The second solution was made up of hydrochloric acid heated at 350°C. The HPHT diamond seed was then cleaned by mild agitation in a beaker containing acetone and then methanol. Throughout the growth process, the substrate temperature was measured with a 0.96 μm wavelength monochromatic optical pyrometer with an emissivity of 0.1. Two-color pyrometer

temperature measurements were also made under the same experimental conditions and were approximately 100 K higher than the one-color measurements over the 800 K – 1200 K temperature range of the experiments presented here. The pyrometer was placed on a tripod which was kept fixed at a constant position for all temperature measurements. This ensured that all temperature measurements were made under the same experimental conditions. By using the emissivity of 0.1, the measurements presented here can be directly compared with measurements from previous publications [16], [18], [20]. All the diamond growing experiments made use of a 2.45 GHz, 10 kW Cober/Muegge microwave magnetron power supply that was operating at the low end of its recommended power operating ranges, i.e. ~2 kW, and additionally was not well filtered. Thus, the microwave power supplied was not constant but was both frequency and amplitude modulated at 120 Hz. The resulting discharges at times even visually flickered. Photographs of the discharge revealed that the visual discharge oscillated with respect to time at 120 Hz during the complete process cycle, and sometimes depending on the power and pressure input conditions would turn off during part of the 120 Hz cycle [152]. Thus, all the experimental results described here are considered to be excited by an unfiltered microwave power supply, i.e. are not excited by CW microwave power. While it is well known that pulsed microwave power in the range of 100 – 250 Hz can influence MWPACVD diamond growth rates [58], [75], [153]–[155], it is difficult to say how varying the discharge that is used here might change the growth rate over the growth rates from a purely CW excited discharge. However, the variability of the power supply is pointed out here, because it might result in growth rates that are considerably different from the growth rates from a purely CW excited discharge.

The CVD diamond growth procedure involved two steps. The first was a three-hour H₂ plasma etch step. The following process parameters were used for the plasma etching: the H₂ flow rate was 400 sccm and the substrate temperature was held at 850°C – 980°C. The second step was the diamond growth step. Specifically, SCD growth was experimentally investigated over the following subset of process variables: (1) pocket holders with a width of $w = 6.0$ mm and four different depths of $d_1 = 2.0$ mm, $d_2 = 2.3$ mm, $d_3 = 2.6$ mm, and $d_4 = 2.9$ mm (see Figure 5(a)), (2) input powers being adjusted versus time between 3.5 kW and 1.8 kW, and (3) growth times being varied between 10 – 74 hours. Thus, the pocket depth dimensions were varied from 1/3 to 1/2 of the width of the top of the pocket opening.

The following experimental variables were held fixed: (1) HPHT seed size, 3.7 mm x 3.7 mm x 1.4 mm, (2) total flow rate = 420 sccm, and (3) methane concentration = 5%. The substrate temperature was monitored after every thirty minutes during all experiments and was held approximately constant at 1020°C \pm 5°C during each experiment. During the process run the discharge pressure was 240 Torr, and the input microwave power recipe varied versus time over the process cycle run. Input power was varied from run to run between the range of 3.5 kW to 1.8 kW due to the varying pocket depths and the thicknesses, c , of the different substrate holders.

The thickness gain of the grown SCD substrate was measured by a Solartron DR600 linear encoder measurement with an accuracy of 0.01 mm. The average diamond thickness was determined by measuring at the four corners and at the center of each grown substrate and then these five measurements were averaged. A digital microscope KEYENCE VHX-5000 was used to capture the optical images of the top surfaces. Optical

images of the top surface were taken of each experimental run. The top surface area was then calculated from these images by drawing the outline of the irregular top surface and software VHX-500 determined the area based on the shape and the size of the top surface. The irregular shapes and the jagged edges of the top surfaces are taken into account by the VAX-500 software integration techniques. Variable pressure scanning electron microscopy (VP - SEM), a Zeiss EVO LS 25 was performed to analyze the surface morphology and the crystal shapes of the SCD grown substrates. The quality of the grown SCD substrates was also investigated by using birefringence imaging and SIMS analysis techniques.

5.2. The Single Crystal Diamond Growth Process

5.2.1 The SCD growth recipe: constant temperature deposition

The growth recipe required varying incident power (P_{inc}) as a function of the growth time to hold T_s constant throughout an entire growth process run. Thus, P_{inc} was adjusted during an individual CVD growth process run to compensate for the T_s variations. For a better understanding of the process cycle, an example of the variation of P_{inc} and T_s versus time as is shown in Figure 5.2, for a typical generic reactor. The first step is to place the HPHT diamond seed in the pocket holder. Next, the gases flow into the quartz bell jar chamber; the discharge is ignited and the initial operating condition is established at $T_s \approx 1020^\circ\text{C}$, $p = 240$ Torr at time $t = 0$.

If P_{inc} is held constant as the deposition time increases, then as is shown in Figure 5.2 T_s increases versus time from operating point A to point B. This occurs because, as diamond deposition proceeds, the CVD SCD volume increases, and the SCD grows

thicker up into the discharge. Other reactor characteristics also change over time, such as PCD deposition on the substrate holder, film deposition on the reactor walls, etc. These changes result in a varying reactor operating field map curve as a function of the growth time.

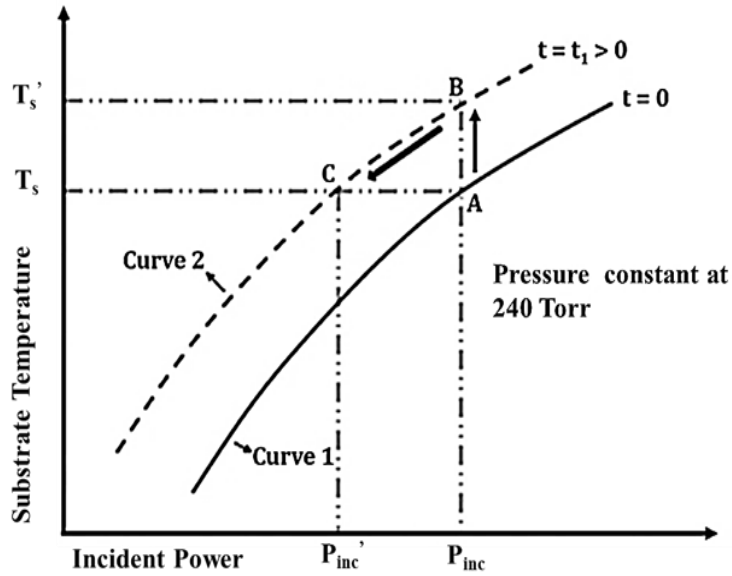


Figure 5. 2 Reactor operating field map

In order to achieve a constant T_s during the growth process, P_{inc} must be continuously decreased throughout the process cycle. Examples of such a variation of the P_{inc} as a function of the growth time is shown in Figure 5.3 (a) and (b). By continuously adjusting the P_{inc} (red curve in Figure 5.3 (a) and the blue curve in Figure 5.3 (b)) T_s is held approximately at $\sim 1020^\circ\text{C}$ throughout the entire process (black points in Figure 5.3(a) and (b)). Each pocket holder depth had different reactor deposition conditions. Therefore, an individual power versus time growth recipe had to be developed for each pocket holder depth. As a result, both the input power variation and the deposition cycle times are

different for each holder depth. However, the power variation versus time recipes have similar power versus graphical time shapes; i.e. the power variation versus time initially starts at a high initial value and then gradually decreases versus time until the process cycle is ended.

A typical experimental variation of power versus time recipe is as follows: the initial starting input power is 3000 W and with a corresponding measured discharge microwave power density of 494 W/cm³. As the process cycle develops versus time the input power is continuously reduced and the process ending input power is 2600 W with a corresponding microwave power density of 428 W/cm³. Thus, over the process cycle, both the input power and the discharge power density are reduced by a similar 13%.

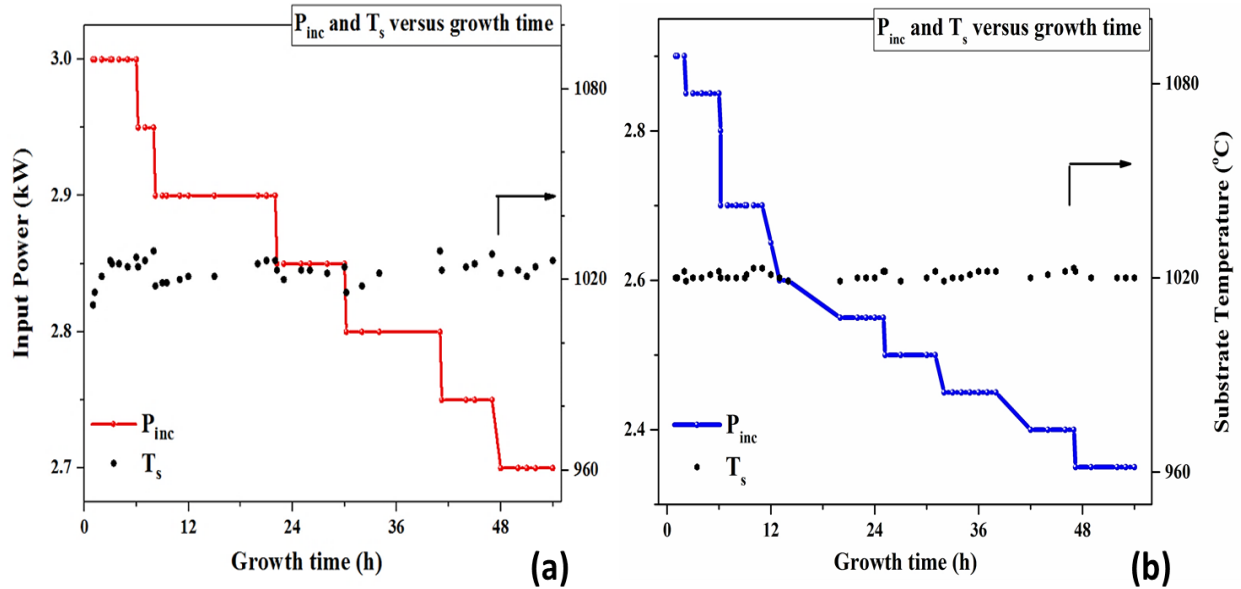


Figure 5. 3 Diamond growth recipe versus time for pocket depth of (a) $d_2 = 2.3$ mm and (b) $d_3 = 2.6$ mm.

5.2.2 Stopping the SCD growth process

An important step during the growth cycle is ending the process at the right time. The growth process cycle is ended when the diamond starts to grow out of the pocket. This prevents the growth of the PCD rim. An example of the top surface of the diamond crystal when growth is stopped before the top surface protrudes out the pocket is shown in Figure 5.4 (a). The smooth part in the center of the photo is the top surface of the grown diamond, and the rough surface surrounding the SCD, is the PCD which grows on the holder. In Figure 5.4 (b) the yellow rectangle represents the original HPHT cross-sectional area, and the blue shape represents the grown CVD diamond cross-sectional area. Figure 5.4 (c) displays optical microscope images from a single process cycle run of 60 hours (ACH02), with a thickness of 1.60 mm and growth rate of 26.5 $\mu\text{m/h}$. The diamond was grown using a pocket holder with a depth of $d_3 = 2.6$ mm and was stopped before the top surface grew out of the pocket. The top growth surface shows a circular surface morphology with a flat and smooth surface. This is displayed in Figure 5.4 (b). There is no evidence of PCD on the top surface or on the edges of the grown substrate.

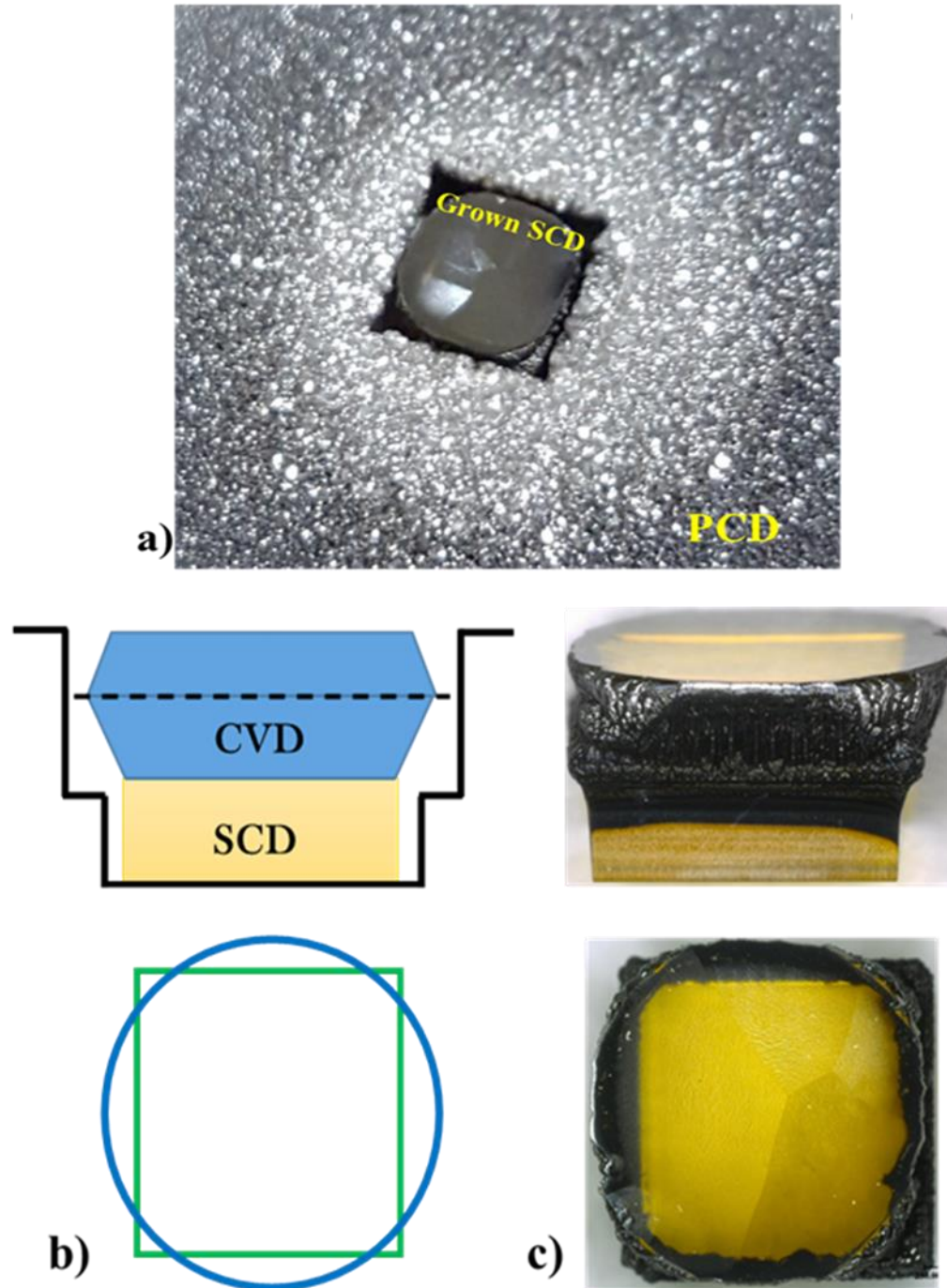


Figure 5. 4 (a) As-grown uncleaned SCD with the top surface is still entirely within the 2.6 mm deep pocket; (b) cross-sectional schematics when the grown diamond (in blue) is still within the pocket; (c) optical microscope images of side and top views of as-grown and

Figure 5.4 (cont'd)

cleaned diamond substrate (ACH02). Note that the bottom yellow region is the original HPHT diamond seed. The green square represents the original seed boundary.

In contrast, Figures 5.5 (a) and (c) displays optical microscope images for a process cycle of 48 hours (ACH22-b), with a thickness of 1.51 mm and growth rate of 31.5 $\mu\text{m/h}$. The diamond substrate was grown using a pocket holder with the depth of $d_2 = 2.3$ mm. Here the process was not stopped before the SCD protruded into the discharge. When that happens, the SCD top surface grows into the discharge, and a PCD rim is formed on the edges as shown in Figure 5.5 (b) and (c). Note in Figures 5.5 (a) the smooth part in the center of the photo is the top surface of the grown diamond with a PCD rim. The rough surface, surrounding the growing SCD, is the PCD which grew on the holder and into the top surface of the SCD. In Figure 5.5 (b) the dark blue area represents the PCD diamond grown on the SCD surface, the light blue represents the grown SCD material, and the yellow rectangle represents the HPHT diamond seed. These examples demonstrate the importance of stopping the experiments at the appropriate growth time.

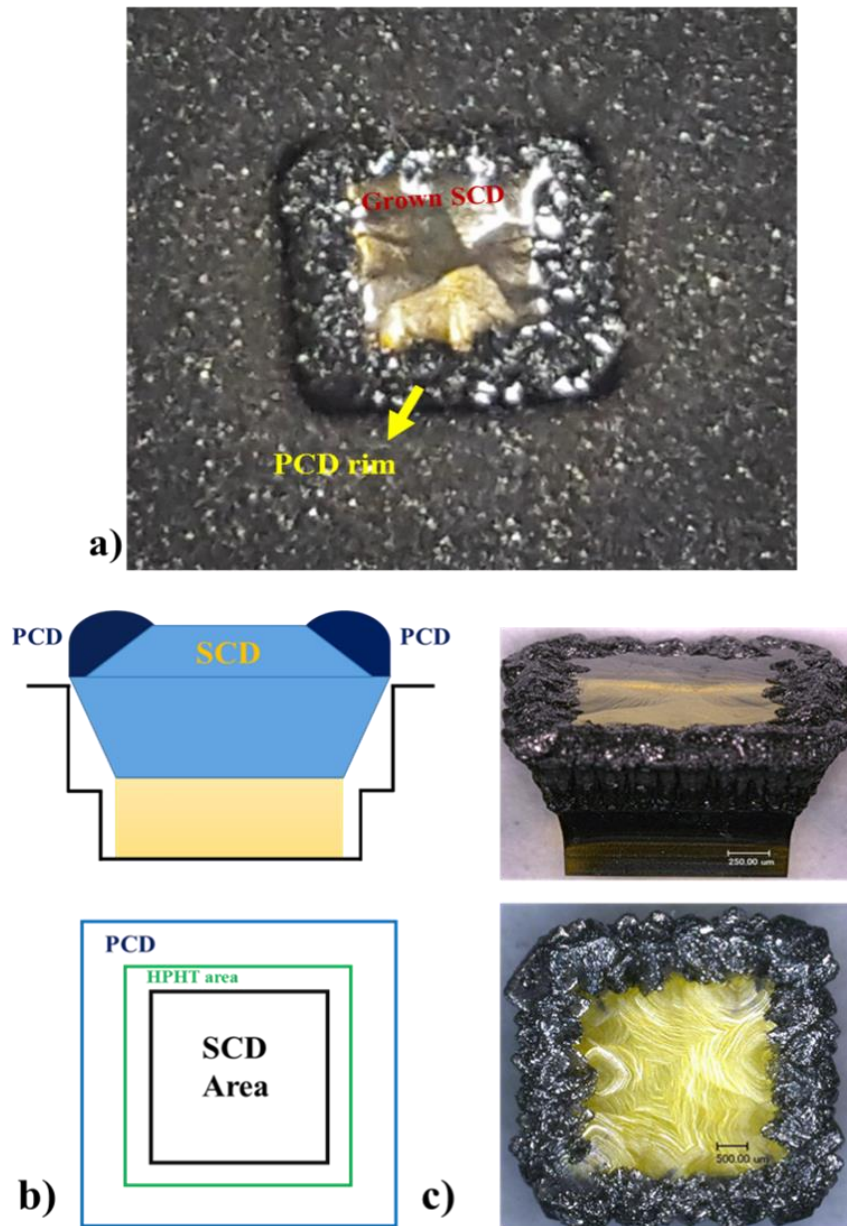


Figure 5. 5 The ACH22-b SCD which has grown out the pocket; **(b)** the associated cross-sectional schematic of the grown SCD when it has grown out of pocket; **(c)** optical microscope images of side and top view of a grown diamond substrate (ACH22-b).

5.2.4 Varying the input power and adjusting the reactor for the different pocket holder depth recipes.

The pocket depths, d_n , and the associated thicknesses, c , of the molybdenum holder design shown in Figure 5.1 (a) were varied from one pocket depth experiment to another. Additionally, in order to achieve a constant temperature growth recipe from process cycle to process cycle both of the input power and the holder thickness, c , were increased as d_n was increased. Thus for each particular d_n run the reactor had to be: (1) slightly readjusted to operate in the safe and efficient operating regime [141] and (2) slightly adjusted over a different input power range as d_n was varied. When using deeper pockets and thicker holders, operation at the higher input power ranges was required. All the different growth recipes for the different pocket depths looked similar versus time to the recipe shown in Figure 5.2. The major difference between the recipes was that the deeper pockets required higher input powers over the entire process cycle. For example, the beginning input powers for the 2.0 mm and 2.9 mm pocket depths were 2.3 kW, and 3.5 kW respectively. As the process cycle evolved versus time for all of the pockets, the input power decreased with time and a similar way, but the deeper pockets had higher power levels over the entire process cycle recipe.

5.3. Experimental Results

5.3.1 SCD Growth versus time

Two groups of exploratory experiments were performed to improve the understanding of the SCD growth process and to identify the right time to stop the process. These exploratory experiments were conducted using two typical diamond pocket depths: $d_2 =$

2.3 mm and $d_3 = 2.6$ mm. The process cycle times depended on the size of the pocket depths. For d_2 , the cycles times were 10, 24, and 48 hours; while for d_3 the cycle times were: 10, 24, 48, and 60 hours. Table 1 summarizes the different growth parameters and output variables for the process run identified as the three ACH22 cycle runs and another four ACH21/ACH02 process cycle runs. All seven experiments represented individual experimental runs that were started from a new seed. T_s was kept constant at 1020°C throughout each individual process cycle run. A T_s measurement was recorded and the power input was adjusted every thirty minutes. The growth rates that are summarized in Table 5.1 are the thickness gain divided by the growth time. Thus, this growth rate is an average growth rate over the entire process cycle time. The instantaneous growth rate may vary from this average rate during the process cycle.

Table 5. 1 Growth parameters for SCD growth using the $d_2 = 2.3$ mm and $d_3 = 2.6$ mm pocket holder depths.

Pocket depth	Sample	Process cycle (h)	Thickness gain (mm)	Average growth rate ($\mu\text{m/h}$)	Area (mm^2)	Normalized area
$d_2 = 2.3\text{mm}$	ACH22	10	0.274	27.3	16.7	1.22
	ACH22-a	24	0.717	30.0	20.95	1.53
	ACH22-b	48	1.520	31.5	21.7	(2.36)**; (0.87)*
$d_3 = 2.6\text{mm}$	ACH21	10	0.289	28.9	16.8	1.22
	ACH21-a	24	0.705	29.4	16.6	1.21
	ACH21-b	48	1.464	30.5	18.6	1.35
	ACH02	60	1.600	26.5	13.2	0.97

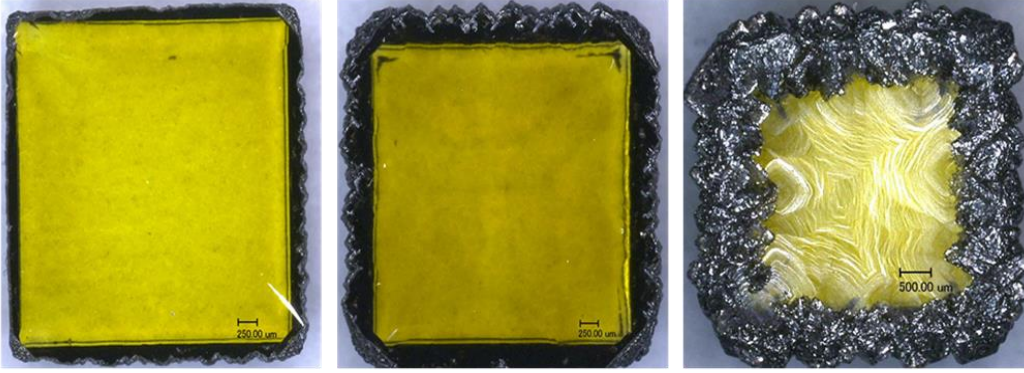
*Useful SCD surface: **Includes the PCD rim

Figures 5.6 (a) – (g) display images of the top surface areas of the substrates that are listed in Table 1. All the grown substrates display a smooth and flat top surface without any defects or PCD except for the sample ACH22-b, which is smooth and flat in the center, but, as is shown in Figure 5.6 (c), the top surface is surrounded by an outer PCD rim. The as grown surfaces are very flat. The corners do not differ more than $\pm 2 \mu\text{m}$ when compared with the center thickness. As discussed previously in section 3.2, sample ACH22-b grew out of the pocket and into the plasma for approximately the last 10 hours of its process cycle leading to the formation of PCD.

The data in Table 5.1 and Figures 5.6 (a) and (d) demonstrate that after the 10 hours of the deposition process, even though two different pocket depths were used; the resulting CVD grown diamonds surfaces were very similar at this early time in the growth cycle. The top surface areas of both samples were the same, 16.7 mm^2 with d_2 and 16.8 mm^2 with d_3 .

After 24 hours, the top surface area and the average growth rate decreased slightly as the pocket depth increased. From Table 5.1 it can be seen that the deeper pocket appears to have a somewhat reduced average thickness growth and also restricts the outward growth (see for example – ACH21-a versus ACH22-a). Subsequently, samples ACH21-b and ACH22-b which were grown for 48 hours, displayed dramatically different output growth results and morphologies. These differences were not surprising since ACH22-b, which was grown in a 2.3 mm depth pocket, was protruding from the pocket at the end of its cycle and ACH21-b was still inside the pocket when the process was stopped. At the end of its cycle, ACH22-b had a PCD rim as is shown in Figures 5.5 and 5.6 (c).

$d_2 = 2.3 \text{ mm}$

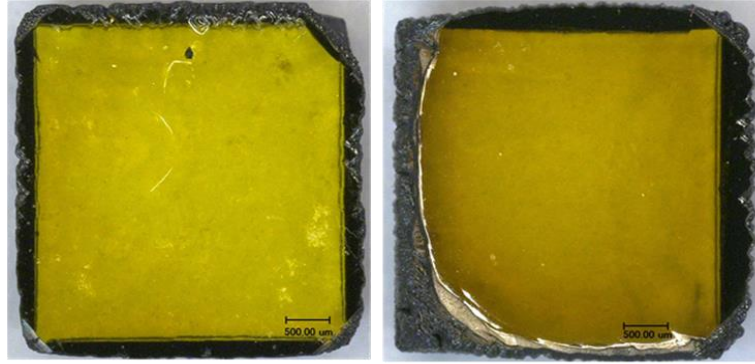


(a) ACH22

(b) ACH22-a

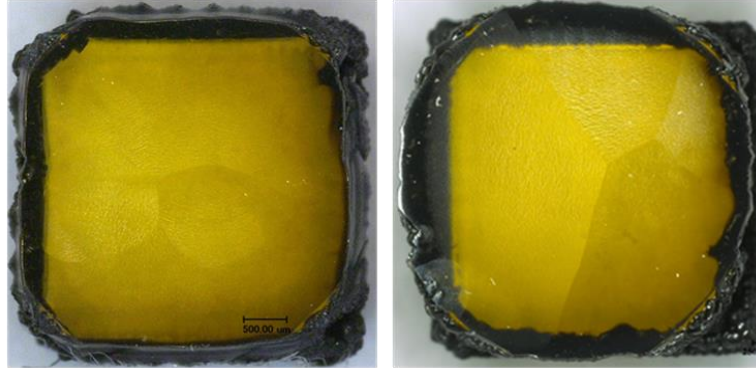
(c) ACH22-b

$d_3 = 2.6 \text{ mm}$



(d) ACH21

(e) ACH21-a



(f) ACH21-b

(g) ACH02

Figure 5. 6 Optical microscope top surface images of substrates samples listed in Table 1. For $d_2 = 2.3 \text{ mm}$ (a) 10 hours, (b) 24 hours, and (c) 48 hours. For $d_3 = 2.6 \text{ mm}$ (d) 10 hours, (e) 24 hours, (f) 48 hours and (g) 60 hours.

The top surface of ACH22-b protruded out of the pocket during the last approximately 10 hours of the process cycle. Once the top surface grew out of the pocket, the top surface was directly exposed to the intense plasma discharge, and the electromagnetic fields are concentrated on the edges of the diamond, and the deposition process accelerates and appears similar to that which shown in Figure 5.5. Consequently, the substrate temperature is non-uniform, and this results in the growth of a PCD rim. This PCD rim is responsible for the increased top surface area of 21.7 mm² for ACH22-b as indicated in Table 1. The thick PCD rim also had grown inward and upwards on the SCD surface. Hence, the useful SCD surface area decreased. In this case, the top useful single crystal surface area decreased to 0.87 times of the initial original HPHT diamond seed area (see Figures 5.5 (b) and 5.5 (c)).

At the end of the process cycle, ACH22-b measured a thickness gain of 1.520 mm and an average thickness growth rate of 31.5µm/h. This run can be compared to the similar ACH21-b run displayed in Figure 5.6 (f). The difference between these two runs is that ACH21-b run was ended before it protruded from the 2.6 mm depth pocket and as a result, it displays no PCD rim. Sample ACH21-b has a thickness gain of 1.464 mm and an average growth rate of 30.5 µm/h. Its top surface remained below the final holder surface. The ACH02 experiment lasted 60 hours. When the run was completed, the top surface of the SCD was just starting to protrude out of the pocket. Figure 5.6 (g) shows that the top surface is smooth, flat, and without any visual defects and is not surrounded by a PCD rim. Its shape is circular and the normalized surface area is 0.97, which is just slightly smaller than the original square HPHT diamond seed area.

5.3.2 SCD growth versus pocket holder depth

The results from eleven different growth versus depth experiments are summarized in Table 2 and in Figures 5.7 – 5.9. The experiments were performed using constant T_s deposition recipes, i.e. $1020 \pm 5^\circ\text{C}$, similar to the one shown in Figure 5.3. The growth time was varied from 40 hours to 74 hours for each run. The length of the process cycle was experimentally determined, by visually observing the location of the top surface and then stopping the process before the SCD protruded into the discharge as discussed in section 5.2.2. The experiments that were not stopped on time developed a PCD rim, similar to ACH22-b. Those experiments were not included in the table because they were grown out of the desirable growth recipe conditions. The average growth rates listed in Tables 5.1 and 5.2 are plotted versus pocket depth in Figure 5.8. As indicated in Figure 5.8 the growth rate is a maximum for the shallow pockets and decreases as the pocket depth increases.

Figures 5.7 (a) – (d). Although Figure 5.7 just shows four of the eleven samples, all the other samples listed in Table 5.2 displayed a smooth top surface without a PCD rim around the edges of the top surfaces. It was also observed that the grown diamond in pocket holder depths of 2.0 mm and 2.3 mm exhibited jagged edges and a square top surface. These samples grew outward and upward as a function of the time at an average growth rate of approximately $30 \mu\text{m/h}$. As a result, expanded areas as large as 26.5 mm^2 were obtained. For these pockets, the total area increased to almost twice, i.e. 1.6 – 1.94 times, of the original HPHT diamond seed area.

Table 5. 2 Summary of different growth versus depth experiments for eleven samples at a substrate temperature of $1020 \pm 5^{\circ}\text{C}$.

Pocket depth	Sample	Pocket depth (mm)	Process cycle (h)	Thickness gain (mm)	Average growth rate ($\mu\text{m/h}$)	Normalized area
$d_1 = 2.0$ mm	ACH31	2.0	40	1.20	30.0	1.94
	ACH44	2.0	40	1.17	29.5	1.61
$d_2 = 2.3$ mm	ACH26	2.3	42	1.22	29.1	1.78
$d_3 = 2.6$ mm	ACH09	2.6	50	1.40	28.0	1.40
	ACH21-b	2.6	48	1.46	29.8	1.32
	ACH27	2.6	50	1.43	28.6	1.33
	ACH08	2.6	55	1.49	27.1	1.35
	ACH02	2.6	60	1.60	26.5	0.96
	ACH11	2.6	74	1.93	26.1	0.57
$d_4 = 2.9$ mm	ACH35	2.9	45	1.06	23.5	1.10
	ACH47	2.9	50	1.38	27.3	0.85

Optical microscope images of selected samples from Table 5.2 are displayed in

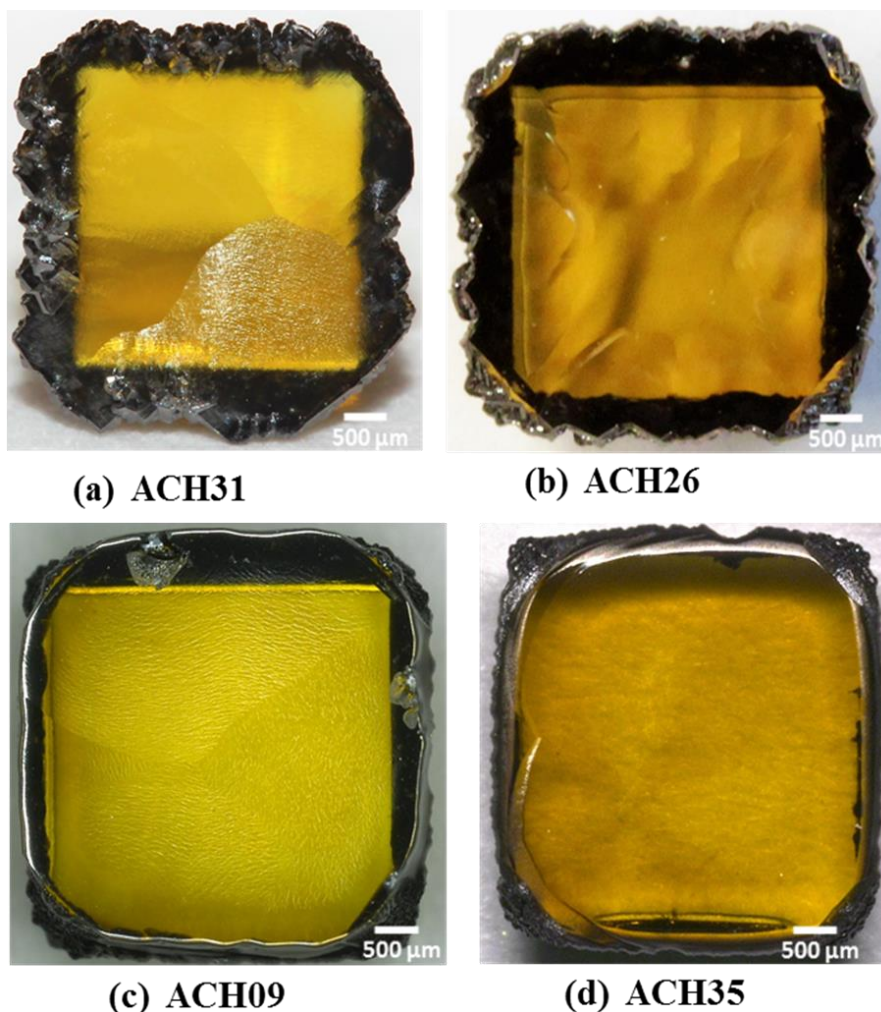


Figure 5. 7 Optical microscope images of the typical samples shown in Table 2 that were grown in pocket depths of (a) 2.0 mm, (b) 2.3 mm, (c) 2.6 mm and (d) 2.9 mm.

The samples grown in pocket depths of 2.6 mm and 2.9 mm exhibited smooth edges rather than the jagged edges that were observed in the shallower pockets. The measured average growth rates were 23 – 30 $\mu\text{m}/\text{h}$ (see Figure 5.8). However, the final resulting shapes were octagonal and circular and the final surface area gain varied from 1.5 times to less than the original seed area; i.e. the deeper the pocket, the smaller the final surface

area. One sample, ACH11, exhibited a decreased area gain of 0.57 from the original seed area after 74 hours of growth. It was found that longer process cycles and deeper pocket depths had smaller area gains.

The shape of the top surface varied as the crystal thickness increased. The final crystal shape was a function of growth time and pocket depth. This can be more clearly understood by referring to the data presented in Table 5.1 and Figure 5.6. As is shown in Figures 5.6 (d) and (e) after 10 and 24 hours respectively of the process cycle, the diamond was grown uniformly on the entire surface, and the top area was almost square shaped. However, after continuing the growth versus time beyond 24 hours the surface area decreased and changed from square shaped to the octagon shape and even for a longer run, ACH02, into a circular shape. This is indicated in the data presented Figures 5.6 (d) – (g) and in Table 5.1, and pictorially by the red line shapes surrounding the images of the SCD top surfaces in Figure 5.8.

When using the 2.3 mm pocket the growth rate increases with time. For example, see the data points in Table 1 for 2.3 mm pocket depth. The lower average growth rates are from, the shorter growth times, and the average growth rate gradually increases as the time increased. This suggests that the instantaneous growth rates slightly increase as the diamond grows thicker and the top surface approaches the pocket opening.

The data for the 2.6 mm pocket still depends on time but in a different way than 2.3 mm pocket depth. When the growth times vary between 48 to 55 hours the average growth rates vary over the narrow range of 27 – 30 $\mu\text{m/hr}$ and the final top surface shapes are an octagon. However, if the growth time is much larger, i.e. 60 – 74 hours the growth seems to decrease with time and the final shape changes to a circle.

This is illustrated by the two data points: (1) ACH02 grown for 60 hours and (2) ACH11 which was grown for 74 hours. In these longer runs, the average growth rate decreases and the final top surface changes from an octagon to a circle and the surface area are smaller than the original seed. During these two longer runs the diamond grows out of the original molybdenum pocket but is still in an “effective extended new pocket” that is created by the additional deposited PCD on the holder. This extended pocket phenomenon as already mentioned in reference [20]. As the growth proceeds, the average deposition rate decreases and the shape of the top surface becomes a circle, but there is no PCD rim formed.

For a better understanding of how the pocket depth influences growth, the results in Table 5.2 were summarized in Figure 5.9. It is a plot of the lateral growth rate (V_{110}) and the vertical growth rate (V_{100}). It displays the growth rate ratio between the outward surface, represented by V_{110} and upward surface, represented by V_{100} . The ratio between both rates was calculated with the help of scanning electron microscope (SEM) images.

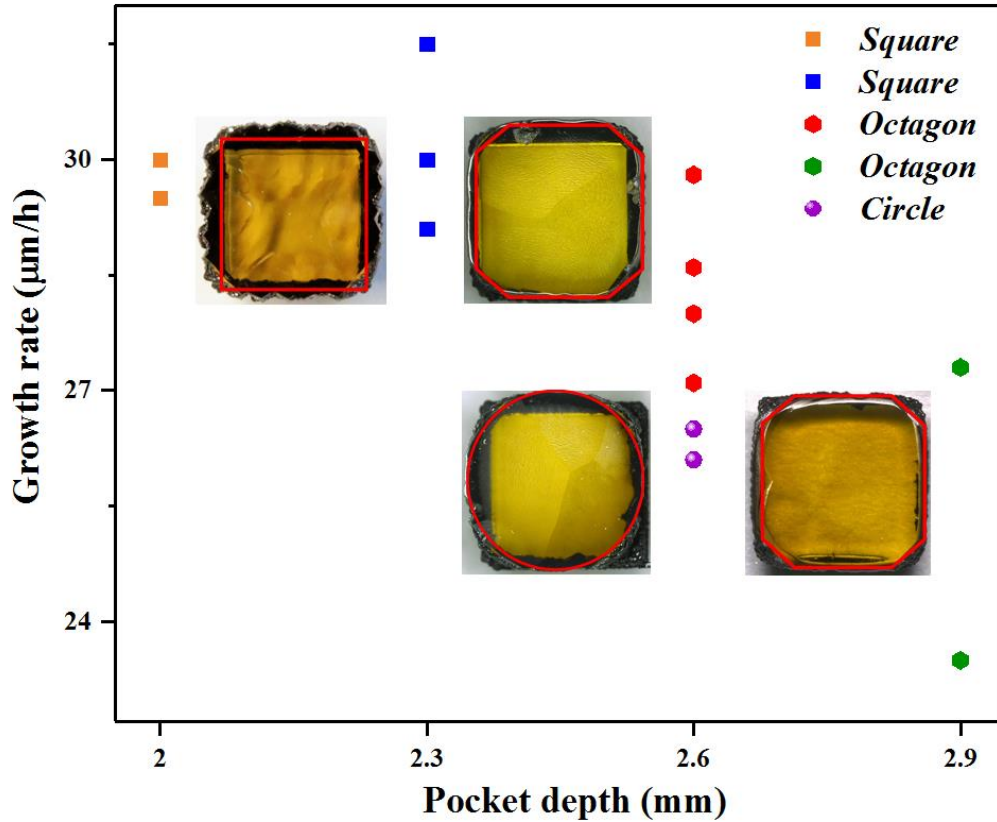


Figure 5. 8 Morphology shapes and the growth rate versus pocket holder depth for experimental data for Table 5.1 and Table 5.2. The square surface is associated with pocket depths of 2.0 and 2.3 mm. The circular surface is associated with long runs of the pocket depth of 2.6 mm, and the octagon shape surface is associated with the shorter runs that used the pocket depths of 2.6 and 2.9 mm.

Images of the corner of each substrate reveal the crystal shapes and allow the monitoring of the diamond outward growth. The SEM images show that substrates that were grown in pockets depths of d_1 and d_2 lead to a fast and a uniform growth of the entire surface with the resulting final square area. For example, a fast-outward growth was observed for sample ACH31 that grew in the shallow pocket ($d_1 = 2$ mm). In contrast,

sample ACH35 which grew in a deeper pocket ($d_4 = 2.9$ mm) showed a very slow outward growth as compared to the growth in the vertical direction.

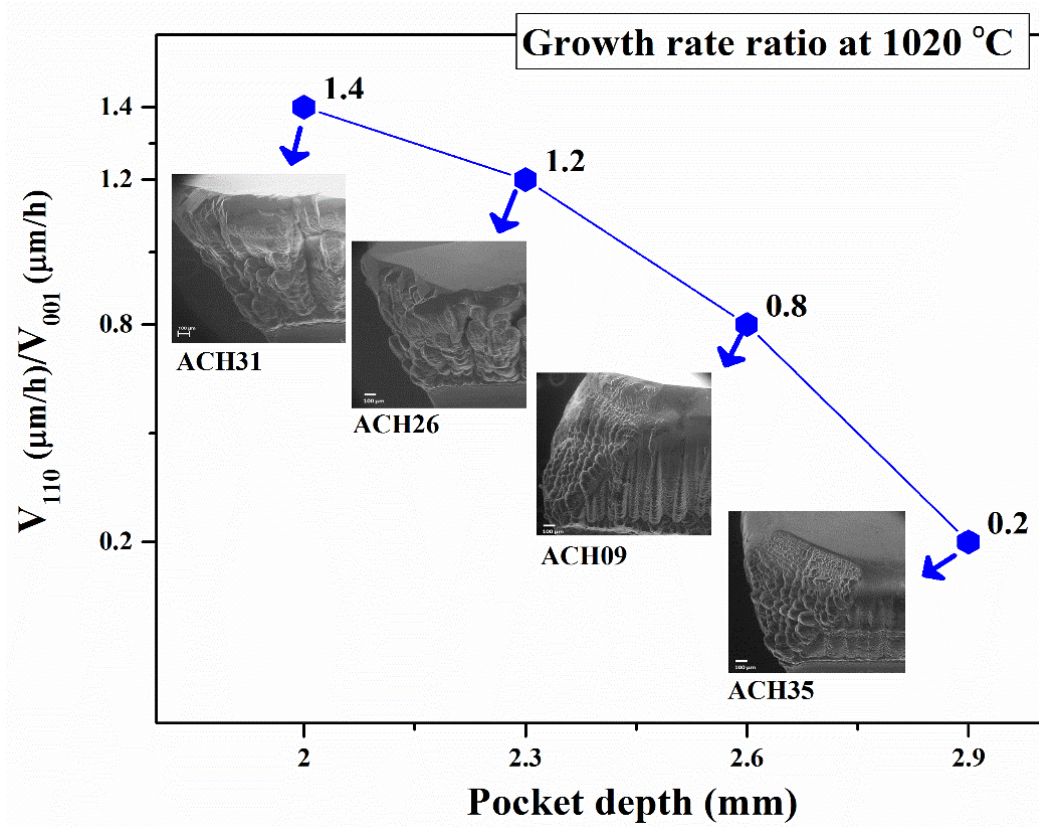


Figure 5. 9 The ratio between lateral growth rate, V_{110} , and vertically growth rate, V_{100} , versus pocket depth. Insets are SEM images of the corners of the SCD substrates.

Figure 5.10 displays a plot of the normalized lateral area gain versus the vertical thickness gain for the data listed in Table 5.2. The vertical axes, (normalized lateral area gain) is the final CVD lateral area gain, i.e. the final CVD lateral area divided by the initial HPHT seed area (3.7×3.7 mm²). The dashed horizontal line represents the original normalized HPHT seed surface area. For the case considered in this investigation, the

seed surface area is 13.7 mm^2 . In Figure 5.10, this area has been normalized with respect to the seed area of 13.7 mm^2 .

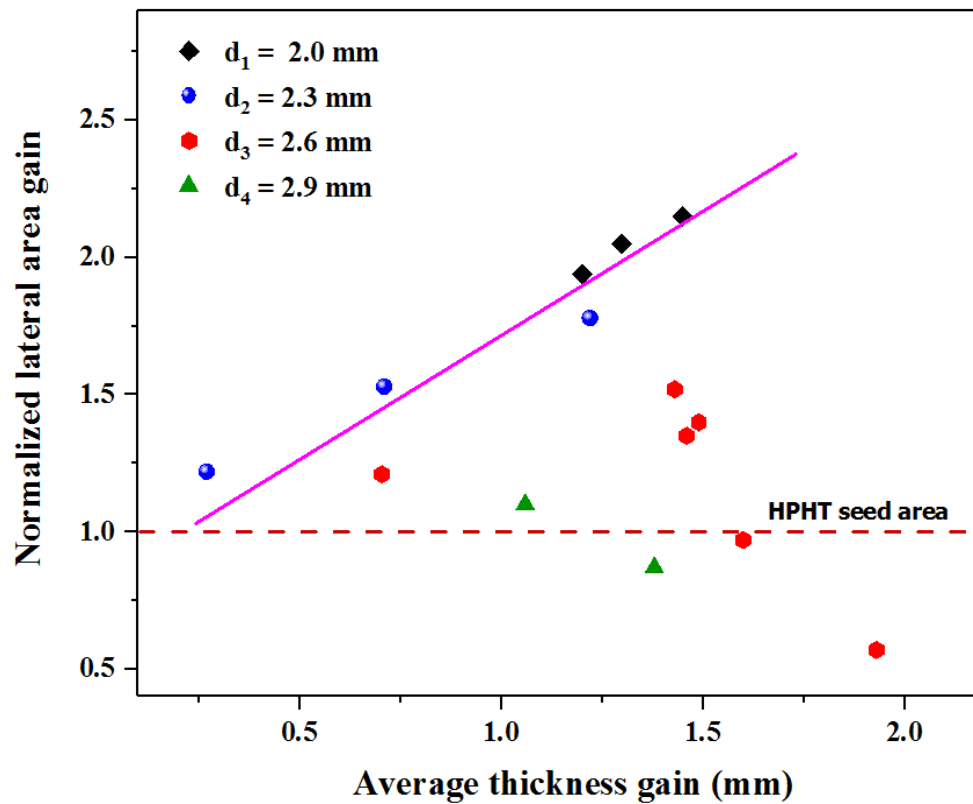


Figure 5. 10 Plot summarizing the normalized lateral CVD area gain versus vertical thickness gain for different pocket depths for the experimental data listed in Tables 5.1 and 5.2.

The purple line in Figure 5.10 is the “best fit” curve that was drawn in reference [20] between experimental data points. It indicates the behavior of the lateral area gain versus thickness gain data points that were presented in [20]. It is reproduced in Figure 5.10 as

a reference curve for comparison with the experimental data that is presented in Tables 5.1 and 5.2.

In Figure 5.10 the experimental data points from Table 5.2 are grouped by pocket depth. It can be readily observed that the shallow pockets have a larger area gain than the deeper pockets. d_1 and d_2 pockets yield the largest normalized area gain. These two pocket holders can grow SCD with area gains of 1.6 – 1.95 before their top surfaces protrude out of the pocket. The deeper pockets, i.e. d_3 and d_4 have top surfaces that are smaller than the purple benchmark curve. The deeper pockets and the longer runs end up with the smallest process ending surfaces. The long duration runs resulted in a smaller or no lateral area gain. See for example ACH11 and ACH47. Their top surfaces are smaller than the original seed. The experimental data for the 2.6 mm pocket clearly indicates that the thicker crystals produce a smaller top surface. The data indicate that under the initial constraints of this investigation there is an optimum pocket depth for an area gain. That occurs for the shallow pockets; i.e. for $d = 2.0$ mm – 2.3 mm.

5.4 SCD Plate Characterizations

5.4.1 Overview

In order to characterize the grown substrates, freestanding, SCD plates were obtained by laser cutting perpendicular to the growth direction to remove the HPHT seeds from the CVD grown substrates. Then the plates were mechanically polished on both sides to reduce roughness. Examples of these freestanding plates are shown in Figure 5.11. Note that the edges of the plate ACH33 were also laser trimmed and polished. CVD diamond grown in the reactor C has been characterized by Raman spectroscopy and IR-UV

transmission measurements, and the results have been reported elsewhere [16], [18]. The Raman FWHM were as low as $\sim 1.75 - 1.8 \text{ cm}^{-1}$ and the transmission measurements showed that the SCD grown with reactor C was of similar quality to type IIa diamond. Summarized below are typical birefringence and SIMS measurements performed on diamond plates obtained from the ACH20 and ACH33 experiments.

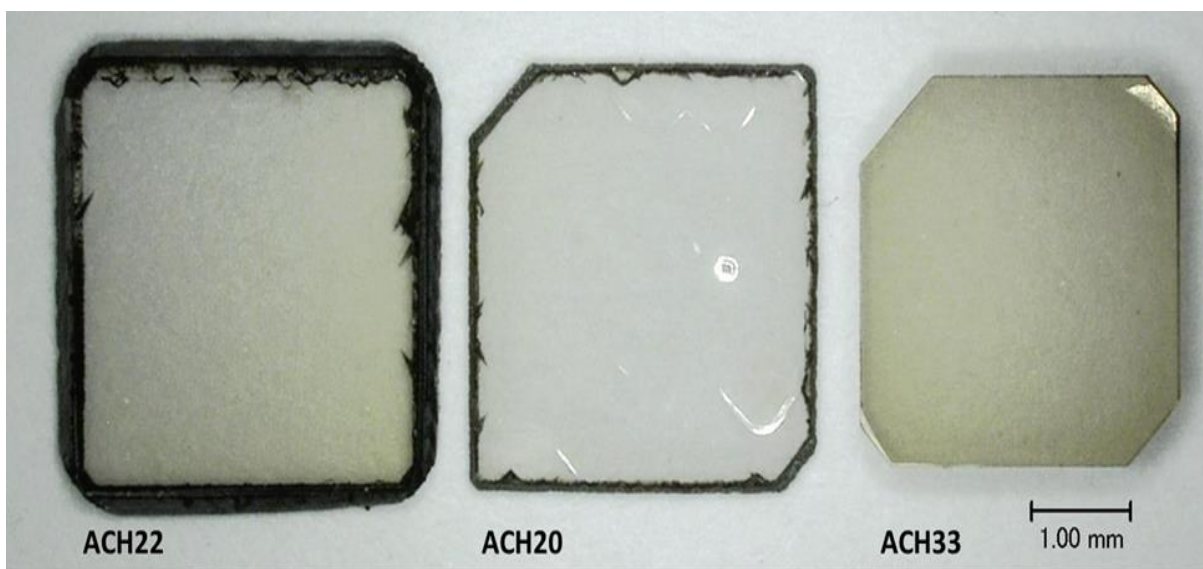


Figure 5. 11 CVD plates after laser cutting and mechanical polishing. The measured thickness gain for each sample was: $274 \mu\text{m}$ for ACH22, $255 \mu\text{m}$ for ACH20 and $600 \mu\text{m}$ for ACH33.

5.4.2 Birefringence imaging

Birefringence imaging was performed to obtain information about the distributions of internal stress and dislocations throughout the crystal lattice. The images of the CVD

plates were taken with a Nikon ME600 optical microscope and with an external polarizer and analyzer. The birefringence images were taken at 5000 ms exposure time. Figures 5.12 (a) and (b) show two examples of the as – grown SCDs along with the birefringence image of their associated, freestanding diamond plate.

The first SCD CVD sample, ACH20, is shown in Figure 5.12 (a) along with the birefringence image of its freestanding plate. ACH20 was grown for 10 hours in a pocket holder $d_2 = 2.3$ mm. The measured thickness gain was 255 μm with a growth rate of 28 $\mu\text{m/h}$. The birefringence image is dark indicating low stress in the crystal structure. This can be observed especially in the center of the plate. However, the three edges show some bright spots indicating some stress. This stress is probably related to the jagged edges that were observed (See Figures 5.6 (a) and 6 (b)) in the CVD growth results of the d_3 pocket.

The second SCD CVD sample ACH33 grown for 24 hours with a measured thickness gain of 600 μm thick with a growth rate of 27 $\mu\text{m/h}$ in a holder depth of d_3 . See Figure 5.12 (b). Similar to the ACH20 birefringence, the birefringence ACH33 image displays a dark low-stress interior with the exception of two butterfly-shaped patterns. The edges show three bright spots indicating some small points of stress at the edge of the sample. The two butterfly shaped patterns seen in the birefringence image of ACH33 are typical of threading dislocations which are defects in the lattice structure and are observed along the (100) growth direction ([156], [157]). The two butterfly patterns also coincide with the 2 globular shaped defects on the surface of the as-grown ACH33 substrate (Figure 5.12 (b)). These are most likely due to bundles of dislocations originating from the underlying seed or originate from the surface of the seed. This is not a typical result. The diamond

plates that are more commonly grown appear similar to that shown in Figure 5.12 (a). However, Figure 5.12 (b) is displayed here to illustrate what can occur when the original seed or the initial seed deposition surface had some imperfections.

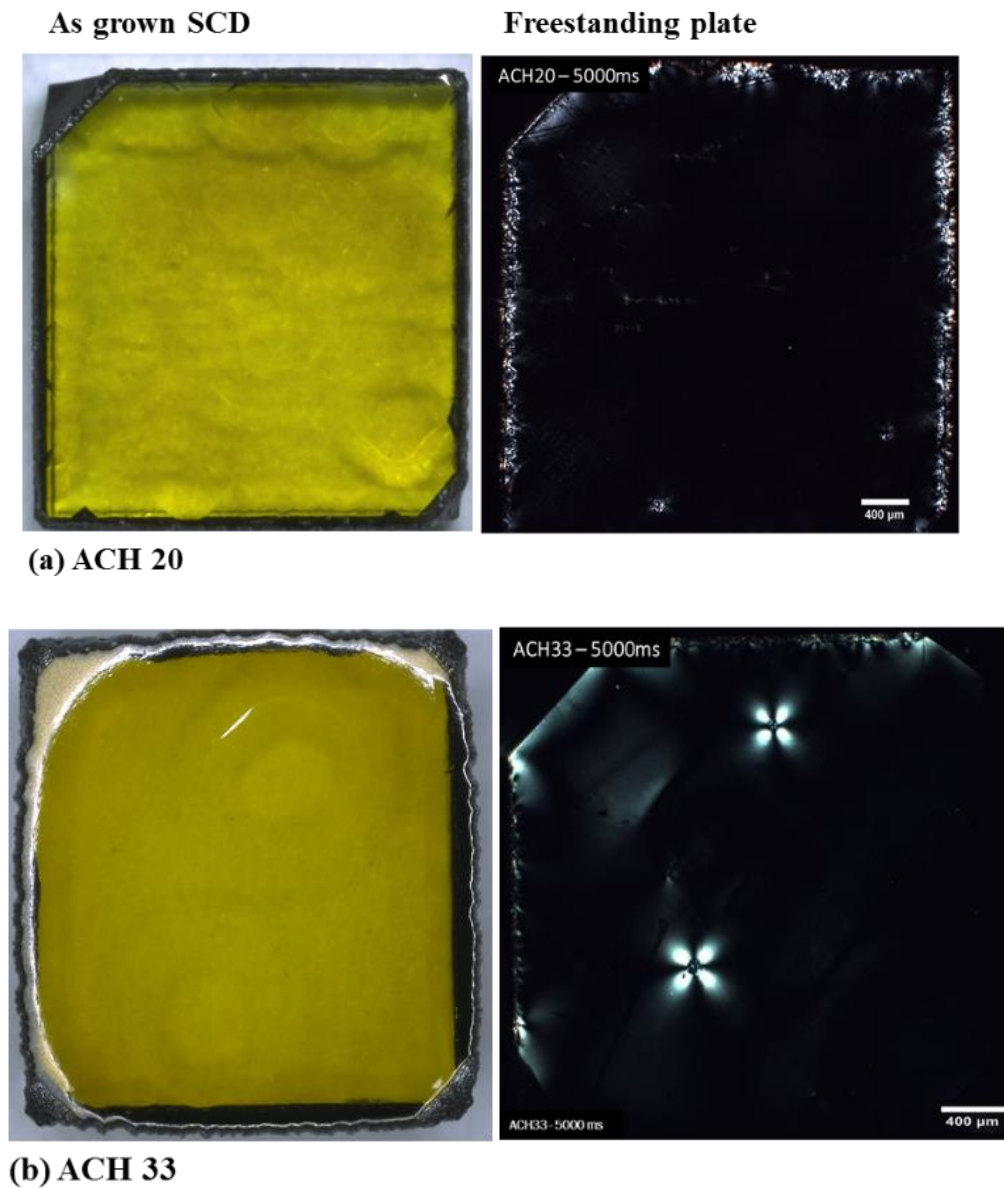


Figure 5. 12 Examples of two as-grown SCD with their corresponding birefringence images. (a) ACH20 and (b) ACH33.

5.4.3 Etch pits analysis

Etch pits analysis was performed on the surface of a free-standing CVD plates, ACH09, ACH20, and ACH33 using hydrogen plasma etching. The substrates were etched at 240 Torr for 1 hour with a pure hydrogen discharge. The substrate temperature was measured at $\approx 1000^{\circ}\text{C}$ at a constant microwave power of 2.5 kW. The average etch rate was between 2 - 5 $\mu\text{m/h}$. The etch pits densities were calculated with MATLAB images processing presented in Chapter 3, section 3.8.5.

Figure 5.13 (a) shows an optical microscope image of the polished and trimmed ACH33 plate, and an enlargement selected area on the surface (marked in a black circle). A large number of etch pits are concentrated around the polishing grooves on the surface. The recorded etch pit density of such plate was $\sim 1.3 \times 10^3 \text{ cm}^{-2}$, and the etch rate was $\approx 2.1 \mu\text{m/h}$. As shown in the images, the pits were either not present around the middle of the plate or they were minimal or were present at low density. The birefringence image for this plate exhibited low stress, especially in the center. Even though these results were anticipated, it was also expected to observe pits around the two butterfly patterns revealed for birefringence image (Figure 5.12 (a)). However, etch pits were not present. The result suggests the need of a more aggressive etching were the temperature and the process time are increased. Figure 5.13 (b) displayed optical microscope images of the CVD plate, ACH20, on which the top surface remained unpolished. After 1 hour of plasma hydrogen exposure, $\approx 1.8 \mu\text{m}$ on the uneven grown surface was etched. Random concentrations of pits were observed along the longitudinal direction, i.e. (010) direction, as indicated in the enlarged image of the selected area in Figure 5.13 (b). These pits

distribution could be attributed to dislocations that arise from the HPHT seed. The average etch pit density was calculated to be $\approx 3.8 \times 10^4 \text{ cm}^{-2}$.

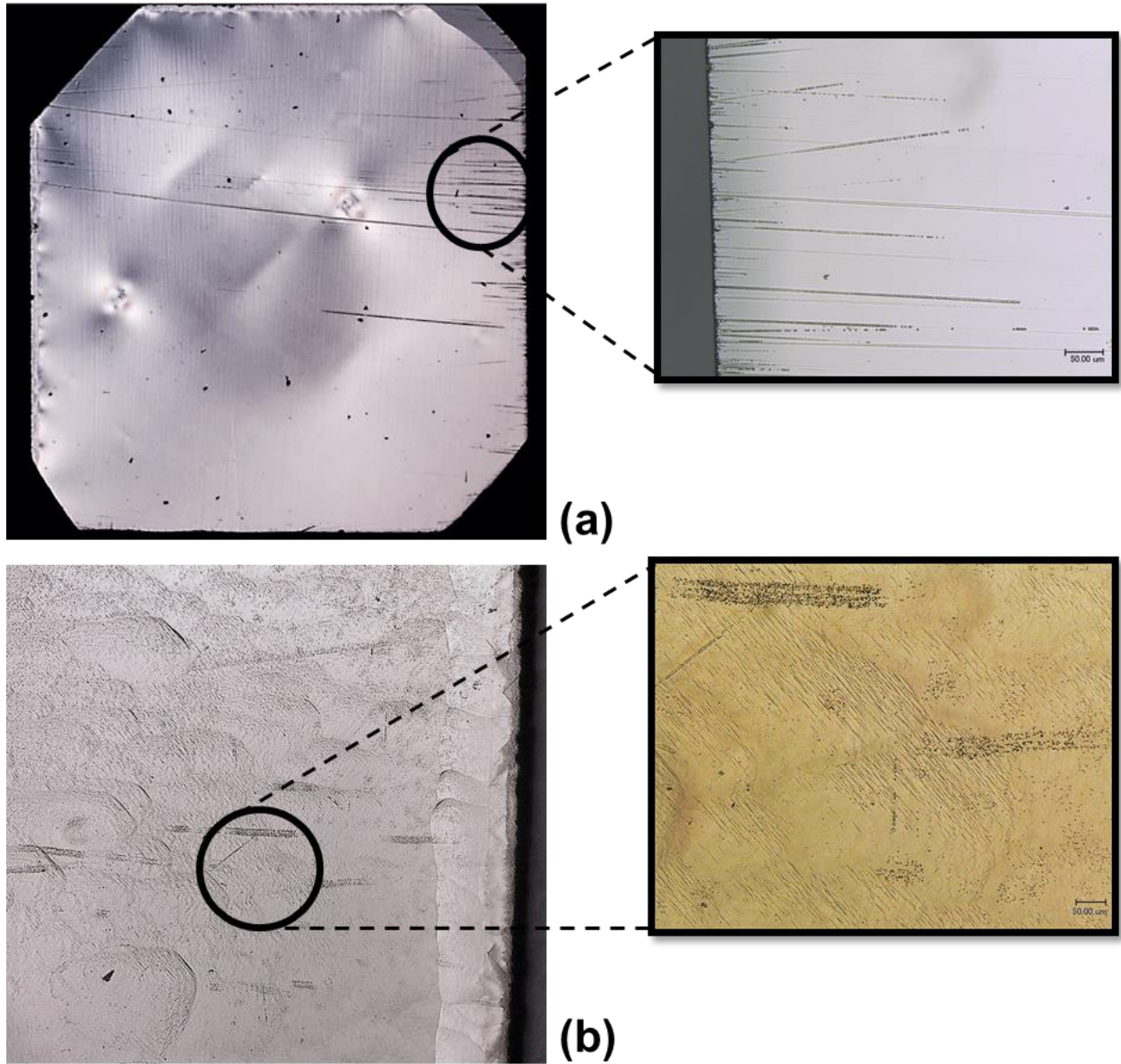


Figure 5. 13 (a) Etched surface of the polished CVD plate ACH33 and (b) Etched surface of a unpolished CVD plate ACH20.

The shape and dimensions of the pits were analyzed and calculated with SEM images. Figure 5.14 shows SEM images of the etched diamond area on the unpolished CVD plate ACH09. The etch pit density was calculated to be $\approx 1 \times 10^4 \text{ cm}^{-2}$, and the etch rate was $\approx 5.3 \text{ }\mu\text{m}$. Cross-sectional profiles along the lines crossing the center of the pits are shown in Figure 5.14 (a) and (b). These images show hollow pits symmetrically aligned with the (110) growth direction. The depth of the pits was measured and varied between $1.8 \text{ }\mu\text{m}$ – $2.2 \text{ }\mu\text{m}$. The width was measured between $2.5 \text{ }\mu\text{m}$ – $9.5 \text{ }\mu\text{m}$, as shown in Figure 5.14 (c).

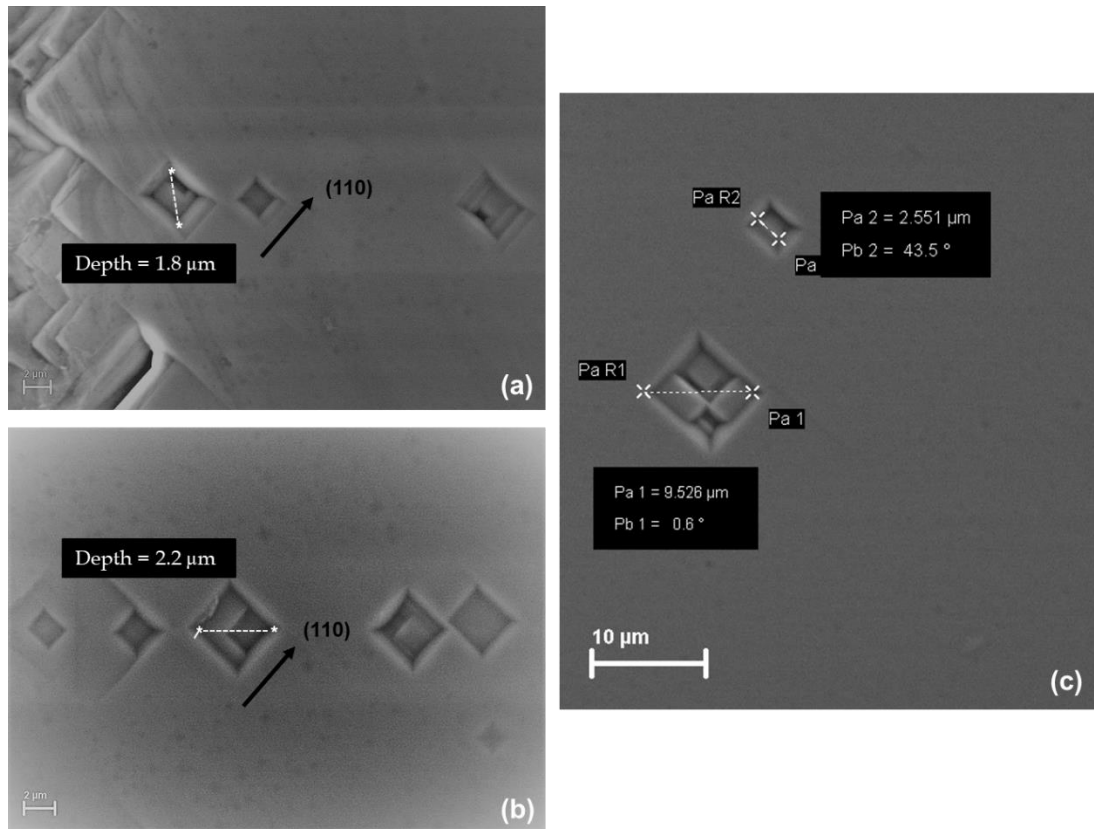


Figure 5. 14 SEM images of the pits in three different areas on CVD plate ACH09 (a) one side at the edge, (b) somewhere at the center (c) somewhere on the center of the top surface.

The results of the etch pits densities were compared with some recent results reported from 2016. See Figure 5.16.

All the plates etch pits densities calculated have significant low values in comparison with the HPHT seed, even in comparison with previously reported results [142], [124]. The polished plate (ACH33) showed the lowest defect density on the surface. However, an aggressive etch is recommended. These results still seem high as compared with the most recent results reported by Tallaire et al. [122] in which the etch pits density was \approx

$2 \times 10^3 \text{ cm}^{-2}$. Nevertheless, their investigation used a different growth approach. See Chapter 2, section 2.6.3. Despite the tremendous improvement size and quality of the CVD diamond substrates, the objective of low dislocation density material is still unachieved.

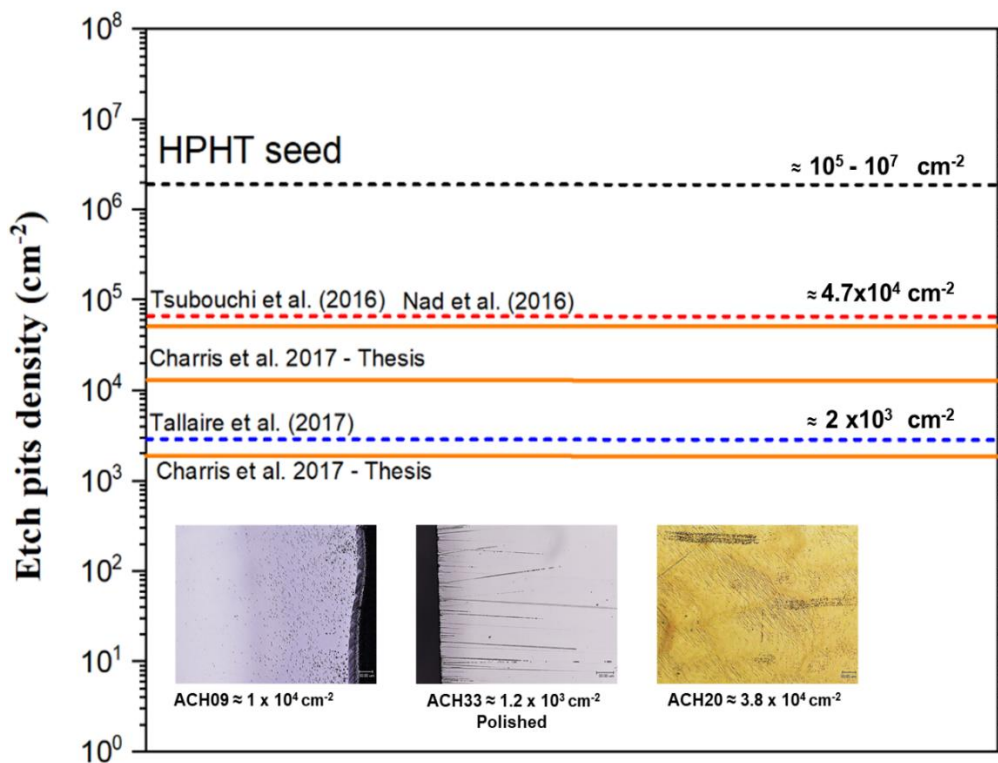


Figure 5. 15 Comparison of the etch pit density with recent results.

5.4.4 Secondary ion mass spectroscopy (SIMS)

SIMS measurements were performed in order to verify the nitrogen concentration in the grown CVD plates. SIMS was carried out by Evans Analytical Group (EAG). Figure 5.13 shows the depth profile of nitrogen concentration in SCD CVD plates ACH33 and

ACH20. The red line shown in the two figures indicates the detection limit (2×10^{15} atoms/cm³) of the instrument provided by EAG. As shown in the Figure 5.13 the nitrogen concentration is constant until at least 13 μm depth into the bulk of the CVD sample. The nitrogen concentrations in the CVD plate ACH33 is approximately 50 ppb, and for ACH20 it was 140 ppb.

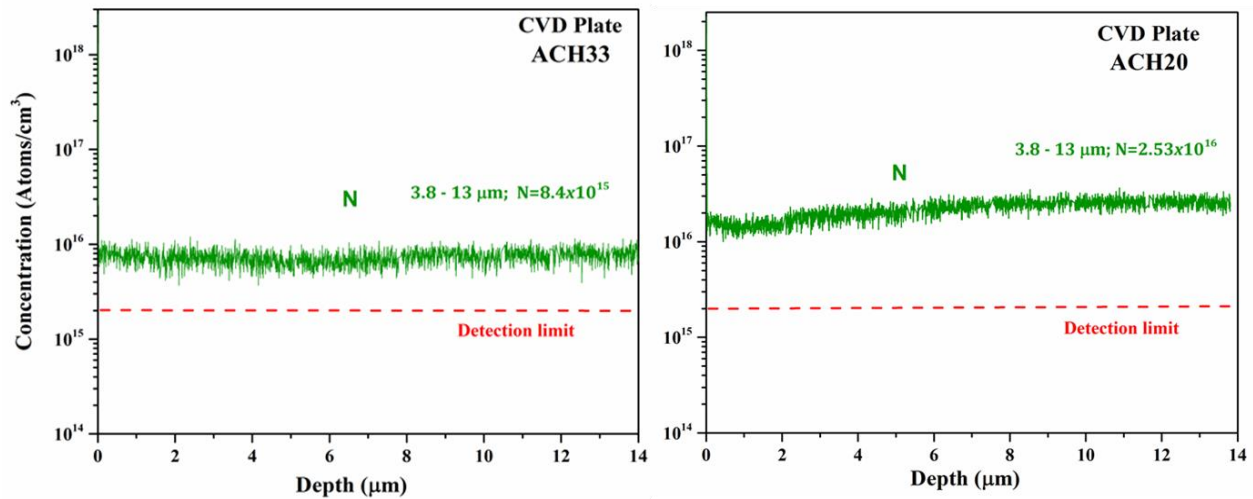


Figure 5. 16 Nitrogen concentration in (a) SCD CVD plate ACH33 and (b) SCD CVD plate ACH20. The red line indicates the detection limit of the instrument.

5.5 SCD growth versus methane concentration

5.5.1 Growth Conditions

Methane concentration is defined as the flow rate ratio of methane gas to total gas, which is typically composed of hydrogen. Because the methane gas flow rate is negligibly small under typical growth conditions, the methane concentration is often defined as the

flow rate ratio of methane gas to hydrogen gas (CH_4 / H_2). Here, effects of the methane concentration on the diamond growth process are discussed.

The effect of the CH_4 concentrations on the growth surface morphologies and growth rate was studied at a constant pressure of 240 Torr and a constant substrate temperature of $1020^\circ\text{C} \pm 5^\circ\text{C}$. The substrate temperature was controlled by the adjusted the microwave input power. The input power was relatively high between 2.8 kW – 3.3 kW for this set of experiments. Four experiments were performed in a pocket holder with $d = 2.6$ mm and $w = 6.0$ mm at 4%, 5%, 6% and 7% methane concentration. The experiments were conducted at 48 hours, however, at 7% CH_4 the experiment had to be stopped due to the soot formation on the quartz dome walls.

5.5.2 Linear and Lateral Growth Rates

Figure 5.17 shows the growth rate of grown diamond substrates as a function of the methane concentration. The plot on the insert on the bottom side of the figure is the variation on the microwave power as a function of the methane concentration. The higher input power was 3.5 kW with a total microwave power density (MWPD) calculated of 580 W/cm^3 at 4% methane concentration. The lowest input power was 2.4 kW with a total MWPD calculated of 404 W/cm^3 at 7% methane concentration.

In the range from 4% to 6%, the linear and lateral growth rate showed a strong linear dependence with methane. When methane increases from 4 to 6, the linear growth rate also increased from $23.7 \mu\text{m/h}$ to $29.0 \mu\text{m/h}$. The high MWPD with a moderate methane concentration (4% - 6%) create an appropriate diamond growth condition which increases the growth rates while the quality of the surfaces is improved. This is attributed that the

density number of atomic hydrogen increased with increasing the plasma density, the hydrogen etching effect on the diamond growth rates is important under moderate methane concentrations at high MWPD conditions. Similar results have been reported by [49], [54], [158], [12], [16].

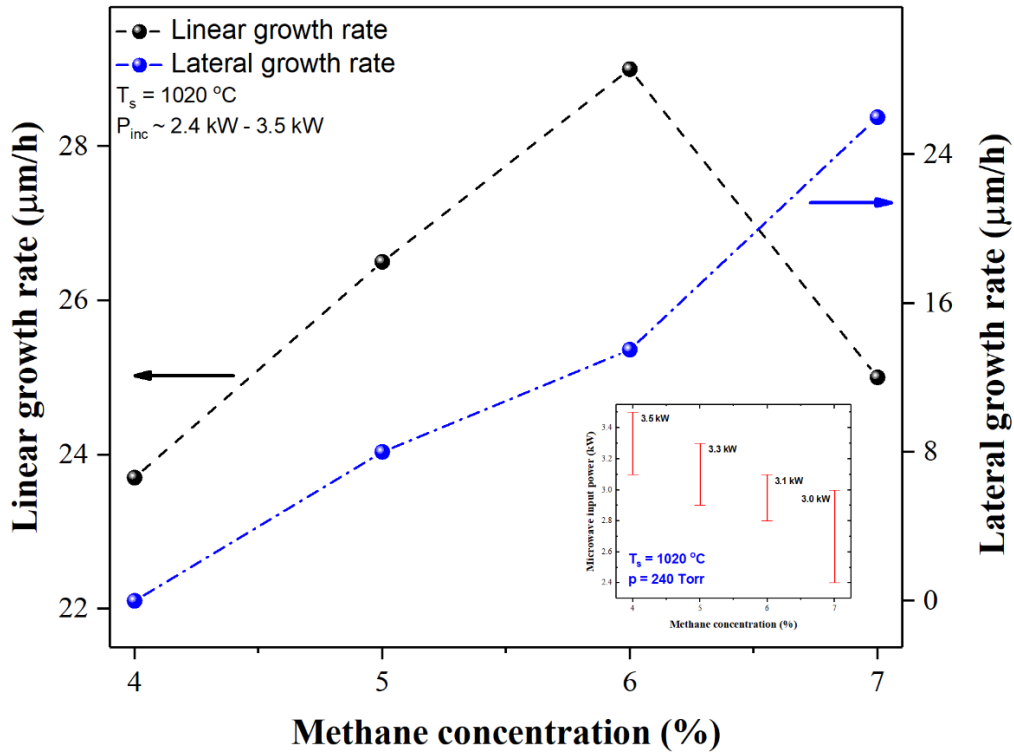


Figure 5.17 Growth rates of CVD diamond grown as a function of the methane concentration under growth conditions of 3.5 kW - 2.4 kW, 1020 °C and 240 Torr.

An important observation is the lateral growth rate at 4% methane, it was calculated as zero. There was no lateral growth on the grown CVD diamond substrate. It might be due to the pocket depth; Figure 5.9 showed that the lateral growth rate for substrates

grown in the same pocket depth ($d = 2.6 \text{ mm}$) are low in comparison with substrates grown by using shallow pockets. This fact suggests as the pocket depth increases, the lateral growth rate of the substrates decreases significantly and is decelerated at low methane concentrations.

Although some authors have extensively reported an increased growth rate at high methane concentrations [12], [16], [49], in this study, the linear growth rate at 7% methane decreased. The growth rate of 7% was measured at $25 \text{ }\mu\text{m/h}$ while the lateral growth rate remains almost the same, i.e. $26 \text{ }\mu\text{m/h}$. This is a decrease in the growth rate of 13.8% over the growth rate of the grown CVD diamond at 6%. As suggested by Teraji et al. [54], this could be a consequence of the incorporation of graphite in the diamond crystal. Diamond growth is difficult to continue if the diamond growth surface is covered considerably with non-diamond phases.

It was expected a linear trend in the growth rate for as a function of the methane concentration at a constant temperature. However, a decreased of almost 14% was observed in the substrate which grew at higher methane concentration. This experiment was performed at low MWPD, calculated at 404 W/cm^3 . This result indicated a decrease of 30%. This fact supports that the growth rate mainly depends on substrate temperature which is mainly controlled by microwave power. It is required to increase both parameters, i.e. MPWD and T_s , in order to have high lateral and linear growth rates.

5.5.3 Surface morphology

Figure 5.18 shows the optical microscope images of the top surface of the CVD diamond substrates grown at $1020 \text{ }^\circ\text{C}$ with 4%, 5%, 6% and 7% of CH_4 . The substrate

grown at 4% exhibited a smooth surface with small step-bunching, as is shown at high magnification image in Figure 5.19 (a). However, this step-bunching does not represent significant changes in the top surface morphology. This morphology could be a consequence of a high etch rate by atomic hydrogen during growth enhanced at high microwave power (3.5 kW). Similar results have been reported by [49], [59].

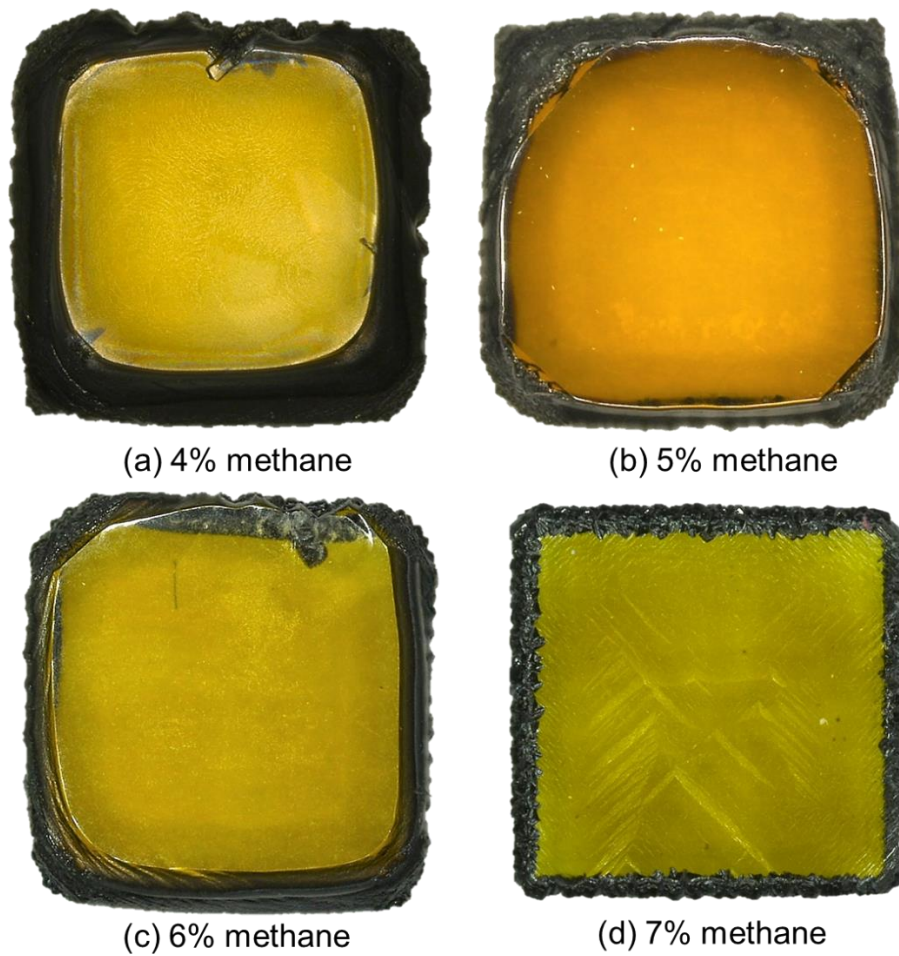


Figure 5.18 Optical microscope images of the top surface of grown SCD substrates for methane concentrations of (a) 4%, (b) 5%, (c) 6% and (d) 7%.

With 5% and 6% of CH₄, the diamond top surfaces displayed very smooth morphologies without any defects and with no evidence of PCD as is shown in Figure 5.18 (b) and (c). High magnification image of substrate grown at 5% methane is displayed in Figure 5.19 (b), a perfectly flat surface is revealed.

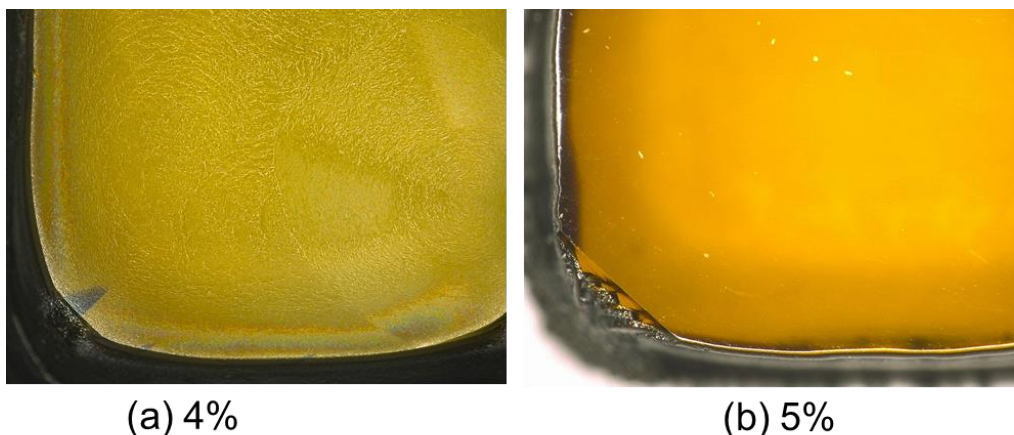


Figure 5. 19 Optical high magnification images of substrate grown at (a) 4 % methane and (b) 5 % methane.

With 7% of methane, step-bunching were observed macroscopically in some parts of the top surface, mainly in the center, Figure 5.15 (d). Although the top surface is not perfectly flat, there are no major defects on the surface.

5.6 Summary Remarks

Thick (1.2 – 1.9 mm) high quality and low-stress diamond crystals were grown in a pocket holder in one continuous process cycle run. It was shown, through diamond growth versus time studies, that MPACVD SCD grows without a PCD rim if during the growth cycle the top surface of the SCD remains inside and below the pocket opening. If the SCD

protrudes out of the pocket a PCD rim forms. At high pressures of 240 Torr, PCD rimless SCD can be routinely grown inside a pocket holder, and the pocket holder is an excellent, hot, thermal environment to grow SCD and to investigate the fundamentals of SCD growth.

The final (process ending) shape and area of the top SCD surface varies with pocket depth and process time. Shallow pockets ($d = 2.0$ mm and 2.3 mm) result in square SCD surfaces, and deep pockets ($d = 2.6$ mm and 2.9 mm) result in the octagon and circular shapes. Shallow pockets have enhanced lateral growth rates and larger area gains. Deeper pockets do not grow larger area SCD crystals but have reduced lateral growth rates and reduced area gains and often result in final SCD crystals with smaller ending surface areas than the areas of the ordinal seeds.

Given the initial constraints of this study, i.e. given the dimensions of our pocket opening, the pocket depths, deposition time and input powers, there is a range of optimal pocket depths that can grow SCD both vertically and horizontally. Those pocket depths appear to be 2.0 – 2.6 mm (Figure 9). In these pockets, the growth rate was $\sim 30 - 27$ $\mu\text{m}/\text{h}$. For the shallow pockets, the final top SCD surface area increased to almost twice the original HPHT diamond seed area and then the lateral growth rate was close to the vertical growth rate. These experiments have demonstrated that moving to higher pressure, higher power density and low N_2 growth conditions result in high growth rates with improved quality and almost stress-free SCD. Thick, PCD rimless, high quality, and low-stress SCD were grown under these conditions.

The etching experiments on the grown SCD plates have displayed low defect densities. The analysis of such plates with etch pit density measurements has shown a reduction in

etch pit density in CVD SCD plates to $\approx 10^4$ etch pits/cm². Further work needs to be done to optimize the growth process to produce even lower defect SCD plates.

Smooth SCD surfaces were grown at 4%, 5%, and 6% methane and the lateral growth was significantly increased with methane. A higher methane concentration of 7% resulted in a change of surface morphology and a decrease on the linear growth rate. Further work is needed investigate the variation of methane concentration as a function of the growth rate, MWPD and substrate temperature.

CHAPTER 6

SINGLE CRYSTAL DIAMOND GROWTH: (1) USING VARIABLE POCKET HOLDER APERTURES AND (2) ADDING AN RE-GROWTH EXPERIMENTAL RUN

6.1 Introduction

Chapters 4 and 5 investigated SCD pocket growth where the pocket was fixed with a constant reference geometry, and then the pocket depth was varied from that fixed reference geometry. In this chapter, SCD pocket growth is experimentally investigated to understand how this SCD growth technique can be extended to further enlarge both the grown crystal thickness and the top growing surface area. Two groups of experiments are performed in this chapter: in group (1) the pocket aperture is increased and varied to explore SCD growth as a function of pocket aperture size, and in group (2) SCD growth is investigated where using newly designed holders another experimental run is added to the diamond growth of the first run.

It was found in Chapter 5 that shallow pockets grew diamond substrates with jagged edges and the largest top surface areas. On the other hand, deeper pocket grew thick

diamond substrates with smooth edges, flat surfaces, and reduced top surface areas. In the research activities of Chapter 5 only the pocket depth was varied in order to investigate diamond pocket holder growth while still producing a flat top surface with smooth edges.

Based on the results of Chapter 5, it was decided to investigate the SCD growth where the pocket depth was held constant while the pocket aperture was varied. In this chapter, the holder depth was held constant at $d = 2.6$ mm or 2.9 mm for three different pocket aperture widths of: $w_1 = 6.0$ mm, $w_2 = 6.6$ mm, and $w_3 = 7.0$ mm. Also, a set of complementary experiments were performed with constant pocket depths of $d = 2.9$ mm again using three different apertures, i.e. w_1 , w_2 , w_3 . The substrate holder was redesigned in order to accommodate the different aperture widths. The redesign had constant dimensions, such as holder thickness ($c = 3.2$ mm) and inner pocket width (1 mm). The pocket aperture width was the only parameter adjusted. See Figure 3.16 for the details of the substrate holder.

In this chapter, the experimental data revealed that after increasing the pocket holder aperture, the lateral growth was enhanced substantially. Significant improvements in the lateral growth rate were observed at the early stage of each experiment. However, the thick PCD which grew on the substrate holder and in the pocket walls influenced the lateral growth. It was difficult to prevent the growth of PCD on the substrate holder. In order to avoid or minimize the PCD growth on the substrate holder and thereby interrupt the lateral SCD growth on the growing SCD substrate, a set of re-growth experiments were performed. Here, one more growth step is added to the smooth and large diamond top surface of the first growth step. A few selected, grown SCD substrates were used for

re-growth experiments, and a new pocket holder was designed to allow the expansion of the top surface area. The pocket holder depth was increased from $d = 2.6$ mm to $d = 4.0$ mm and the aperture width from $w = 7.0$ mm to $w = 8.2$ mm. At the end of the first growth step, the grown diamonds were taken out of the substrate holder, were acid cleaned and then were placed in the new pocket holder design for the re-growth experiments. In these additional growth experiments, the diamond top surface was further enlarged.

6.2 Experimental Details: Variation of the Pocket Aperture

The set of experiments were carried out in the MPACVD reactor C configuration at 240 Torr and microwave power density of approximately 500 W/cm^3 . SCDs were grown on $3.5 \text{ mm} \times 3.5 \text{ mm} \times \approx 1.4 \text{ mm}$ HPHT type Ib diamond seeds for 12 – 60 hours with H_2 flow rates of 400 sccm and a methane concentration of 5%. During each experiment, the substrate temperature was monitored every thirty (30) minutes and was held approximately constant at $1020^\circ\text{C} \pm 5^\circ\text{C}$ during each experiment. Figure 5.3 provides examples of a typical growth process recipe. In order to prevent the growth a PCD rim the growth process cycle was ended when the diamond started to emerge from and grow outside of the pocket.

The pocket holder was redesigned from the holders used in Chapter 5 to accommodate the different size pocket apertures. The redesign slightly adjusted the holder thickness, c , for the pocket depths of $d = 2.9$ mm to allow the diamond growth to take place within the appropriate substrate temperature window. During each process cycle, a substrate pocket holder was placed in the reactor as shown in Figure 5.1 (b).

6.3 Experimental Results: Variation of the Pocket Aperture

6.3.1 SCD Growth versus time

Two groups of experiments that investigated the upward and outward growth of the SCD at a constant pocket holder depth of $d = 2.6$ mm were performed. These experiments used two different pocket apertures: $w_2 = 6.6$ mm and $w_3 = 7.0$ mm. The cycle varied from 12 hours to 55 hours, depending on the aperture. For $w_2 = 6.6$ mm the process cycle runs times were 12, 16, 24, 30, 48, 50 and 55 hours. The process cycle runs times for $w_3 = 7.0$ mm were 12, 30 and 45 hours. Table 6.1 summarizes the different growth parameters and output variables for each aperture size. For all the experiments presented, T_s was kept constant at 1020°C throughout each individual process cycle run by adjusting the microwave input power versus time. In all of these set of experiments, the growth process was stopped before the top surface grew out of the pocket.

The linear growth rates that are summarized in Table 6.1 are the thickness gain divided by the growth time. Thus, this growth rate is an average growth rate over each entire process cycle for each experimental run. The lateral growth rates are calculated with the dimensions of the outward growth length divided by the run cycle growth time. See section 3.7.2 for details on the lateral growth calculations.

Optical microscope images from Table 6.1 are shown in Figure 6.1 (a) – (f) and Figure 6.2 (a) – (d). Figure 6.1 shows images of top and side views of the substrates that were grown using aperture $w_2 = 6.6$ mm. Figure 6.2 shows images of top and side views of the substrates that were grown using aperture $w_3 = 7.0$ mm. All the samples listed in Table 6.1 exhibited smooth and flat top surfaces without a PCD rim around the edges of the top surfaces.

Table 6.1 Growth parameters for SCD growth using the $w_2 = 6.6$ mm and $w_3 = 7.0$ mm pocket holder apertures at a constant pocket depth of $d = 2.6$ mm

Pocket width (w)	Sample	Process cycle (h)	Thickness gain (mm)	Linear growth rate ($\mu\text{m/h}$)	Lateral growth rate ($\mu\text{m/h}$)	Area (mm^2)	Normalized area
6.6 mm	ACH54	12	0.335	27.1	48.0	22.6	1.65
	ACH56	16	0.450	28.0	38.3	23.2	1.70
	ACH53	24	0.676	28.2	27.0	24.0	1.75
	ACH52	30	0.828	27.6	22.1	24.3	1.78
	ACH57	48	1.300	27.0	14.2	24.6	1.82
	ACH58	50	1.440	28.9	14.0	24.6	1.80
	ACH55	55	1.530	27.8	10.0	22.0	1.60
7.0 mm	ACH79	12	0.348	29.0	52.2	23.6	1.73
	ACH71	30	0.855	28.5	27.4	27.5	2.01
	ACH78	45	1.310	28.8	20.0	28.7	2.10

Additionally, all the grown SCD have square crystal top surfaces. However, many of the surfaces have jagged edges while a few surfaces have smooth edges. For example, samples ACH54, ACH56, ACH53, ACH52, ACH57, ACH58, ACH55, ACH79, ACH71, and ACH78 all have jagged edges. Sample ACH58 exhibits partially smooth and partially jagged edges while ACH55 exhibits only smooth edges. When using pocket holder apertures of $w_2 = 6.6$ mm and $w_3 = 7.0$ mm, the linear upward growth rate remained unchanged between 28 – 29 $\mu\text{m/h}$ while the top surface area slowly increased as a function of the time up to 45 hours and then slightly decreased

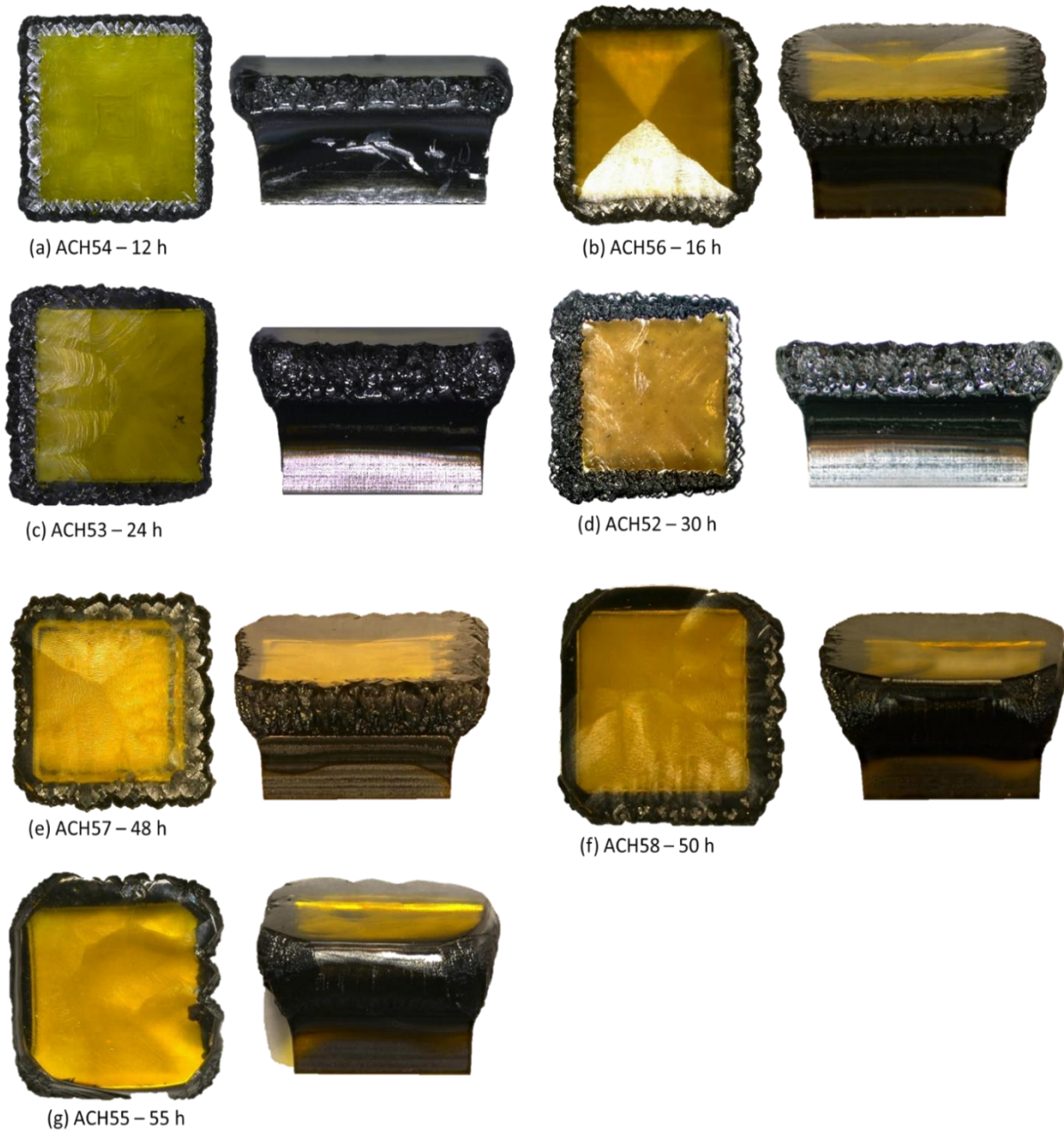


Figure 6.1 Optical microscope top surface images of substrates listed in Table 6.1, for $w_2 = 6.6$ mm (a) 12 hours, (b) 16 hours, (c) 30 hours, (d) 30 hours, (e) 48 hours, (f) 50 hours, and (g) 55 hours. Note that ACH55 has smooth edges and a decreasing top surface.

It also was observed that the substrates were grown within the range from 12 to 55 hours using aperture $w_2 = 6.6$ mm grew upward as a function of the time at approximately the same average growth rate, i.e. an average linear growth rate of $28 - 29 \mu\text{m/h}$. However, the lateral growth rates varied as a function of the time from $48 \mu\text{m/h}$ at 12 hours to $10 \mu\text{m/h}$ at 55 hours. This experimental data clearly indicates the lateral growth rate is faster at the early stages of the growth process. After 48 hours of the growth process, the lateral growth slowed considerably, while the vertical linear growth continued at $\sim 27 - 28 \mu\text{m/h}$. The grown substrates exhibited almost the same normalized top surface normalized area of approximately $1.70 - 1.80$ times.

The fast-lateral growth rates during the first stages of growth that are observed from the data in Table 6.1 were first noted in work described in Chapter 4 sections 4.4 and 4.6. In the experiments described in Chapter 4, the input power was increased during the early stages of the process cycle in order to enhance the early lateral growth rates. The results presented here in Tables 6.1 and 6.2 strengthen the observation of early fast lateral growth rates if the coupled variable, input power/ substrate temperatures, is maintained at the appropriate levels

Smooth edges were observed in substrates grown with longer process cycles, i.e. 50 and 55 hours. The maximum total outward lateral growth was calculated for those substrates grown at 48 hours and 50 hours with an average normalized top surface area of 1.81 times more than the initial HPHT diamond seed area. However, a decrease of 11% in the area gain was observed in the ACH55 substrate which grew with the longest process cycle time of 55 hours. This is attributed to the thick PCD layer that grew over time in the top of the substrate holder and around the pocket walls suppressing the SCD

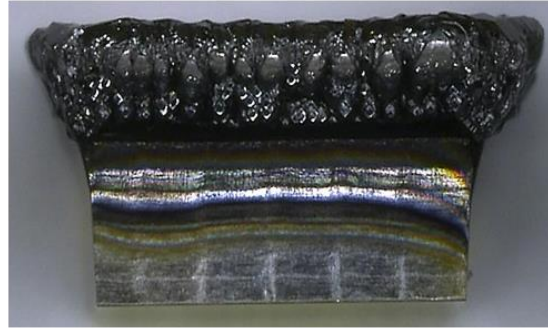
outward growth. Thus, process cycles longer than 50 hours resulted in smaller final top surface areas. Similar results were found in Chapter 5 by using the same pocket depth ($d = 2.6$ mm) and a smaller aperture width of $w_1 = 6.0$ mm.

Figures 6.2 (a), (b) and (c) display smooth and flat surfaces for the three substrates grown using a pocket holder with $w_3 = 7.0$ mm and a pocket holder depth of 2.6 mm. These substrates were grown with growth process cycles of 12, 30 and 45 hours. The measured average total linear growth rate was $29 \mu\text{m/h}$. As in the previous case, the faster lateral growth rates were for the substrates grown for the shortest time of 12 hours. It was measured at $52.2 \mu\text{m/h}$. The total average lateral growth rate of $20 \mu\text{m/h}$ was calculated for the substrate grown for 45 hours, which was the longest experimental run. As a result, expanded areas as large as 28.7 mm^2 were obtained in a single run. For this pocket holder configuration, i.e. $d = 2.6$ mm and $w_3 = 7.0$ mm, the total area increased up to 2.1 times of the initial HPHT diamond seed area. When using pocket holder apertures of $w_2 = 6.6$ mm and $w_3 = 7.0$ mm, the linear growth rate remained unchanged between $28 - 29 \mu\text{m/h}$ while the top surface area increased as a function of the time up to 50 hours.

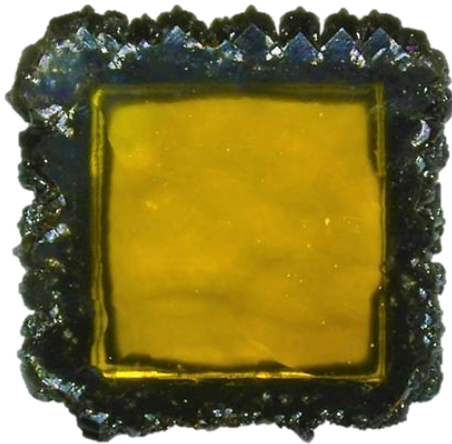
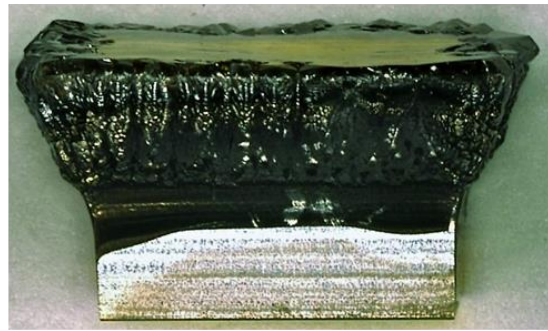
For a better understanding of how the pocket aperture size influences the lateral growth of the SCD, a separate additional set of experiments were performed using a fixed pocket holder configuration of $d = 2.9$ mm and $w_3 = 7.0$ mm. The results from the four-different growth process are summarized in Table 6.2 and Figure 6.3 (a) – (c).



(a) ACH79 – 12 h



(b) ACH71 – 30 h



(c) ACH78 – 45 h



Figure 6.2 Optical microscope top surface images of substrates listed in Table 6.1, for $w_3 = 7.0$ mm (a) ACH79 after 12 hours of growth, (b) ACH71 after 30 hours, and (c) ACH78 after 45 hours of growth.

Table 6.2 Growth parameters for SCD growth using $w_3 = 7.0$ mm pocket holder aperture
at pocket depth of $d = 2.9$ mm

Pocket width (w)	Sample	Process cycle (h)	Thickness gain (mm)	Linear growth rate ($\mu\text{m/h}$)	Linear growth rate ($\mu\text{m/h}$)	Area (mm^2)	Normalized area
7.0 mm	ACH73	12	0.309	25.8	52.4	23.6	1.73
	ACH67	40	1.00	25.1	24.1	30.6	2.24
	ACH70	45	1.12	25.0	20.9	30.1	2.20
	ACH72	50	1.23	24.6	20.1	31.5	2.30

The experiments were performed using constant T_s deposition recipes, i.e. $1020 \pm 5^\circ\text{C}$. The growth time was varied at 12, 40, 45 and 50 hours for single individual runs. The grown substrates exhibited smooth and flat surfaces with jagged edges and square top surfaces. These substrates grew upward as a function of the time at an average linear growth rate of $\approx 25 \mu\text{m/h}$. As a result, expanded areas were obtained as large as 31.5 mm^2 , and the total area gain increased to 2.3 times of the initial HPHT diamond seed area. This increase is the highest obtained for CVD growth on a standard ($3.5 \text{ mm} \times 3.5 \text{ mm}$) HPHT diamond seed in a single run.

The results from Chapter 5 showed grown substrates that displayed different crystal shapes, i.e. square, octagon, circle, depending on the pocket depth. Contrary to those results, all the substrates listed in Table 6.1 and Table 6.2 that were grown with apertures of 6.0 mm and 7.0 mm displayed the same final square crystal shape.

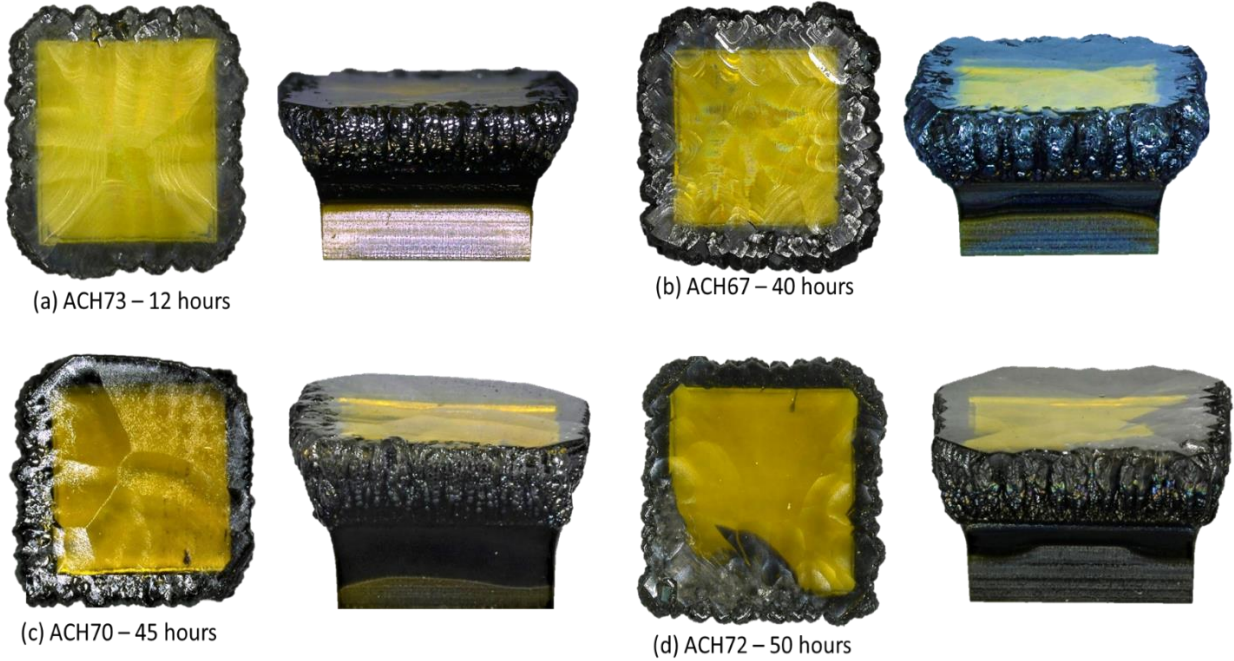


Figure 6. 3 Optical microscope top surface and side view of images of substrates listed in Table 6.2, for $w_3 = 7.0$ mm a constant pocket depth of $d = 2.9$ mm (a) 45 hours, (b) 40 hours and (c) 50 hours. Note: that the substrate ACH72 have a dark spot on the left bottom side it is a crack on the top surface that was produced at the experimental run when the substrate was removed from the pocket.

It was observed for the data from Table 6.1 and 6.2 that the total average lateral growth rate decreases as a function of the growth time. Figure 6.4 summarizes the total lateral growth rate for all the pocket apertures (including data from Chapter 5) at 12 and 45 hours of growth time. At 45 hours, the lower growth rates are from, the narrow pocket aperture, i.e., 6.0 mm and the lateral growth rate gradually increases as the aperture size is increased. Using the same pocket aperture, i.e. 6.0 mm, the total lateral growth rate decreases from $24.9 \mu\text{m/h}$ to $7.2 \mu\text{m/h}$ as the run is extended from 12 hours to 45 hours.

A higher initial lateral growth rate of 52.2 $\mu\text{m/h}$ was measured for the wider pocket aperture, i.e. 7.0 mm at 12 hours of growth time. For all shorter growth times, these results indicated that the lateral growth rate is significantly larger, i.e. it more than doubles, as the pocket aperture is increased.

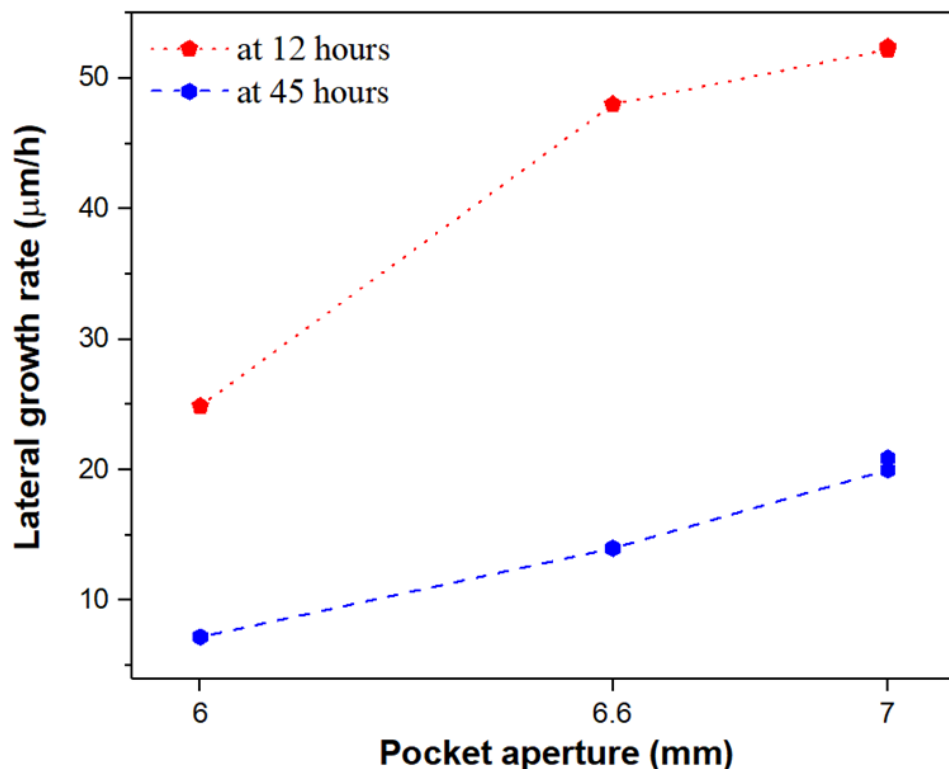


Figure 6.4 The total average lateral growth rate versus pocket aperture at 12 and 45 hours of growth time

Results from Chapter 5 and these results indicated that the linear vertical growth rate becomes slower with deeper pocket holders. Also, the top surface areas enlarged as the pocket aperture size increased. Based on these experimental results it is speculated that

the diamond could have grown even larger with enlarged surface areas and with slight thickness gains by using deeper pockets (3.0 mm – 3.3 mm) and wider apertures (7.3 mm – 7.6 mm).

6.3.2 SCD growth versus growth time, pocket width, and pocket depth: the evolution of the crystal versus time.

To better understand how the pocket aperture plays a significant role in the lateral growth of CVD diamond substrates, the results of the normalized area gain versus growth time are plotted in Figure 6.5. All the substrates listed in Table 6.1 and Table 6.2, as well as selected results from Chapter 5 for a pocket holder with $d = 2.6$ mm and $w = 6.0$ mm, are summarized in Figure 6.5.

The experimental data points are grouped by the pocket width at a constant pocket depth of 2.6 mm. Two pairs of eight substrates, which were grown in separate pockets with $w_1 = 6.0$ mm and $w_2 = 6.6$ mm, are plotted and represented by the red and the blue curves, respectively. Three substrates which were grown in a pocket with $w_3 = 7.0$ mm, and $d = 2.6$ mm are also plotted and represented by the orange curve. Also included are a set of four experiments grouped by fixed pocket geometry of $d = 2.9$ mm and $w = 7.0$ mm (the black curve in the figure). All the curves begin at $t = 0$ and grow from the original HPHT seed surface area of 13.7 mm^2 : Note that at $t = 0$, i.e. at the start of the experiment, the normalized area is one.

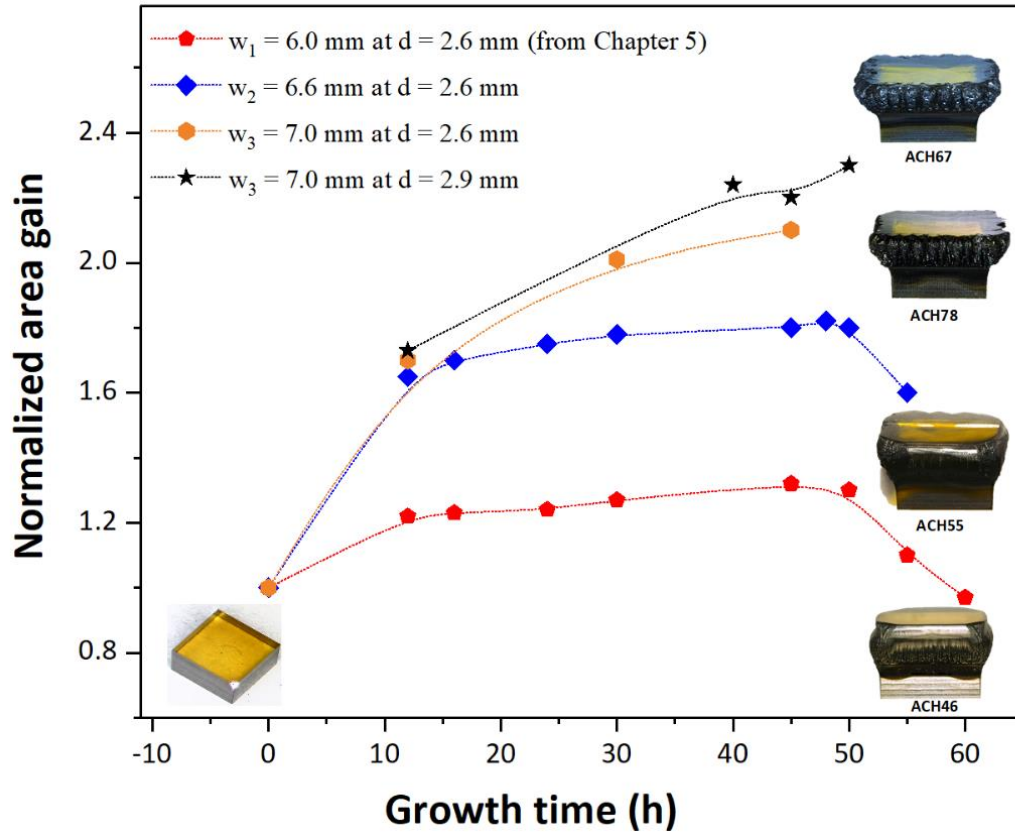


Figure 6.5 Normalized area gain versus growth time at different pocket configurations from experimental data provided in Table 6.1, Table 6.2, and selected results of Chapter 5 grown in pocket depth of 2.6 mm.

It can be readily observed that the pockets with wider apertures reached larger area gains than the narrower pockets apertures. The pockets with an aperture width of $w_3 = 7.0$ mm yield the largest normalized area gain. This particular pocket holder geometry (at $d = 2.6$ mm) can grow SCD with area gains up to 2.1 times before their top surfaces start to decrease.

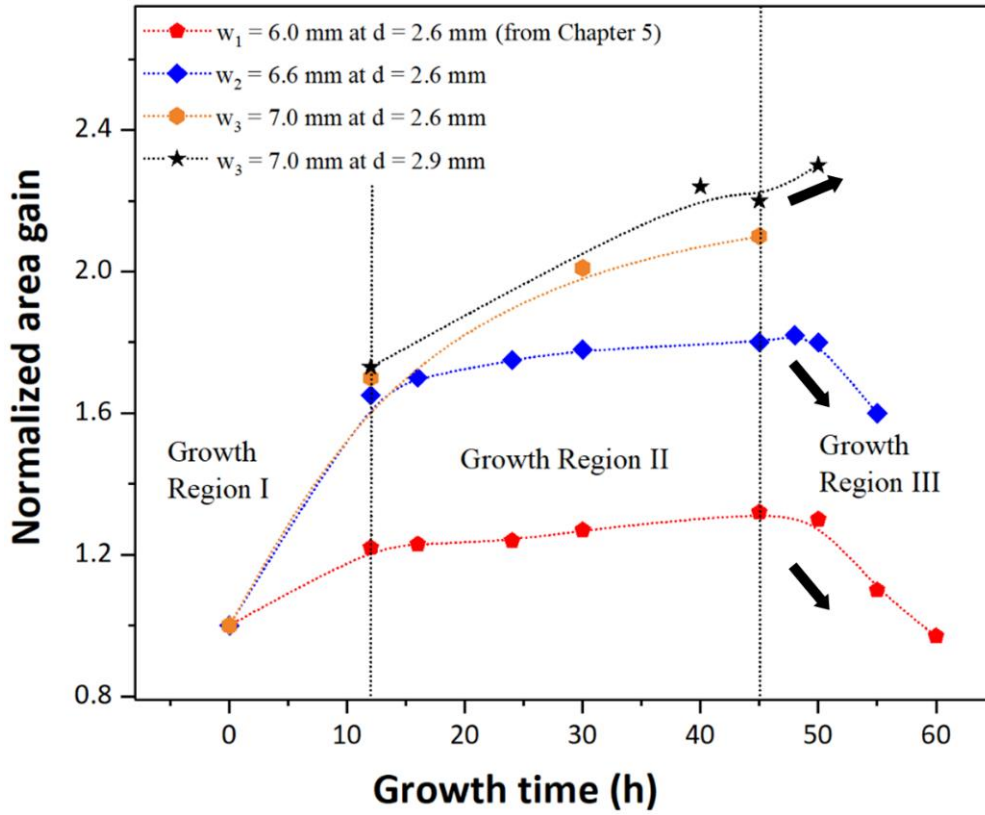


Figure 6.6 Plot summarizing the normalized lateral CVD area gain versus growth time for different pocket apertures and depths for the experimental data listed in Tables 6.1, Table 6.2, and selected data from Table 5.2.

The deeper and wider pocket geometry, i.e. $d = 2.9$ mm and $w_3 = 7.0$ mm, can grow SCD with a top surface area gain up to 2.3 times in a single run. The narrow apertures and the longer runs resulted in smaller final SCD surface area gains. Opposite to this trend, the wider apertures and the longer runs resulted in a larger top surface area gains.

The experimental data displayed in Figure 6.6 is broken into three growth time regions. Growth region I describe the initial growth over the first 12 -15 hours where lateral growth rates are high, i.e. $> 25 \mu\text{m/h}$ and exceed the vertical growth rate. Rapid lateral growth

occurs in this time region for all four pocket holder geometries and the fastest lateral growth rate, i.e. 52 $\mu\text{m/h}$ was measured for the wider pocket apertures. Growth region II is called the “crystal thickness growth” region. Here, the lateral growth is significantly slowed over time by the presence of the pocket walls, while the linear growth continues at a rate of 27 – 29 $\mu\text{m/h}$. Also, during this time a thick PCD layer starts to grow over the substrate holder. Growth region III is identified as the PCD overgrowth region. This growth region is dominated by the growth of a thick PCD layer on the top substrate holder. In region II the PCD layer on the substrate holder thickens with time and after 45 hours; i.e. at the beginning of region III growth, the PCD starts to grow into and fill the aperture opening. In this region, the effective aperture width starts to decrease and thus the top growing surface of the SCD decreases. At the end of a long run that extends into region III, the total top surface area can be less than the initial HPHT seed area. The formation of PCD on the substrate holder thus limits the growth of an ever expanding SCD top surface. This indicates that the growth of PCD on the holder should be avoided.

An example of the growth behavior in these three regions is presented in Figure 6.7. Photographic (see Chapter 7 for information on the photographic technique) images were captured in each growth region to evaluate the SCD lateral growth. In Figure 6.7 the opaque yellow polygon layer represents the original HPHT seed inside the pocket. Six polygons were copied and carefully overlaid on each growth stage of the diamond. The orange polygon layer outlines the growing SCD during the indicated time frames of 12, 24, 40, 50 and 55 hours. As can be seen from the photographs, the lateral growth occurs at the early stage of growth, i.e. growth region I. In growth region II, after 40 hours onwards the lateral growth is slowed, and the linear vertical growth remains steady at ~

28 μ /hr. Finally, in growth region III, the overgrowth of PCD on the substrate holder and into the walls of the pocket is observed which either interrupted the lateral growth or decreased it. This is clearly confirmed from the analysis of the photos that is presented in Chapter 7.

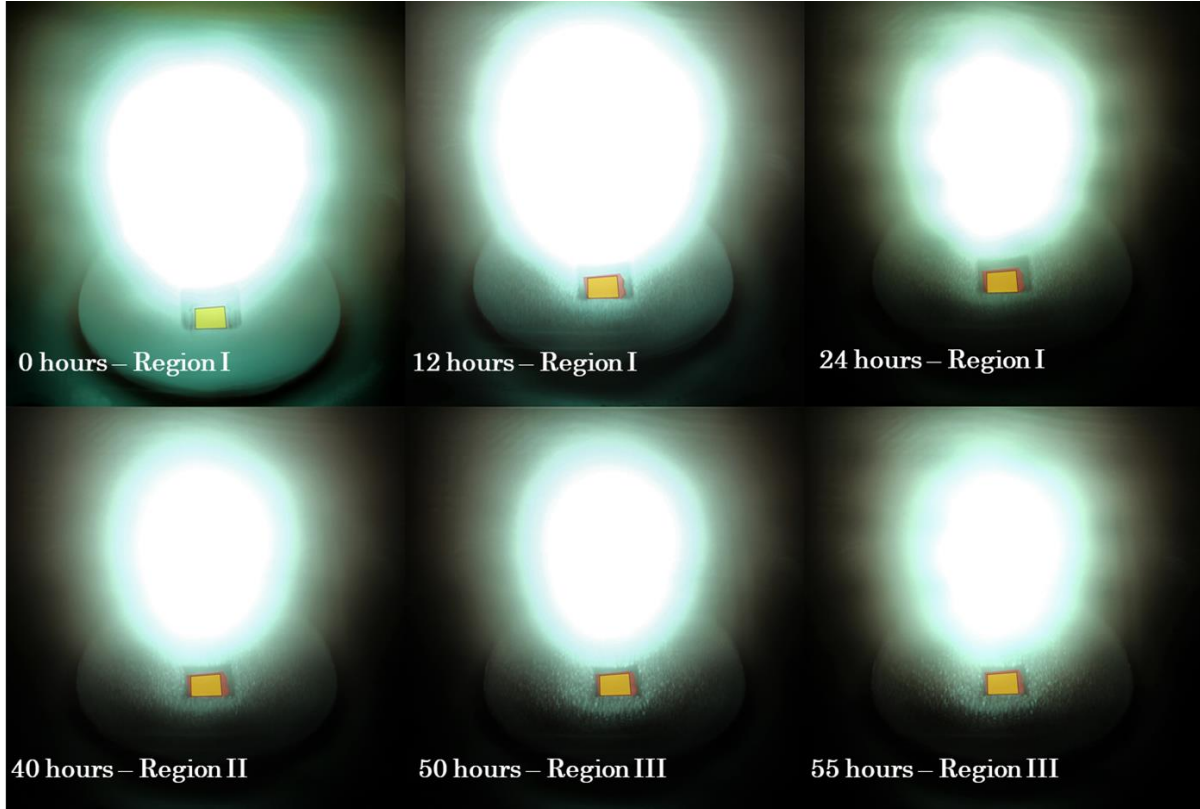


Figure 6. 7 Photographic images in the frame time of 0, 12, 24, 40, 50 and 55 hours. The opaque yellow polygon layer represents the HPHT seed inside the pocket. The orange polygon layer identifies and outlines the grow SCD during the indicated time frames.

Figure 6.8 displays a plot of the lateral growth rate (V_{110}) and the vertical growth rate (V_{100}). The experimental data in the curves in this figure is calculated from the data

displayed in Fig. 6.7. It displays the growth rate ratio between the outward, lateral surface growth, represented by V_{110} and upward surface growth, represented by V_{110} and upward surface, represented by V_{100} . The ratio between both rates was calculated with the data in Figure 6.7 and from Table 6.1 and 6.2. The substrates that were grown in the wider pocket apertures, i.e. 7.0 mm lead to an initial fast and uniform growth of over the entire surface resulting rapidly expanded the surface area at the beginning of the process cycle. For example, the faster growth was observed for a substrate that grew in the wider pocket ($V_{110}/V_{100} = 1.7$).

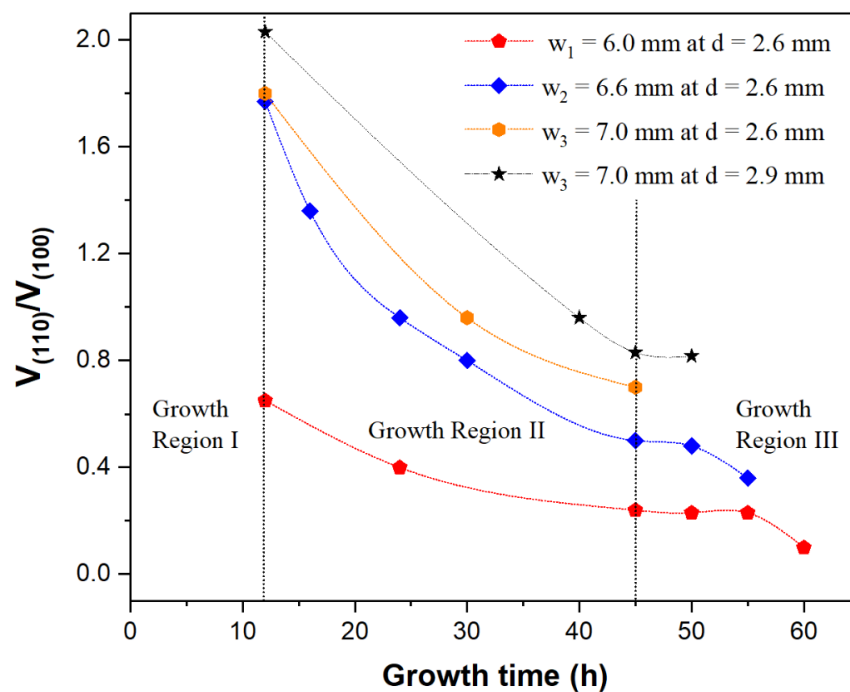


Figure 6. 8 The ratio between lateral growth rate, V_{110} , and vertically growth rate, V_{100} , versus growth time for three different pocket holder apertures.

In contrast, the substrates that grew in the narrow pocket ($w = 6.0$ mm) showed a slower initial growth rate. After the initial fast lateral growth period during region I the lateral growth rate decreased as a function of the time. This behavior was true for all apertures. The narrow apertures and the longer runs resulted in smaller final SCD surface areas. Opposite to this trend, the wider apertures and the longer runs resulted in a larger top surface area. This is caused by the PCD growing on the substrate holder and into the pocket walls as a function of the time in region II and III as a function of the time. Hence, the longer runs make the effective pocket aperture decrease over time resulting in smaller final SCD top surfaces areas. The wider apertures keep the aperture wide enough to allow for more outward growth and eventually the further enlargement of the final surface area before the PCD growth modifies the process.

In region III the diamond surface area could either continue to increase or start to decrease versus time depending on the aperture. The data indicate that after 45 hours (growth region III) the diamond surface area is determined by the aperture size. The lateral growth shows a trend that implies the continued to lateral growth until the top surface area fills the wider apertures. The black arrows in Figure 6.6 are used to represent either an increasing (up) or a decreasing (down) top surface area growth trend.

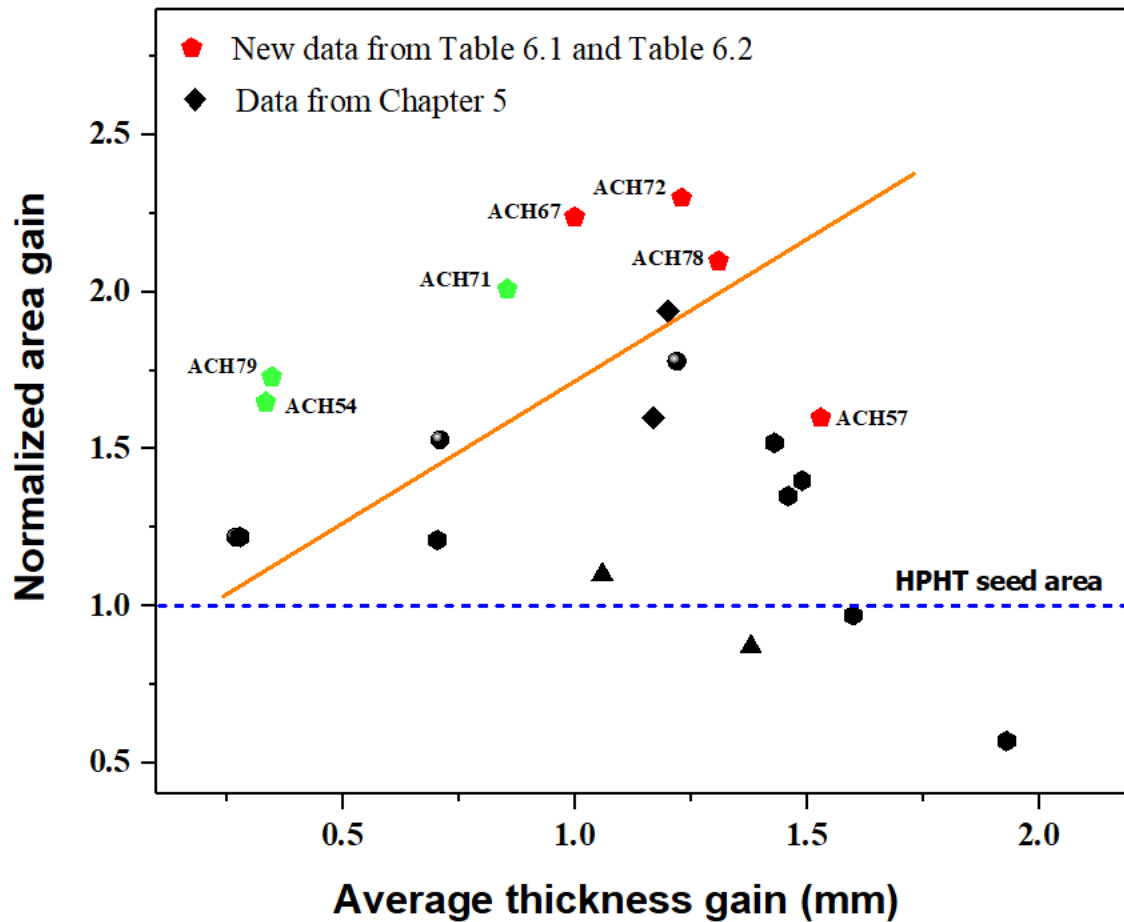


Figure 6.9 Plot summarizing the normalized lateral CVD area gain versus vertical thickness gain for different pocket holder geometries for the experimental selected data from Table 6.1 and Table 6.2 and the results of Chapter 5. Short run data and long run data from this section are indicated by the grown and res data points respectively.

In order to compare, the recent experimental data with the results found in Chapter 5, Figure 6.9 shows a reference plot of the normalized lateral area gain versus the vertical thickness gain. This figure was used in Chapter 5 (Figure 5.10). In Figure 6.9 all the experimental data points from Chapter 5 are grouped by pocket depth and are

represented by all black polygons. Selected data points from Table 6.1 and Table 6.2 are represented either: (1) by the red polygons which represent the long run data, or (2) by the green polygons which represent the short run data from Tables 6.1 and 6.2.

For all the experiments presented in this chapter, the longer runs that extend into region III ends up with the smallest surfaces areas. See for example ACH55. The shorter runs up to 45 hours end up with enlarged surfaces areas. This is caused by the PCD growth on the substrate holder. See for example ACH67 and ACH78. The experimental data for the $w = 7.0$ mm holder aperture clearly indicates a significant improvement in the enlargement of the final diamond top surface.

A comparison of the short run and long data points indicated the growth in the three growth regions: (1) a quick lateral growth (see ACH54 and ACH79) over the first 0.3 mm of thickness, (2) a slower lateral growth over the next 0.7 mm of thickness growth and (3) a decrease in top surface area over the next ~ 0.5 mm of thickness growth. This already has been indicated in Figure. 6.6. The short run data points indicate that the wider apertures allow the rapid initial growth of enlarged surface areas.

6.3.3 Summary Remarks: Variation of the Pocket Aperture

Enlarged diamond top surfaces were grown in variable pocket holder apertures as one continuous growth process. It was discovered that the long growth experiments could be divided into three growth regions: (1) region I where the lateral growth was high, (2) region II with (a) a steady thickness (vertical) growth and (b) a diminished lateral growth that is limited by the proximity of the pocket walls and (3) region III where the growth is effected and limited by the growth of PCD on the substrate holder and into the pocket

aperture itself. Additionally, it was found, the linear and lateral growth rate decrease as the pocket depth increased from 2.6 mm to 2.9 mm. Those results are similar all holder apertures, i.e. 6.0 mm, 6.6 mm and 7.0 mm. More specifically wider pocket apertures have a significantly enhanced lateral growth rates and larger areas gain. Narrow pocket apertures have an increased top surface area up to 45 hours of the growth process. After 45 hours, a trend to decrease the lateral growth was observed in all the substrates grown in a 2.6 mm pocket depth and apertures of 6.0 mm and 6.6 mm. See example blue and red curves in Figure 6.5. The larger surface areas were grown on the pocket holder with $d = 2.9$ mm and $w = 7.0$ mm. The normalized lateral area gain measured was 2.3 times that the initial HPHT diamond seed.

6.4 Experimental Details: SCD Re-growth and Expanding Surfaces

The set of experiments were carried out in the MCPR reactor C configuration at 240 Torr and microwave power density of 700 W/cm^3 . SCDs were grown on smooth and flat CVD SCD top surfaces with areas of approximately of $5 \text{ mm} \times 5 \text{ mm} \times \approx 1.4 \text{ mm}$ for 40 – 50 hours with H_2 flow rates of 400 sccm and a methane concentration of 5%. The substrate temperature was carefully monitored and was held approximately constant at $1020^\circ\text{C} \pm 5^\circ\text{C}$ during each experiment. The growth process cycles were terminated when the diamond started to grow outside of the pocket. The experiments presented here are exploratory in nature and do not represent the results from a complete and optimized investigation.

A new pocket holder was designed to accommodate the larger grown substrates. The substrate holder dimensions were selected based on the earlier results from Chapter 6,

i.e. the larger aperture pocket holder designs. The design adjusted the holder thickness, c , the pocket depth, and the pocket aperture ($c = 4.5$ mm, $d = 4.0$ mm and $w = 8.2$ mm). This design is displayed in Figure 3.18. The dimensions of the pocket holder allow that the diamond growth takes place within the appropriate substrate temperature window. During each process cycle, a pocket holder was placed in the reactor as shown in Figure 5.1 (b).

Long growth process cycles are imperative to grow thick and large volume SCDs. However, as has been discussed in Chapter 5 and section 6.3.2, the high growth rate of PCD on the substrate holder disturbs the SCD growth. Therefore, the re-growth is an alternative growth method to one continuous SCD growth process. The re-growth process involves adding an additional growth step on the top of one already grown substrate with smooth and enlarge top surface areas. Before the second growth step, a new pocket holder was designed and then was used in the second growth step. After the 1st growth run was completed, the substrates were cleaned and analyzed. The cleaning process was described in section 3.4.1.

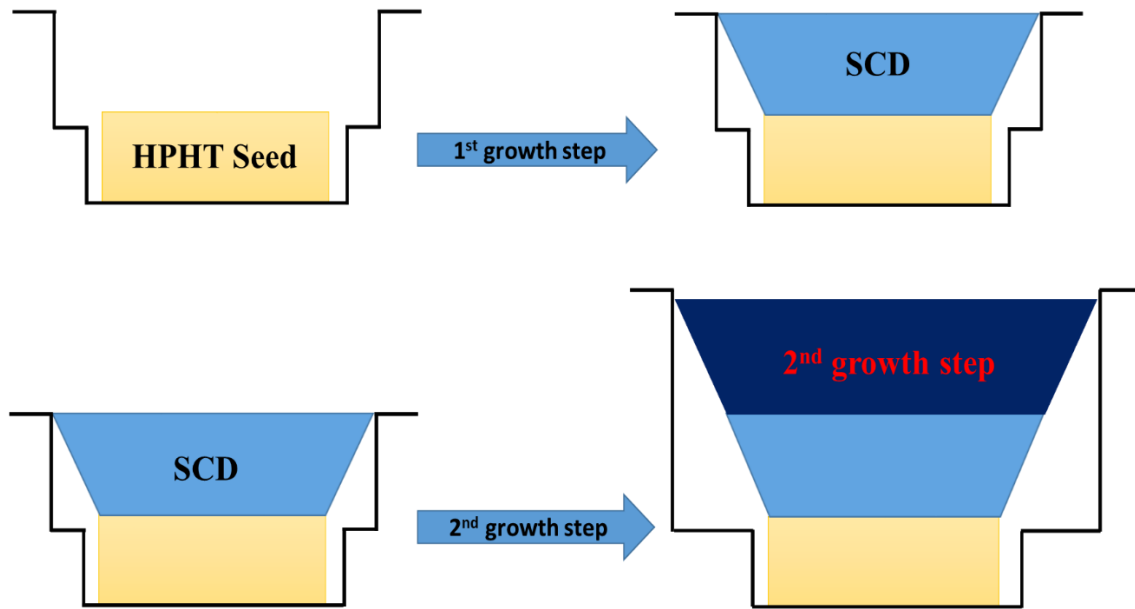


Figure 6.10 Schematic of the re-growth process. After the 1st growth step process, the grown substrate is placed in an optimized substrate holder.

Figure 6.10 shows a flow diagram of this process. This figure describes the re-growth process using an optimized pocket holder design.

6.5 Experimental Results: SCD Re-growth and Expanding Surfaces

6.5.1 SCD Re-growth Criteria

In order to continue expanded areas without producing defect on the new surfaces, the 2nd growth entirely depends on the 1st grown surface. The first diamond growth step must satisfy certain growths criteria. The following criteria were listed in order to continue expanding the top surface at the same time that the smoothness and uniformity of the diamond surfaces are maintained. The first growth step should have:

1. Smooth and flat surface, to avoid the propagation of the defects in the second growth step
2. With no evidence of PCD and with no jagged edges
3. Evenly grown top surfaces, i.e. $\sim 4.5 \text{ mm} \times 4.5 \text{ mm}$
4. Due to the pocket design, the thickness of the substrate should be more than 1.0 mm.

An example of two substrates that do not meet these growth criteria are shown in Figure 6.11 and Figure 6.12. Figure 6.12 displays optical microscope images of the grown substrate ACH26 after the 1st and 2nd growth steps. ACH26 was first grown in one step for 46 hours, with a thickness of 1.22 mm and a growth rate of $\sim 29.1 \text{ } \mu\text{m/hr}$. The top surface of the SCD substrate was uneven with no major defects on the surface and had jagged edges. The dimensions of the first growth surface for this substrate was 24.08 mm^2 . Thus, the lateral surface area of the CVD SCD substrate increased by ~ 1.8 times over the initial SCD seed surface area (i.e. 13.69 mm^2).

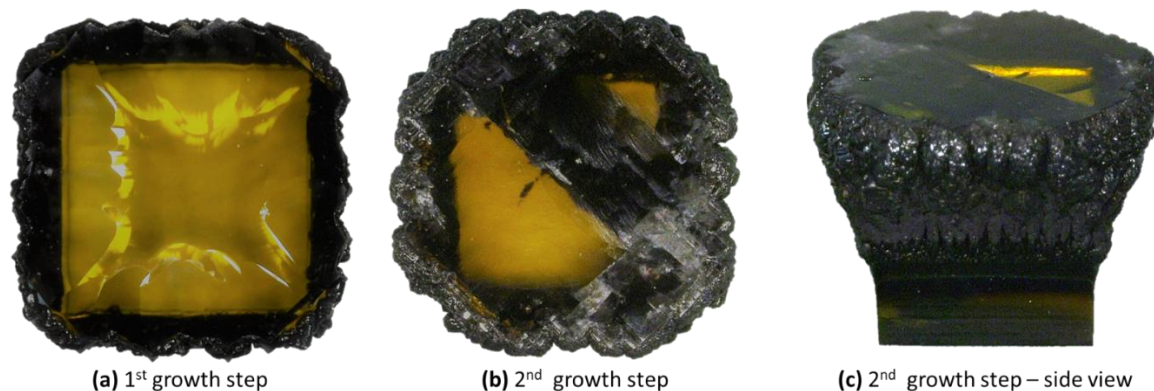


Figure 6.11 Optical microscope images of (a) top view of ACH26 after the 1st growth step, (b) top view of ACH26-2 after the 2nd growth step, and (c) side view of the ACH26-2.

During the second growth step, the surface was expanded up to 34.8 mm². This is ~ 2.6 times over the initial HPHT seed and 1.4 times over the 1st growth step. It is an increase of growth area of 40% over the 1st growth step. It was observed significant defects on the top surface, and the edges maintained their jagged appearance. It is considered that the uneven surface was propagated up to cause a crack on the top surface, which is identified as the black band on the top surface. See Figure 6.11 (b). The 2nd growth was performed for 45 hours at a growth rate of 25.4 μm/h.

Another example is shown in Figure 6.12. ACH36 was grown in one step for 43 hours, with a thickness of 1.0 mm and at a growth rate of ~23 μm/hr. The top surface of the CVD SCD substrate is a smooth and flat surface, with no evidence of PCD and with smooth edges. The dimensions of the growth surface of this substrate was 15.2 mm². Thus, the lateral surface area of the CVD SCD substrate increased by ~ 1.1 times over the initial SCD seed surface area (i.e. 13.69 mm²).

After 30 hours of the 2nd growth step, the substrate exhibited almost the same morphology of the 1st growth. The substrate ACH36-2 displayed smooth and flat surface. The top surface area increased up to 19.5 mm². It is ~ 1.28 times over the initial HPHT seed and just 1.42 times over the 1st growth step.

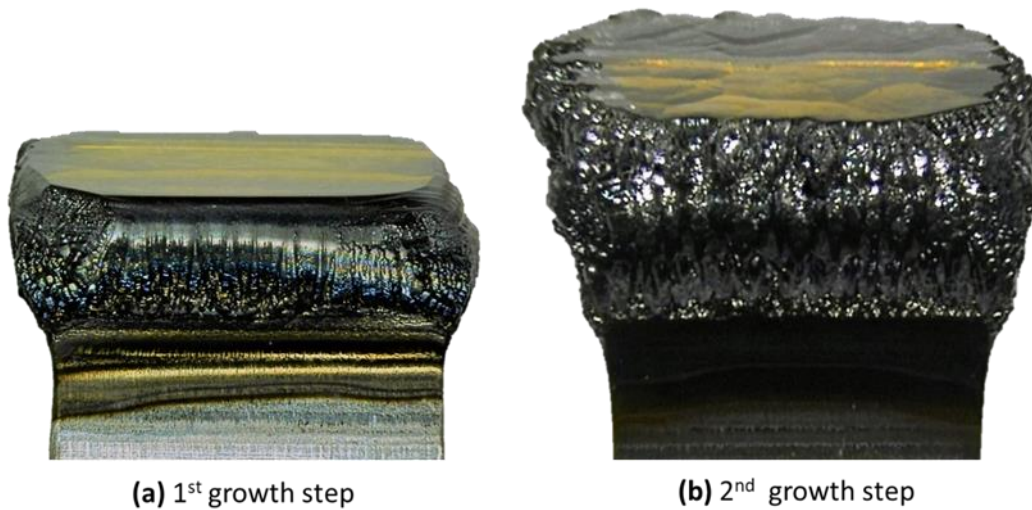


Figure 6. 12 Optical microscope side view images of ACH36 after the (a) 1st growth step and (b) 2nd growth step.

These examples demonstrate the importance of conducting the re-growth process on expanded, smooth and flat surfaces to enable the continuation of growing expanding surfaces without major defects.

6.5.2 SCD Re-growth – Expanded surfaces

Three different re-growth experiments were performed to continue expanding the top diamond surfaces. These experiments used a constant temperature of 1020°C \pm 5°C over

the growth process and used a 4.0 mm deep pocket holder. Figure 6.13 (a) - (d) shows examples of the PCD rimless and enlarged SCD areas of the first runs, ACH23, ACH27 and ACH73. Note the improvement on the top surface over the substrate ACH26 showed in Figure 6.11. ACH23 was grown in one step for 40 hours, with a thickness of 1.20 mm, and a growth rate of 30 $\mu\text{m/hr}$. Similarly, ACH27 was grown in one step for 45 hours, with a thickness of 1.16 mm and a growth rate of $\sim 26.6 \mu\text{m/hr}$. Both SCD CVD substrates were selected for regrowth.

The top surfaces of the both CVD SCD substrates are smooth and flat with no major defects on the surface. The dimensions of the growth surface for these two substrates were 23.28 mm^2 and 22.1 mm^2 , respectively. Thus, the lateral surface area of the CVD SCD substrate increased by ~ 1.7 times for ACH23 and ~ 1.6 times for ACH27 over the initial SCD seed surface area. The outward growth of the SCD substrates is clearly seen in Figure 6.13 (a) and (c).

The substrates were analyzed and then placed in the optimized pocket holder to continue growth. As a result, as shown in Figure 6.12 (b) and (d), expanded top surfaces have been successfully grown. ACH23-2 was re-grown for 50 hours at a growth rate of 28.7 $\mu\text{m/h}$ and now had a total thickness of 2.64 mm. The red dotted lines in the substrates represent the boundary between the first and second growth steps. After a total time of 90 hours, the dimension of the total top surface was 34.22 mm^2 . The lateral surface area of the CVD SCD substrate increased by 2.5 times. ACH27-2 was re-grown for 45 hours, produced a total thickness of 2.32 mm, and had a growth rate of 25.2 $\mu\text{m/h}$. The total growth time was 90 hours, the dimension of the total top surface was 27.56 mm^2 and the total top surface increased by 2.1 times.

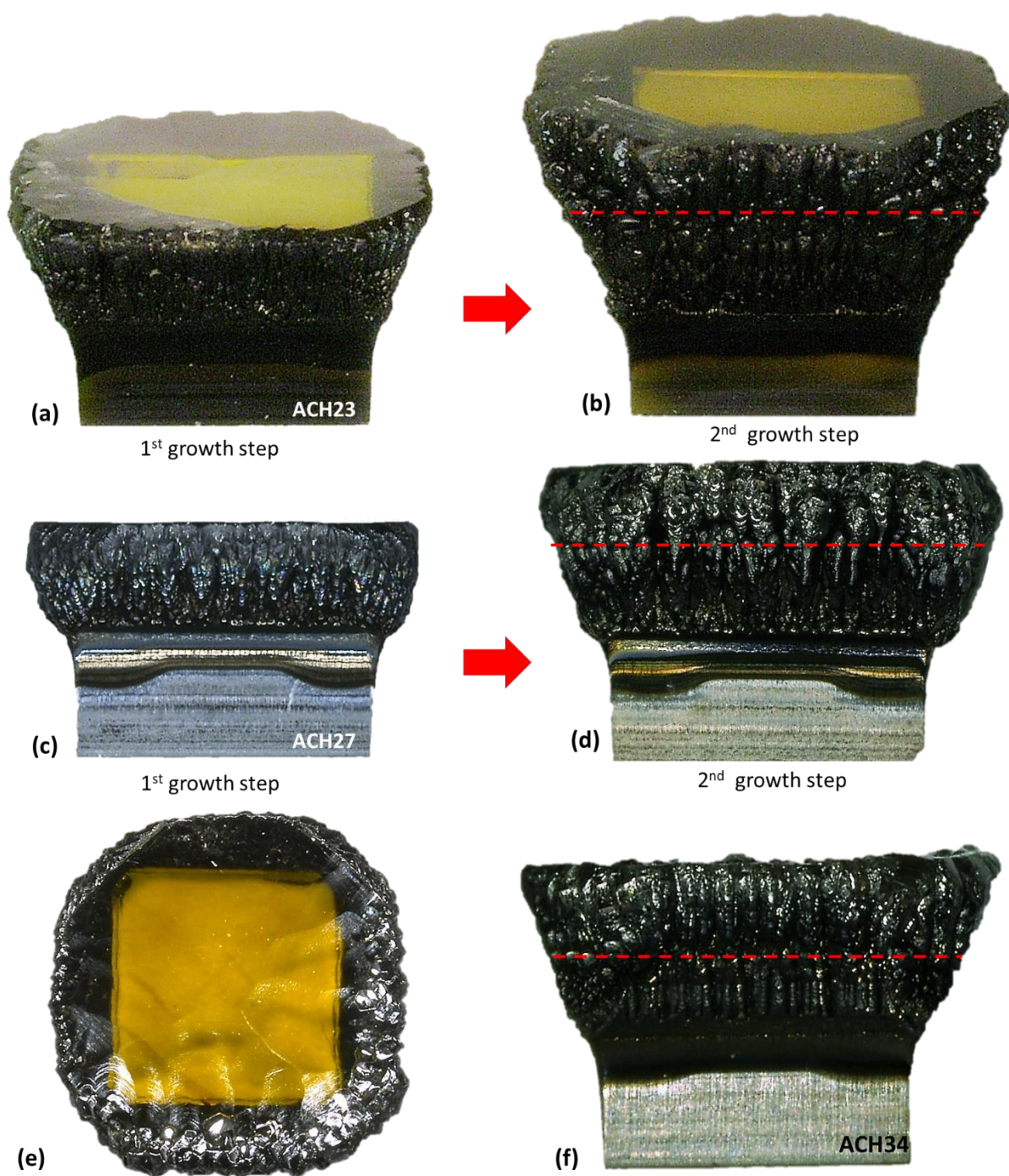


Figure 6. 13 Optical microscope side view of (a) and (b) substrate ACH23 after the 1st and 2nd growth step, (a) and (b) substrate ACH27 after the 1st and 2nd growth step, and (e) top view and (f) side view of substrate ACH34 after the 1st and 2nd growth step.

Finally, ACH34 was grown in one step for 20 hours, with a thickness of 552 μm , and a growth rate of 27.6 $\mu\text{m/hr}$. The second growth step was conducted for 40 hours at a growth rate of 27.5 $\mu\text{m/hr}$ with a total thickness gain of 1.65 mm. The resulting CVD SCD substrate increased by 2.2 times.

The normalized lateral area gain versus the vertical thickness gain for the re-growth exploratory details plotted in Fig. 6.14. All the experiments that were regrown on uneven and non-expanded surfaces developed defects and smaller surfaces, similar to ACH26 and ACH36. Those experiments were not included in the plot of Figure 6.14 because they were re-grown out of the desired growth criteria.

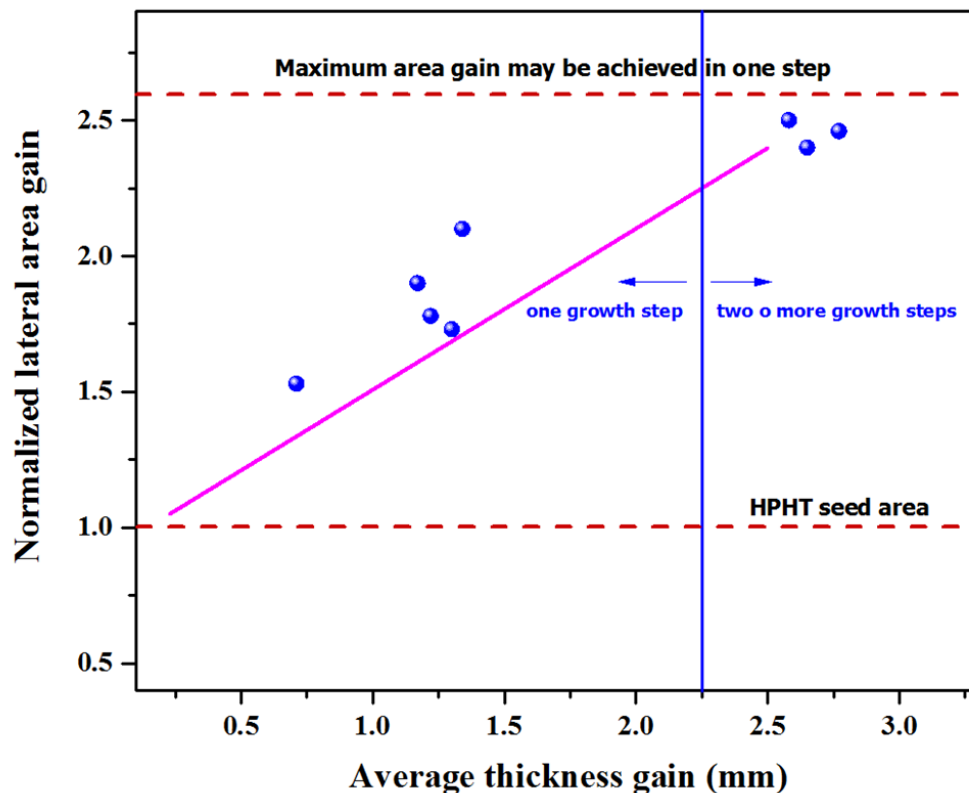


Figure 6. 14 Normalized lateral area gain versus vertical thickness gain

In Figure 6.14, three regrown data points were plotted and are compared with the growth on typical substrates described in Chapter 5. The results of these experiments show the improvement of the thickness and the top surface area. The linear thickness increased from approximately 1.5 mm to 2.6 mm, and the normalized area gain increased from approximately 1.9 times to 2.5 times. The two dotted horizontal lines in the plot represent the normalized original HPHT seed area, and the maximum area gain may be achieved in one growth step with the pockets used in the experiments that are described in Chapter 5. The pink line in Figure 6.14 is the best fit curve that was drawn in reference [20] between experimental data for previous results reported.

6.5.3 Summary Remarks: SCD Re-growth and Expanding Surfaces

After a designing, a new substrate pocket holder, thick CVD SCD substrate up to 2.6 mm were grown when one additional growth step was added. The total top surfaces were re-grown and had final surface areas of up to 2.5 times over the initial HPHT seed. This new pocket holder geometry can re-grow SCD both vertically and horizontally. For this pocket geometry, the final top surface is expanded while the smoothness remains the same. These exploratory experiments have demonstrated that by adding a second growth step and by growing at constant substrate temperature additional CVD SCD can be added to the SCD grown in the first step. The newly grown SCD had high lateral growth rates and further enlarged the final SCD surface areas.

CHAPTER 7

PHOTOGRAPHIC EVALUATION OF THE SCD SURFACE GROWTH VERSUS TIME

7.1 Introduction

The broad investigation carried out in previous chapters revealed that the growth of different SCD crystal shapes closely depends on growth time, substrate temperature, and pocket geometries. It was also found that the growth of PCD on the substrate holder plays a decisive role in the growth of large volume SCDs. Presently, the maximum SCD area gain, achieved for a single growth run is 2.3 times and when a second growth run was added the top surface could be expanded 2.6 times. Before research activities move forward in the exploration of more pocket holder geometries, it is important to understand and assess the growth evolution of the SCDs versus time in order to continue to enlarge the crystal area even further than 2.6 times.

This chapter presents a new experimental technique that attempts to measure the in-situ evolution of the lateral SCD growth versus time by using photographs and video recording. Photographs are helpful to observe the lateral growth at a specific growth time.

The videos provide further information about the plasma behavior and also provide an overview of actually how the SCD top surface evolves and grows versus time.

The data presented here was collected from a few experimental runs already shown in previous chapters. Thus, here is an exploratory study based on high-resolution photographs. The experimental data presented here does not include all the data that was measured, but due to the large number of photos that were measured many of the photos could be omitted without affecting the accuracy of the final results. The photographic plasma diagnostic techniques presented here have proved very useful in recording the plasma and the diamond growth behaviors versus time, and are expected to be very usefully employed in future experimental microwave plasma studies at MSU.

7.2 Photographic Images Processing and Video Creation

High-resolution pictures of the growth process were taken using a CANON EOS 60D 8.2-megapixel semi-professional digital single-lens reflex camera with 60-mm lens. The photographs were taken at a high angle through a screened window located adjacent to the pyrometer. The window is at the top of the bell jar. The camera was located at a fixed position on a tripod outside of the reactor at an incident angle of approximately 75° to maintain a comparable fixed reference position. For comparison between the images, all parameters were held constant for all experimental conditions. For example, the focal length was kept at 60 mm, 1/5 focal aperture, ISO 100 and the camera was perfectly focused on the substrate rather than the bell jar or cavity spy hole (screened window). The experimental setup is displayed in Figure 7.1. The Canon EOS 60D camera has a port on the right side of a remote switch with a type N3 terminal in which an appropriate

pinout was connected. The timer was set to take a picture every 2 minutes. See section 3.2.6 for more details about the camera settings. The video of each set of experiments was created based on a sequence of the photographs captured during each growth process.

All photographs were taken at the following operational condition: the pressure of 240 Torr, methane concentration of 5% and total gas flow of 420 sccm. The camera automatically takes pictures after the plasma ignition.

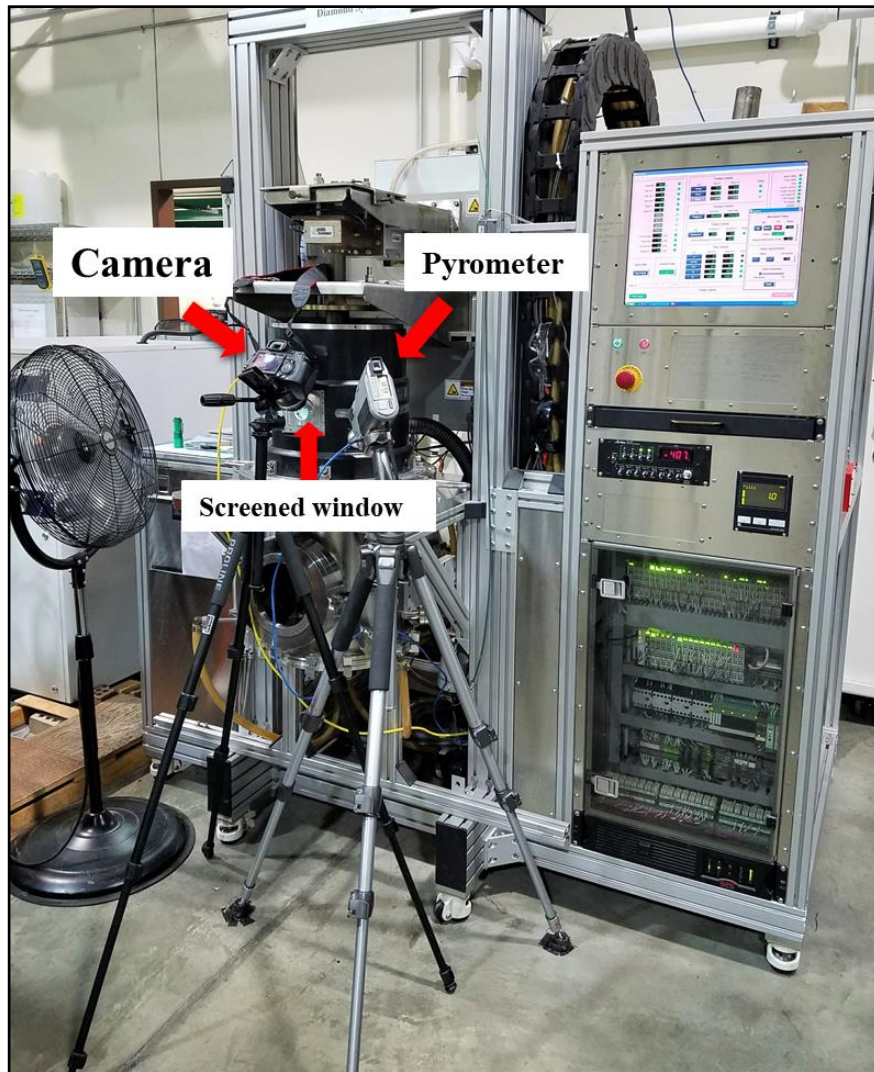


Figure 7.1 Experimental setup for photographs and video recording for SCD lateral growth analysis

The growth process continues operating in prescribed growth recipe, i.e. constant substrate temperature, while the camera captures the SCD lateral growth over time. At the end of the process, all images are processed and analyzed.

7.3 Data Acquisition

The process of data acquisition presented here is the result of software created specifically for the analysis of the growth of diamond inside a pocket holder based on image analysis. The camera setup and software are still under exploratory analysis and development.

After processing the videos from 15 different experiments, the horizontal growth of the SCD over time was clearly observed. Also, the initial fast growth of the PCD on the substrate holder and into the pocket walls was captured after approximately 12 hours. Thus, it was decided to select several images from different growth times to analyze the SCD and PCD growth carefully. During the lengthy growth process experiments, the number of images to select and analyze became larger. Typically, increments in sets of 20 photos were chosen until reaching a total of approximately 80 photos per experiment. Hence, the software displayed the first photo where the area of the SCD and PCD are selected. The process is repeated until the latest photo of the set. The complete process is schematically represented in Figure 7.2.

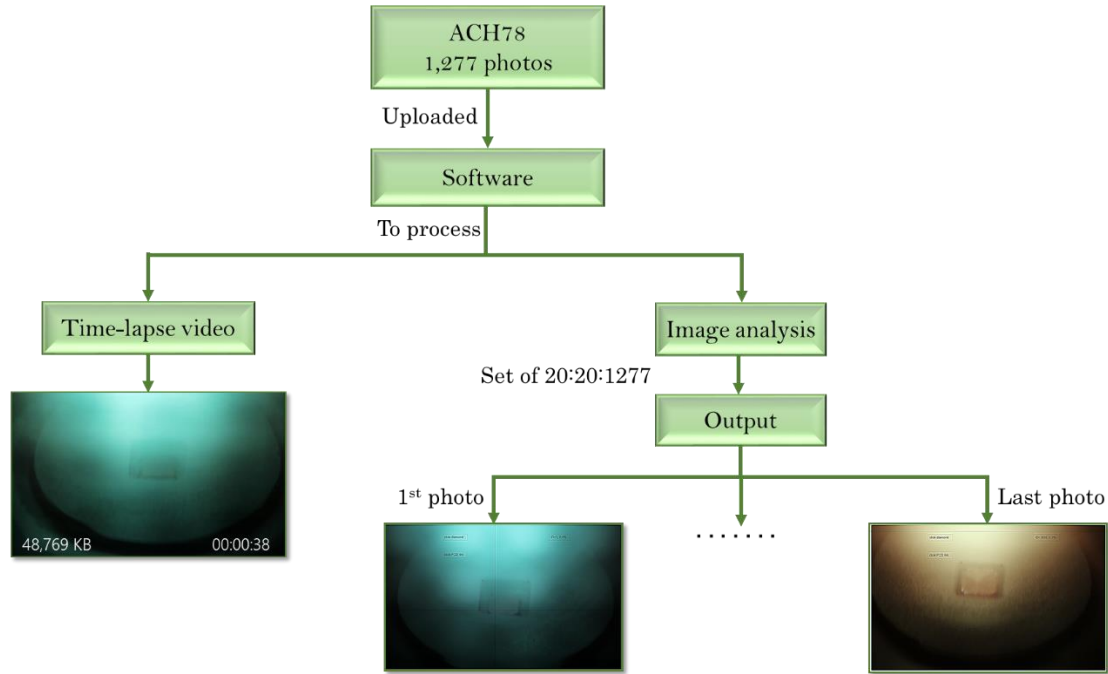


Figure 7.2 Schematic of the data acquisition process. The photographed experiment showed in the flow diagram is ACH78. A total of 1277 pictures were captured.

After the process is completed, the area of the SCD and PCD as a function of the time is provided by the software. Since this is an image-processing software, all the measurements are in pixels versus time. The equation to convert the area from pixels to mm^2 can be written as follow:

$$\left(\frac{A_i}{A_n} = [\text{mm}^2 / \text{pixels}] \right) \quad (21)$$

$$\frac{[\text{mm}^2]}{\text{pixels}} \times (A_f [\text{pixels}]) = A_{\text{SCD}} [\text{mm}^2] \quad (22)$$

where A_i is the initial area measured on the seed at $t = 0$, i.e. $\sim 3.6 \text{ mm} \times 3.6 \text{ mm}$ for one HPHT seed, A_n is the area at n time - measured in pixel - calculated by the software, and A_f is the final area. The result of this ratio is multiplied by the final area calculated by the software. As a result, the area is converted to mm^2 for subsequent comparison with the area measured manually with calibrated instruments. This latter data was presented in chapter 5 and 6. Also, the lateral growth rate can be calculated using these values. A similar approach is used to calculate the area of the PCD that grew into the pocket. The area is calculated using the difference between the area of the pocket aperture at $t = 0$ and the area of the pocket after the growth process is completed.

7.4 Preliminary Results

Here are presented the results of three experiments that grew in different pocket apertures, such as ACH64, ACH55, and ACH78 that were grown in pocket apertures of $w_1 = 6.0 \text{ mm}$, $w_2 = 6.6 \text{ mm}$ and $w_3 = 7.0 \text{ mm}$, respectively. The photographed experiment ACH64 was grown at constant substrate temperature for 48 hours at a growth rate of 26 um/h . The measured total thickness was 1.21 mm , and the total top surface area was 17.65 mm^2 . Thus, the substrate top surface area grew 1.3 times. The total number of photos captured for this experiment was 1030. The experimental data for substrates ACH55 and ACH78 were given in Table 6.1. A total amount of 430 and 1,277 photos were collected for the experiments ACH55 and ACH78 respectively. All the images were uploaded and processed by the software. Increments in sets of 15 photos were selected to calculate the lateral growth area on the SCD and the PCD on substrate ACH64. Similarly, increments in sets of 5 photos were chosen on substrate ACH55 and

increments in sets of 20 photos were selected on substrate ACH78. As a result, the initial area, the final area and the lateral growth rate calculated by the software for the SCD in summarized in Table 7.1. Also, the table displays the measured values for each grown substrate, i.e. measured by an instrument. Table 7.2 summarized the initial area, the final area and the inward PCD growth calculated by the software.

Table 7.1 Measured and calculated values of the SCD areas and SCD lateral growth rate for ACH64, ACH55, and ACH78. An instrument manually collected the measured values, and the software collected the calculated.

Sample	Method	A_i (mm ²)	A_f (mm ²)	$V_{(110)}$ ($\mu\text{m}/\text{h}$)
ACH64	Measured	13.0*	17.6	6.3
	Calculated	12.9	14.3	1.9
ACH55	Measured	13.0*	22.0	10.0
	Calculated	12.8	17.8	5.6
ACH78	Measured	13.0*	28.7	20.0
	Calculated	12.2	25.4	16.0

** This is the HPHT seed area.*

Table 7. 2 Calculated values of the PCD inward growth on the pocket wall for experiments: ACH64, ACH55, and ACH78.

Sample	Method	A_i (mm ²)	A_f (mm ²)	Inward growth rate (μm/h)
ACH64	Measured	36.0*	--	--
	Calculated	36.8	20.43	15.4
ACH55	Measured	43.6*	--	--
	Calculated	43.5	22.5	16.8
ACH78	Measured	49.0*	--	--
	Calculated	48.2	33.1	13.8

**These are the pocket aperture areas.*

Note: that the pocket aperture width represents the initial PCD area and the pocket aperture size after completed the experiment represents the final PCD area. Thus, the PCD inward growth rates were calculated using the length of the PCD that grew into the pocket. It is the difference between the pocket width before and after the growth process. The software calculated the final PCD areas for all these exploratory analyses. These values were not measured for any of the experiments. Hence, the PCD inward growth rates presented here are based on the experimental data that was measured photographically by the images and not by the final experimental measurements made after a run was completed.

The values provided from the photo software calculations differs from the experimental data that was measured presented in Chapters 5 and 6. The SCD final area had a calculated percent error of 23% for the substrate ACH64 and ACH55 and 13% for ACH78. The lateral SCD growth rate had a calculated percent error within 25 - 44% between the

experimental data and the image-based data. Despite the differences in values, the growth regions identified in Chapter 6 can also be observed using this approach.

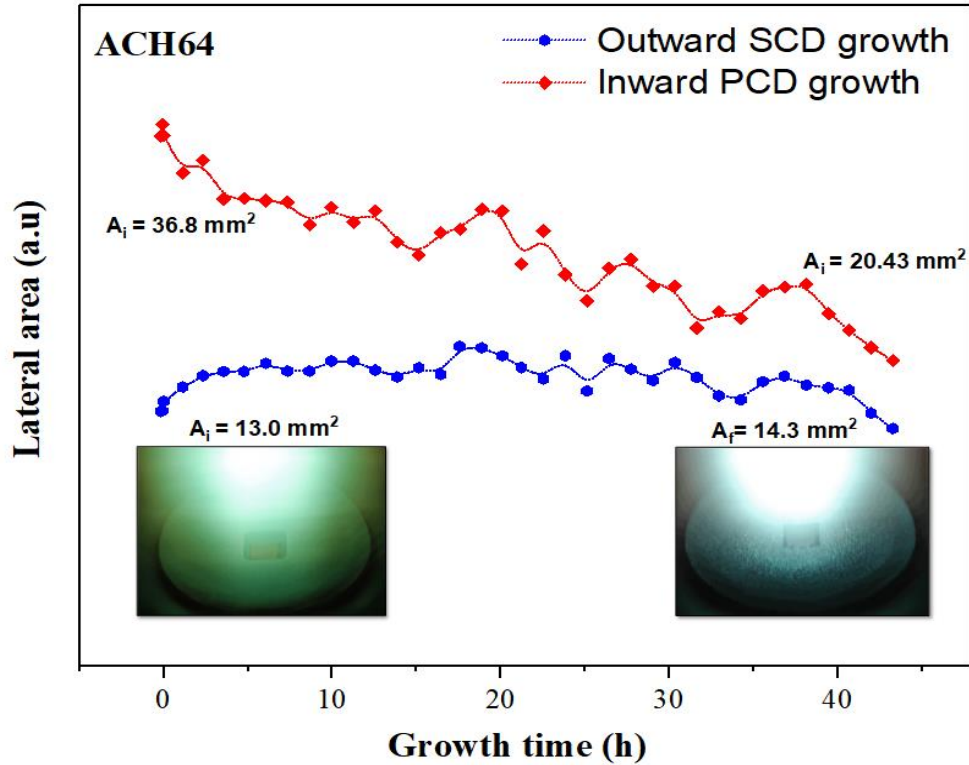


Figure 7.3 The outward SCD growth and the inward PCD growth versus growth time for substrate ACH64.

The outward SCD growth and the inward PCD growth versus time for substrate ACH64 are plotted in Figure 7.3. The images on the insert on the bottom side of the figure are the photographs at the beginning and just before finishing the experiment. The based-images data showed the fast SCD lateral growth on the early stage of the growth process during approximately the first 15 hours. Then, the lateral growth of the SCD is slowed, and the PCD starts the rapid growth into the pocket walls, and as results, the pocket

aperture decreases. See the red curve in Figure 7.3. Finally, the latest growth stage is led by the faster PCD growth into the pocket and the reduction in the final SCD top surface area. The image-based analysis for ACH64 confirmed the results found in Chapter 5 and 6 where the three growth regions were identified.

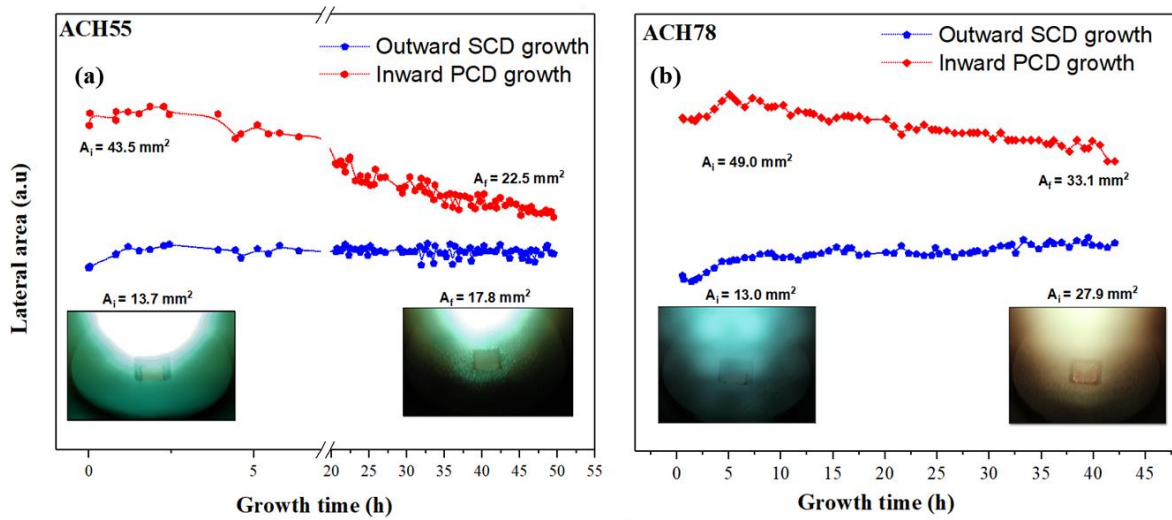


Figure 7.4 The outward SCD growth and the inward PCD growth versus growth time for (a) substrate ACH64 and (b) substrate ACH78.

Figure 7.4 (a) and (b) shows the outward SCD growth and the inward PCD growth versus time for substrate ACH64 and ACH78 respectively. Both figures followed the same trend observed for ACH64. Note that the gap between the SCD area and the PCD area decreases, due to the decrease of the pocket aperture. Also, this can be seen in the insert images on the bottom side of each figure.

7.5 Summary Remarks

Photographs were automatically taken every two minutes of the entire growth process in order to observe the SCD growth over time. The photos show the evolution of the lateral SCD growth as a function of the time. Also, they show the overgrowth of the PCD on the substrate holder and into the walls of the pocket.

It was confirmed by the images processing method that after ~ 45 hours the SCD area decreased due to the growth of PCD into the pocket. The PCD inward growth rate into the pocket was calculated as high as ~ 17 $\mu\text{m}/\text{h}$.

The SCD lateral growth calculations based on the images showed low values in comparison with the values measured manually and reported in chapter 5 and 6. The calculated error was up to 44% for the substrates grown with a longer run. These inaccurate results are in part attributed to the angled camera position. Also, due to the distortion of the image that might have occurred in looking through the quartz dome.

This image-based approach has been not optimized for accurate values. Further research on the optimization the method and the relocation the camera will be needed. However, this approach is expected to be very usefully employed in future experimental microwave plasma studies at MSU.

CHAPTER 8

SUMMARY AND FUTURE WORK

8.1 General Summary

This thesis explored MPACVD the MPACVD growth of SCD using the “pocket holder” geometry shown in Figure 3.15 and Figure 5.1. One important objective was to learn how the pocket holder geometry influences the diamond deposition process. With this objective in mind an experimental investigation was carried out which primarily varied the pocket dimensions while all other input variables were held fixed. However, the experimental plan deviated from this plan by making a few necessary exceptions and allowing the following input variables also to vary: (1) in order to maintain a constant substrate temperature, the input power had to be varied over time within each process cycle run. (2) In one set of experiments, the substrate temperature was purposely varied versus time in in order to achieve an improved final grown SCD. (3) The experimental run time was allowed to vary from 10 hours to in a few cases to over 90 hours, and (4) in one set of experiments the methane concentration was varied. The experiments varied the pocket dimensions, like the depth and aperture width, one small step per experimental run at a time. Using the MCPR reactor C (see Figure 3.14) single crystal diamond growth

was experimentally investigated over a large input variable space. Individual experimental run times were varied between ~10 hours to 60 hours.

Especially, the following experimental variables were varied one variable at a time per run: (1) the pocket depth, d_i , between 2.0 mm – 4.0 mm, (2) the pocket aperture width, w_i , between 6.0 mm and 7.0 mm and (3) the process cycle run time from about ~10 hours to about 60 hours for the single run experiments and it was varied up to 90 hours for the re-growth experiments, and in (4) one set experiments the methane concentration was varied between 4% and 7%.

The following input variables were held constant: (1) excitation frequency was fixed at 2.45 GHz; (2) flow rate was held at ~ 420 sccm; (3) for most of the experiments the methane concentration was fixed at 5%, and then one set experiment it was varied from 4% to 7%; (4) the operating pressure held constant at 240 Torr; and as indicated in the paragraph above (5) the deposition time was varied between 10 hours and 60 hours. The coupled input power/substrate temperature input variable was varied by adjusting the substrate thermal cooling rate and the input power where the reactor operated between the substrate temperature SCD deposition window of 950 – 1200 °C. Typically the experiments required between 2.0 kW – 3.5 kW of input power to achieve the desired substrate temperature.

8.2 Accomplishments

High quality, stress-free SCDs and PCD rim free SCD were grown with both an expanding surface top surface and an increasing thickness [125], [159]. Linear growth rates were between 24 – 30 $\mu\text{m/h}$ and surface area gains of 2.1 – 2.3 times for a single run and 2.5 times for an additional growth step. These experiments have demonstrated that moving to high pressure, higher power density and low N_2 growth conditions result in high growth rates with improved quality and almost stress-free SCD. Thick, PCD rimless, high quality, and low-stress SCD were grown. The etching experiments on the grown SCD plates have displayed low defect densities. The analysis of such plates with etch pit density measurements has shown a reduction in etch pit density in CVD SCD plates to $\approx 10^4$ etch pits/ cm^2 [160].

It was discovered that PCD grown rim could be eliminated by using the proper pocket size, and by stopping the run before the SCD diamond emerged from the pocket. The process has to be stopped before the growing SCD starts to emerge from the pocket. It was found that a PCD rim could reappear when the methane concentrations were varied above > 6% and also simultaneously shoot formation in the reactor also occurred under these conditions.

It was found that SCD growth in a pocket could grow PCD rimless SCD with expanding surface areas. The growth of thicker and larger area SCD without creating a PCD rim was facilitated by real time controlling the process, i.e. varying power and substrate temperature, versus time. Large area and PCD rimless growth could be optimized by applying the appropriate input power/substrate temperature process recipe.

It was discovered that the evolution of the diamond crystal growth in the pocket growth could be divided into three growth regions: (1) region I where the lateral growth was high, (2) region II with (a) a steady thickness (vertical) growth and (b) a diminished lateral growth that is limited by the proximity of the pocket walls and (3) region III where the growth is affected and limited by the growth of PCD on the substrate holder and into the pocket aperture itself.

In the initial growth region I, the lateral SCD growth can be high ($\sim 52 \mu\text{m/h}$) if the appropriate power/temperature recipe is applied. Typically, this requires that the $T_s > 1000^\circ\text{C}$. Then the initial SCD growth is over the entire seed surface, and also the SCD grows both vertically and horizontally. This leads a SCD growth with an initially expanding surface. In this growth region, the growing SCD surface area expands horizontally at high growth rates in the pocket and approaches and is limited by the pocket walls.

In growth region II is mainly vertical. The lateral growth continues although at a much slower rate. The lateral growth is limited by the presence of the pocket walls. Vertical growth continues throughout this region at about the same rate of typically, $27 - 29 \mu\text{m/h}$.

In growth region III the SCD growth is affected and limited by the growth PCD on the top surface of the substrate holder, and eventually into the aperture of the pocket and there by reduces the effective deposition aperture area. The top surface area contracts and become smaller; i.e. the lateral growth becomes negative. This is undesirable, and the PCD growth on the substrate holder should be avoided.

As the pocket aperture is increased, the upward growth rate is almost steady at $27 - 29 \mu\text{m/h}$. The growth rate slightly increases as the aperture width increases from 6.0 mm to 7.0 mm . Upward growth rate only slightly increases as time increases from $12 - 50$

hours, and decreases at 55 hours. In all the experiments, the initial (10 – 15 hour) lateral growth rate is very high, for example, 48 – 52 $\mu\text{m/h}$, in the early phases of growth in region I. In region II the lateral growth rate significantly slows as the lateral growth is inhibited by the presence of the walls of the pocket.

Finally, this thesis activity introduces a new photographic method to evaluate the top surfaces versus growth time. The photographic plasma diagnostic techniques have proved very useful in recording the plasma and the diamond growth behaviors versus time. The results of the growth evaluation present significant differences with the measured manually results. The accuracy of these first photo measurement results should be improved in future diamond growth research activities at MSU. More work needs to be done in order to employ this method in future microwave plasma studies.

8.3 Publications Resulting from this Dissertation Research

The detailed experimental SCD growth in a fixed pocket holder geometry at variable substrate temperature and variable microwave input power as a function of the time described in this dissertation has been published [125].

The detailed experimental SCD growth in a variable pocket holder depth at a constant substrate temperature versus time that is described in this dissertation has been published [159].

8.4 Future Work

Based on the current results presented in this dissertation, there are a number of recommendations that should be investigated further. Listed below are examples of future work:

1. Explore the SCD growth on larger initial starting seeds. For example, the future experiments should start with 7.0 mm x 7.0 mm seeds and bigger starting pockets.
2. Explore SCD growth with a series of three to ten short 10 – 15-hour experiments that use aperture widths and depths that favor the large initial lateral growth rates and growing relatively thin CVD SCD but with large area top surfaces. Each experimental run would deposit about a 0.3 – 0.5 mm thick CVD substrate with a top surface that is expanding at the rate of a surface gain of 1.5 – 1.7 per run.
3. Explore the growth process at even deeper and wider pocket, such as $d = 3.3$ mm and $w = 8.0$ mm. This would further increase the lateral growth rate in shorter runs.
4. Re-growth in surfaces with expanded areas more than 2.3 times. It could allow further increased the top surface.
5. Investigate the growth process in a pocket holder at higher pressures, such as 450 – 500 Torr. The discharge power density and species densities would increase further, which might increase the final diamond size, increase the diamond growth rate and could improve the diamond quality even further.
6. Explore the photographic evaluation method. This would be useful to evaluate in-situ the lateral diamond growth. This suggests re-designing the cavity shell and installing a camera closely and perpendicular to the top of the seed.

REFERENCES

REFERENCES

- [1] J. J. Gracio, Q. H. Fan, and J. C. Madaleno, "Diamond growth by chemical vapour deposition," *J. Phys. D Appl. Phys. J. Phys. D Appl. Phys.*, vol. 43, no. 43, pp. 374017–374017, 2010.
- [2] E. W. John Wilks, *Properties and Applications of Diamond*, 1st ed. 1991.
- [3] R. S. Balmer *et al.*, "Chemical vapour deposition synthetic diamond: materials, technology and applications.," *J. Phys. Condens. Matter*, vol. 21, no. 36, p. 364221, 2009.
- [4] H. O. Pierson, "HANDBOOK OF CARBON , GRAPHITE , DIAMOND AND FULLERENES by."
- [5] M. Gabrysch, "Electronic Properties of Diamond."
- [6] A. S. Barnard, *The Diamond Formula. Diamond Synthesis: a gemmological perspective*. Oxford: Butterworth-Heinemann, 2000.
- [7] J. E. Field, "The Properties of Natural and Synthetic Diamond," *Cryst. Res. Technol.*, vol. 28, no. 5, p. 602, 1993.
- [8] M. SSchreck, J. Asmussen, S. Shikata, J.-C. Arnault, and N. Fujimori, "Large-area high-quality single crystal diamond," *MRS Bull.*, vol. 39, no. June, pp. 504–510, 2014.
- [9] F. Silva, K. Hassouni, X. Bonnin, and A. Gicquel, "Microwave engineering of plasma-assisted CVD reactors for diamond deposition.," *J. Phys. Condens. Matter*, vol. 21, no. 36, p. 364202, 2009.
- [10] Y. Mokuno, A. Chayahara, Y. Soda, Y. Horino, and N. Fujimori, "Synthesizing single-crystal diamond by repetition of high rate homoepitaxial growth by microwave plasma CVD," *Diam. Relat. Mater.*, vol. 14, no. 11–12, pp. 1743–1746, 2005.
- [11] Y. Mokuno, A. Chayahara, Y. Soda, H. Yamada, Y. Horino, and N. Fujimori, "High rate homoepitaxial growth of diamond by microwave plasma CVD with nitrogen addition," *Diam. Relat. Mater.*, vol. 15, no. 4–8, pp. 455–459, 2006.
- [12] M. Muehle, "PROCESS DEVELOPMENT TO SOLVE CRITICAL CHALLENGES MOVING TOWARDS TWO INCH SINGLE CRYSTALLINE DIAMOND WAFERS," Michigan State University, 2017.
- [13] C. S. Yan, Y. K. Vohra, H. Mao, and R. J. Hemley, "Very high growth rate chemical

- vapor deposition of single-crystal diamond,” *Proc. Natl. Acad. Sci.*, vol. 99, no. 20, pp. 12523–12525, 2002.
- [14] Q. Liang *et al.*, “Recent advances in high-growth rate single-crystal CVD diamond,” *Diam. Relat. Mater.*, vol. 18, no. 5–8, pp. 698–703, 2009.
 - [15] E. V. Bushuev *et al.*, “Express in situ measurement of epitaxial CVD diamond film growth kinetics,” *Diam. Relat. Mater.*, vol. 72, pp. 61–70, 2017.
 - [16] J. Lu, Y. Gu, T. A. Grotjohn, T. Schuelke, and J. Asmussen, “Experimentally defining the safe and efficient, high pressure microwave plasma assisted CVD operating regime for single crystal diamond synthesis,” *Diam. Relat. Mater.*, vol. 37, pp. 17–28, 2013.
 - [17] D. G. Goodwin, “Scaling laws for diamond chemical-vapor deposition. I. Diamond surface chemistry,” *J. Appl. Phys.*, vol. 74, no. 11, pp. 6888–6894, 1993.
 - [18] Y. Gu, J. Lu, T. Grotjohn, T. Schuelke, and J. Asmussen, “Microwave plasma reactor design for high pressure and high power density diamond synthesis,” *Diam. Relat. Mater.*, vol. 24, pp. 210–214, 2012.
 - [19] “20161108 Issued Patent TEC2007-0078-01.pdf.” .
 - [20] S. Nad, Y. Gu, and J. Asmussen, “Growth strategies for large and high quality single crystal diamond substrates,” *Diam. Relat. Mater.*, vol. 60, pp. 26–34, 2015.
 - [21] K. E. S. and J. P. Dismukes, *Synthesis diamond: emerging CVD science and technology*, 1st ed. 1997.
 - [22] A. G. Inc, “No Title.” [Online]. Available: <http://www.galleries.com/>.
 - [23] Jeremy Harvey, “No Title,” *University of Bristol, Physical and Theoretical Chemistry*. [Online]. Available: <http://www.chm.bris.ac.uk/pt/harvey/gcse/covalent.html>.
 - [24] J. E. Field, *The Properties of Diamond*, 1st editio. Academic Press Inc., 1979.
 - [25] F. P. BUNDY, H. T. HALL, H. M. STRONG, and R. H. WENTORF, “Man-Made Diamonds,” *Nature*, vol. 176, no. 4471, pp. 51–55, 1955.
 - [26] W. G. Eversole, “No Title,” United States Patent No. 303187 and 303188 (1962)No. 303187 and 303188, 1962.
 - [27] B. V. Spitsyn, L. L. Bouilov, and B. V. Derjaguin, “Vapor growth of diamond on diamond and other surfaces,” *J. Cryst. Growth*, vol. 52, no. PART 1, pp. 219–226, 1981.

- [28] S. Matsumoto, Y. Sato, M. Kamo, and N. Setaka, "Vapor Deposition of Diamond Particles from Methane," *Jpn. J. Appl. Phys.*, vol. 21, no. Part 2, No. 4, pp. L183–L185, 1982.
- [29] S. S. Matthias Schreck , Jes Asmussen and and N. F. Jean-Charles Arnault, "Large-area high-quality single crystal diamond," *MRS Bull. suppl. CVD Diamond--Research, Appl. Challenges*, vol. 39.6, p. 504–510., 2014.
- [30] D. D. Hof, J. A. Dinsmore, S. Barber, R. Suhr, and T. R. Scofield, "Advocacy : The T . R . A . I . N . E . R . Model," vol. 2, no. 1, pp. 15–28, 2009.
- [31] C. Station, "General electric company schenectady, new york," *Power*, vol. 3, no. 4, pp. 2030–2036, 1987.
- [32] H. M. BUNDY, F. P. Strong, "Behavior of Metals at High Temperatures and Pressures," *Solid State Physics-Advances Res. Appl.*, vol. 13, pp. 81–146, 1962.
- [33] B. W. Paul M, "Diamond thin films: a 21st-century material," *Phil. Trans. R. Soc. Lond. A*, vol. 358, no. Tennant 1797, pp. 473–495, 2000.
- [34] S. Matsumoto, Y. Sato, M. Tsutsumi, and N. Setaka, "Growth of diamond particles from methane-hydrogen gas," *J. Mater. Sci.*, vol. 17, no. 11, pp. 3106–3112, 1982.
- [35] J. E. B. F. G. Celii, "Diamond Chemical Vapor-Deposition," no. 42, pp. 643–684, 1991.
- [36] M. Kamo, "Synthesis of diamond from gas phase and its properties," *Synthesis (Stuttg.)*, vol. 7, no. 2, pp. 7–12, 1990.
- [37] T. F. Diamond, C. Vapour, and D. Methods, "Thin Film Diamond by Chemical Vapour Deposition Methods," pp. 21–30, 1992.
- [38] K. E. Spear, "Diamond -Ceramic Coating of the Future," *Perspective*, vol. 91, no. 72, pp. 171–91, 1989.
- [39] M. Frenklach, "The role of hydrogen in vapor deposition of diamond," *J. Appl. Phys.*, vol. 65, no. 12, pp. 5142–5149, 1989.
- [40] M. N. R. Ashfold, P. W. May, C. A. Rego, and N. M. Everitt, "Thin film diamond by chemical vapour deposition methods," *Chem. Soc. Rev.*, vol. 23, no. 1, p. 21, 1994.
- [41] S. J. Harris, "Mechanism for diamond growth from methyl radicals," *Appl. Phys. Lett.*, vol. 56, no. 23, pp. 2298–2300, 1990.
- [42] S. Farhat, C. Findeling, F. Silva, K. Hassouni, and A. Gicquel, "Role of the plasma composition at the surface on diamond growth," *J. Phys. IV Fr.*, vol. 8, p. Pr7-391-Pr7-399, 1998.

- [43] D. Takeuchi, H. Watanabe, S. Yamanaka, H. Okushi, and K. Kajimura, "Homoepitaxial diamond films grown by step-flow mode in various misorientation angles of diamond substrates," *Diam. Relat. Mater.*, vol. 9, no. 3, pp. 231–235, 2000.
- [44] M. Kamo, H. Yurimoto, and Y. Sato, "Epitaxial growth of diamond on diamond substrate by plasma assisted CVD," *Appl. Surf. Sci.*, vol. 33–34, no. C, pp. 553–560, 1988.
- [45] K. Hayashi, S. Yamanaka, H. Okushi, and K. Kajimura, "Stepped growth and etching of (001) diamond," *Diam. Relat. Mater.*, vol. 5, no. 9, pp. 1002–1005, 1996.
- [46] D. Takeuchi *et al.*, "High quality homoepitaxial diamond thin film synthesis with high growth rate by a two-step growth method," *Diam. Relat. Mater.*, vol. 8, no. 6, pp. 1046–1049, 1999.
- [47] H. Watanabe, D. Takeuchi, S. Yamanaka, H. Okushi, K. Kajimura, and T. Sekiguchi, "Homoepitaxial diamond film with an atomically flat surface over a large area," *Diam. Relat. Mater.*, vol. 8, no. 7, pp. 1272–1276, 1999.
- [48] C.-S. Yan and Y. K. Vohra, "Multiple twinning and nitrogen defect center in chemical vapor deposited homoepitaxial diamond," *Diam. Relat. Mater.*, vol. 8, no. 11, pp. 2022–2031, 1999.
- [49] A. Tallaire, J. Achard, F. Silva, R. S. Sussmann, and A. Gicquel, "Homoepitaxial deposition of high-quality thick diamond films: Effect of growth parameters," in *Diamond and Related Materials*, 2005, vol. 14, no. 3–7, pp. 249–254.
- [50] G. Bogdan *et al.*, "Growth and characterization of near-atomically flat, thick homoepitaxial CVD diamond films," *Phys. Status Solidi Appl. Mater. Sci.*, vol. 202, no. 11, pp. 2066–2072, 2005.
- [51] T. Teraji and T. Ito, "Homoepitaxial diamond growth by high-power microwave-plasma chemical vapor deposition," *J. Cryst. Growth*, vol. 271, no. 3–4, pp. 409–419, 2004.
- [52] O. A. Williams and R. B. Jackman, "High growth rate MWPECVD of single crystal diamond," *Diam. Relat. Mater.*, vol. 13, no. 4–8, pp. 557–560, 2004.
- [53] O. A. Williams and R. B. Jackman, "Homoepitaxial growth for surface conductive device applications," *Diam. Relat. Mater.*, vol. 13, no. 2, pp. 325–328, 2004.
- [54] T. Teraji, "Chemical vapor deposition of homoepitaxial diamond films," *Phys. Status Solidi*, vol. 203, no. 13, pp. 3324–3357, 2006.
- [55] C. Wang, M. Irie, and T. Ito, "Growth and characterization of hillock-free high quality

- homoepitaxial diamond films,” *Diam. Relat. Mater.*, vol. 9, no. 9, pp. 1650–1654, 2000.
- [56] A. Tallaire, J. Achard, F. Silva, O. Brinza, and A. Gicquel, “Growth of large size diamond single crystals by plasma assisted chemical vapour deposition: Recent achievements and remaining challenges,” *Comptes Rendus Physique*, vol. 14, no. 2–3, pp. 169–184, 2013.
 - [57] T. Bauer, M. Schreck, H. Sternschulte, and B. Stritzker, “High growth rate homoepitaxial diamond deposition on off-axis substrates,” *Diam. Relat. Mater.*, vol. 14, no. 3–7, pp. 266–271, 2005.
 - [58] J. Achard, A. Tallaire, R. Sussmann, F. Silva, and A. Gicquel, “The control of growth parameters in the synthesis of high-quality single crystalline diamond by CVD,” *J. Cryst. Growth*, vol. 284, no. 3–4, pp. 396–405, 2005.
 - [59] N. Lee and A. Badzian, “A study on surface morphologies of (001) homoepitaxial diamond films,” *Diam. Relat. Mater.*, vol. 6, no. 1, pp. 130–145, 1997.
 - [60] N. Lee and A. Badzian, “Effect of misorientation angles on the surface morphologies of (001) homoepitaxial diamond thin films,” *Appl. Phys. Lett.*, vol. 67, no. 1, p. 2011, 1995.
 - [61] N. Lee and A. Badzian, “Effect of methane concentrations on surface morphologies and surface structures of (001) homoepitaxial diamond thin films,” *Appl. Phys. Lett.*, vol. 67, no. 1, p. 2011, 1995.
 - [62] K. Hayashi, S. Yamanaka, H. Watanabe, T. Sekiguchi, H. Okushi, and K. Kajimura, “Diamond films epitaxially grown by step-flow mode,” *J. Cryst. Growth*, vol. 183, pp. 338–346, 1998.
 - [63] A. Tallaire *et al.*, “Characterisation of high-quality thick single-crystal diamond grown by CVD with a low nitrogen addition,” *Diam. Relat. Mater.*, vol. 15, no. 10, pp. 1700–1707, 2006.
 - [64] P. Martineau, M. Gaukroger, R. Khan, and D. Evans, “Effect of steps on dislocations in CVD diamond grown on {001} substrates,” *Phys. Status Solidi Curr. Top. Solid State Phys.*, vol. 6, no. 8, pp. 1953–1957, 2009.
 - [65] A. Tallaire *et al.*, “Dislocations and impurities introduced from etch-pits at the epitaxial growth resumption of diamond,” *Diam. Relat. Mater.*, vol. 20, no. 7, pp. 875–881, 2011.
 - [66] F. K. De Theije, J. J. Schermer, and W. J. P. Van Enckevort, “Effects of nitrogen impurities on the CVD growth of diamond: Step bunching in theory and experiment,” *Diam. Relat. Mater.*, vol. 9, no. 8, pp. 1439–1449, 2000.

- [67] A. Gicquel, E. Anger, M. F. Ravet, D. Fabre, G. Scatena, and Z. Z. Wang, "Diamond deposition in a bell-jar reactor: influence of the plasma and substrate parameters on the microstructure and growth rate," *Diam. Relat. Mater.*, vol. 2, no. 2–4, pp. 417–424, 1993.
- [68] J. Asmussen and D. K. Reinhard, *Diamond Films Handbook*. Marcel Dekker, 2002.
- [69] C. J. Chu, R. H. Hauge, J. L. Margrave, and M. P. D'Evelyn, "Growth kinetics of (100), (110), and (111) homoepitaxial diamond films," *Appl. Phys. Lett.*, vol. 61, no. 12, pp. 1393–1395, 1992.
- [70] G. Bogdan, M. Nesládek, J. D'Haen, K. Haenen, and M. D'Olieslaeger, "Freestanding (100) homoepitaxial CVD diamond," *Diam. Relat. Mater.*, vol. 15, no. 4–8, pp. 508–512, 2006.
- [71] D. Takeuchi, H. Watanabe, S. Yamanaka, H. Okushi, and K. Kajimura, "Defects in device grade homoepitaxial diamond thin films grown with ultra-low CH₄/H₂ conditions by microwave-plasma chemical vapor deposition," *Phys. Status Solidi a-Applications Mater. Sci.*, vol. 174, pp. 101–115, 1999.
- [72] T. Teraji, S. Mitani, and T. Ito, "High rate growth and luminescence properties of high-quality homoepitaxial diamond (100) films," *Phys. Status Solidi Appl. Res.*, vol. 198, no. 2, pp. 395–406, 2003.
- [73] K. W. Hemawan, T. A. Grotjohn, D. K. Reinhard, and J. Asmussen, "Improved microwave plasma cavity reactor for diamond synthesis at high-pressure and high power density," *Diam. Relat. Mater.*, vol. 19, no. 12, pp. 1446–1452, 2010.
- [74] X. Li, J. Perkins, R. Collazo, R. J. Nemanich, and Z. Sitar, "Investigation of the effect of the total pressure and methane concentration on the growth rate and quality of diamond thin films grown by MPCVD," *Diam. Relat. Mater.*, vol. 15, no. 11–12 SPEC. ISS., pp. 1784–1788, 2006.
- [75] A. Tallaire, J. Achard, F. Silva, and A. Gicquel, "Effect of increasing the microwave density in both continuous and pulsed wave mode on the growth of monocrystalline diamond films," *Phys. Status Solidi Appl. Mater. Sci.*, vol. 202, no. 11, pp. 2059–2065, 2005.
- [76] L. S. Pan, *Diamond: Electronic Properties and Applications*. KLUWER ACADEMIC PUBLISHERS, 1995.
- [77] R. Locher, C. Wild, N. Herres, D. Behr, and P. Koidl, "Nitrogen stabilized ???100??? texture in chemical vapor deposited diamond films," *Appl. Phys. Lett.*, vol. 65, no. 1, pp. 34–36, 1994.
- [78] W. Müller-Sebert, E. Wörner, F. Fuchs, C. Wild, and P. Koidl, "Nitrogen induced

- increase of growth rate in chemical vapor deposition of diamond,” *Appl. Phys. Lett.*, vol. 759, p. 759, 1995.
- [79] Q. Liang *et al.*, “Enhanced growth of high quality single crystal diamond by microwave plasma assisted chemical vapor deposition at high gas pressures,” *Appl. Phys. Lett.*, vol. 94, no. 2, p. 24103, 2009.
 - [80] S. A. Catledge and Y. K. Vohra, “Effect of nitrogen addition on the microstructure and mechanical properties of diamond films grown using high-methane concentrations,” *J. Appl. Phys.*, vol. 86, no. 1, pp. 698–700, 1999.
 - [81] I. Sunagawa, “Growth and Morphology of Crystals,” *Forma*, vol. 14, no. 358, pp. 147–166, 1999.
 - [82] Y. Bar-Yam and T. D. Moustakas, “Defect-induced stabilization of diamond films,” *Nature*, vol. 342, pp. 786–787, 1989.
 - [83] G. Z. Cao, J. J. Schermer, W. J. P. van Enckevort, W. A. L. M. Elst, and L. J. Giling, “Growth of {100} textured diamond films by the addition of nitrogen,” *J. Appl. Phys.*, vol. 79, no. 3, pp. 1357–1364, 1996.
 - [84] D. Raabe and T. Liu, “Influence of nitrogen doping on growth rate and texture evolution of chemical vapor deposition diamond films,” *Appl. Phys. Lett.*, vol. 94, no. 2, pp. 2–5, 2009.
 - [85] J. Lu, “SINGLE CRYSTAL MICROWAVE PLASMA ASSISTED CHEMICAL VAPOR DIAMOND SYNTHESIS AT HIGH PRESSURES AND HIGH POWER DENSITIES,” 2013.
 - [86] S. Nad, “GROWTH AND CHARACTERIZATION OF LARGE , HIGH QUALITY SINGLE CRYSTAL DIAMOND SUBSTRATES VIA MICROWAVE PLASMA ASSISTED CHEMICAL VAPOR DEPOSITION By Shreya Nad A DISSERTATION Submitted to Michigan State University in partial fulfillment of the requirements fo,” 2016.
 - [87] M. A. Elliott, P. W. May, J. Petherbridge, S. M. Leeds, M. N. R. Ashfold, and W. N. Wang, “Optical emission spectroscopic studies of microwave enhanced diamond CVD using CH₄/CO₂ plasmas,” *Diam. Relat. Mater.*, vol. 9, pp. 311–316, 2000.
 - [88] Y. Meng *et al.*, “High optical quality multicarat single crystal diamond produced by chemical vapor deposition,” *Phys. Status Solidi a-Applications Mater. Sci.*, vol. 209, no. 1, pp. 101–104, 2012.
 - [89] Q. Liang *et al.*, “Enhancing the mechanical properties of single-crystal CVD diamond,” *J. Phys. Condens. Matter*, vol. 21, no. 36, p. 364215, 2009.

- [90] Y. Meng *et al.*, “Enhanced optical properties of chemical vapor deposited single crystal diamond by low-pressure/high-temperature annealing,” *Proc. Natl. Acad. Sci. U. S. A.*, vol. 105, no. 46, pp. 17620–17625, 2008.
- [91] A. Chayahara *et al.*, “The effect of nitrogen addition during high-rate homoepitaxial growth of diamond by microwave plasma CVD,” *Diam. Relat. Mater.*, vol. 13, no. 11–12, pp. 1954–1958, 2004.
- [92] Z. B. Feng, A. Chayahara, Y. Mokuno, H. Yamada, and S. Shikata, “Raman spectra of a cross section of a large single crystal diamond synthesized by using microwave plasma CVD,” *Diam. Relat. Mater.*, vol. 19, no. 2–3, pp. 171–173, 2010.
- [93] H. Yamada, A. Chayahara, Y. Mokuno, and S. ichi Shikata, “Numerical and experimental studies of high growth-rate over area with 1-inch in diameter under moderate input-power by using MWPCVD,” *Diam. Relat. Mater.*, vol. 17, no. 7–10, pp. 1062–1066, 2008.
- [94] Y. Mokuno, a. Chayahara, H. Yamada, and N. Tsubouchi, “Improving purity and size of single-crystal diamond plates produced by high-rate CVD growth and lift-off process using ion implantation,” *Diam. Relat. Mater.*, vol. 18, no. 10, pp. 1258–1261, 2009.
- [95] H. Yamada, A. Chayahara, and Y. Mokuno, “Short-pulse excitation of microwave plasma for efficient diamond growth,” *Appl. Phys. Lett.*, vol. 109, no. 9, p. 92102, 2016.
- [96] H. Yamada, A. Chayahara, Y. Mokuno, Y. Soda, Y. Horino, and N. Fujimori, “Modeling and numerical analyses of microwave plasmas for optimizations of a reactor design and its operating conditions,” *Diam. Relat. Mater.*, vol. 14, no. 11–12, pp. 1776–1779, 2005.
- [97] H. Yamada, A. Chayahara, Y. Mokuno, Y. Horino, and S. Shikata, “Numerical analyses of a microwave plasma chemical vapor deposition reactor for thick diamond syntheses,” *Diam. Relat. Mater.*, vol. 15, no. 9, pp. 1389–1394, 2006.
- [98] H. Yamada, A. Chayahara, and Y. Mokuno, “Simplified description of microwave plasma discharge for chemical vapor deposition of diamond,” *J. Appl. Phys.*, vol. 101, no. 6, 2007.
- [99] H. Yamada, A. Chayahara, Y. Mokuno, and S. ichi Shikata, “Simulation with an improved plasma model utilized to design a new structure of microwave plasma discharge for chemical vapor deposition of diamond crystals,” *Diam. Relat. Mater.*, vol. 17, no. 4–5, pp. 494–497, 2008.
- [100] H. Yamada, A. Chayahara, Y. Mokuno, and S.-I. Shikata, “Microwave plasma generated in a narrow gap to achieve high power efficiency during diamond

- growth," *Diam. Relat. Mater.*, vol. 18, no. 2–3, pp. 117–120, 2009.
- [101] H. Yamada, "Numerical Simulations to Study Growth of Single-Crystal Diamond by Using Microwave Plasma Chemical Vapor Deposition with Reactive (H , C , N) Species," vol. 51, no. 100, pp. 1–7, 2012.
 - [102] Y. Horino, A. Chayahara, and Y. Mokuno, "High-Rate Growth of Large Diamonds by Microwave Plasma Chemical Vapor Deposition with Newly Designed Substrate Holders," *New Diam. Front. Carbon Technol.*, vol. 16, pp. 63–69, 2006.
 - [103] H. Yamada, A. Chayahara, Y. Mokuno, Y. Horino, and S. Shikata, "Simulation of temperature and gas flow distributions in region close to a diamond substrate with finite thickness," *Diam. Relat. Mater.*, vol. 15, no. 10, pp. 1738–1742, 2006.
 - [104] H. Yamada, A. Chayahara, Y. Mokuno, Y. Horino, and S. Shikata, "Simulation of microwave plasmas concentrated on the top surface of a diamond substrate with finite thickness," *Diam. Relat. Mater.*, vol. 15, no. 9, pp. 1383–1388, 2006.
 - [105] Y. Mokuno, A. Chayahara, and H. Yamada, "Synthesis of large single crystal diamond plates by high rate homoepitaxial growth using microwave plasma CVD and lift-off process," *Diam. Relat. Mater.*, vol. 17, no. 4–5, pp. 415–418, 2008.
 - [106] N. Tsubouchi, Y. Mokuno, H. Yamaguchi, N. Tatsumi, A. Chayahara, and S. Shikata, "Characterization of crystallinity of a large self-standing homoepitaxial diamond film," *Diam. Relat. Mater.*, vol. 18, no. 2–3, pp. 216–219, 2009.
 - [107] N. Tsubouchi, Y. Mokuno, A. Chayahara, and S. Shikata, "Crystallinity of freestanding large undoped single crystal diamond plates produced using pre-ion-implanted substrates and lift-off processes," *Diam. Relat. Mater.*, vol. 19, no. 10, pp. 1259–1262, 2010.
 - [108] H. Yamada, A. Chayahara, Y. Mokuno, N. Tsubouchi, S. I. Shikata, and N. Fujimori, "Developments of elemental technologies to produce inch-size single-crystal diamond wafers," *Diam. Relat. Mater.*, vol. 20, no. 4, pp. 616–619, 2011.
 - [109] H. Yamada, A. Chayahara, H. Umezawa, N. Tsubouchi, Y. Mokuno, and S. Shikata, "Fabrication and fundamental characterizations of tiled clones of single-crystal diamond with 1-inch size," *Diam. Relat. Mater.*, vol. 24, pp. 29–33, 2012.
 - [110] H. Yamada, A. Chayahara, Y. Mokuno, H. Umezawa, S. I. Shikata, and N. Fujimori, "Fabrication of 1 inch mosaic crystal diamond wafers," *Appl. Phys. Express*, vol. 3, no. 5, pp. 1–4, 2010.
 - [111] M. Marchywka, P. E. Pehrsson, D. J. Vestyck, and D. Moses, "Low energy ion implantation and electrochemical separation of diamond films," *Appl. Phys. Lett.*, vol. 63, no. 25, pp. 3521–3523, 1993.

- [112] F. Silva *et al.*, "Single crystal CVD diamond growth strategy by the use of a 3D geometrical model: Growth on (113) oriented substrates," *Diam. Relat. Mater.*, vol. 17, no. 7–10, pp. 1067–1075, 2008.
- [113] F. Silva *et al.*, "High quality, large surface area, homoepitaxial MPACVD diamond growth," *Diam. Relat. Mater.*, vol. 18, no. 5–8, pp. 683–697, 2009.
- [114] A. Tallaire *et al.*, "Growth strategy for controlling dislocation densities and crystal morphologies of single crystal diamond by using pyramidal-shape substrates," *Diam. Relat. Mater.*, vol. 33, pp. 71–77, 2013.
- [115] J. Achard, F. Silva, O. Brinza, A. Tallaire, and A. Gicquel, "Coupled effect of nitrogen addition and surface temperature on the morphology and the kinetics of thick CVD diamond single crystals," *Diam. Relat. Mater.*, vol. 16, no. 4–7 SPEC. ISS., pp. 685–689, 2007.
- [116] A. Secroun, A. Tallaire, J. Achard, G. Civrac, H. Schneider, and A. Gicquel, "Photoconductive properties of lightly N-doped single crystal CVD diamond films," *Diam. Relat. Mater.*, vol. 16, no. 4–7 SPEC. ISS., pp. 953–957, 2007.
- [117] P. Djemia, A. Tallaire, J. Achard, F. Silva, and A. Gicquel, "Elastic properties of single crystal diamond made by CVD," *Diam. Relat. Mater.*, vol. 16, no. 4–7 SPEC. ISS., pp. 962–965, 2007.
- [118] F. Silva, X. Bonnin, J. Scharpf, and A. Pasquarelli, "Microwave analysis of PACVD diamond deposition reactor based on electromagnetic modelling," *Diam. Relat. Mater.*, vol. 19, no. 5–6, pp. 397–403, 2010.
- [119] A. Gicquel *et al.*, "Quantitative analysis of diamond deposition reactor efficiency," *Chem. Phys.*, vol. 398, no. 1, pp. 239–247, 2012.
- [120] F. Silva, X. Bonnin, J. Achard, O. Brinza, A. Michau, and A. Gicquel, "Geometric modeling of homoepitaxial CVD diamond growth: I. The {100}{111}{110}{113} system," *J. Cryst. Growth*, vol. 310, pp. 187–203, 2008.
- [121] M. Naamoun *et al.*, "Reduction of dislocation densities in single crystal CVD diamond by using self-assembled metallic masks," *Diam. Relat. Mater.*, vol. 58, pp. 62–68, 2015.
- [122] A. Tallaire, O. Brinza, V. Mille, L. William, and J. Achard, "Reduction of Dislocations in Single Crystal Diamond by Lateral Growth over a Macroscopic Hole," *Adv. Mater.*, vol. 29, no. 16, pp. 1–5, 2017.
- [123] G. Wu, M.-H. Chen, and J. Liao, "The influence of recess depth and crystallographic orientation of seed sides on homoepitaxial growth of CVD single crystal diamonds," *Diam. Relat. Mater.*, vol. 65, pp. 144–151, 2016.

- [124] S. Nad and J. Asmussen, "Analyses of single crystal diamond substrates grown in a pocket substrate holder via MPACVD," *Diam. Relat. Mater.*, vol. 66, pp. 36–46, 2016.
- [125] S. Nad, A. Charris, and J. Asmussen, "MPACVD growth of single crystalline diamond substrates with PCD rimless and expanding surfaces," *Appl. Phys. Lett.*, vol. 109, no. 162103, pp. 0–4, 2016.
- [126] K. Kuo and J. Asmussen, "An experimental study of high pressure synthesis of diamond films using a microwave cavity plasma reactor," *Diam. Relat. Mater.*, vol. 6, pp. 1097–1105, 1997.
- [127] S. S. Zuo, M. K. Yaran, T. A. Grotjohn, D. K. Reinhard, and J. Asmussen, "Investigation of diamond deposition uniformity and quality for freestanding film and substrate applications," *Diam. Relat. Mater.*, vol. 17, no. 3, pp. 300–305, 2008.
- [128] J. Zhang, "An investigation of electromagnetic field patterns during microwave plasma diamond thin film deposition," *J. Vac. Sci. Technol. A Vacuum, Surfaces, Film.*, vol. 8, no. 1990, p. 2124, 1990.
- [129] J. Zhang, "Experimental development of microwave cavity plasma reactors for large area and high rate diamond film deposition," Michigan State University, 1993.
- [130] D. Zhang and T. Cui, "Department of Mechanical Engineering , University of Minnesota , Minneapolis , Minnesota , USA," vol. 1996, no. I, pp. 362–365, 2011.
- [131] K. Kuo, "Microwave assisted plasma CVD of diamond films using thermal-like plasma discharge," Michigan State University, 1997.
- [132] Y. Gu, "THE NEW GENERATION MICROWAVE PLASMA ASSISTED CVD REACTOR FOR DIAMOND SYNTHESIS," 2011.
- [133] J. Asmussen *et al.*, "Process and Apparatus for diamond Synthesis," US 9487858 B2, 2009.
- [134] Canon, "CANON EOS 20D Digital Manual," 2014. [Online]. Available: <http://gdlp01.c-wss.com/gds/9/0900000259/01/EOS20DIM-EN.pdf>.
- [135] R. Diaz and A. Charris, "DS4 Box: Complement for DS4 (Diamond System 4). Michigan State University," 2017. [Online]. Available: <https://github.com/RDiazPR/DS4>.
- [136] [Http://www.bris.ac.uk/Depts/Chemistry/MOTM/diamond/diamond.htm](http://www.bris.ac.uk/Depts/Chemistry/MOTM/diamond/diamond.htm), "University of Bristol, School of Chemistry." .
- [137] J. Asmussen, "Microwave Plasma Source Technologies: A Fifty Year Evolution

from Unwanted Discharges to Free Radical Sources, to Low Pressure and Temperature Plasma Processing, to Gem Quality Diamond Synthesis,” in *AVS 62nd International Symposium*, 2015.

- [138] J. Asmussen, T. a. Grotjohn, and T. Schuelke, *Advances in Plasma Synthesis of UNCD Films*, Second Edi. Elsevier Inc., 2012.
- [139] W.-S. Huang, “Microwave Plasma Assisted Chemical Vapor Deposition of Ultra-nanocrystalline Diamond Films VOLUME I,” Michigan State University, 2004.
- [140] “HPHT Sumitomo.” [Online]. Available: <http://www.sumicarbide.com/materialsgroup/crystalu.htm>.
- [141] S. Nad, Y. Gu, and J. Asmussen, “Determining the microwave coupling and operational efficiencies of a microwave plasma assisted chemical vapor deposition reactor under high pressure diamond synthesis operating conditions,” *Rev. Sci. Instrum.*, vol. 86, no. 7, 2015.
- [142] J. Lu, Y. Gu, and J. Asmussen, “A Description of The Experimental Microwave Discharge Behavior Versus Pressure , Power and Reactor Geometry for MPACVD Diamond Synthesis Reactors,” vol. 43, no. 15, p. 153001, 2012.
- [143] L. EAG, “SECONDARY ION MASS SPECTROMETRY (SIMS).” [Online]. Available: <http://www.eaglabs.com/mc/secondary-ion-mass-spectrometry.html>.
- [144] R. C. Microscopy, “Optical Birefringence.” [Online]. Available: <http://www.olympusmicro.com/primer/lightandcolor/birefringence.html>.
- [145] O. A. Ivanov, A. B. Muchnikov, V. V Chernov, S. A. Bogdanov, A. L. Vikharev, and J. E. Butler, “Experimental study of hydrogen plasma etching of (1 0 0) single crystal diamond in a MPACVD reactor,” *Mater. Lett.*, vol. 151, pp. 115–118, 2015.
- [146] N. Tsubouchi, Y. Mokuno, and S. Shikata, “Characterizations of etch pits formed on single crystal diamond surface using oxygen/hydrogen plasma surface treatment,” *Diam. Relat. Mater.*, vol. 63, pp. 43–46, 2016.
- [147] Y. Mokuno, A. Chayahara, H. Yamada, and N. Tsubouchi, “Large Single Crystal Diamond Plates Produced by Microwave Plasma CVD,” *Mater. Sci. Forum*, vol. 615, no. 617, pp. 991–994, 2009.
- [148] H. Yamada, A. Chayahara, Y. Mokuno, Y. Kato, and S. Shikata, “A 2-in. mosaic wafer made of a single-crystal diamond,” *Appl. Phys. Lett.*, vol. 104, no. 10, pp. 10–14, 2014.
- [149] O. Brinza *et al.*, “Dependence of CVD diamond growth rate on substrate orientation as a function of process parameters in the high microwave power density regime,”

Phys. Status Solidi Appl. Mater. Sci., vol. 205, no. 9, pp. 2114–2120, 2008.

- [150] C. J. Widmann, W. Müller-Sebert, N. Lang, and C. E. Nebel, “Homoepitaxial Growth of Single Crystalline CVD-diamond,” *Diam. Relat. Mater.*, vol. 64, pp. 1–7, 2016.
- [151] A. B. Muchnikov, A. L. Vikharev, A. M. Gorbachev, D. B. Radishev, V. D. Blank, and S. A. Terentiev, “Homoepitaxial single crystal diamond growth at different gas pressures and MPACVD reactor configurations,” *Diam. Relat. Mater.*, vol. 19, no. 5–6, pp. 432–436, 2010.
- [152] J. Lu, “Single Crystal Microwave Plasma Assisted Chemical Vapor Diamond Synthesis at High Pressures and High Power Densities,” 2013.
- [153] A. B. Muchnikov, A. L. Vikharev, A. M. Gorbachev, and D. B. Radishev, “Comparative study of homoepitaxial single crystal diamond growth at continuous and pulsed mode of MPACVD reactor operation,” *Diam. Relat. Mater.*, vol. 20, no. 8, pp. 1225–1228, 2011.
- [154] A. L. Vikharev *et al.*, “Comparison of pulsed and CW regimes of MPACVD reactor operation,” *Diam. Relat. Mater.*, vol. 12, no. 3–7, pp. 272–276, 2003.
- [155] A. Tallaire *et al.*, “Multiple growth and characterization of thick diamond single crystals using chemical vapour deposition working in pulsed mode,” *J. Cryst. Growth*, vol. 291, no. 2, pp. 533–539, 2006.
- [156] Y. Kato, H. Umezawa, H. Yamaguchi, and S. Shikata, “X-ray topography used to observe dislocations in epitaxially grown diamond film,” *Jpn. J. Appl. Phys.*, vol. 51, no. 9, 2012.
- [157] H. Pinto and R. Jones, “Theory of the birefringence due to dislocations in single crystal CVD diamond,” *J. Phys. Condens. Matter*, vol. 21, p. 364220, 2009.
- [158] T. Teraji, M. Hamada, H. Wada, M. Yamamoto, and T. Ito, “High rate growth and electrical/optical properties of high-quality homoepitaxial diamond (100) films,” *Diam. Relat. Mater.*, vol. 14, no. 11–12, pp. 255–260, 2005.
- [159] A. Charris, S. Nad, and J. Asmussen, “Exploring constant substrate temperature and constant high pressure SCD growth using variable pocket holder depths,” *Diam. Relat. Mater.*, vol. 76, no. December 2016, pp. 58–67, 2017.
- [160] T. Grotjohn, A. Hardy, M. Becker, A. Charris, J. Asmussen, and T. Schuelke, “Diamond Based Power Electronics: Material and Devices - MRS Europe,” 2016.